2018

NCREE Research Programs and Accomplishments

National Center for Research on Earthquake Engineering
National Applied Research Laboratories

Contents

Development of Wave Spectra under Northeast Monsoons Offshore of Changhua, Taiwan

Yuan-Shiang Tsai[1] and Tsung-Jen Teng[2]

蔡原祥 [1]、鄧崇任 [2]

Abstract

In the design of support structures for offshore wind turbines, the JONSWAP spectrum is usually used to calculate fatigue loadings induced by waves in the frequency domain. It is interesting to study whether the wave spectra observed in the Taiwan Strait agrees with the JONSWAP spectrum. Buoy observations of the surface elevation acted on by northeast monsoons were employed to calculate the wave spectra with the ensemble average grouped by wave ages. The results show that the spectral peak energy grows and the frequency of the spectral peak decreases with the increase of the wind speed. The mean spectra with young wave ages show good agreement with the JONSWAP spectrum, while the lower frequency portions show higher energy. This indicates that the sea state developed offshore of Changhua is a mixture of wind waves and swells.

Keywords: JONSWAP, northeast monsoon, wave age, wave spectrum

Introduction

The development of the offshore wind energy industry has attracted a great deal of attention in Taiwan. With an annual mean wind speed of over 7 m s^{-1}, the potential wind power is estimated to be at least 6–10 GW in the Taiwan Strait. There is a specific site offshore of Changhua in the mid-south coast of Taiwan where it is planned to construct several large-scale wind farms. For the design of support structures for the wind turbines, it is essential to assess the characteristics of the surface waves according to the sea states by analyzing the wave spectra, which is very helpful for calculating the loading of wave-induced fatigue using the frequency-domain method.

The wave spectra most widely applied in engineering practice are the Pierson–Moskowitz (P-M) spectrum and the JONSWAP spectrum (Pierson 1964, Moskowitz 1964, Hasselmann *et al.* 1973). The P-M spectrum describes the fully developed sea state, observed from long-term observations in the North Sea. In contrast, the well-known JONSWAP spectrum is the measurement result of the Joint North Sea Wave Project (JONSWAP) conducted in the North Sea off the west coast of Denmark, which was restricted by a fetch-limited condition with the wind waves in developing. The JONSWAP model is a generalized formulation of the P-M model obtained by multiplying a peak-enhancement factor which describes the sea state.

It is not clear whether the JONSWAP spectrum is applicable to surface waves in the Taiwan Strait, where they are mainly generated by the seasonal trade winds mixed with the sea–land circulation raised by thermal buoyancy. This is substantially different from the situation in the North Sea (Tsai *et al.* 2018). In this respect, using local data to clarify whether the JONSWAP spectrum can be adopted as a wave simulator for the Taiwan Strait area is important for the design of the wind turbines to be used there.

One year of buoy data recorded offshore of Changhua was used to calculate the wave amplitude spectrum and make a comparison with the JONSWAP spectrum. The present study restricted the atmospheric stratification to be neutral for the northeast monsoon season. Tsai *et al.* (2018) showed that the mixed sea state in combination with wind waves and swells was formed offshore of Changhua in the winter season. To quantify this complex sea state, the wave age C_p/U_{10} is used, where C_p represents the phase velocity at the spectral peak and U_{10} represents the wind speed at 10

[1]Associated Researcher, National Center for Research on Earthquake Engineering
[2] Research Fellow, National Center for Research on Earthquake Engineering

m in height, to relate the wind and wave coupling. Hence, the spectra are grouped by the bins of wave ages and we further use the bins of mean wind speed to produce the ensemble average of the wave spectra.

Wave spectrum models

The P-M spectrum describes a sea state with mature waves; that is, the waves cannot absorb any more energy under the wind action. The spectrum is formulated as follows:

$$S(f) = \alpha_{PM} \frac{g^2}{(2\pi)^4} f_p f^{-5} exp\left[-\frac{5}{4}\left(\frac{f}{f_p}\right)^{-4}\right] \tag{1}$$

where f denotes frequency, f_p denotes spectral peak frequency, H_s denotes significant wave height, and α_{PM} denotes a constant depending on the wind speed.

The JONSWAP spectrum characterizes the growth of waves under the fetch-limited condition. Hence, the ocean waves are unlikely to be fully developed. A peak-enhancement factor is implemented to modify the P-M spectrum. The resulting well-known JONSWAP spectrum is expressed as follows:

$$S(f) = \alpha_J \frac{g^2}{(2\pi)^4} f^{-5} exp\left[-\frac{5}{4}\left(\frac{f}{f_p}\right)^{-4}\right] \gamma^{exp\left[-0.5\left(\frac{f-f_p}{\sigma f_p}\right)^2\right]} \tag{2}$$

where g is gravitational acceleration, α_J represents the Phillips constant, $\alpha_J = \pi^4\left(5H_s^2 f_p^4/g^2\right)(1 - 0.287 ln\gamma)$, σ represents the parameter of spectral width ($\sigma = 0.07$ for $f \le f_p$ and $\sigma = 0.09$ for $f > f_p$), and γ represents the peak-enhancement factor:

$$\gamma = \begin{cases} 5 & for \ \frac{T_p}{\sqrt{H_S}} \le 3.6 \\ exp\left(5.75 - 1.15\frac{T_p}{\sqrt{H_S}}\right) & for \ 3.6 < \frac{T_p}{\sqrt{H_S}} \le 5 \\ 1 & for \ 5 < \frac{T_p}{\sqrt{H_S}} \end{cases} \tag{3}$$

where T_p represents the period at the spectral peak.

Buoy data processing

The buoy data were recorded over one year from August 2012 to July 2013 offshore of Fangyuan, Changhua County, located approximately 14 km from the coast. Detailed descriptions of the wind speed and wave measurements and instrumentations were provided by Tsai *et al*. (2018).

The power law was used to convert the wind speed observed at 2.9 m to the equivalent wind speed at 10 m in height:

$$\frac{U_{10}}{U_r} = \left(\frac{z_{10}}{z_r}\right)^{\alpha} \tag{4}$$

where z_{10} denotes the height at 10 m, z_r and U_r denote the reference height and wind speed at the observation height of 2.9 m respectively, and α denotes the power exponent. With neutral stratification and assuming that the wind profile of the power law is equivalent to the logarithmic profile, at the height of 10 m the power exponent is approximated by:

$$\alpha \approx 0.1\phi_m\left(\frac{z}{L}\right) \tag{5}$$

where $\phi_m\ (z/L) = kz/u_*(\partial\ u/\partial\, z)$ represents the dimensionless wind shear with the following relation:

$$\phi_m\left(\frac{z}{L}\right) = \begin{cases} 1 + b\frac{z}{L}, & z/L < 0 \\ \left(1 - a\frac{z}{L}\right)^P, & z/L > 0 \end{cases} \tag{6}$$

where a = 15, b = 4.7, and p = −1/4 in the flat and homogeneous terrain (Businger *et al*. 1971).

An algorithm was written in C++ with iterations combining Eqs. (4), (5), and (6) to calculate U_{10}, in which the power exponent was given an initial value of 0.1. The convergence of the power exponent occurred with $|\alpha_I - \alpha_o| < 10^{-3}$, where α_1 was the solution of the next iteration of α_o.

The time series of the vertical accelerations observed by the buoy were directly integrated to obtain the vertical displacements, indicating the surface wave amplitudes:

$$\eta(t) = Hp\left(\iint(\ddot{z}(t)dt)dt\right) \tag{7}$$

where *Hp* denotes the high-pass filter and $\ddot{z}$ is the acceleration in the vertical direction, which is corrected for the buoy motion using the relation:

$$[\ddot{x}, \ddot{y}, \ddot{z}] = \boldsymbol{TA} \tag{8}$$

where $\boldsymbol{A}$ denotes axial accelerations recorded by the buoys and $\boldsymbol{T}$ denotes the coordinate transformation matrix for the coordinate of the rotation frame of the reference coordinates. The formulation of the transformation matrix is given by Edson *et al*. (1998).

The waves associated with northeast monsoons having wind directions of $\theta > 350°$ and $\theta < 45°$ were selected for the spectral analysis. Furthermore, wind and wave misalignment larger than 30° was excluded in the analysis. 10-min data sets were grouped by wave age with bins of 0.6, 0.8, 1.2, and 2.5

and wind speed bins of 2 m/s. The 10-min time series of wave records were transformed into wave amplitude power spectra using the Fast Fourier Transform. Ensemble averages were produced at each group of wave ages and wind speeds. For a mixed sea state, the criteria to distinguish wind waves and swells is when $C_p/U_{10} > 1.2$ for mature wind waves and $C_p/U_{10} < 1.2$ for young wind waves still in the development stage (Drennan *et al*. 1999).

Results

For northeast monsoons under neutral stratification and ignoring sea states represented by wave ages, overall averages of $U_{10n} = 11.88$ m/s, $H_s = 2.5$ m, and $C_p/U_{10n} = 1.05$ were obtained. Figure 1 shows the ensemble average of the wave spectrum in comparison with the JONSWAP spectrum. The spectral peak is located at $f_p = 0.125$ Hz, namely, where $T_p = 8$ s. Using Eq. (3), the peak-enhancement factor is calculated to be $\gamma = 1$. The results show that the JONSWAP spectrum underestimates the wave energy around the spectral peak. Theoretically, there should be a peak-enhancement factor that yields the observed value of the spectral peak and so the inconsistency is due to the fact that Eq. (3) does not appear to give the correct amount of amplification. Hence, for this long-term average, Eq. (3) failed to predict the observed peak value.

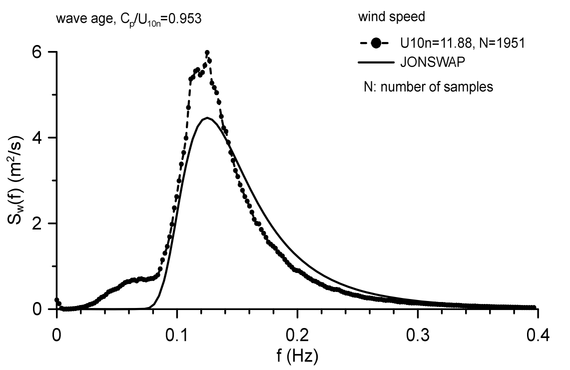

Figure 1 Total ensemble average for the wave spectrum with northeast monsoons with $U_{10n} = 11.88$ m/s, $H_s = 2.5$ m, $T_p = 8$ s, and $C_p/U_{10n} = 1.05$ in comparison with the JONSWAP spectrum.

For Fig. 1, it is noted that, for the JONSWAP spectrum with frequency less than 0.8, the wave energy is insignificant, implying the absence of long-period waves or swells in the limited-fetch condition of the North Sea. This is different from conditions in the Taiwan Strait because there the wind direction is generally and approximately parallel to the coast. Hence, the development of surface waves is under the long-duration and long-fetch conditions, resulting in the existence of long-period waves with $f < 0.8$ as shown in Figure 1. Further investigations are required to understand the offshore structural loads caused by these low-frequency waves.

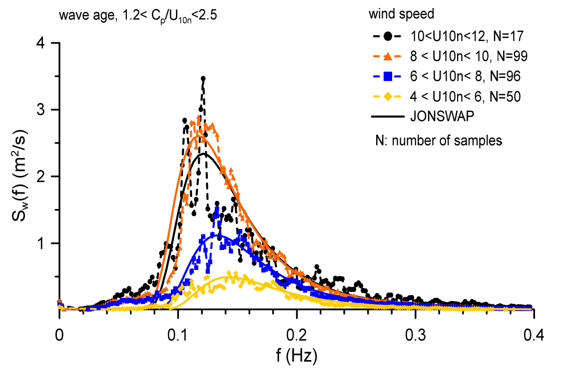

Figure 2 Wave spectra calculated for wave ages $1.2 < C_p/U_{10n} < 2.5$ in comparison with the JONSWAP spectrum.

The disagreement between the observed and JONSWAP spectra may be attributed to an incorrect representation of the sea state using the total mean values of H_s and T_p. This is because the formation of the actual sea state is complex. For example, wave growth is not significant for short durations or fetches under the action of strong winds, owing to the delay effect when energy transfers from wind to waves. This creates the scenario of having strong winds but insignificant wave growth at the site. In contrast, if an extreme wind field such as a super typhoon forms a thousand kilometers away, the generated waves can absorb the wind energy to form swells after travelling a long distance, giving rise to weak winds but large waves at the site. Hence, to describe the relation between wind and waves, the wave age appears to be an appropriate parameter.

Figure 2 shows the wave spectra with wave ages of $1.2 < C_p/U_{10n} < 2.5$ with the subgroups divided according to wind speed, with bins of 2 m/s. The observed spectra are consistent with the JONSWAP prediction. For these mature waves, except for the wind speed range of $10 < U_{10n} < 12$, which had less samples, the spectral peak increases and the peak frequency decreases with the increase of wind speed. All three wind speed ranges show a peak-enhancement factor of $\gamma = 1$, which is related to the definition of mature waves ($C_p/U_{10n} > 1.2$).

The development of the spectra at different wind speeds in the range of $0.8 < C_p/U_{10n} < 1.2$ is demonstrated in Fig. 3. The growth of the spectrum is consistent with Fig. 2, that is, with the increase of wind speed, the spectral energy increases and the peak frequency decreases. The observed spectra are analogous to the JONSWAP spectrum and the P-M spectrum when $\gamma = 1$. For wave ages less than the case given in Fig. 1, the spectrum shape is sharp and narrower and shows a significant increase of the spectral peak energy. The wave ages identify the waves as not being mature but this is inconsistent with the spectra displayed in Fig. 2 with $\gamma = 1$, denoting the mature sea state. In addition, the spectra show that the shape on the left side of the peak is slightly steeper than that of JONSWAP, indicating that the width parameter $\sigma = 0.09$ with $f \le f_p$ may not exactly fit the observation. It is noted that for the high wind speed range $16 < U_{10n} < 18$ in the low-frequency portion with $f < 0.06$ there is significant wave energy, which is unlike the JONSWAP spectrum.

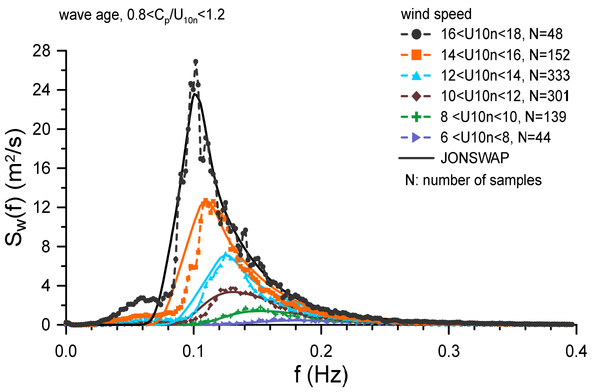

Figure 3 Wave spectra calculated at wave ages of $0.8 < C_p/U_{10n} < 1.2$ in comparison with the JONSWAP spectrum.

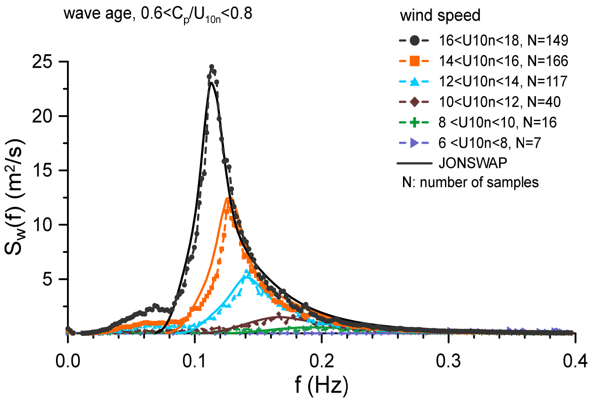

Figure 4 Wave spectra calculated at wave ages of $0.6 < C_p/U_{10n} < 0.8$ in comparison with the JONSWAP spectrum.

Figure 4 demonstrates the spectrum with wave ages in the range of $0.8 < C_p/U_{10n} < 1.2$. Generally, the spectral features are consistent with those described in Fig. 3. The spectral shape becomes sharper and narrower than those shown in Fig.3, resulting in better agreement with the prediction of the JONSWAP spectrum. The γ values are less than 1 under this condition of younger wave ages. The wave energy appears in the low-frequency portion of the spectrum with strong wind action, which is different to the JONSWAP spectrum. This reveals that the swells are generated by the long fetch acted on by the northeast monsoon in winter, proving the mixed sea state of offshore Changhua. In this circumstance, the ultimate load and fatigue caused by the mixed sea state in combination with the wind waves and swells acting on the support structures of wind turbines requires further investigation.

Conclusions

The study of wave spectra generated by the northeast monsoon shows that by using the parameter of wave age to classify the sea state, the ensemble averages of wave spectra are in agreement with the JONSWAP spectrum, particularly for younger wind waves. The wave energy observed at low frequencies, however, indicates that the surface waves contain wind waves and swells, which form the complex sea state, and this is slightly different to the JONSWAP spectrum. The calculation shows that the peak-enhancement factor, described by H_s and T_p, with $\gamma = 1$ representing the fully developed sea, is not consistent with the wave age for mature waves as defined by C_p/U_{10} >1.2.

References

Businger, J. A., J. C. Wyngaard, Y. Izumi, and E. F. Bradley (1971) Flux-profile relationships in the atmospheric surface layer, *Journal of Atmospheric Science*, 28, 181-189.

Drennan, W. M., Kahma, K. K., and Donelan, M. A. (1999) On the momentum flux and velocity spectra over waves, *Boundary-layer Meteo*., 92, 489-515.

DNVGL (2016) Loads and site conditions for wind turbines, DNVGL-ST-0437, DNV GL AS

Edson, J. B., Hinton, A. A., Prada, K. E., Hare, J. E., and Fairall, C. W. (1998) Direct covariance flux estimates from mobile platforms at sea, *J Atmos. Oceanic Tech.*, 15, 547-561.

Hasselmann, K., Bamett, T.P., Bouws, E., Carlson, H., Cartwright, D.E., Enke, K., Ewing, J.A., Gienapp, H., Hasselmann, D.E., Kruseman, P., Meerbrug, A., Mliller, P., Olbers, DJ., Richter, K., Sell, W., Walden, H. (1973) Measurements of wind-wave growth and swell decay during the Joint North Sea Wave Project (JONSWAP). Dtsch. Hydrogr. Z., A 80 (12), 95 pp.

Moskowitz, L. (1964) Estimates of the power spectrums for fully developed seas for wind speeds of 20 to 40 knots. *J. Geophys. Res.,* 69, 5161–5179.

Pierson W. J. (1964) The interpretation of wave spectrum in terms of the wind profile instead of the wind measured at a constant height. *J. Geophys. Res.,* 69, 5191–5203.

Tsai, Y. S., Chang, W. T., Yu, C. M. and Yang, W. C. (2018) General sea state and drag coefficient observed near shore in Taiwan Strait, Procedia IUTAM, **26**, 204-213

Site Amplification of the Strong-motion Stations in Taiwan Derived from Their Shallow Shear-wave Velocity

Che-Min Lin[1], Chun-Hsiang Kuo[2], Jyun-Yan Huang[3]

林哲民 [1]、郭俊翔 [2]、黃雋彥 [3]

Abstract

In our previous study, the one-dimensional shallow shear-wave velocity (Vs) profiles of the Taiwan Strong Motion Instrumentation Program (TSMIP) stations were estimated using the Receiver Function (RF) technique. However, the accuracy of the velocity models should be evaluated for further applications. In this study, the records of the TSMIP stations are analyzed using the horizontal to vertical spectral ratio (HVSR) method to get the observed site effects. The theoretical transfer function of the Vs profile can be calculated for every station because the estimated shallow Vs profiles are from the ground surface to the deep bedrock and include the range where the seismic site effect principally occurs. The calculated transfer functions can be seen as the one-dimensional theoretical seismic site effects of the TSMIP stations and can be compared with the observed HVSRs from the seismic records. All these comparisons indicate that the shallow Vs profiles of the TSMIP stations, as obtained using the RF method, are mostly reliable and represent the real seismic site effect. The site predominant frequency and site characteristics of a station can be reproduced by the theoretical transfer function. Misestimates may come from 3D structural effects, surface waves, and attenuation effects. These Vs profiles and the combined model of the shallow part that dominates the seismic site effect will benefit ground motion predictions and numerical simulations in seismology and earthquake engineering.

Keywords: TSMIP, Strong-motion Station, Site effect, Shear-wave Velocity

Introduction

Located at the convergence boundary of the Philippine Sea plate and the Eurasian plate, the high seismic hazard is an essential issue of Taiwan. The island is covered by many sedimentary basins, including the Taipei Basin (TB), Ilan Plain (IP), Western Coastal Plain (WCP), Pingtong Plain, etc. The basins are vulnerable to earthquakes because the soft and thick sedimentary usually amplifies and extends the seismic waveforms by its site effect to affect the safety of structures and induce earthquake disasters. To reduce earthquake disasters, it is important to clarify the seismic site effect and its origin within each region.

When seismic waves propagate through the strata with different velocities beneath a site, seismic waves will focus or disperse based on Snell's law to increase or reduce energy. This means that the seismic site effect at a site is controlled by the velocity structure of the strata, especially the shallow part between the near-surface soil and hard bedrock. Therefore, the one-dimensional shallow shear-wave velocity (Vs) profiles of the Taiwan Strong Motion Instrumentation Program (TSMIP) stations were all estimated using the Receiver Function (RF) technique in our previous study (Lin et al., 2018). The results include not only the Vs profile but also site parameters such as the engineering bedrock, Vs30 (the average shear-wave velocity of the top thirty meters of the ground) and $Z_{1.0}$ (the depth of the velocity horizon where the shear-wave velocity reaches 1.0 km/sec). This will benefit seismology and earthquake engineering in the future, though the accuracy of the velocity models should be evaluated for future applications. In this study, the observed earthquake records of the TSMIP stations are used to check that the estimated velocity profiles agree with the real site effect.

---

[1] Associate Researcher, National Center for Research on Earthquake Engineering

[2] Research Fellow, National Center for Research on Earthquake Engineering

[3] Assistant Researcher, National Center for Research on Earthquake Engineering

Observed Site Effect

The Central Weather Bureau (CWB) started the TSMIP in 1990 and distributed strong motion stations in metropolitan areas and near-fault regions to collect seismograms. The TSMIP network can collect abundant and high-quality strong motion data. This was particularly proven through the near-fault data collected from the 1999 Chi-Chi earthquake which has contributed significantly to seismology and engineering.

The TSMIP strong-motion stations are all installed at free-field sites. Every seismic record collected by the TSMIP stations contains the site effect of ground motion at the sites. The observed site characteristics of a station provide a basis for evaluating and comparing its velocity profile. In this study, the records of 763 TSMIP stations, collected between 1992 and 2013, are analyzed. This includes the shallow shear-wave velocity profiles estimated in our previous study. Some records with low waveform qualities and peak ground accelerations (PGA) higher than 60 gal were eliminated. The numbers of records used for stations vary and can be between several records and hundreds of records. Because it is hard to find a nearby reference station at a rock site for most of the TSMIP stations, we use the horizontal to vertical spectral ratio (HVSR) method, also called the single-station method, to calculate the seismic site effect. This method assumes that the site effect mostly only affects the horizontal component but not the vertical component (Nakamura, 1989; Lermo and Chávez-García, 1993). In the analysis, the three-component waveforms after the S-wave arrivals were used to calculate the Fourier Spectra. The vertical spectrum is divided by the vector sum of the two horizontal spectra to get the HVSR. A HVSR means the variation of seismic waveforms in the frequency domains is induced by the site characteristics. A higher ratio of HVSRs at a frequency signifies higher site amplification. All the HVSRs of a station are averaged to get a final HVSR that presents its observed seismic site effect.

Figure 1 shows the three-component waveforms of an earthquake and the average HVSR of station TAP104. The amplification of the HVSR focusing on the higher frequency band between 10 and 20 Hz reflect that the site is hard. The largest spectral ration of the HVSR is at 15.22 Hz, which is seen as the predominant frequency for site TAP104. Generally, the predominantly high frequency indicates a hard site with a higher velocity or thinner sediment; the low predominant frequency means a soft site with a lower velocity or thicker sediment.

The variation of the seismic site effect in Taiwan can be presented in detail by the HVSRs of 763 TSMIP stations. Figure 2 shows the distribution of the predominant frequencies of the HVSRs observed at all the TSMIP stations in Taiwan. Most of the stations located inside of the sedimentary basins have predominant site frequencies lower than 3 Hz. The stations located at the Western Foothill Region and mountain region, expect some sitting on river valleys or local sedimentaries, have high predominant frequencies. The overall site characteristics of the real seismic records agree with the regional background geology in Taiwan. If the shallow velocity profiles of the TSMIP stations are accurate enough, their theoretical site effects should exhibit the same or similar characteristics with the observed and true ones shown here.

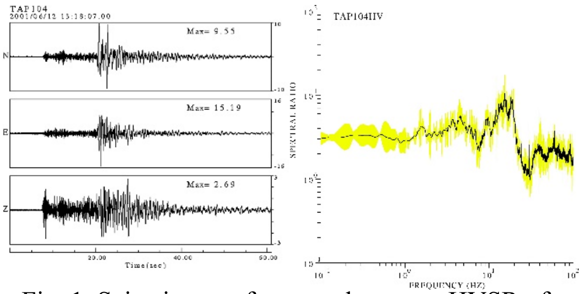

Fig. 1. Seismic waveforms and average HVSR of the TAP104 station

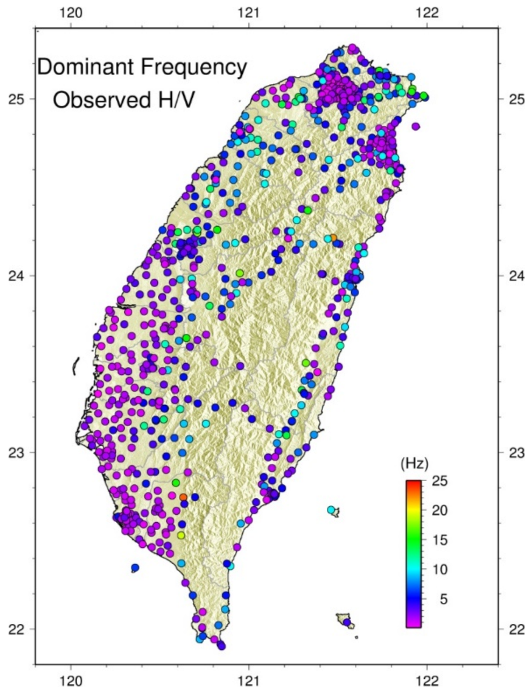

Fig. 2. Predominant frequencies of the HVSRs observed at all TSMIP stations in Taiwan

Theoretical Transfer Function of Vs Profile

The one-dimensional shallow Vs profiles of the 763 TSMIP stations estimated using RF analysis include the major interface from the surface alluvial deposit with a Vs lower than 0.3 km/sec to the hard bedrock with a Vs higher than 2 km/sec. The depth range of the profiles varies with the site geology. The depths of the Vs profiles for the sites at sedimentary basins are typically larger than 2 km, and the hard site at mountain regions may only be several hundred meters or less (Lin et al., 2018).

The theoretical transfer function of the Vs profile can be calculated for every station based on the Haskell Matrix (Haskell, 1960) for the vertical incident SH-wave. A transfer function of the strata is the reaction of a seismic wave propagated through them in the frequency domain because the shallow Vs profiles we estimated are from the ground surface to the deep bedrock and include the range where the seismic site effect principally occurs. The calculated transfer functions can be seen as the one- dimension theoretical seismic site effects of the TSMIP stations and can be compared with the observed HVSRs.

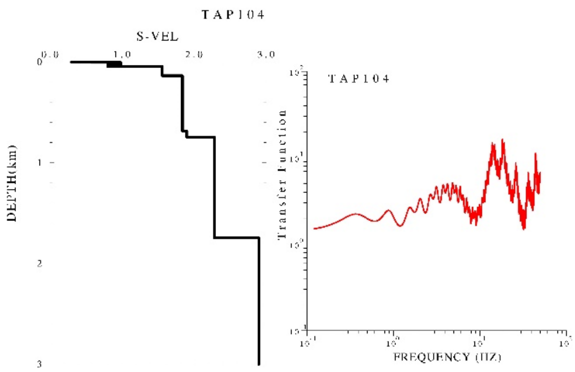

Fig. 3. Shallow shear-wave velocity profile of the TAP104 station and the corresponding theoretical transfer function

Figure 3 shows the shallow Vs profile of the TAP104 station and the corresponding theoretical transfer function. TAP104 is located at the Hsieh-ho Power Plant in Keelung. The Vs is about 0.3 km/sec at the ground surface and quickly increases to 1 km/sec and 1.56 km/sec at a depth of six meters and forty meters, respectively. The Vs of TAP104 then reaches 2.0 km/sec at a depth of 0.75 km. The high Vs near the ground surface indicates a shallow bedrock beneath the TAP104 station. The theoretical transfer function of the Vs profile we calculated is similar to the observed HVSR in Fig. 1. The frequency band of amplification between 10 and 20 Hz and the predominant frequency at 15.01 Hz are both close to the HVSR. Figure 4 presents the distribution of the predominant frequencies of the theoretical transfer functions for all the TSMIP stations. The theoretical predominant frequencies exhibit a similar trend to the seismic record data. The lower predominant frequencies are distributed in the plains, while the higher predominant frequencies are distributed in the mountain regions.

Results and Discussion

According to the resemblance between the observed HVSRs from seismic records and the theoretical transfer functions of the Vs profiles for the TAP104 station, this kind of comparison can help us evaluate the shallow Vs profiles of the TSMIP stations. There are more comparisons shown in Fig. 5. The theoretical transfer functions mostly agree with the observed HVSR, especially for the frequency band near or lower than the predominant frequency. The theoretical amplitudes are usually higher than the observation at the frequency band higher than the predominant frequency, although their curves are roughly similar to each other. This is likely to have occurred due to two factors. Firstly, the surface wave in real seismic records may depress the real site amplification in the frequency band higher than the dominant frequency thus resulting in an overestimate of the high-frequency band. Secondly, the Haskell matrix does not include the attenuation effect, which decreases the high-frequency energy a lot.

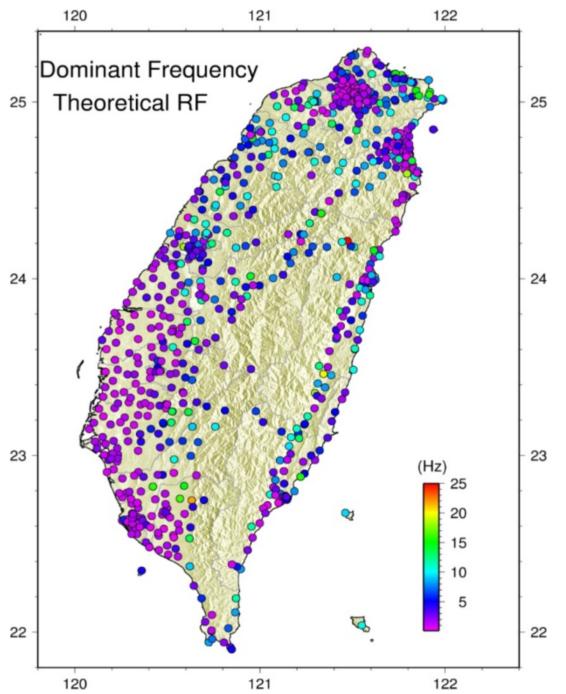

Fig. 4. Predominant frequencies of the theoretical transfer functions calculated for all the TSMIP stations in Taiwan

Of course, some stations present a large difference between their observed HVSRs and theoretical transfer functions. Here, we combine the linear correlation with the error of the predominant frequency to define the goodness of fit between the observed and theoretical site effect. Figure 6 shows the goodness of fit between the observed HVSRs and theoretical transfer functions for all TSMIP stations. Most stations have a goodness of fit higher than 0.5. This means that the Vs profiles we estimated approximately reflect the real seismic site effect observed in records. There are about fifty stations with a goodness of fit higher than 0.7. The Vs profiles of these cases usually contain only one interface with high-velocity contrast at the shallow part. This kind of profile produces a simple HVSR with a large peak at high frequency and can be easily simulated by the RF method. The stations that produce a low goodness of fit mostly sit in the mountain region or at the boundary of basins. Complex three-dimensional structural effects may result in the misestimate of our one-dimensional profile.

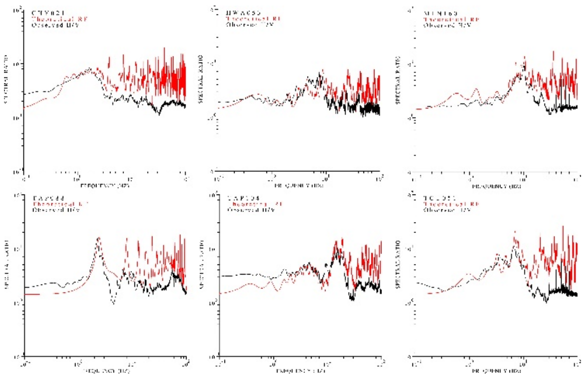

Fig. 5. Comparisons between observed HVSRs from seismic records and theoretical transfer functions for six stations

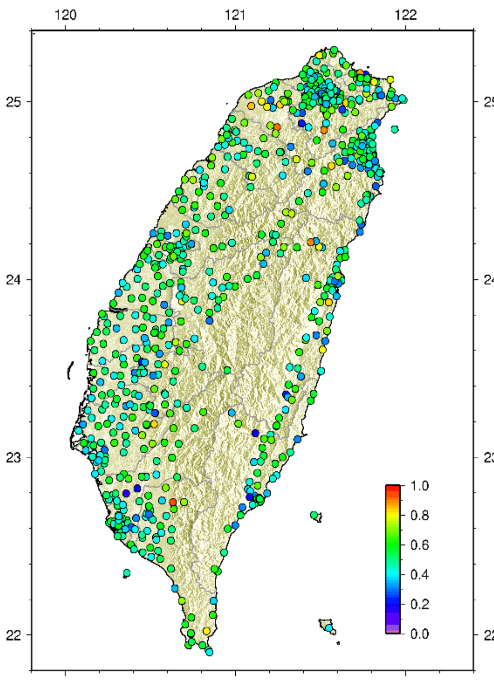

Fig. 6. Goodness of fit between observed HVSRs from seismic records and theoretical transfer functions of the TSMIP stations

Figure 7 presents the comparisons between the measured and theoretical predominant frequencies. The Vs30 values of the TSMIP stations are also labeled (Kuo et al., 2017). The error distribution of the theoretical predominant frequencies against the measured ones shows some overestimate and underestimate at the sites located in the mountain region or at the boundary of basins. The errors of 66% of stations are lower than 10%. Moreover, over 80% of stations have errors lower than 30%.

All the results demonstrate that the shallow Vs profiles of the TSMIP stations we estimated using the RF method are mostly reliable and represent the real seismic site effect. The site predominant frequency and site characteristics of a station can be reproduced by the theoretical transfer function. The misestimates may come from 3D structural effects, surface waves, and attenuation. These Vs profiles and the combined model of the shallow part that dominates the seismic site effect will benefit ground motion predictions and numerical simulations in seismology and earthquake engineering.

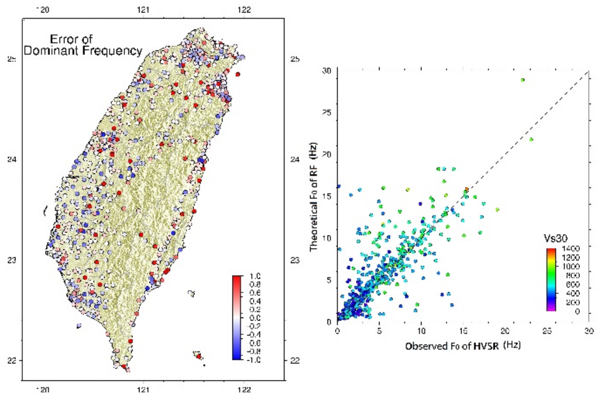

Fig. 7. Comparisons between the seismic record observations and theoretical predominant frequencies. The left figure is the error distribution of the theoretical values. The right figure shows the comparisons with the Vs30 values

References

Haskell N. A. (1960), “Crustal reflection of plane SH waves,” J. Geophys Res., 65, 4147-4150.

Lermo, J., and Chávez-García, F. J. (1993), “Site effect evaluation using spectral ratios with only one station,” Bull. Seism. Soc. Am., 83, 1574-1594.

Nakamura, Y., (1989), “A method for dynamic characteristics estimation of subsurface using microtremor on the ground surface,” QR of RTRI, 30, 1, 25-33.

Kuo, C. H., Lin, C. M., Chang, S. C., Wen, K. L., and Hsieh, H. H., (2017), “Site Database for Taiwan Strong Motion Stations,” NCREE-17-004, technical report (in Chinese), pp. 80.

Lin, C. M., Kuo, C. H., Huang, J. Y., Hsieh, H. H., Si, C. C., and Wen, K. L. (2018), “Shallow Shear-wave Velocity Structures of TSMIP Stations in Taiwan,” NCREE-18-019, technical report (in chinese), pp. 141.

Strong Motion Characteristics of the 2018 Hualien Earthquake

Chun-Hsiang Kuo[1], Jyun-Yan Huang[2], Che-Min Lin[3], Ting-Yu Hsu[4], Shu-Hsien Chao[3], and Kuo-Liang Wen[5]

郭俊翔 [1]、黃雋彥 [2]、林哲民 [3]、許丁友 [4]、趙書賢 [3]、溫國樑 [5]

Abstract

The maximum observed peak ground acceleration and peak ground velocity at various stations during the 2018 Hualien, Taiwan earthquake were 594 Gal and 146 cm/s, respectively. Pulse-like velocities were observed at all stations within 4 km from the Milun Fault. The horizontal spectral accelerations of the pulse-like records indicated two obvious amplifications approximately at periods of 1.0 s and 2.0 s. Natural frequencies of 0.8 to 1.5 Hz were observed in the region near the Milun Fault using microtremor measurements. The spectral acceleration peak approximately at periods of 2.0 s is mostly seen in the east-west direction, indicating typical fault-normal seismic radiation from the fault rupture. Consequently, we contend that the amplifications of the spectral acceleration at approximately 1.0 s and 2.0 s were caused by site amplification and the rupture front, respectively. The site amplification at the 1.0 s period may have been one reason for the collapse of medium-rise buildings during this earthquake.

Keywords: Hualien earthquake, strong motion, site amplification, pulse-like velocity

Introduction

A destructive earthquake with a moment magnitude (M_W) of 6.4 occurred offshore to the north of Hualien City on February 6, 2018, resulting in 17 fatalities, 285 injured, more than 175 damaged buildings, and two damaged bridges that spanned the faults. An apparent slip of the Milun Fault was observed during the earthquake, although the epicenter was roughly 12.5 km offshore of the surface fault trace. According to the report released by the Central Weather Bureau (CWB), the epicenter was located at 121.7297°E and 24.1007°N (Fig. 1), the focal depth was 6.31 km, and the M_W was 6.2. The CWB calculated the focal mechanism using the centroid moment tensor solution and broadband seismic data obtained from Taiwan. The strike/dip/rake of the two obtained nodal planes were 216°/56°/26° and 111°/69°/144°. The United States Geological Survey (USGS) and Global Centroid Moment Tensor Project (GCMT) calculated similar focal mechanisms but a larger magnitude of 6.4. The Central Geological Survey (CGS) in Taiwan found clear left-lateral slips along the Milun and Lingding faults after the Hualien earthquake according to both GPS observations and field investigations. The real fault plane thus had to have struck in an approximately north–south direction, specifically 216°/56°/26°.

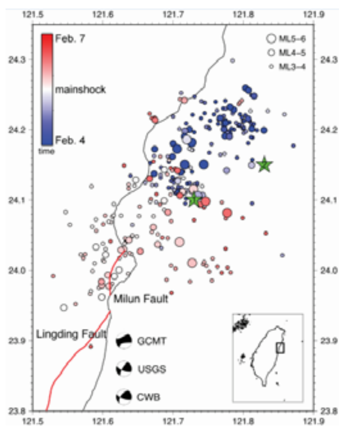

Fig. 1. Spatial and temporal distribution of the foreshocks, mainshock, and aftershocks during February 4–7, 2018

[1] Research Fellow, National Center for Research on Earthquake Engineering
[2] Assistant Researcher, National Center for Research on Earthquake Engineering
[3] Associate Researcher, National Center for Research on Earthquake Engineering
[4] Assistant Professor, National Taiwan University of Science and Technology
[5] Professor, National Central University

Strong Motion Observation

The CWB has installed more than 800 free-field strong motion stations throughout Taiwan, and the NCREE recently constructed the Seismic Array of NCREE in Taiwan (SANTA), which is a network of 37 real-time data collection stations equipped with strong motion and broadband sensors. Kuo et al. (2019) combined data from 270 stations in the CWB network and the 37 stations in the NCREE network to analyze the strong ground motion characteristics that occurred during the Hualien earthquake.

The maximum observed peak ground acceleration (PGA) was 594 Gal (NS component) with an epicentral distance of 12.6 km, which was recorded at the HWA057 station; the maximum observed peak ground velocity (PGV) was 146 cm/s (EW component) with an epicentral distance of 19.1 km, which was recorded at the HWA014 station. The shake map of the PGA, PGV, and spectral accelerations of 0.3 s (Sa0.3) and 1.0 s (Sa1.0) is depicted in Fig. 2. Taiwan determines the official intensity of earthquakes using only the PGA. The intensity level of 7 on that scale (PGA > 400 Gal), which is the highest level on the CWB scale, was recorded at five stations. These stations are sporadically distributed from North to South across a range of 60 km. We also used a separate unofficial intensity scale that uses comparable PGV and found that an intensity level of 7 (PGV > 75 cm/s) was recorded at 10 stations, all of which were located along the Milun Fault. The fragmentary distribution of the short-period response acceleration Sa0.3 between 800 Gal and 1200 Gal was similar to that of the PGA; however, the distribution pattern of the long-period response acceleration Sa1.0 was similar to that of the PGV. High PGV and/or Sa1.0 along the Milun Fault indicates that Hualien City suffered strong shaking with a period of 1.0 s, which may have been the major cause of the collapses of the four medium-rise buildings.

The strong ground motions recorded were compared with the ground motions estimated using the Chao17 GMPE (Chao et al., 2017), which was developed using data from Taiwan only. The comparison is presented in Fig. 3. Because of the lack of a reliable finite-fault model, we used the hypocentral distances of the stations for most of the intensity measures. For the near-fault stations, we directly used the distance from the stations to the Milun Fault as the shortest distance to the rupture (Rrup) because clear surface ruptures along the fault were observed after the mainshock. Fig. 3 depicts the comparison in terms of horizontal PGA, Sa1.0, and Sa3.0. The GMPEs are plotted using Vs30 of 240, 360, and 760 m/s for various site amplifications. The observed horizontal motions were converted into their RotD50 components, which is the median ground motion over all horizontal orientations. In this case we were particularly interested in the near-fault results (open circles). The estimated and observed ground motions were similar for short periods (PGA), but the estimates were smaller than the observed ground motions for long periods (Sa1.0 and Sa3.0). The Chao17 GMPE still does not take into account long-period ground motions caused by the forward-directivity effect, which would account for the obvious underestimation in the near-fault region.

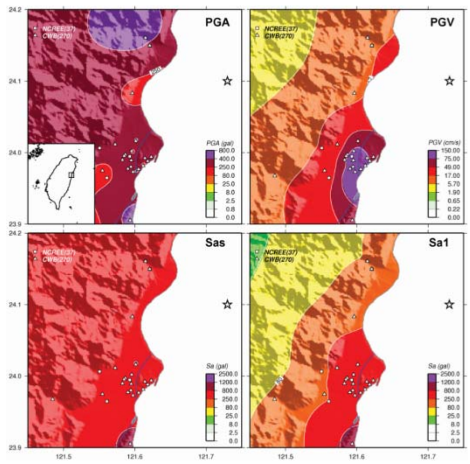

Fig. 2. Spatial distribution of intensity measures in terms of PGA, PGV, Sas, and Sa1

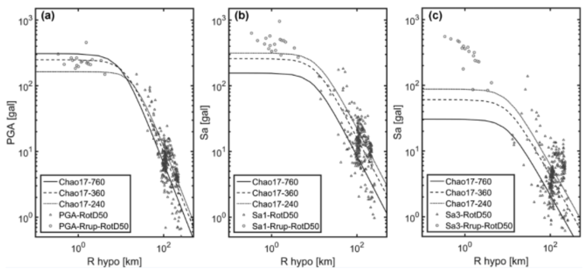

Fig. 3. Observed and estimated ground motions from the Chao17 GMPE, assuming Vs30 = 240, 360, and 760 m/s.

Seismic Site Conditions

Seismic site conditions in the near-fault region were investigated to understand the site effect and to further determine the strong ground motion behavior. Especially at the near-surface, S-wave velocity (Vs) has a major influence on seismic wave amplifications. Various Vs values and layer thicknesses can amplify seismic waves at specific frequencies in different ways. Vs30 is a continuous number that relates to the stiffness of the ground layers. For the sake of convenience and generality, Vs30 has been widely used to account for site amplifications in various approaches to strong ground motion prediction. In recent years, a new site parameter has been introduced into advanced GMPEs in Next Generation of Attenuation (NGA) projects to account for sedimentary depth (i.e., Z1.0) and to increase the accuracy of ground motion predictions. Z1.0 is the depth from the surface to the top of the layer with Vs > 1 km/s. Combining Vs30 and Z1.0 enables us to consider both the velocity and depth of soft sediments using GMPEs.

Kuo et al. (2017) obtained Vs30 data based on the Vs profiles logged at most of the free-field strong motion stations (Kuo et al. 2012) and then used estimations of Vs30 values to supplement missing data (data that were not logged). Z1.0 data from the same network were obtained from logged Vs profiles, microtremor arrays, receiver functions, or MHVSR inversions. We extracted the site parameters of the Hualien area to generate the distributions depicted in Fig. 4. The white triangles represent stations with parameters, and the other grids were interpolated into 0.3 arc minutes (~0.5 km) using the block average method from Generic Mapping Tools. The Vs30 map indicates that the Vs30 in the Hualien area is mostly between 360 and 760 m/s and belongs to site class C; however, part of Hualien City is site class D, with a Vs30 between 240 and 360 m/s. Borehole data indicate that the shallow layers in this region are composed of sand, clay, and gravel. The soft soils are primarily distributed to the west of the Milun Fault, along with the alluvium (Holocene),where the Z1.0 map shows a sedimentary thickness of roughly 300 m. To the east of the Milun Fault there is a terrace with higher topography and velocity, along with the Milun Formation (Pleistocene), where the sedimentary thickness is between 100 m and 200 m. Therefore, the maximum depth difference of approximately 200 m across the Milun Fault is likely due to the different geological conditions.

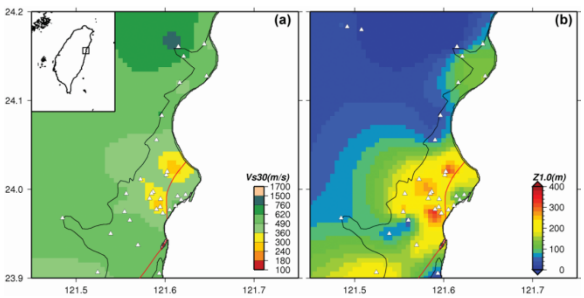

Fig. 4. Distributions of (a) Vs30 and (b) Z1.0.

Another well-known approach to understanding site effects is microtremor measurement. Fig. 5 depicts contours of the dominant frequencies of MHVSRs in the Hualien area. The black dots indicate single-station measurements, and the other grids were interpolated. We assert that the resonant frequency of S-wave amplification should be similar to that of MHVSR because clear peaks (for sufficiently high impedance contrast) can be seen in most of the MHVSRs in this region. The predominant frequencies in downtown Hualien are 0.8 to 1.5 Hz (yellow and green), changing to 1.2 to 1.5 Hz (green) to the west and further increasing to more than 1.5 Hz in the mountain range (blue). The locations of the microtremor measurements are different from those used in Fig. 4, and thus the distribution of the predominant frequency (Fig. 5a) is not as similar as those of Vs30 and Z1.0 (Fig. 4). Three MHVSRs near the collapsed buildings (red dots: no. 1, 2, and 4) are shown as well as an additional MHVSR for comparison (red dot: no. 3). All of them exhibit an obvious peak at 1 Hz, which indicates a uniform predominant frequency in the area (yellow).

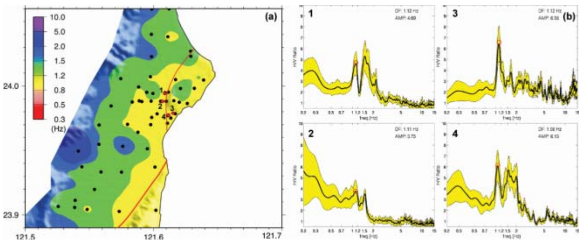

Fig. 5. MHVSR results in the Hualien region.

Near-Fault Ground Motions

Typical near-fault strong ground motions were recorded at all stations on both sides of the Milun Fault within 4 km during the 6.4 M_W Hualien mainshock, which is the distance between the S019 station and the Milun Fault. Somerville et al. (1997) contended that pulse-like velocities are usually observed in fault-normal and fault-parallel directions because of the S-wave radiation and fling effects in cases of strike-slip faulting. We adopted the pulse indicator method proposed by Shahi and Baker (2014) to identify the distribution of pulse-like velocities and maximum pulse direction for each station. The results clearly indicate that pulse-like velocities were observed on both sides of the Milun Fault and that the maximum pulses were mostly in the fault-normal direction (EW), especially near the southern portion of the Milun Fault. In this case, the pulse-like velocities were observed at stations along the Milun Fault with epicentral distances ranging from 15.5 km (HWA028) to 25.4 km (HWA060). The PGV contour demonstrates that the maximum PGV was larger than 120 cm/s and was observed at the southern end of the Milun Fault.

We thus know that the seismic site conditions (Vs30 and Z1.0) at the left and right sides of the Milun Fault are different; however, pulse-like velocities were observed on both sides and were strongest mostly in the fault-normal direction. Because most stations at locations having various site conditions recorded very similar strong motions, i.e. pulse-like velocities in the same direction (EW), we speculate that the pulse-like velocities recorded in the mainshock were not caused by the basin-edge effect.

The largest velocities and co-seismic displacements occurred at stations HWA019 and HWA014, which are located to the east and west of the south end of the Milun Fault, respectively. The co-seismic displacements indicate slight movements of approximately 0.5 m to the north and south at the east and west sides of the Milun Fault, indicating slipping to the left during the mainshock.

The three-component spectral accelerations at the 17 stations with velocity pulses were then calculated. They included 15 Taiwan Strong Motion Instrumentation Program (TSMIP) stations and two NEEWS stations (S009 and S019). Distinct peaks of spectral accelerations at periods of approximately 2.0 s were evident at most stations, especially from the EW (fault-normal) direction. The long-period peaks of spectral accelerations were identified as pulse-like waves; however, this revealed the problem that long-period accelerations go beyond the design and maximum considered spectra. The spectral accelerations of the 17 stations with velocity pulses were superimposed with the 475-year and 2500-year design spectra (CPA, 2011), as displayed in Fig. 6a. Although both design spectra considered the maximum site amplification and near-fault factors for a conservative comparison, the spectral accelerations at periods longer than 1.5 s still exceeded the most conservative design spectra for this region. Fig. 6b indicates the average result of the normalized spectral accelerations at the 16 stations with velocity pulses. Station HWA060 was not included because it is located near the Lingding Fault but not the Milun Fault. The closest stations to the collapsed medium-rise buildings, HWA008 and HWA019, recorded an obvious spectral acceleration peak at approximately 1.0 s from the NS component and another peak at approximately 2.0 s from the EW component. On the basis of microtremor analysis, we presume that the 1.0 s peak was also amplified by the local site effect and that the 2.0 s peak in the fault-normal direction might have been caused by the asperity, forward directivity amplification, and radiation pattern of the shear dislocation on the fault.

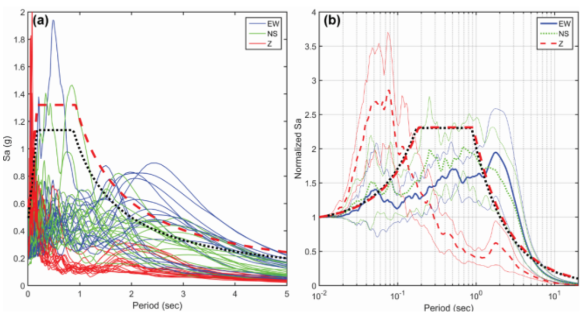

Fig. 6. (a) Spectral accelerations at the 17 stations that recorded pulse-like velocities and the design spectra (black and red dotted lines); (b) Average three-component spectral accelerations at 16 stations.

Conclusions

With the benefit of data from high-density free-field strong motion stations, we were able to analyze the Hualien earthquake by using a dozen near-field recordings. The Milun Fault, which passes through Hualien City from the north to the south, exhibited obvious strike-slip faulting during this event, and thus all 16 stations within 4 km on both sides of the fault recorded a large-amplitude and long-period velocity pulse. The major disaster caused by this event—the collapse of four medium-rise buildings—may have also been influenced by site amplifications at a period of approximately 1.0 s. The other peak in spectral acceleration occurred at a longer period of roughly 2.0 s in a fault-normal direction (EW) and was thus presumably generated by the asperity, forward directivity amplification, and seismic radiation of the shear dislocation on the fault.

References

Chao, S. H., Chen, Y. H., Hsu, C. C., and Lin, P. S. (2017), "Development of horizontal Taiwan ground motion model for crustal earthquake and subduction earthquake", Technical Report of National Center for Research on Earthquake Engineering, NCREE-17-009, 228 pp. (In Chinese)

CPA (2011), "Seismic design code and commentary for buildings", 2011 Edition, Construction and Planning Agency, Ministry of the Interior, Taipei, Taiwan. (In Chinese)

Kuo, C. H., Wen, K. L., Hsieh, H. H., Lin, C. M., Chang, T. M., and Kuo, K. W. (2012), "Site Classification and Vs30 estimation of free-field TSMIP stations using the logging data of EGDT", *Eng. Geol.* 129-130, 68-75.

Kuo, C. H., Lin, C. M., Chang, S. C., Wen, K. L., and Hsieh, H. H. (2017), "Site Database for Taiwan Strong Motion Stations", Technical Report of National Center for Research on Earthquake Engineering, NCREE-17-004, 80 pp. (In Chinese)

Kuo, C. H., Huang, J. Y., Lin, C. M., Hsu, T. Y., Chao, S. H., and Wen, K. L. (2019), "Strong ground motion and pulse-like velocity observations in the near-fault region of the 2018 Mw 6.4 Hualien, Taiwan earthquake", *Seismol. Res. Lett.* 90(1), 40-50.

Shahi, S. K. and Baker, J. W. (2014), "An efficient algorithm to identify strong-velocity pulse in multicomponent ground motions", *Bull. Seism. Soc. Am.* 104, 2456-2466.

Somerville, P. G., Smith, N. F., Graves, R. W., and Abrahamson, N. A. (1997), "Modification of empirical strong ground motion attenuation relations to include the amplitude and duration effects of rupture directivity", *Seismol. Res. Lett.* 68, 199-222.

(This report is modified from the published paper by Kuo et al. (2019))

Seismic Monitoring of the Tatun Volcano Group

Ya-Chuan Lai[1], Li-Chin Chang[2], Cheng-Horng Lin[3], Min-Hung Shih[4]

賴雅娟[1]、張麗琴[2]、林正洪[3]、史旻宏[4]

Abstract

A system, including seismic monitoring, crustal deformation, volcanic gas analyses, and geothermal measurement, has been established to monitor the volcanic activity of the Tatun Volcano Group. The real-time monitoring data will be useful in understanding the mechanism and behavior of volcanic eruptions, thereby alerting the public to possible volcanic activity and reducing the subsequent volcanic hazards. In general, seismic monitoring provides critical information for the evaluation of the possibility of volcanic eruption. Prior to volcanic eruptions, the hydrothermal system or magma becomes active, accompanied by many micro-earthquakes. Therefore, through the high-density seismic network, the temporal or spatial variations of seismicity in the Tatun volcano area will provide evidence of possible volcanism.

Keywords: Tatun Volcano Group, volcano monitoring, eruption, seismicity

Introduction

A number of volcanic activities and eruptions have happened in recent years, with some of these events resulting in heavy casualties. The phreatic eruption of Mount Ontake took place in 2014, killing dozens of climbers. The volcanic pyroclastic flow from the 2018 eruption of the Fuego volcano in Guatemala caused nearly 200 deaths and destruction of numerous villages. At the same time, the volcanic activity in Kilauea, Hawaii, did not cause casualties, but it did cause huge residential losses. The threat of volcanic disasters to human activity and society has significant impact on human life and safety, residential property, and the environment. Given these concerns, one must ask if there is such a volcano threat for the Tatun Volcano Group (TVG), in the northern part of Taiwan located in the Pacific volcanic chains.

The high helium isotope ratio, ranging from 5 to 7, found by Yang *et al*. (1999) implies that a magma chamber probably exists beneath the TVG. Furthermore, the last eruption at the TVG was 5–6 thousand years ago as determined from ash dating (Belousov *et al*., 2010). It has been concluded that the TVG is an active volcano, using the definition that an active volcano is one that has erupted during the past 10,000 years. The recent results from geological, geochemical, geophysical, and seismic observations also infer that the TVG is still active (Murase *et al*., 2014; Pu *et al*., 2014). Recently, a deep magma reservoir has been found from both S-wave shadows and P-wave delays in seismic observations (Lin, 2016).

Volcanic activities such as fumaroles, hot springs, and steam have been recently observed in the TVG. Since the distance between the TVG and Taipei metropolitan area is less than 20 km, there may be a strong volcanic impact if the TVG is active again in the future. Thus, how to improve understanding of the volcanic characteristics and activities in the TVG is not only an interesting scientific issue but also a matter of the safety of the Taipei metropolitan area. In order to monitor volcanic activity, various observation systems are being employed, including seismic observations, crustal deformation, volcanic gas analyses, and geothermal measurements. In addition to establishing long-term databases of the TVG and the corresponding characteristics, it is also helpful to understand the mechanism and behavior of volcanic eruptions, and thereby be alert to possible volcanic events, thus reducing possible losses caused by volcanic hazards.

1 Project Associated Researcher, National Center for Research on Earthquake Engineering
2 Project Assistant Researcher, National Center for Research on Earthquake Engineering
3 Research Fellow, Institute of Earth Sciences, Academia Sinica
4 Postdoc Fellow, Institute of Earth Sciences, Academia Sinica

Seismic Network

In order to monitor the seismic activity of the Tatun volcano area, a broadband seismic network was set up in 2003. The number of stations continued to increase, thus improving the capability of earthquake detection. In late 2007, there were a total of twelve seismic stations. Then, after some changes were made in 2008 to improve the signal resolution and location accuracy, Guralp CMG-6TD seismographs were installed. By the end of 2013, the number of broadband seismic stations had reached twenty, consequently the number of earthquakes detected has increased. During this period, the distribution of seismic networks mainly covered the area from Mt. Cising to Dayoukeng. In 2014, in order to increase the coverage of the survey area, a circular sub-array was added in the periphery of the main network.

At present, the seismic network is composed of forty broadband stations that monitor the activities of the TVG. Not only the low-frequency signals of internal vibration, but also the narrow-frequency noise generated by pressure can be clearly recorded by such a dense seismic network.

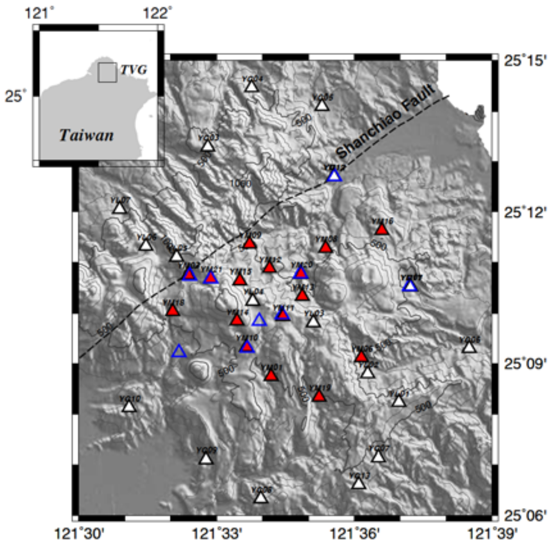

Fig. 1. The distribution of the seismic network of the TVG.

Background Seismicity

In general, seismic monitoring provides critical information to evaluate the possibility of volcanic eruption. A typical magma chamber is located at depths ranging from several to tens of kilometers. Volcanic eruption often results from molten magma migrating from the chamber to the surface. When the magma uplifts, many micro-earthquakes will be triggered along the path of magma migration. In other words, we can use the detection seismicity to determine the possible eruption time, location, and scale.

More than 20,000 micro-earthquakes have been detected between 2004 and 2018 by the dense seismic array in the Tatun volcano area. The distribution of seismicities shows several features. First, most events occurred on the southeast side of the Shanchiao fault, which is a normal fault dipping to the southeast. Significant clustering of the micro-earthquakes can be observed around Mt. Cising and Dayoukeng, where hydrothermal activities are high from geochemical observations. Secondly, the focal depths of the events primarily range from subsurface to 5 km, except the 2014 Shihlin earthquake sequences. Third, the magnitudes for most of the micro-earthquakes were less than 2.0 (Fig. 4). In particular, the catalog was dominated by events with magnitudes less than 1.0 during late 2009 to 2010, both for Mt. Cising and for the Dayoukeng area.

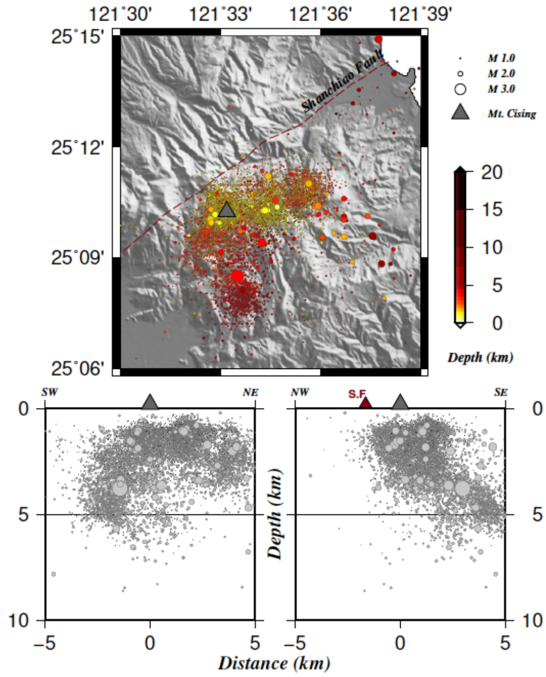

Fig. 2. The background seismicity of the TVG.

The spatial distribution illustrates obvious clustering of seismic activity, primarily in Mt. Cising and Dayoukeng, which are marked by group 1 and group 2. Additionally, a minor group (group 3) in the area between Bayan and Huangtsunshan is observed. The 2014 ML 4.2 Shihlin earthquake sequence occurred in the southern part, where the background seismicity is low.

Clear clusters are also displayed in the cross-section profiles with fault-parallel and fault-perpendicular strikes. Group 1 and group 2 events are concentrated at shallower depths, mostly from the subsurface to 3 km beneath Mt. Cising and Dayoukeng, which is also where the most hydrothermal activity is observed. Group 3 beneath Bayan primarily has limited depth, ranging from 1 to 4 km. It is worth noting that a seismic gap exists between the groups, suggesting that the structures beneath the TVG are very complicated and fragmented, and that the origins of the micro-earthquakes may vary.

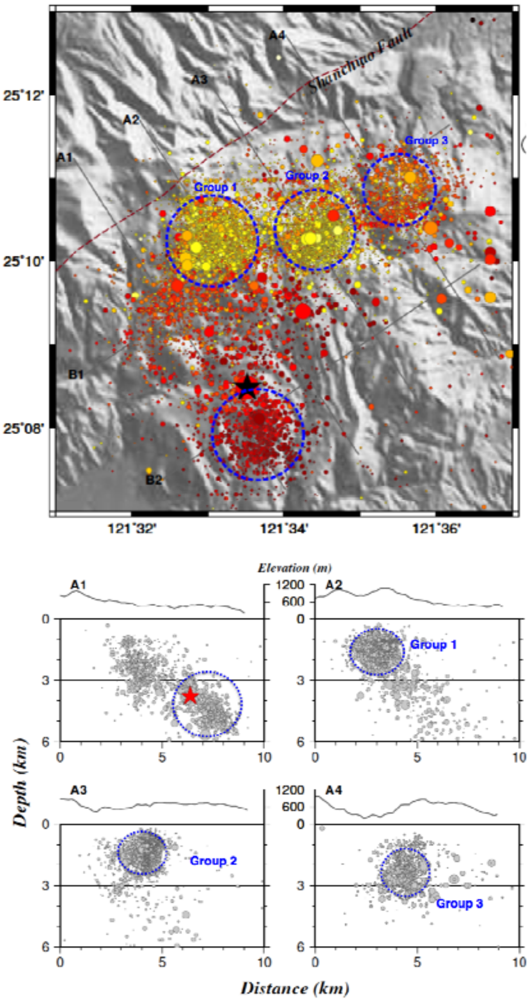

Fig. 3. The cross-sections of micro-earthquakes.

On average, around 150 to 200 earthquakes occur each month in the Tatun volcanic area. These earthquakes are quite small, with the magnitude for most of the micro-earthquakes being less than 1.0. Only 1–2 earthquakes per month are larger than 1.5.

Occasionally, the swarms occurred in Mt. Cising and Dayoukeng. During a limited time period, if hundreds of micro-earthquakes occur within a small area with no significant main-shock among them, this frequent sequence is defined as a swarm. This is very different from the microseismic activities of faulting, which are considered to be due to the activity of the hydrothermal system or magma.

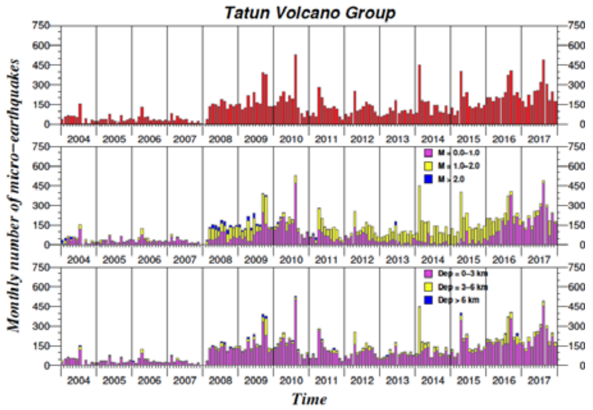

Fig. 4. Statistics on the number of microseisms of the TVG.

Recent variation of seismicity

Although the average number of microseisms that occur in the TVG is 150–200 per month, the seismicity seen in 2018 shows obvious temporal and spatial variation. The number of microseisms reached 486 in March, twice the average, and then significantly decreased to 81 in November, the lowest in 2018.

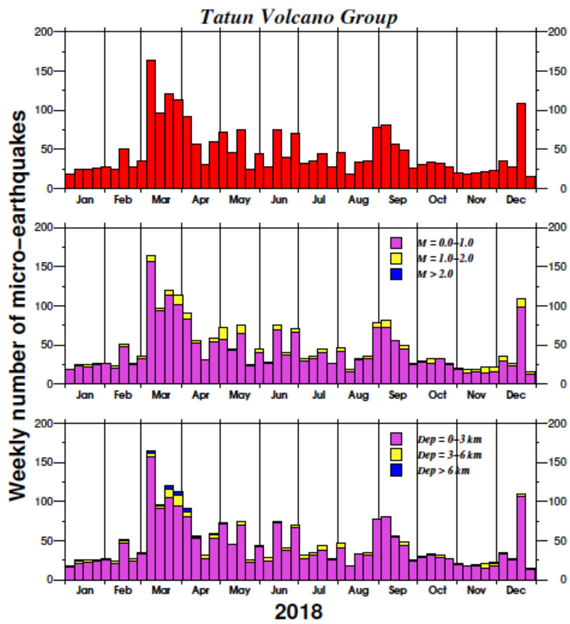

Fig. 5. Statistics on the number of micro- earthquakes of the TVG during 2018.

Overall, earthquake activity was high for several months after March, and then seismic activity decreased in October. Both the temporal variation and the seismicity in 2018 reveal an evident spatial variation, as seen in Fig. 6. The distribution of microseisms during 2018 is still mainly clustered in the Mt. Cising and Dayoukeng area, which is consistent with the past background seismic activity. However, it is worth noting that the seismicity of Dayoukeng and Bayan is more active than that of Mt.

Cising.

A number of swarms occurred, indicating that the hydrothermal system activity may increase beneath the Dayoukeng and Bayan areas. The observations combined with crustal deformation, geothermal measurements, and results of geochemical analysis do not illustrate synchronous anomalies. There may have been a limited increase in hydrothermal activity. To further understand the short-term and long-term patterns of the seismicity of the TVG, continuous monitoring is necessary.

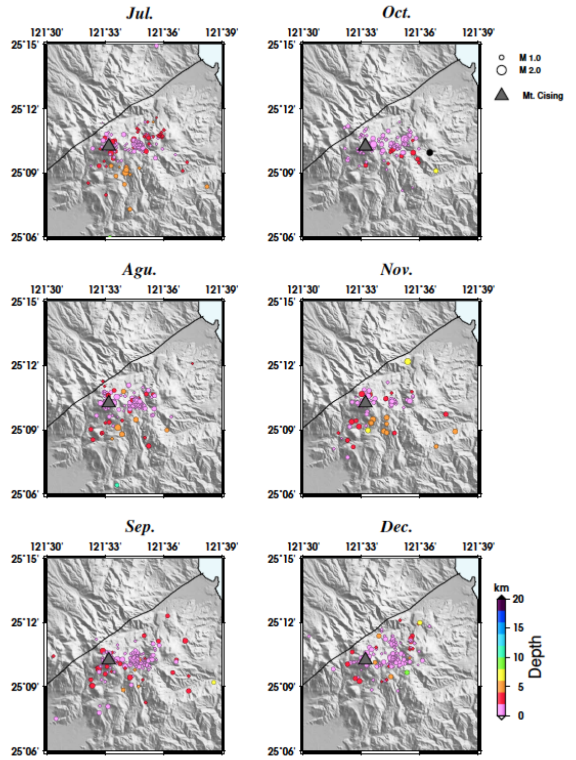

Fig. 6. The monthly seismicity distribution in 2018.

References

Belousov, A., Belousova, M., Chen, C.H. and Zellmer, G.F., J. Volcanol. Geotherm. Res., 191, 205-221, 2010.

Lin, C.H., Evidence for a magma reservoir beneath the Taipei metropolis of Taiwan from both S-wave shadows and P-wave delay, Scientific Reports, 6, 39500, 2016.

Murase, M., Lin, C.H., Kimata, F., Mori, H. and Pu, H.C., J. Volcanol. Geotherm. Res., 286, 30-40, 2014.

Pu, H.C., Lin, C.H., Huang, Y.C., Chang, L.C., Lee, H.F., Leu, P.L., Hsiao, N.C., Chang, C.H. and Yeh, Y.H., Terr. Atm. Ocean. Sci., 25, 625-635, 2014.

Yang, T.F. and Song, S.R., Nuovo Cimento Della Societa Italiana Di Fisica C22, 281-286, 1999.

Correlation between Variations in Chemical Compositions of Volcanic Gas and the Earthquake in Shihlin, Taipei City in 2014

Hsiao-fen Lee[1] and TVO team

李曉芬、大屯火山觀測站團隊

Abstract

The Tatun Volcano Group (TVG) is an active volcano located only approximately 15 km north of metropolitan Taipei. Two nuclear power plants are also located a few kilometers northeast of the TVG. Thus, carefully monitoring the volcanic activity is essential for residents in northern Taiwan. In the past decade, fumarolic gas samples have been regularly collected in order to record the variations in chemical compositions and helium isotope ratios. The results indicate that the volcanic activity of the TVG is stable. On February 12, 2014, an earthquake of Richter magnitude 4.2 occurred in the study area. After the earthquake, HCl concentration increased dramatically in the gas of a few fumaroles. This unique feature is useful for establishing a detailed model to depict the hydrothermal systems of the TVG. We believe that our data will fill a gap in current knowledge of the TVG and can provide crucial information for investigating the tectonic settings of northern Taiwan.

Keywords: Tatun Volcano Group, geochemistry, volcanic fluid variations, seismic events

Introduction

Taiwan is located at the junction of the Eurasian Plate and Philippine Sea Plate, resulting in a complex geological structure in Taiwan. The Tatun Volcano Group (TVG) is located in northern Taiwan, covering an area of approximately 250 km. An analysis of helium isotopes in volcanic gas from the TVG indicated that more than 60% of the helium was from the mantle, suggesting the existence of a magma chamber underneath northern Taiwan. Micro-seismic data demonstrated the existence of fluids or magmatism beneath the TVG. Volcanic ashes were found in the sediments of a core from the Taipei Basin. From the mineral composition, the ashes were inferred to be the product of an eruption event from the TVG. Based on the stratigraphic sequences, this eruption occurred less than 20,000 years ago. Fresh ashes, discovered in the foothills of Mt. Chihsin, suggest that the eruption time was 6,000 years ago. By using S-wave shadows and the P-wave delay, Lin (2017) determined that the magma chamber of the TVG was in the northeast region at a depth of approximately 20 km.

Early on the morning of February 12, 2014 (local time), an earthquake of Richter magnitude 4.2 occurred in the TVG area, and was the largest earthquake recorded in this area in the last decade. The epicenter, as reported by the Central Weather Bureau, was approximately 7 km southeast of Mt. Chihsin, and the depth of the hypocenter was approximately 6 km. Numerous studies have confirmed that the TVG is an active volcano, causing much public speculation on whether the earthquake was related to volcanic activity.

Results from regularly sampled volcanic gas from the primary fumaroles of the TVG, taken over the past decade, are presented here. Gas compositions and helium isotope ratios of the fumarolic gas were analyzed. After the earthquake, it was found that some changes had occurred in the volcanic gas compositions. This study investigated the relationship between seismic activity and hydrothermal systems with respect to these changes and attempted to decipher the characteristics of the hydrothermal systems of the TVG.

[1] Project Associate Researcher, National Center for Research on Earthquake Engineering

Sample collection and analytical methods

Currently, more than ten fumaroles are active in the TVG. Due to limited budget resources in 2013 and because the volcanic gas composition in the area was stable, only five primary fumaroles were selected as regular sampling sites. The sampling frequency was once per month, and the gas compositions and helium isotopes were analyzed to monitor volcanic activity. The sampling locations are shown in Figure 1. Fumarolic gas was sampled using a Giggenbach bottle, which is commonly used by volcanologists. The volume of the Giggenbach bottle was approximately 170 mL, with 50 mL of alkali hydroxide solution kept in the bottle. The collected gas was first analyzed using a gas chromatograph (SRI 8610C) equipped with two thermal conductivity detectors and a flame ionization detector. Subsequently, the concentration of chloride and sulfate ions dissolved in the alkali hydroxide solution was analyzed using an ion chromatograph (Metrohm, 790 Personal). Finally, the concentration of CO_3^{2-} was calculated using an automatic titrator (Metrohm, 702 SM Titrino). The analysis covered H_2O, CO_2, H_2S, SO_2, HCl, CH_4, N_2, H_2, He, Ar, and CO. Iodine was adopted to obtain SO_2/H_2S ratios. Helium was collected and stored in vacuum glass bottles equipped with stopcocks at both ends. Helium isotopes were analyzed using a rare gas mass spectrometer (VG 5400) at the Department of Geosciences, National Taiwan University.

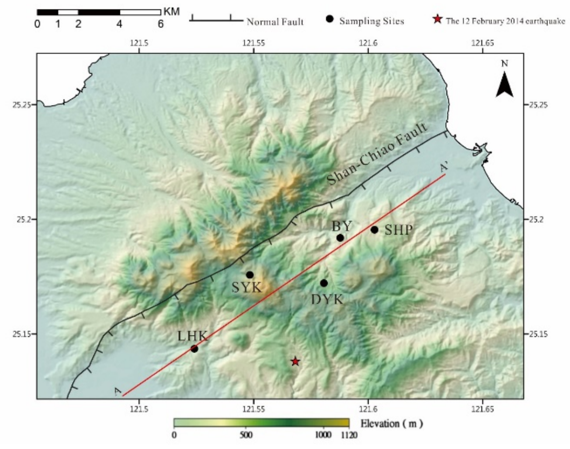

Fig. 1. Distribution of sampling sites. The star is the earthquake epicenter. DYK = Da-you-keng. SYK = Shiao-you-keng. SHP = She-huang-ping. BY = Ba-yan. LHK = Liu-huang-ku. The black line is the Shanchiao Fault, the key geological structure line in this area. The red line is the A–A' profile in Figure 4.

Results and discussion

The earthquake under consideration occurred in 2014 and thus this study presents data from 2013 to 2014. A considerable amount of data on gas compositions and helium isotope ratios is listed in the Appendix. This study focused on several representative indicators of the TVG, including the helium isotope ratio, temperature of fumaroles, variation in CO_2 concentration (dry gas), and S_{total}/CO_2 ratios (Figure 2). From these parameters, no substantial variations were observed before and after the earthquake, indicating that no distinct movement occurred in the magma chamber in the TVG region. Therefore, the correlation between the earthquake and volcanic activity was preliminarily excluded. According to the focal mechanism proposed by the Central Weather Bureau, this earthquake was triggered by a strike-slip normal fault. A fault plane solution analysis indicated that the strike of the fault plane was NW 38° and NE 18°. Although the earthquake was related to the activity of a normal fault, the strike of the fault plane was inconsistent with the direction of the Shanchiao fault. Therefore, correlation between the earthquake and the activity of the Shanchiao fault was also excluded.

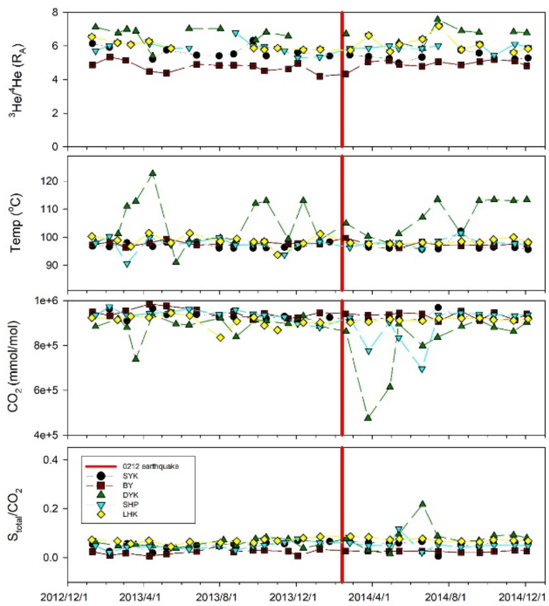

Fig. 2. Variation in the indicators before and after the earthquake, including helium isotopes, temperature, dry gas, and S_{total}/CO_2 ratios. No significant variation occurred in these indicators.

Fumarolic gas samples were collected immediately after the earthquake. According to the results, although numerous parameters related to magma activity did not change, the HCl concentration substantially changed in samples taken from the northeastern fumaroles, including Da-you-keng (DYK), Ba-yan (BY), and She-huang-ping (SHP), after the earthquake. These substantial changes remained stable for two months and subsequently returned to background levels (Figure 3). The HCl concentration of DYK first changed after the earthquake, followed by BY and SHP. The order of temporal variation in the HCl concentration of the three sampling sites was consistent with their distances to the hypocenter.

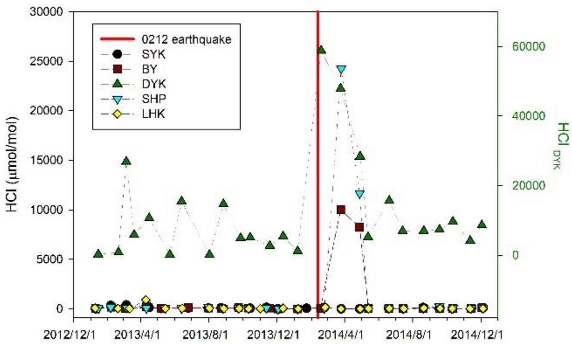

Fig. 3. Variations in the HCl concentration of fumaroles after the earthquake. The green scale on the right is the concentration at DYK.

In addition to the intrusion of magma or seawater, which could cause sharp variations in HCl concentration, there may be several other causes of the increased HCl concentration under normal conditions. A sudden increase in water temperature would reduce the solubility of HCl and lead to the exsolution of HCl from the water in hydrothermal systems. Numerous studies have also suggested that hydrothermal systems could be affected by earthquakes, and the heat flow and Cl concentration in the hydrothermal systems might increase after earthquakes. Lee *et al*. (2008) proposed that more than one hydrothermal system exists underneath the TVG. One was suspected to be at a depth of approximately 1,200 m and another, shallower hydrothermal system was suspected to be at a depth of 600 m. As magmatic gas ascends through the deeper hydrothermal system, most of the acidic gas (HCl, SO_2) dissolves in the water. Therefore, the entry of a large amount of deep fluids into the shallower hydrothermal system would change the compositions of fumarolic gas. The depth of the earthquake was 6 km, and the earthquake may have substantially affected the two hydrothermal systems. The earthquake may have caused the fluids in the deeper hydrothermal system to migrate into areas where degassing systems were highly developed (DYK, BY, and SHP), resulting in a considerable increase in HCl concentration. The interaction was between two hydrothermal systems, and thus no magmatic intrusion would be observed. The HCl concentration returned to normal in only two months after this sudden increase. A possible explanation for this phenomenon is that the fluids from the deeper hydrothermal system ascended to the shallower system after the earthquake, resulting in a sudden change in HCl concentration. Substantial HCl was released within a short time, and after the system stabilized, the HCl concentration returned to the background level.

Notably, the HCl concentration of Shiao-you-keng (SYK), which is located close to the hypocenter, did not change at all. The same phenomenon occurred in the southwestern sampling site, Liu-huang-ku (LHK). Murase *et al*. (2014) proposed that a contraction source and an expansion source existed underneath SYK and DYK. The hydrothermal systems or groundwater systems between the two areas may be connected. However, the passage for deeper fluids to migrate to DYK is relatively smooth. This might explain the difference in the HCl concentrations in SYK and DYK after the earthquake. However, the geochemical variations after the earthquake suggest that the hydrothermal systems of the two sites are not connected. Microseismic data of the TVG revealed that the distribution of the events could be roughly divided into three independent groups. Because the local seismic events were mostly caused by fluid migration in the deep passage, these independent groups suggest that the hydrothermal or groundwater systems are unconnected.

Based on sulfur isotopes of the hot springs and fumaroles, Zou (2011) proposed a model demonstrating the formation of TVG hot springs. In the model, DYK and SYK were divided directly into two independent fumarolic systems. The source of the hot spring and fumaroles in SYK was the shallower hydrothermal system. This concept supported the inference made by this study that this earthquake did not affect the gas composition of SYK. Additionally, in the same model, a fluid passage was proposed to exist between DYK, BY, and SHP. Based on the study of soil gas flux, Wen (2014) suggested that the northeastern sites of DYK and BY share the same gas source. Although SHP exhibited a different degassing passage, SHP and DYK were inferred to be connected at a shallow depth, whereas the degassing passages of SYK and LHK are independent.

From the gas composition, the high helium isotope ratios indicate that the fluids in SYK were derived from magma, and thus it was impossible for SYK not to be affected by deep fluids. The fumarolic gas compositions of the TVG were primarily vapor from heated shallow groundwater systems. Fluids from deep reservoirs may more or less affect the primary composition of fumaroles. According to the results, the fluid exchange between DYK, BY, and SHP was relatively easy, which means that the cracks along the degassing passages in these areas could provide favorable conditions for deep fluids to upwell and be incorporated in the volcanic gas. The degassing passages between the upper and lower hydrothermal systems in SYK and LHK are relatively constrained. SYK is suspected to be more susceptible to the shallower groundwater system than the deeper groundwater system. Thus, even if some deep fluids ascended to the shallow area, its effect was reduced through mixing with a large amount of shallow groundwater. The hydrogen and oxygen isotopes of condensed water in fumarolic gas were analyzed and it was determined that the LHK region exhibits an independent groundwater system. The hydrogen and oxygen isotopes indicate that the source of the groundwater in LHK may be discharge from the Xueshan Range or other watersheds, unlike other sites in which the groundwater source of fumaroles is primarily meteoric water.

Based on the results of the present study and previous geochemical and geophysical studies, this study proposes a new model demonstrating the degassing and hydrothermal systems of the TVG (Figure 4). The shallower hydrothermal system underneath DYK, BY, and SHP is connected. A sizable shallow groundwater system exists underneath SYK, which dilutes the geochemical signature of deep fluids. This shallow groundwater system is suspected to be independent from the other fumaroles. LHK is located on the periphery of the TVG and exhibits an independent shallow hydrothermal system.

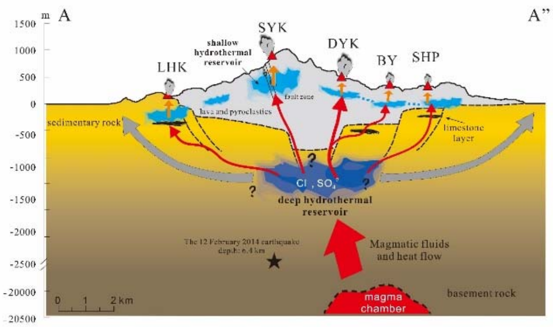

Fig. 4. Schematic profile of the hydrothermal systems in the TVG (modified from Wen et al., 2016). The A–A' profile is shown in Fig. 1.

Another notable variation was the helium isotope ratios of gas collected in DYK. The helium isotope ratios used in this study were corrected using the ratio of air, and severely air-contaminated samples were excluded. The degassing system underneath the DYK area is more developed than those in other sites. This also means that the geological features of this area are relatively fragile and the degassing channels may easily collapse. In the two consecutive months after the earthquake, the helium isotope ratios of gas from the fumaroles in DYK were substantially contaminated with air. Normally, these air-contaminated helium isotope ratios would be excluded, however, this condition in DYK differed from that expected to result from human error. From the long-term monitoring of the helium isotope ratios of volcanic gas in the TVG, Yang (unpublished data) uncovered several events in which the helium isotope ratios decreased after earthquakes. This may be because fractures caused by earthquakes increased the degassing of crustal gas or induced air incorporation in the degassing systems.

Conclusions

Before and after the earthquake on February 12, 2014, volcanic gas compositions, including the isotope ratio, CO_2 concentration, S_{total}/CO_2 ratio, and temperature, were stable, indicating that no deep magmatic fluids were incorporated into the existing hydrothermal systems. Therefore, the possibility that the earthquake was correlated to magmatic activity was excluded. However, the sharp increase in the HCl concentration of fumarolic gas indicates that this earthquake may have affected the deep hydrothermal system, resulting in a short-term hydrothermal intrusion event that caused a drastic change in HCl concentration. The spatial distribution of changes in the HCl concentration at the five sampling sites may be related to the condition of the degassing channels between the shallow and deep hydrothermal systems. The results showed that the shallow hydrothermal system was connected to DYK, BY, and SHP. Temporal variations occurred at these sampling sites after the earthquake, and the variations occurred earlier at areas closer to the epicenter. SYK was affected more substantially by the fluids from the shallow hydrothermal system than by the deep fluids, and did not seem to be connected to DYK. LHK exhibited an independent hydrothermal system and was unaffected by the earthquake.

References

Lee, H.F., Yang, T.F., Lan, T.F., Chen, C.-H., Song, S.R. and Tsao, S. (2008) Temporal variations of gas compositions of fumaroles in the Tatun Volcano Group, northern Taiwan. J. Volcanol. Geotherm. Res. 178, 624-635.

Lin, C.H. (2016) Evidence for a magma reservoir beneath the Taipei metropolis of Taiwan from both S-wave shadows and P-wave delays, Scientific Reports, 6, 39500.

Murase, M., Lin, C.H., Kimata, F., Mori, H. and Pu, H.C. (2014) Volcano-hydrothermal activity detected by precise levelling surveys at the Tatun volcano group in Northern Taiwan during 2006-2013. J. Volcanol. Geotherm. Res. 286, 30-40.

Wen H.Y., Yang, T.F., Lan, T.F., Lee, H.F., Lin, C.H., Sano, Y. and Chen, C.H. (2016) Soil CO2 flux in hydrothermal areas of the Tatun Volcano Group, northern Taiwan. J. Volcanol. Geotherm. Res. 321, 114-124.

Zou, H. W. (2011) Sulfur isotopic compositions of fumarolic samples from TVG hydrothermal area in northern Taiwan, MS Thesis, Inst. Geosci., Nat. Taiwan Univ., 85 pp. (in Chinese)

Monitoring of Some Selected Mud Volcanoes of Southern Taiwan

Vivek Walia[1], Shih-Jung Lin[2], Arvind Kumar[3], Ching-Chou Fu[4] and Cheng-Horng Lin[5]

Abstract

In the present study some mud volcanoes in Kaohsiung (Mao-Tao-San mud volcano) and Pingtung (Wan-Dan mud volcano) areas were selected. The selected mud volcanoes are located above the mud diaper system in southern Taiwan. Different sampling techniques were used to collect samples in and around the said mud volcanoes. Based on eruption and water radon observed data at Mao-Tao-Sen we have proposed that the well no. 2 and well no 3(B) radon variation shows opposite trend to each other and can used as behavior model for the area. Long term investigation will be needed to understand the relationship of mud volcanoes eruption cycle with gas composition variations. It will also help to understand their relationship with tectonic activities in the region.

Keywords: Mud volcano, Soil-gas, Water, Radon, Southern Taiwan

Introduction

Mud volcanoes important characteristics is that it irregularly diffuse volatile substances, fluids, and wet dirt on land (Dimitrov 2002; Kopf et al. 2000; Milkov et al. 2003) which cause damage to life and property, including buildings, crops, and other facilities. Mud volcanoes are not completely identified for their development processes through which over pressured, fine-grained sediments squeeze out to the top from depths of up to many kilometers. They are detected globally, mostly in space of tectonic confining and thick, fast-accumulated sedimentary array (Milkov 2000; Kopf 2003). The first systematical examination on a broad scale abundance of mud volcanoes was performed by Higgins and Saunders (1974).

Mud volcanoes study mainly targeted on land, and to devolve correlations among mud volcanism, hydrocarbons, and regional tectonics they have utilized commercial drill-hole measurements. The main gas component emitted during a mud volcano eruption is methane and it is one of the key greenhouse gases that affect the environment. Computation of total flow from mud volcanoes in the globe consequently has emerged as an attractive subject for debate of the future consequence on the global weather shift (Judd et al. 2002; Etiope and Klusman 2002; Kopf 2003; Milkov et al. 2003). Such monitoring is further of significance for hazard estimation and as an alternate for co-seismic strain exposure (Albarello 2005; Martinelli and Panahi 2005). For this reason, correct computable determination of the release of gas through mud volcanoes are very crucial for aforesaid estimation, whereas decisive results are normally challenging to attain owing to the irregularly of the mud volcanism (Kopf 2003).

Taiwan is situated at a complicated tectonic setting. Natural gas release, hot springs, hydrothermal exercise and mud volcanoes are sufficient in various tectonic fields of Taiwan. Number of mud volcanoes were additionally acclaimed in Taiwan on-land (Shih 1967) and offshore (Liu et al. 1997; Chow et al. 2001). Shih (1967) discovered that there have been sixty four alive mud volcanoes in seventeen land space. Helium measurements for fluid samples from natural gases, hot springs, fumaroles and mud volcanoes of Taiwan has been carried out and results has been displayed by Yang (2002). Based on helium data, three groups were recognized by Yang (2002). (1) Igneous zone, specimen of this zone mostly display recognizable mantle impressions along high $^3He/^4He$ ratios; (2) Central Range zone, most of data of this zone fall in the limit of 0.1 to 0.9RA (RA= $^3He/^4He$ ratio of air). This can be very well interpreted by mixing of crustal components (<0.1RA) and air-saturated water (1.0RA); (3) Coastal Plain zone, normal crustal impressions were accessed for the southwestern mud volcanoes (0.1–0.26RA),

[1] Research Fellow, National Center for Research on Earthquake Engineering
[2] Assistant Research Fellow, National Center for Research on Earthquake Engineering
[3] Associate Research Fellow, National Center for Research on Earthquake Engineering
[4] Associate Research Fellow, Institute of Earth Sciences, Academia Sinica
[5] Research Fellow, Institute of Earth Sciences, Academia Sinica

suggesting that crustal sources are leading in this zone. To find the fluid sources in mud volcanoes and mud pools, gas compositions and isotopic measurements were utilized. Maximum alive mud volcanoes are emitting methane-prevailing gases. Though, some gases have shown unexpected carbon dioxide-dominated and/or nitrogen-excess compositions. This suggests that there are various sources for the gas compositions of mud volcanoes at Taiwan (Yang et al. 2004). Volcanic exertions have number of times altered human life at large extent as well as small extent. Knowing alarming signatures to volcanic eruptions is still unfolded and difficult challenge: seismic tremor and gas emissions for instance has been linked to future eruptive activity in some studies. However the mechanisms are until now not totally known. In the present study soil gas and water geochemistry study has been performed in some selected mud volcanoes in Pingtung and Kaohsiung (Fig. 1) areas to understand the mechanism of the eruption and relationship of mud volcanoes eruption cycle with gas composition variations. Two selected mud volcanoes for the present study, i.e. Wan-Dan (WD) mud volcano in Pingtung and Mao-Tao-San (MTS) mud volcano in Kaohsiung. The selected mud volcanoes are located above the mud diaper system in southern Taiwan.

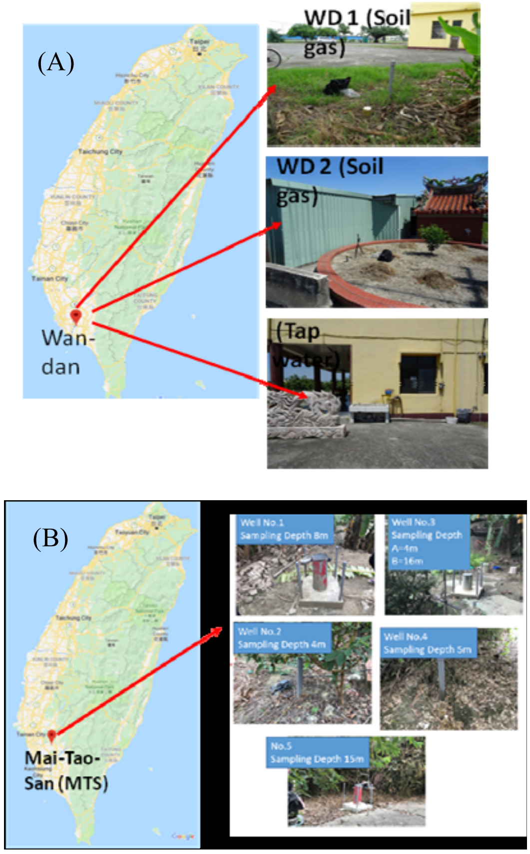

Fig.1. Selected mud volcanoes in southwest Taiwan for present study: (A) Wan-dan mud volcano (B) Mao-Tao-Sen mud volcano

Methodology

To carry out the present investigation for selected mud volcanoes three different sampling techniques have been used to collect samples in and around the said mud volcanoes. Soil gas samples were also be collected at the depth of 1 meter and dissolved gases from the mud volcanic site (or nearby) for radon gas analyses. Soil gas samples and dissolved gas from mud pool/ground water were also analyzed for radon concentration using DURRIDGE RAD7 (Solid-state nuclear track detector) for field surveys and bi-weekly monitoring. The DURRIDGE RAD7 uses a solid state alpha detector. A solid state detector is a semiconductor material (usually silicon) that converts alpha radiation directly to an electrical signal. One important advantage of solid state devices is ruggedness. Another advantage is the ability to electronically determine the energy of each alpha particle. This makes it possible to tell exactly which isotope (polonium-218, polonium-214, etc.) produced the radiation, so that you can immediately distinguish old radon from new radon, radon from thoron, and signal from noise. This technique, known as alpha spectrometry, is a tremendous advantage in sniffing, or grabs sampling, applications. Very few instruments other than the RAD7 are able to do this.

The Nuclear Track technique using the SSNTDs has also been used at some chosen sites in and around the mud volcanic areas. In this passive technique, LR-115 alpha detector films have been used. Before using these films in the field, the laboratory experiments have been carried out in different modes of exposures of LR-115 for the calibration study (Kumar et al. 2013). LR-115 alpha detector films were placed in the augur hole of about 50 cm depths to study the variations in the radon concentrations using radon-thoron discriminator. Radon-thoron discriminator of 25 cm long, has up and down position to place the film detectors. It is based on the large ratio of their half-lives and consequent difference in their diffusion lengths. It can be computed that a length of about 25 cm of an air column is adequate to eliminate thoron almost completely while radon is not much affected. So the film detectors placed at up position records the tracks due to radon alone whereas, the film detectors placed at down position records tracks due to radon and thoron both. The discriminator has been kept in the auger hole of 50 cm depth for a time period of two weeks to one month. After removing the film detectors from the auger hole, it has been etched in 2.5 N NaOH solutions at a stable temperature of 60º C for 90 minutes using the etching machine. Semiautomatic methodology (Arias et al. 2005) has been used for counting the tracks formed in the film detectors. The computed tracks per cm^2 in the films were converted to kBq/m^3 using the calibration factor calculated within the earlier study (Kumar et al. 2013).

Results and Discussions

Two selected mud volcanoes for the present study, i.e. Wan-Dan mud volcano in Pingtung and Mao-Tao-San mud volcano in Kaohsiung (Fig.1). Both mud volcanoes are above the mud diaper system in southern Taiwan.

In preliminary investigations bi-weekly sampling was carried at selected sites at/near both mud volcanoes eruption locations. At Mao-Tao-San (MTS) two sites for soil-gas and five boreholes for water samples (at different depths) were slected for bi-weekly monitoring. Whereas, at Wan-dan (WD) two sites (WD1 and WD2) for soil-gas and one site WD1 for water sample were slected to study their characterization and eruption mechanism. Mao-Tao-San mud volcano almost has fix eruption location; however, in the case of Wan-dan mud volcano the eruption site keep on change with each eruption. The selected two locations for biweekly sampling for Wan-dan mud volcano; WD1 is located near some latest eruption site as comparing WD2.

Water samples have been collected and analyzed bi-weekly for radon gas as well as for other physical parameters at 5 wells at Mai-Tao-San (Fig. 1B) to study the mud volcanoes eruption mechanism. The water sample have been collected at different depths from 4m to 15m. Radon values for MTS water samples ranges from 86Bq/m3 to 26kBq/m^3 for all the boreholes under study with the average values of varies from 1.2kBq/m^3 to 6.9kBq/m^3. Whereas both MTS1 and MTS3 soil-gas samples have recorded comparatively higer values of radon rages from 39.1-7.8kBq/m^3 (with average value of 18.5kBq/m^3) and 38.8-13.8kBq/m^3 (with average value of 20.5kBq/m^3), respectively (Table 1). We have started our investigation with five boreholes and tap water (background values) but later confined to three boreholes as presented in Table 1. Figure 2 & 3 shows the water radon data recorded bi-weekly in different wells at Mai-Tao-San area of south Taiwan along with volcanic eruption in 2018. This study shows that anomalous radon value have been observed before some volcanic eruption during the study time. Based on eruption and radon observed data we have proposed that the well no. 2 and well no 3(B) radon variation shows opposite trend to each other (Fig. 4) and can used as behavior model for the area. But we may need a long-term investigation to understand the relationship of mud volcanoes eruption cycle with gas composition variations. It will also help to understand their relationship with tectonic activities in the region.

We also monitored the radon in water and in soil (using active and passive method) at Wan-dan area of south Taiwan (Fig. 1B). We recorded the radon concentration in soil bi weekly at two points WD1 and WD2 using RAD 7 as well as LR115 films whereas radon in water is monitored in the tap water near to point WD1. Figure 5 shows the radon data recorded in soil gas at WD1, WD2 and recorded data in water at Wan-dan area. An increase in radon

Table 1. Radon data recorded in different wells at Mai-Tao-San.

Position	Average (Bq/m^3)	Std Dev	Maximum (Bq/m^3)	Minimum (Bq/m^3)
MTS 1 (W)	1210	1166	6190	86
MTS 2 (W)	6875	3366	13100	238
MTS 3a (W)	4634	5191	25893	1120
MTS 3b (W)	4020	3899	18341	839
MTS 1 (S)	18549	9102	39100	7780
MTS 3 (S)	20517	7112	38800	13800

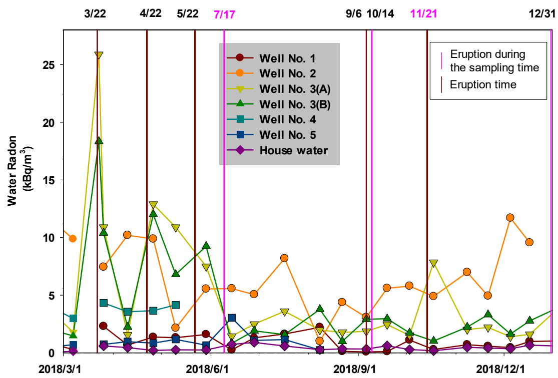

Fig. 2. Bi-weekly radon data recorded in different wells at Mai-Tao-San area of south Taiwan along with mud volcanic eruption.

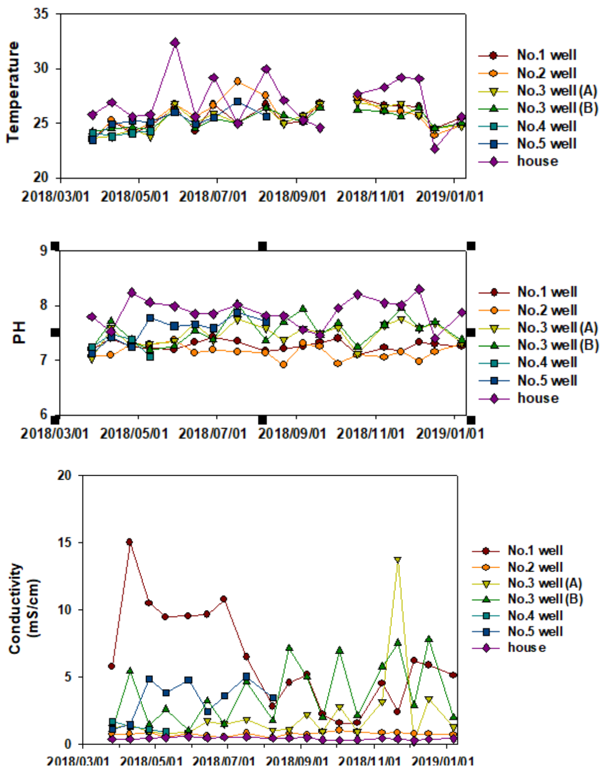

Fig. 3. Bi-weekly radon data recorded in different wells at Mai-Tao-San area of south Taiwan along with mud volcanic eruption.

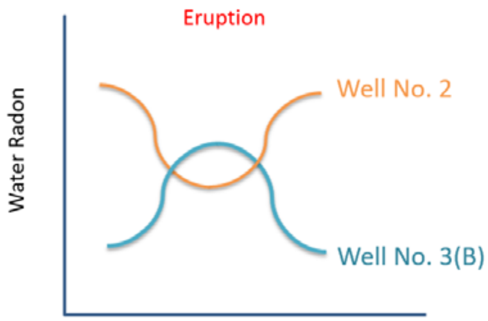

Fig. 4. Proposed model for water radon variation trend for well no. 2 and well no 3(B) with mud volcanic eruption at Mai-Tao-San.

concentrations WD1 both soil-gas as well as water samples have been noted before few eruption (Fig. 5), whereas WD2 soil-gas has not shown any correlation with eruption cycle. However, long term investigation will be needed to understand the relationship of mud volcanoes eruption cycle with gas composition variations. It will also help to understand their relationship with tectonic activities in the region.

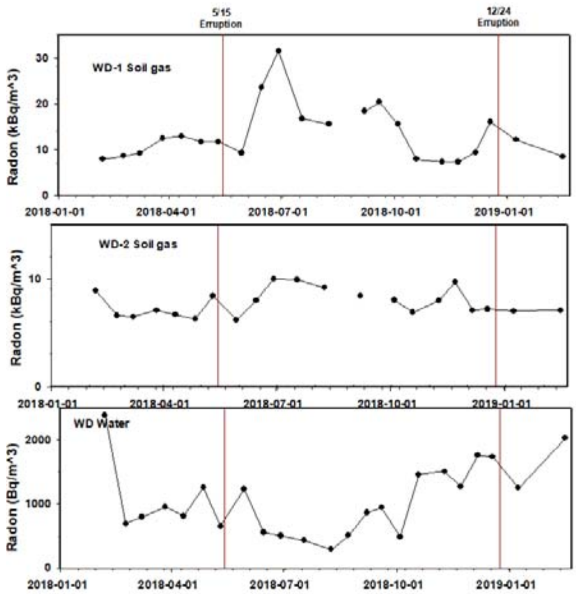

Fig. 5. Bi-weekly radon data recorded in soil-gas and water samples at Wan-dan area of south Taiwan along with mud volcanic eruption.

References

Albarello D (2005) Physical models of mud volcanoes, mud volcanoes as natural strainmeters: a working hypothesis (pp. 239-249). In:Martinelli, G. & Panahi, B. (Eds.). Mud volcanoes, geodynamics, and seismicity. Dordrecht: Springer.

Arias H, Palacios D, Sajo-Bohus L and Viloria T (2005). Alternative procedure for LR 115 chemical etching and alpha tracks counting. Radiation Measurements 40 357 – 362.

Chow. J., Lee, J.S., Liu, C.S., Lee, B.D., Watkins, J.S., (2001). A submarine canyon as the cause of a mud volcano: Liuchieuyu Island in Taiwan. Mar Geol., 176,55–63.

Dimitrov, L.I., (2002). Mud volcanoes—the most important pathway for degassing deeply buried sediments. Earth-Science Reviews 59, 49–76.

Etiope G, Klusman RW (2002) Geologic emissions of methane to the atmosphere. Chemosphere 49:777–789.

Higgins, G. E., and J. B. Saunders, Mud volcanoes – Their nature and origin, Verh. Naturforsch. Ges. Basel, 84, 101– 152, 1974

Judd AG, Hovland M, Dimitrov LI, Gil SG, Jukes V (2002) The geological methane budget at continental margins and its influence on climate change. Geofluids 2:109–126.

Kopf AJ (2003) Comment on the paper ''Methane emission from the mud volcanoes of Sicily (Italy)'' by Etiope et al. Geophys Res Lett 30(2).

Kopf, A., Robertson, A.H.F., Volkmann, N., (2000). Origin of mud breccia from the Mediterranean Ridge accretionary complex based on evidence of the maturity of organic matter and related petrographic and regional tectonic evidence. Marine Geology 166, 65–82

Kumar A, Walia V, Yang TF, Hsien C-H, Lin S-J, Eappen KP, Arora BR (2013) Radon-thoron monitoring in Tatun volcanic areas of northern Taiwan using LR-115 alpha track detector technique: pre calibration and installation. Acta Geophys 61(4):958–976.

Liu, C.S., Huang, I.L, Teng, L.S. (1997). Structural features off southwestern Taiwan. Mar. Geol., 137,305–319.

Martinelli G, Panahi B (2005) Mud volcanoes, geodynamics, and seismicity. Dordrecht: Springer.

Milkov AV, Sassen R, Apanasovich TV, Dadashev FG (2003) Global gas flux from mud volcanoes: A significant source of fossil methane in the atmosphere and the ocean. Geophys Res Lett 30(2):1037.

Milkov, A.V., (2000). Worldwide distribution of submarine mud volcanoes and associated gas hydrates. Mar. Geol., 167, 29–42.

Shih, T.T., (1967). A survey of the active mud volcanoes in Taiwan and a study of their types and the character of the mud. Petrol Geol. Taiwan, 5, 259–311.

Yang, T.F. (2002). 3He ⁄ 4He ratios of fluid samples around Taiwan. Geochimica et Cosmochimica Acta, 66, A859.

Yang, T.F., Yeh, G-H., Fu, C-C., Wang, C-C., Lan, T.F., Lee, H-F., Chen, C-H., Walia, V., Sung Q-C., (2004). Composition and exhalation flux of gases from mud volcanoes in Taiwan. Environmental Geology, 46, 1003–11.

Discussion on the Applicability of F_u-μ Relationship in Current Design Code by Using Ground Motion Records of 2018 Hualien Earthquake

Shu-Hsien Chao[1], Hsun-Jen Liu[2], Chaio-Chu Hsu[3] and Chun-Hsiang Kuo[4]

趙書賢　劉勛仁　許喬筑　郭俊翔

Abstract

Current seismic design code hasn't provided a specific F_u-μ formula for near-fault pulsed-liked ground motion. However, several researches have shown that the near-fault pulsed-like ground motion may induce higher ductility demand under the same strength reduction factor. Besides, the observed horizontal spectral accelerations of some periods from some strong motion stations maintained by Center Weather Bureau (CWB) are higher than the horizontal design response spectrum of the current seismic design code, and most of them are near-fault pulsed-liked ground motion. Based on this point, the relationship between strength reduction factor and ductility of the near-fault pulsed-liked and non-pulse-liked ground motions observed in 2018/02/06 Hualien Earthquake are evaluated in this study to discuss the applicability of the F_u-μ formula in the current seismic design code. The horizontal near-fault pulse-like ground motions as well as the pulse periods observed in 2018/02/06 Hualien Earthquake are identified by using the pulse indicator proposed by Shahi and Baker in 2014. Based on the analysis result, we preliminary concluded that the F_u-μ formula in seismic design code have a certain level of conservativism and can be applicable to near-fault pulsed-liked ground motion. The analysis result in this study can provide a reference for the revision of the seismic design code.

Keywords: near-fault pulse-liked ground motions, strength reduction factor, structural system ductility, 2018 Hualien Earthquake, seismic design code

Introduction

In 2018/02/06 Hualien Earthquake, the observed horizontal spectral accelerations of some periods from some strong motion stations maintained by Center Weather Bureau (CWB) were higher than the horizontal design response spectrum of the current seismic design code. Besides, most of them are near-fault pulsed-liked ground motion. This higher spectral acceleration demand may cause the structures which are designed with current seismic design code go into inelastic stage and induce structural damage. The seismic code actually allows the structures go into inelastic stage with allowable ductility limit, and it also suggests a period-dependent F_u-μ formula to describe the relationship between the strength reduction factor (F_u, the ratio between demand and capacity strength) and the structural system ductility (μ). In the past, several researches have shown that the near-fault pulsed-like ground motion may induce higher ductility demand under the same strength reduction factor (Gillie et. al., 2010). However, current seismic design code hasn't provided a specific Fu-u formula for near-fault pulsed-liked ground motion. Due to this point, the relationship between strength reduction factor and ductility of the near-fault pulsed-liked and non-pulse-liked ground motions observed in 2018/02/06 Hualien Earthquake are evaluated in this study to discuss the applicability of the F_u-μ formula in the current seismic design code. The analysis result in this study can provide a reference for the revision of

[1] Associate Researcher, National Center for Research on Earthquake Engineering
[2] Assistant Researcher, National Center for Research on Earthquake Engineering
[3] Research Assistant, National Center for Research on Earthquake Engineering
[4] Researcher, National Center for Research on Earthquake Engineering

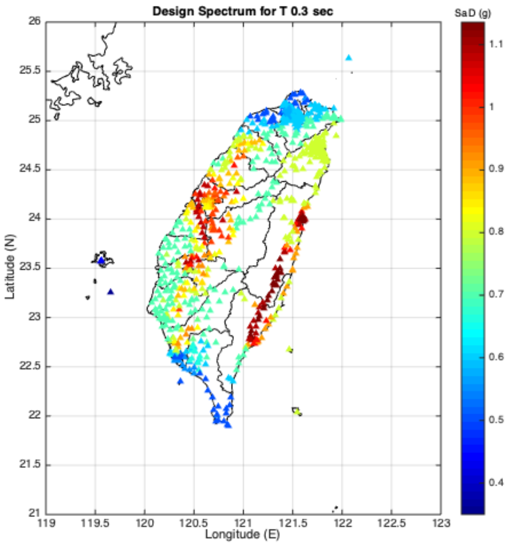

Fig. 1(a). The design spectral acceleration of 475 years return period at the locations of strong motion stations for period 0.3 sec.

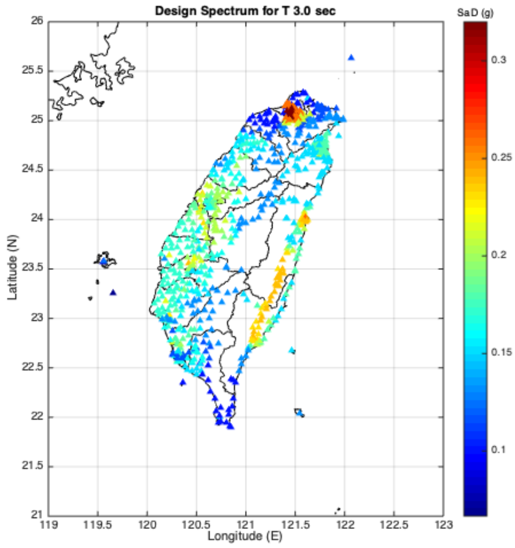

Fig. 1(b). The design spectral acceleration of 475 years return period at the locations of strong motion stations for period 3.0 sec.

the seismic design code.

Analysis Method and Result

In this study, the spectral acceleration of ground motion records collected in 2018/02/06 Hualien Earthquake by the strong motion stations maintained by Center Weather Bureau are calculated to compare with the design spectral acceleration of the location of the respective strong motion stations. In order to derive the design spectral acceleration, only the locations of the strong motion stations with available Vs30 information (Kuo et. al., 2017) are selected. There are 458 locations of the strong motion stations are selected. In order to maintain the characteristics of each ground motion record, we haven't changed the intensity level of the observed ground motion. The observed maximum horizontal spectral acceleration are calculated from two measured horizontal components for each station. The strength reduction factor F_u are calculated by the ratio between the observed maximum horizontal spectral acceleration and the design spectral acceleration for each station. If the value of F_u is larger than 1, that means the observed spectral acceleration is higher than the design spectral acceleration. In this case, the structural ductility μ corresponding to the derived strength reduction factor F_u is evaluated by using nonlinear dynamic time history analysis with assumed hysteretic behavior. The design spectral acceleration with 475 years return period are used in this study as shown in Figure 1(a) and Figure 1(b) for periods 0.3 sec and 3 sec, respectively. The horizontal near-fault pulse-like ground motions as well as the pulse periods observed in 2018/02/06 Hualien Earthquake are identified by using the pulse indicator proposed by Shahi and Baker in 2014 (Baker, 2007; Shahi and Baker, 2014).

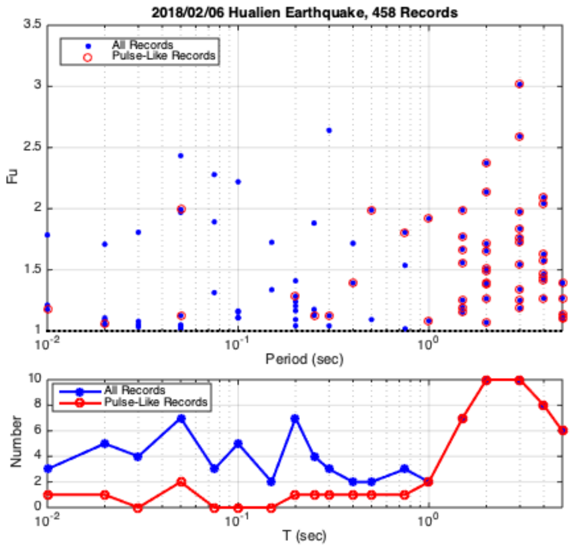

Fig. 2. The F_u analysis result of the selected ground motion records with $F_u > 1$ observed in 2018/02/06 Hualien Earthquake.

Then the F_u-μ relationship difference between near-fault pulsed-liked ground motion and non-pulse-liked ground motion are evaluated.

The F_u analysis result of the selected ground motion records in this study is shown in Figure 2. In this figure, the blue dots shown the F_u results of all selected records, and the red circle shown the F_u results of the near-fault pulse-liked ground motion records in the selected datasets. The record number with $F_u > 1$ is also shown in this figure. For $T < 1$ sec, there are 1 to 7 stations with $F_u > 1$. For $T > 1$ sec, there are 6 to 10 stations with $F_u > 1$, and they are all near-fault pulse-liked ground motions. Figure 3 shows the spatial distribution of the station with $F_u > 1$ for periods 0.3

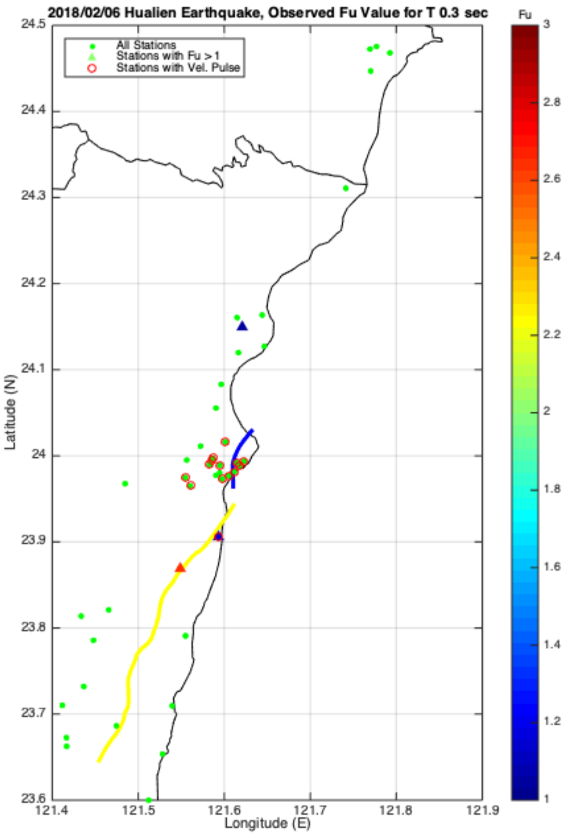

Fig. 3(a). The spatial distribution of all strong motion station (green dots), the strong motion stations with F_u > 1 (triangular dots), and the strong motion stations with near-fault pulse-liked ground motion (red circles) for period 0.3 sec.

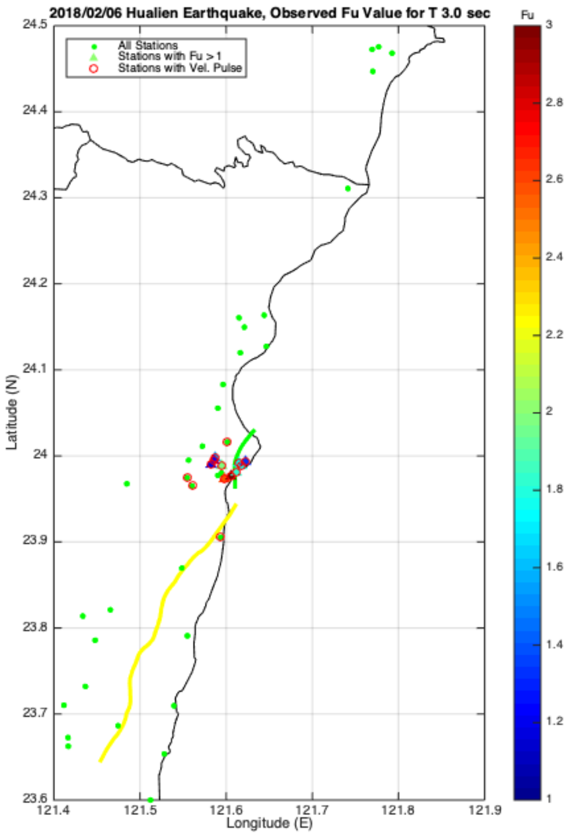

Fig. 3(b). The spatial distribution of all strong motion station (green dots), the strong motion stations with F_u > 1 (triangular dots), and the strong motion stations with near-fault pulse-liked ground motion (red circles) for period 3.0 sec.

sec and 3.0 sec. It is found that all stations with $F_u > 1$ for period 3.0 sec are all nearby the fault. It is shown that the impact of near-fault pulse-liked ground motion for long period structure are significant.

The biaxial hysteretic model proposed by Chao and Loh in 2009 (Chao and Loh, 2009) is used to evaluate the structural system ductility μ under a specific strength reduction factor for each station by using both two horizontal components simultaneously. This model allows the yield of the structural system in any azimuth direction and the development of the plasticity in any azimuth direction. The biaxial interaction behavior of the structural component can be well represented by using this hysteretic model. The calculated structural system ductility of each station is compared to the ductility calculated from the F_u-μ formula in current seismic design code. In order to derive more conservative analysis result of structural system ductility (Chao and Loh, 2003), the elasto-perfect-plastic (EPP) hysteretic loop are used to conduct the nonlinear-inelastic dynamic analysis. The strength deterioration, stiffness deterioration and pinching phenomena of the hysteretic behavior generally observed in reinforced concrete structure are not considered in this study.

Figure 4 shows the F_u-μ relationship in current seismic design code (as shown in the dark dot lines) as well as the structural system ductility (as shown in blue dots) induced by the ground motion with $F_u > 1$ observed in 2018/02/06 Hualien Earthquake for several periods from 0.01 sec to 5 sec. It is found that even some of the near-fault pulsed-liked ground motions induced higher structural system ductility demand than the non-pulse-liked ground motions as shown for periods 0.2 sec and 0.25 sec, most of the structural system ductility induced by the ground motions observed in 2018/02/06 Hualien Earthquake are lower than the ductility calculated by the F_u-μ formula in current seismic design code. Only one near-fault pulse-liked record will induced ductility which is large than seismic design code for period 2.0 sec. Based on the analysis result, we preliminary concluded that the F_u-μ formula in seismic design code have a certain level of conservativism and can be applicable to near-fault pulsed-liked ground motion.

Summary and Conclusions

In this study, the relationship between strength reduction factor and structural system ductility of the non-pulse-liked and the near-fault pulsed-liked ground

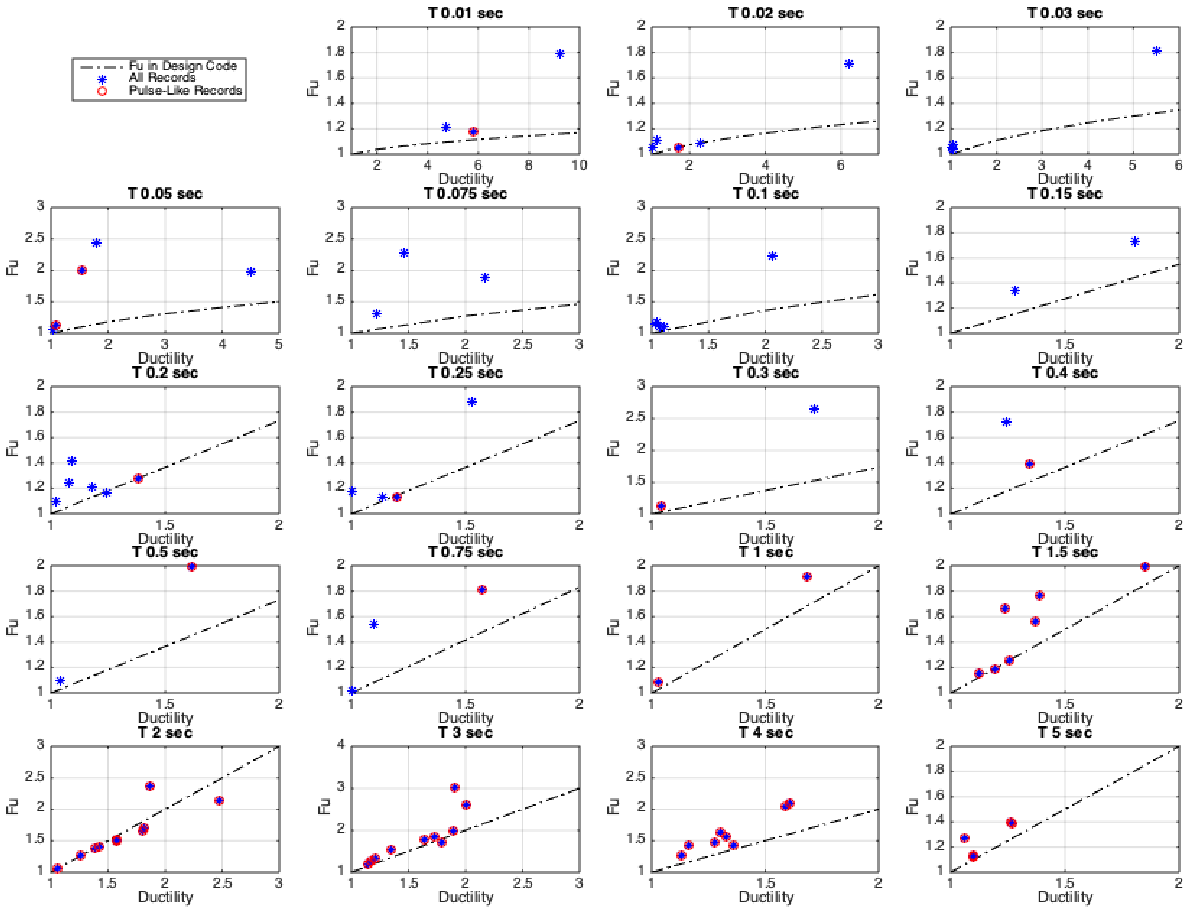

Fig. 4. Comparisons of the F_u-μ relationship in current seismic design code (as shown in the dark dot lines) as well as the structural system ductility (as shown in blue dots) induced by the ground motion with $F_u > 1$ observed in 2018/02/06 Hualien Earthquake for several periods from 0.01 sec to 5 sec.

motions observed in 2018/02/06 Hualien Earthquake are evaluated to discuss the applicability of the F_u-μ formula in the current seismic design code. Based on the analysis result, we preliminary concluded that the F_u-μ formula in seismic design code have a certain level of conservativism and can be applicable to near-fault pulsed-liked ground motion. In the future study, the ground motion records collected in significant earthquakes in Taiwan will be compiled, and the similar analysis approach will be conducted to further make sure the applicability of the F_u-μ formula in current seismic design code.

References

Baker J.W. (2007). Quantitative classification of near-fault ground motions using wavelet analysis. Bulletin of the Seismological Society of America. 97 (5), 1486-1501.

Chao, S.H. and Loh, C.H. (2003), "Development of Design Philosophy for Performance Based Seismic Design: Based on Energy Concept", Master's Thesis, Department of Civil Engineering, National Taiwan University, Taipei, Taiwan.

Chao, S.H. and Loh, C.H. (2009), "Develop Biaxial Hysteretic Model for Reinforced Concrete Structure", International Journal of Non-Linear Mechanics 2009, Volume 44, Issue 7, 745-756.

Gillie, J.L. Rodriguez-Marek, A., McDaniel, C. (2010). "Strength reduction factors for near-fault forward-directivity ground motions," In Engineering Structures, Volume 32, Issue 1, 2010, Pages 273-285.

Kuo, C.H., C.M. Lin, S.C. Chang, K.L. Wen, and H.H. Hsieh (2017). Site Database for Taiwan Strong Motion Stations, NCREE Report, No. NCREE-17-004, National Center for Research on Earthquake Engineering, Taipei, Taiwan.

Shahi, S.K. and Baker, J.W. (2014). "An efficient algorithm to identify strong velocity pulses in multi-component ground motions." Bulletin of the Seismological Society of America, 104(5), 2456–2466.

Ambient Seismic Noise Analysis in Western Foothills

Yu-Chih Huang[1], Che-Min Lin[1], Hung-Hao Hsieh[2], Kuo-Liang Wen[3] and Chau-Huei Chen[4]

黃有志[1]、林哲民[1]、謝宏灝[2]、溫國樑[3]、陳朝輝[4]

Abstract

The Western Foothills geologic province is located along the deformation front of the Taiwan Orogen. This area includes highly active faults and a complex seismogenic structure that have historically caused serious damage. A temporary seismic network with around 40 broadband seismometers had been set up between Hsinchu and Tainan County and had been operated for about two years by the National Center for Research on Earthquake Engineering (NCREE) to monitor the seismicity surrounding the three Science Parks. Meanwhile, the characteristics of ground motion and fault activity could be further studied. The theorems for analyzing ambient seismic noise to investigate subsurface velocity structures have been proved and generally accepted. Data quality of daily vertical components was preliminarily assessed to calculate the cross-correlation function (CCF) for each station pair in the 1–15-s period band. The daily CCFs were stacked monthly and the monthly CCFs were then stacked to retain coherent signals for acquiring time-domain empirical Green's functions (TDEGFs) and Rayleigh-wave phase-velocity dispersion curves. Tomography was applied to construct Rayleigh-wave phase-velocity maps and shallow crustal S-wave velocity (Vs) structures were also obtained.

Keywords: Western Foothills, ambient seismic noise, velocity structures

Introduction and Motivation

Taiwan is located on a complex convergent plate boundary zone where the Philippine Sea plate interacts with the Eurasian plate and it is accompanied by high seismicity and complex tectonics (Tsai et al., 1977; Tsai, 1986). According to the observations of long-term Global Positioning Systems (GPS), major crustal deformations are concentrated along the suture zones of the Longitudinal Valley and deformation front of the Taiwan orogeny (Hsu et al., 2009; Ching et al., 2011). Active faults are primarily recognized and located along the strike of the Western Foothills and its boundaries. The densely populated cities in the western coastal plain are situated on thick alluvium and are threatened by seismic-wave amplification and soil liquefaction (Kuo et al., 2015).

A temporary seismic network for monitoring the behaviors of seismicity and ground motion had been established in three Science Parks. They were operated between 2006 and 2010 by the NCREE, with ~40 Güralp CMG-6TD broadband seismometers. The sub-networks were deployed, starting from Hsinchu Science Park (operated ~5 years), then the Southern Taiwan Science Park (operated for ~4 years) and finally the Central Taiwan Science Park integrated the whole network from Hsinchu to Tainan County (operated for ~2 years) (Fig. 1; Lin et al., 2010). Based on observations, we know the activity and seismicity of the active faults in the three Science Parks and Western Foothills. These parameters are important in helping to assess hazards and for numerical simulations for potential seismic risks.

Previous research of the Science Parks network was focused on locating seismic events and using travel-time tomography to understand the tectonic and velocity structures. Since the basic theorem of ambient seismic noise analysis has been verified, the investigations of subsurface velocity structures have provided important constrains in various parts of the world, with routine data processing over the past decade. In this study, we obtained the TDEGF by

[1] Associate Researcher, National Center for Research on Earthquake Engineering
[2] Assistant Researcher, National Center for Research on Earthquake Engineering
[3] Professor, National Central University
[4] Professor, National Chung Cheng University

calculating the CCF for each station pair and analyzing daily vertical components of continuously recording ambient seismic noise signals. Tomography and inversion methods were employed to further obtain shallow crustal Vs structures beneath the Western Foothills.

Fig. 1. The temporary broadband seismic network in the three Science Parks operated by the NCREE (modified from Google Earth).

Methods and Data Processing

Ambient seismic noise is caused by a variety of factors, such as human activities, atmospheric pressure changes, and the interaction of ocean waves with the coast and seafloor (Webb, 2007). The TDEGF can be obtained from the cross-correlation of station pairs with simultaneous and continuous ambient seismic noise signals (Fig. 2; Weaver, 2005). This method uses diffuse wave fields with passive structural signals contained in ambient seismic noise. After long-term stacking, the weak coherent signals could be enhanced. The particle motion is like surface wave propagation, hence it exhibits dispersion properties related to the underground velocity structures.

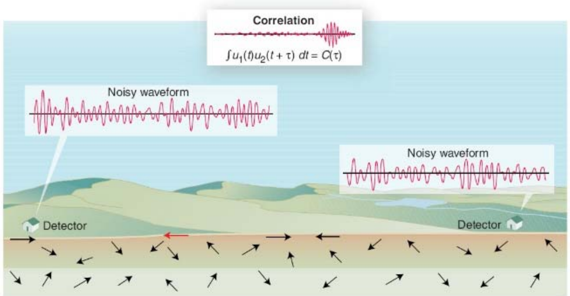

Fig. 2. The basic concept of the TDEGF derived from ambient seismic noise signals (Weaver, 2005).

The depth range of the obtained velocity structure is positively related to the aperture of the seismic network, and its lateral resolution is positively related to the density of path coverage. The study region will have good lateral resolution if the seismic stations distribute densely and homogeneously. Besides, it is unnecessary to spend lots of time waiting for sufficient seismic records, or pondering about how inhomogeneous source distributions will affect the lateral resolution, like travel-time tomography. Hence, the method can provide good constrains on velocity structures in areas with relatively low seismicity.

Figure 3 shows the data analysis procedures of the ambient seismic noise in this study. First, we performed baseline corrections of the seismograms and the data quality was preliminarily assessed. After data preparation, the daily CCFs were calculated using one-bit cross-correlation and spectral whitening for enhancing the spectral energy of the ambient seismic noise. Therefore, we simply used continuous recordings without removing earthquake signals. The obtained CCFs exhibit a high signal-to-noise ratio (SNR). The basic concepts of these two methods have been verified and regularly utilized for research on ambient seismic noise (Cupillard and Capdeville, 2010).

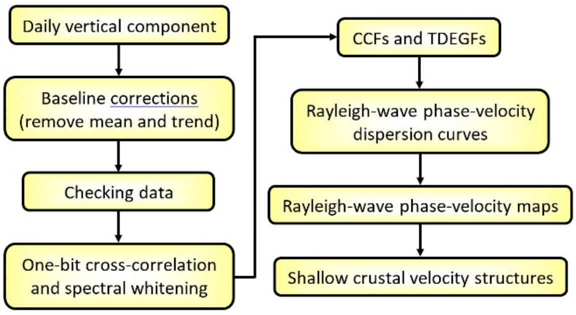

Fig. 3. Data processing of the ambient seismic noise analysis in this study.

The basic theory of the TDEGF can be represented as follows:

$$C_{AB}(t) \approx \int_0^{tc} v_A(\tau) v_B(t+\tau)\, d\tau \qquad (1)$$

where t is the time; $v_A(t)$ and $v_B(t)$ are the continuously recorded seismic data for A and B stations; tc is the total cross-correlation time (i.e. daily length in this study); $C_{AB}(t)$ is the derived CCF for station pair A and B. After stacking daily CCFs long-term, relatively stable and representative CCF for each station pair can be derived.

The TDEGF is further obtained from the time-derivative of the CCF as shown below:

$$\frac{dC_{AB}(t)}{dt} = -\hat{G}_{AB}(t) + \hat{G}_{BA}(-t) \approx -G_{AB}(t) + G_{BA}(-t) \qquad (2)$$

where $\hat{G}_{AB}(t)$ and $\hat{G}_{BA}(-t)$ represent the TDEGF, which are assumed equal to the real time domain Green's function $G_{AB}(t)$ and $G_{BA}(-t)$; $\hat{G}_{AB}(t)$ is the TDEGF recorded at station B for a fictitious source at station A; $\hat{G}_{BA}(-t)$ is the time-reversed TDEGF at A for a fictitious source at B. For an isotropic distribution of the noise sources we expect $\hat{G}_{AB}(t)$ and $\hat{G}_{BA}(-t)$ to be time-symmetrical. However, $\hat{G}_{AB}(t)$ and $\hat{G}_{BA}(-t)$ are usually asymmetrical due to uneven distribution of noise sources (Fig. 4; Stehly et al., 2006). Whether TDEGF is symmetrical or asymmetrical, we stack $\hat{G}_{AB}(t)$ and $\hat{G}_{BA}(-t)$ to enhance the symmetric component. Hence, the effect of uneven distribution of ambient seismic noise sources could be suppressed. Basing on Yao et al. (2006), Rayleigh-wave phase-velocity dispersion curves are further measured from the TDEGF (Fig. 5).

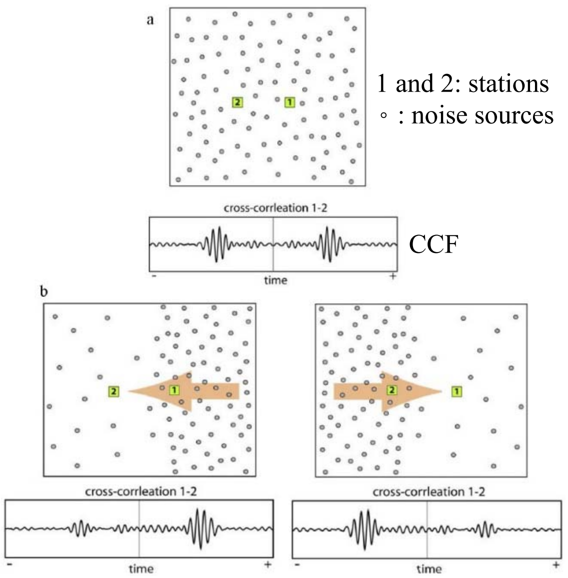

Fig. 4. The (a) symmetry and (b) asymmetry of TDEGFs (Stehly et al., 2006).

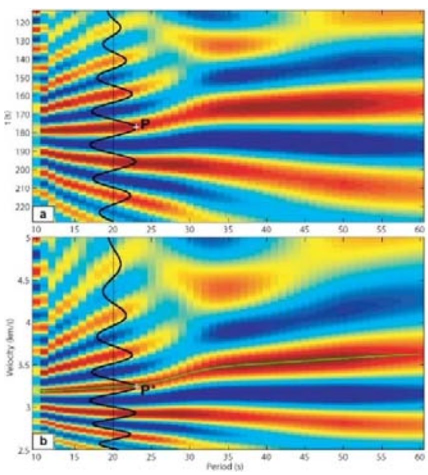

Fig. 5. From (a) TDEGF to measure (b) Rayleigh-wave phase-velocity dispersion curves (green line; Yao et al., 2006).

Preliminary Results and Future Studies

The three sub-networks are ~80 km in size with an average interstation distance of ~10 km. The integrated temporary broadband seismic network for monitoring active faults in western Taiwan covers the three Science Parks with dimensions of ~220 km in the longitudinal direction and ~70 km in the transverse direction. In total, 48 seismic stations (i.e., 1128 station pairs) comprise the network, among which 60% of the station pairs are within a distance of between 20 and 100 km (Fig. 6).

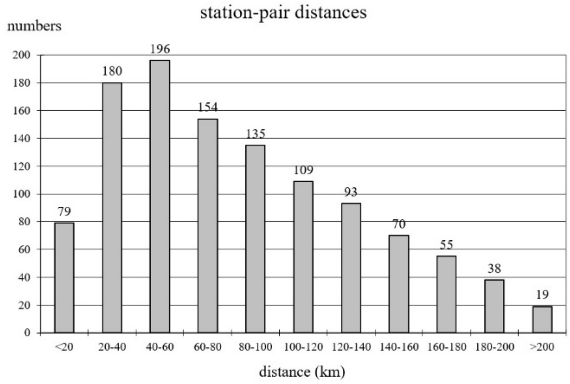

Fig. 6. Statistics of interstation distance for all station pairs.

Daily CCFs were calculated with a 200-s lag time in the 1–15-s period band for all station pairs. Figure 7 demonstrates examples of the calculated daily and stacked monthly CCFs for two station pairs. The station pair N203-N208 is at a short distance of 18 km and shows high consistency and SNR of daily CCFs. Conversely, N203-N219 is at a long distance of 178 km and presents relatively low consistency and SNR of daily CCFs. However, after long-term stacking of 48 monthly CCFs, the representative CCF of station pair N203-N219 can still be acquired.

Figure 8 presents the final average monthly 1–15 s CCFs versus the interstation distance for all station pairs, with clear surface wave propagation at an average apparent velocity of 2.5 km/s. In the near future, phase image analysis and far-field approximation methods will be employed to measure the Rayleigh-wave phase-velocity dispersion curves for each station pair. Subsequently, the tomographic method will be applied for constructing Rayleigh-wave phase-velocity maps with numerous grid points. At every grid point, Rayleigh-wave phase-velocity dispersion curves will be extracted from the obtained phase-velocity maps. The shallow crustal Vs structures will then be further constructed with two-dimensional and three-dimensional demonstrations.

More stations belonging to other seismic networks should be searched and combined in a broader region surrounding the Western Foothills and western coastal plain. The path coverage and lateral resolution could then be improved. Lateral velocity variations might show dramatic patterns on either sides of active faults or among different geologic provinces. The obtained shallow crustal velocity structures could help to construct strong ground motion, which is particularly important for seismic hazard mitigation of the densely populated metropolitan areas in western Taiwan.

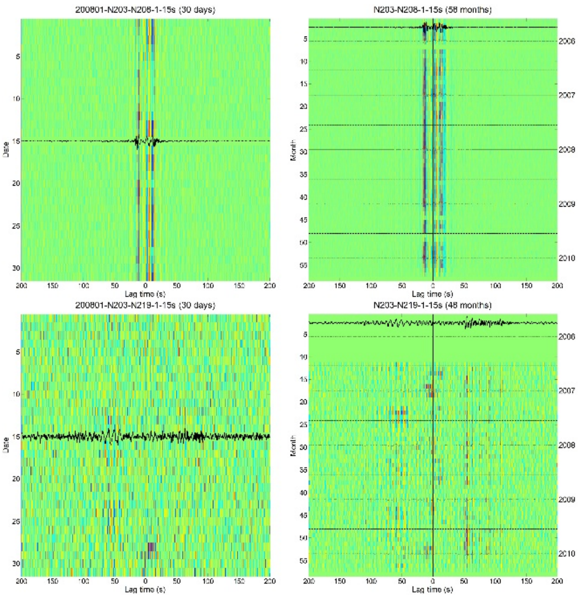

Fig. 7. Examples of 1–15 s CCFs for two station pairs at a short distance (above; N203-N208) and long distance (below; N203-N219); daily CCFs (left; in January 2008) and monthly CCFs (right; between January 2006 and November 2010). The solid black lines indicate the averages of daily and monthly CCFs.

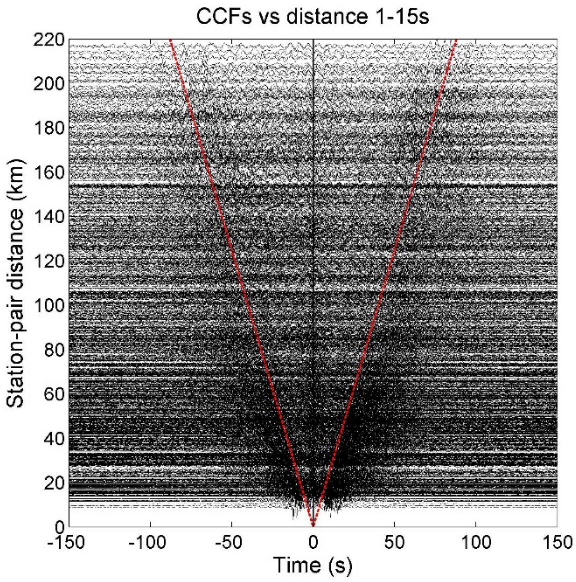

Fig. 8. The final average monthly 1–15 s CCFs versus interstation distance for all station pairs. Red dash lines mark the TDEGF signals with apparent velocity of 2.5 km/s.

References

Ching, K. E., Hsieh, M. L., Johnson, K. M., Chen, K. H., Rau, R. J., and Yang, M. (2011), “Modern vertical deformation rates and mountain building in Taiwan from precise leveling measurements and continuous GPS observations, 2000-2008”, *J. Geophys. Res.* 116, B08406.

Cupillard, P., and Capdeville, Y. (2010), “On the amplitude of surface waves obtained by noise correlation and the capability to recover the attenuation: a numerical approach”, *Geophys. J. Int.* 181, 1687-1700.

Hsu, Y. J., Yu, S. B., Simons, M., Kuo, L. C., and Chen, H. Y. (2009), “Interseismic crustal deformation in the Taiwan plate boundary zone revealed by GPS observations, seismicity, and earthquake focal mechanisms”, *Tectonophys.* 479, 4-18.

Kuo, C. H., Chen, C. T., Wen, K. L., Lin, C. M., Hsieh, H. H. (2015), “Investigation of Shallow S-wave Velocity Profile-Western Plain of Taiwan”, NCREE-15-005, NCREE, Taipei. (In Chinese)

Lin, C. M., Chang, T. M., Wen, K. L., Hsieh, H. H., Chen, A. B., Chang, L. C., and Kuo, C. H. (2010), “Micro-Earthquake Monitoring of Science Parks in Taiwan”, NCREE-10-020, NCREE, Taipei. (In Chinese)

Stehly, L., Campillo, M., and Shapiro, N. M. (2006), “A study of the seismic noise from its long-range correlation properties”, *J. Geophys. Res.* 111, B10306.

Tsai, Y. B. (1986), “Seismotectonics of Taiwan”, *Tectonophys.* 125, 17-37.

Tsai, Y. B., Teng, T. L., Chiu, J. M., and Liu, H. L. (1977), “Tectonic implica- tions of the seismicity in the Taiwan region”, *Mem. Geol. Soc. China* 2, 13-41.

Weaver, R. L. (2005), “Information from seismic noise”, *Science* 307, 1568-1569.

Webb, S. C. (2007), “The Earth's 'hum' is driven by ocean waves over the continental shelves”, *Nature* 445, 754-756.

Yao, H., van der Hilst, R. D., and de Hoop, M. V. (2006), “Surface-wave array tomography in SE Tibet from ambient seismic noise and two-station analysis - I. Phase velocity maps”, *Geophys. J. Int.* 166, 732-744.

Experimental Study of Near-Fault Effects on the Sloshing Mode of Liquid in a Storage Tank – Test Plan

Juin-Fu Chai[1] Fan-Ru Lin[2] Wei-Hung Hsu[3]

柴駿甫[1]、林凡茹[2]、徐瑋鴻[3]

Abstract

During earthquakes, most damage, except for buckling, in water storage tanks is caused by liquid sloshing, especially under long-period and long-duration ground motions. This is because the sloshing frequency of the water is low and the period is similar to the pulse period of near-fault ground motions. For nuclear power plants, such sloshing may cause sinking and the complete collapse of the floating roofs of specific tanks. It may also cause fire in oil tanks, and cooling water loss in the spent fuel pool. Therefore, it is worth paying attention to the resonant effect of near-fault ground motions on the sloshing mode of water storage tanks.

An experiment is implemented to study the resonant response of the sloshing mode. The purpose of this experiment is to estimate the sloshing height and the associated total volume of water splashing out of a tank under near-fault ground motions, and also to determine the relationship between the resonant response and the input velocity pulse. This paper describes the test plan in detail, consisting of (1) the design of the scaled storage tank and water depth and (2) the selection and processing of input motions including the original near-fault ground motions, extracted velocity pulse, and extracted bandpass signals for resonance analysis, as well as the impulse motion for free vibration.

Keywords: storage tank, shaking test, near-fault ground motion, fluid-solid interaction

Introduction

In past earthquake events, damage to storage tanks or loss of their liquid content has been observed, resulting from unexpected extreme fluid–structure interactions. In industrial factories, some damage on tank roofs or at the top parts of tank walls has been caused by fluid sloshing behavior (SQUG, 2008). In nuclear power plants (NPPs), water has splashed out of the spent fuel pool, causing the release of radioactive material (TEPCO, 2007).

According to the Haroun–Housner model (Haroun & Housner, 1981), the fluid–structure response of a flexible tank during seismic excitation consists of three principal modes: the sloshing mode (also called a convective mode), the impulsive mode (also referred to as a flexible mode), and the rigid mode. In order to assess the seismic demand caused by sloshing modes, the industrial standard ACI 350.3-06 (ACI, 2010) gives equations to evaluate the sloshing frequency of stored water in a circular tank:

$$T_c = \left(\frac{2\pi}{\lambda}\right)\sqrt{D} \quad (1)$$

and

$$\lambda = \sqrt{3.68g\tanh\left[3.68\left(\frac{H_L}{D}\right)\right]}, \quad (2)$$

where T_c is the natural period of the first mode of sloshing, D is the internal diameter of the circular tank and H_L is the design depth of the stored water. The guidelines, ACI 350.3-06 and GIP-3A (GIP, 2001), give equations that can be used to estimate sloshing height h_s:

$$h_s = IR\left(\frac{S_a}{g}\right) \quad (3)$$

and:

$$h_s = 0.837R\left(\frac{S_a}{g}\right), \quad (4)$$

Respectively, where I is the importance factor, R is the internal radius of the circular tank, and S_a is the 0.5% damped horizontal design spectral acceleration of the ground or floor on which the tank is mounted at the frequency of the sloshing mode.

For outdoor large-scale reinforced-concrete (RC)

[1] Research Fellow, National Center for Research on Earthquake Engineering

[2] Associated Researcher, National Center for Research on Earthquake Engineering

[3] Project Assistant Researcher, National Center for Research on Earthquake Engineering

tanks in NPPs, the impulsive frequencies are usually above 20 Hz and are higher than the frequency content of general ground motions. On the other hand, the seismic response of the top portion of the fluid content in such tanks is mainly controlled by the low-frequency sloshing mode, which might be resonant with the low-frequency velocity pulse of near-fault ground motion. Figure 1 depicts an outdoor cylindrical RC condensate storage tank in a NPP in Taiwan.

Fig. 1. Condensate storage tank in a NPP

As depicted in Figure 2, for the same zero-period acceleration (0.67 g), the 5% damped spectral acceleration values at the sloshing frequency of the near-fault ground motions recorded in the 1999 Chi-Chi earthquake are higher than the value of the NUREG/CR-0098 design spectrum (Newmark & Hall, 1978). Based on Baker's study (Baker, 2007), the general period of velocity pulses of near-fault ground motions is between 0.4 and 12.9 seconds (0.078–2.5 Hz). This implies that the sloshing mode may be resonant with near-fault ground motion.

This study aims to investigate the dynamic behavior of the sloshing mode, and focuses on discussing the resonance phenomenon caused by near-fault ground motion. In order to examine the rationality of the evaluation equations provided by typical guidelines, a series of shaking table tests were executed to discuss possible influential parameters that might affect the sloshing period T_c and sloshing height h_s. In this paper, the test plan including the design of the tank specimen and input motion, is described in detail.

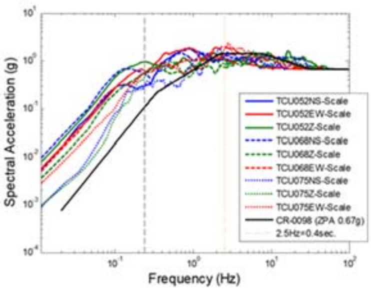

Fig. 2. Response spectrum of ground motion

Design of the Tank Specimen

To investigate the sloshing behaviors of water stored in vertical tanks, shaking table tests for circular scaled tanks were implemented. To design the tank specimens, the sloshing frequencies of water stored in a circular tank need to be examined. Figure 3 shows the relationship between the sloshing frequencies and depth of stored water to the internal radius ratio (H/R) from Eqs. (1) and (2). It shows that the sloshing frequency will increase and converge to a constant value as H/R increases.

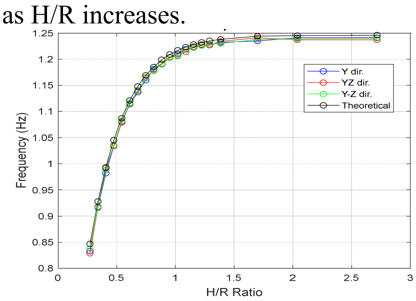

Fig. 3. The relationship between sloshing frequency and *H/R*

In the study, the design of the scaled tanks was limited by the dimensions of the shaking table, with the water levels kept above a specific level to avoid the tanks having uncovered bottoms. Hence, the experimental sloshing frequencies are expected to be slightly greater than the sloshing frequencies of the outdoor tanks. To investigate the sloshing behaviors of different water levels, two sets of the scaled tanks were designed with an internal diameter of 0.6 m. One set was for H/R = 1 and the other set was for H/R = 2. Each set had two testing tanks, including one high tank and one low tank. The two tanks with equal water level were subjected to the same input motion simultaneously. Using the design of the heights of the two tanks, the sloshing height can be measured from the high tank, and the volume of water splashing out of tank can be estimated from the low tank. Therefore, the relationship between the sloshing height and the associated total volume of water splashing out of the tank can be found. Considering the factors described above and following the design procedure of the scaled tanks shown in Figure 4, the sloshing frequencies were designed to be below 1.25Hz. The internal dimensions of the tanks, the water levels, and the corresponding sloshing frequencies per Eq. (1) are shown in Table 1. Table 2 shows that the tanks have higher frequencies than the sloshing frequencies of the stored water found through FEM modal analysis. Finally, the tanks were made of A36 steel. Outside each scaled tank was a water receiving tank to avoid water splashing onto the shaking table. One of the design models is shown in Figure 5. The tank specimens were anchored to the shaking table with M30 bolts during the shaking tests (Figure 6).

Table 1 Dimensions and sloshing frequencies of the tank specimens

Circular tanks					
Set	Inside radius (m)	Tank heights (m)	Water levels (m)	H_L/R	Sloshing frequencies (Hz)
1	0.3	0.5	0.3	1	1.2037
	0.3	1	0.3	1	1.2037
2	0.3	0.7	0.6	2	1.2337
	0.3	1.2	0.6	2	1.2337

Table 2 Modal analysis results.

Circular tanks			
Set	Tank heights (m)	Thickness (m)	Frequencies of 1st mode(Hz)
1	0.5	0.0103	364.96
	1	0.0103	181.28
2	0.7	0.0103	272.16
	1.2	0.0103	141.16

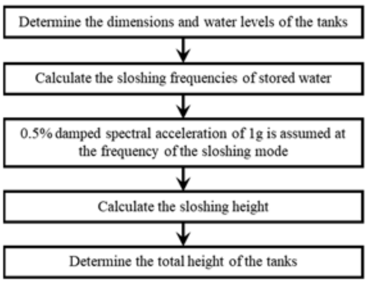

Fig. 4. Design procedure for the scaled tanks

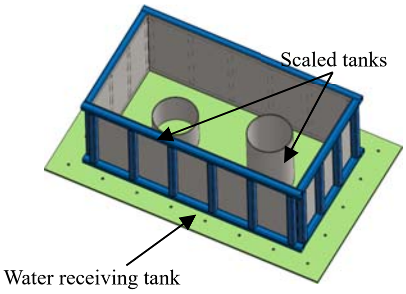

Fig. 5. Circular tank test specimens

Fig. 6. Tank specimens located on the shaking table

Input Motion

In order to investigate the basic dynamic characteristics and seismic behavior of the contained water, the testing methods and respective input motions were selected as follows (Figure 7):

(1) System-identification tests: As shown in Figure7 and Figure 8, sine-sweep survey and impulse tests were adopted in this study. The purpose of the sine-sweep survey is to obtain more distinct modal shapes of the water surface. Figure 9 shows that the spectral acceleration values of the impulse motion in the range from 0.3 to 2 Hz are approximately 0.14g.

(2) Near-fault ground motion tests: Referring to the definition proposed by Baker (2007), 91 near-fault motions with pulse-like properties were selected from 3551 records stored in the PEER NGA West database (PEER Center). The database provides the period of the velocity pulse (T_p) through wavelet analysis and the period of the peak spectral velocity (T_{Sv}) of the fault-normal (FN) component of each ground motion. As shown in Table 3 and Figure 10, in order to observe the effects of T_p and T_{Sv} on sloshing height, eight records of five earthquake events were selected from the 91 records, based on the comparison of T_p and T_{Sv} values to the predicted sloshing frequency of 1.2 Hz for the tested water levels of 30 cm and 60 cm. According to Eqs. (3) and (4), the sloshing height h_s is controlled by the spectral acceleration at the sloshing frequency. In order to observe other near-fault ground motion parameters that my possibly influence sloshing height, each FN component of the tested ground motion was scaled to anchor the 0.5% damped spectral acceleration to 1.0 g at the sloshing frequency of 1.2 Hz. The scaled FN, fault-parallel (FP), and vertical components of each ground motion were kept in their original proportions unless restricted by the shaking table limits. Peak values of each normalized motion are depicted in Table 4.

(3) Velocity-pulse and residual motion tests: In order to clarify the effects of velocity pulses at resonance or non-resonance frequencies on the sloshing height with comparison to the original near-fault ground motion test results, the velocity pulses and residual motions were extracted from RSN 451 and RSN 1550 with the MATLAB wavelet analysis codes provided by Baker (2007). Using the comparison between the sloshing height values resulting from the original near-fault ground motions, velocity- pulses and residual motions, the contribution from long-period pulse energy or the resonant response to the sloshing behavior can be clarified.

(4) Band-pass and residual motion tests: In addition to the wavelet analysis of velocity time histories, a band-pass frequency analysis for the acceleration of RSN 1550 was performed in the frequency range of 0.730 Hz to 1.324Hz. According to Eqs. (3) and (4), since the spectral acceleration values of the band-pass motion are almost the same as the original ground motions, the band-pass motion is predicted to excite the resonant response of water sloshing, similar to the original ground motion.

Table 3 Basic information on the ground motions.

RSN	Event	Station	T_P (sec)	T_{Sv} (sec)
1051	Northridge-01	Pacoima Dam (upper left)	0.896	0.733
1529	Chi-Chi, Taiwan	TCU102	9.723	2.543
568	San Salvador	Geotech Investig Center	0.861	0.647
1503	Chi-Chi, Taiwan	TCU065	5.740	4.453
1050	Northridge-01	Pacoima Dam (downstr)	0.504	0.445
1550	Chi-Chi, Taiwan	TCU136	10.326	0.940
828	Cape Mendocino	Petrolia	2.996	0.733
451	Morgan Hill	Coyote Lake Dam (SW Abut)	0.952	0.688

Table 4 Peak values of the normalized motions.

RSN	PGA *(g)*			PGV *(m/s)*			PGD *(m)*		
	FN	FP	Vert.	FN	FP	Vert.	FN	FP	Vert.
1051	0.494	0.526	0.441	0.384	0.174	0.179	0.082	0.025	0.041
1529	0.305	0.181	0.129	0.824	0.808	0.498	1.726	1.203	0.400
568	0.613	0.265	0.293	0.451	0.379	0.088	0.073	0.109	0.016
1503	0.362	0.242	0.118	0.615	0.362	0.308	0.879	0.566	0.310
1050	0.843	0.414	0.322	0.845	0.327	0.242	0.107	0.049	0.023
1550	0.285	0.277	0.096	0.684	0.946	0.270	1.877	1.562	0.400
828	0.288	0.295	0.077	0.383	0.283	0.096	0.119	0.122	0.094
451	0.455	0.604	0.216	0.348	0.392	0.087	0.057	0.078	0.013

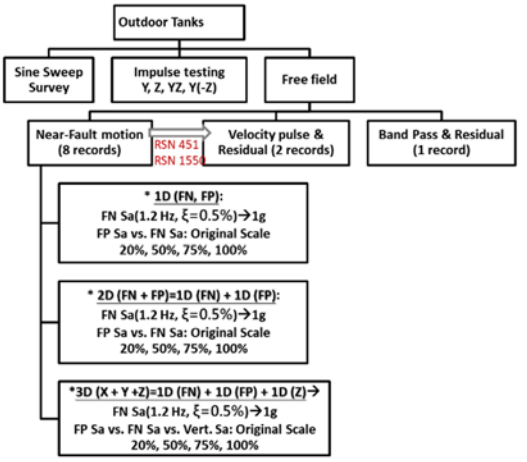

Fig. 7. Input motion categories.

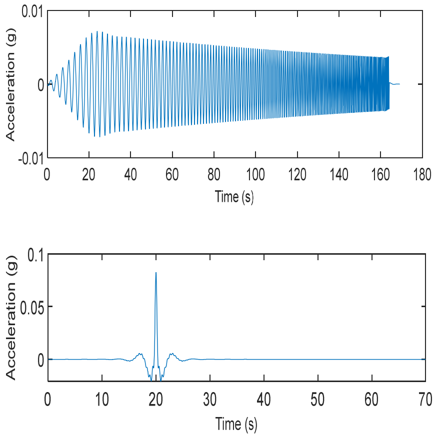

(a)

(b)

Fig. 8. Inputs for system identification.

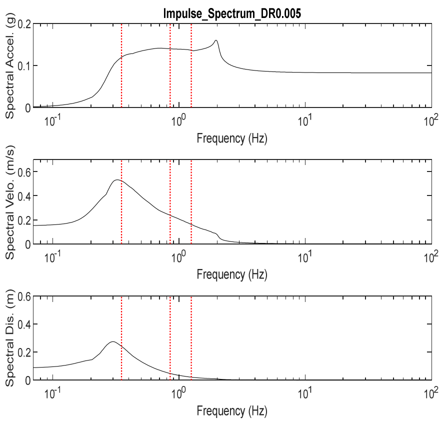

Fig. 9. Response spectrum of impulse motion.

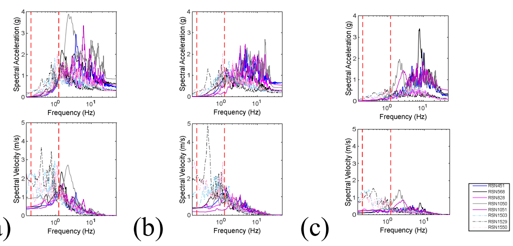

(a) (b) (c)

Fig. 10. Normalized near-fault ground motions in: (a) FN, (b) FP and (c) vertical directions.

Conclusions

The purpose of this experiment was to estimate the sloshing height and the associated total volume of water splashing out of a tank under near-fault ground motions. This paper described the design of a scaled storage tank and water depth, and the selection and processing of input motions including original near-fault ground motions, extracted velocity pulses, extracted bandpass signals for resonance analysis, and the impulse motion for free vibration. Finally, two sets of scaled tanks were designed with internal diameters of 0.6 m to investigate the sloshing behaviors of different water levels (H/R =1 and H/R =2). Eight near-fault ground motions were selected to determine the relationship between the resonant response and the input velocity pulse. For related preliminary test results, please refer to the content of the accompanying paper titled “Experimental Study of Near-Fault Effects on the Sloshing Mode of Liquid in a Storage Tank – Test Results”.

References

ACI Committee 350.3-06 (2010), “Seismic Design of Liquid-Containing Concrete Structures and Commentary”, American Concrete Institute, Farmington Hills, MI.

GIP, Rev. 3A. (2001), “Generic Implementation Procedure for Seismic Verification of Nuclear Plant Equipment”, SQUG.

Haroun, M.A. & Housner, G.W. (1981), “Seismic design of liquid-storage tanks”, Journal of the Technical Councils of the American Society of Civil Engineers, Vol. 107, No. TCI, pp. 191-207.

Jack W. Baker (2007), “Quantitative Classification of Near-Fault Ground Motions”, Bulletin of the Seismological Society of America, Vol. 97, No. 5, pp. 1486–1501.

Newmark N. M. & Hall W. J. (1978), “Development of Criteria for Seismic Review of Selected Nuclear Power Plants”, Technical Report NUREG/CR-0098, U.S. NRC.

PEER Center, University of California, PEER NGA West database, https://ngawest2.berkeley.edu/

The Seismic Qualification Utility Group (SQUG) (2008), “Seismic evaluation training course”, Rev. 4.2.

Tokyo Electric Power Company (TEPCO) (2007), “Impact of the Niigata Chuestu-oki Earthquake on the TEPCO Kashiwazaki-Kariwa Nuclear Power Station and Countermeasures”.

Comparison of Fourier Amplitude Spectra of Strong Ground Motions from Taiwan and California Region

Jyun-Yan Huang[1] Che-Min Lin[2] Chun-Hsiang Kuo[3] and Kuo-Liang Wen[4]

黃雋彥[1]、林哲民[2]、郭俊翔[3]、溫國樑[4]

Abstract

The ground motion prediction equation (GMPE) is widely used around the world. Development of a local GMPE can help to predict possible future earthquakes of specific magnitudes and distance ranges, but in many regions the historical earthquake database will have some gaps (lack of data with specific magnitude ranges). In this case, databases from foreign regions might help to decide the trend of the regression feature of the extrapolated part, but regional differences should be considered carefully, owing to different seismological structures and geological settings. In this study, spectral differences of the Fourier amplitude spectra of strong ground motions are first compared for Taiwan and the California region. For these two regions, there have been a sufficient number of shallow crustal earthquake events to thoroughly consider spectral differences for similar magnitudes, hypocenter distances, site classifications, *etc*. The preliminary results show significant differences between the low-frequency and high-frequency bands that mainly relate to the seismogenic depth of the source and the site effect. The highlighted features of regional differences can help generate an adjustment factor for foreign GMPEs and extend the available source-scaling relationships for future possible large earthquakes.

Keywords: Regional difference, Taiwan, California, FAS

Introduction

According to seismic records for historical earthquakes, since digital records began in the 1990s, the largest earthquake in Taiwan was the 1999 Chi-Chi earthquake with Mw 7.6, and this was fully captured by the Taiwan Strong Motion Instrumentation Program. It is very important to have comprehensive ground motion data to generate a precise ground motion prediction equation (GMPE) for the prediction of future possible earthquakes. However, because there are insufficient records in Taiwan for large earthquakes, extrapolation to magnitude 8 or greater would be inappropriate on account of the significant gaps in the data for both magnitude and distance. Other regions that have a large amount of earthquake data might be able to fill the abovementioned gaps and would be an important foreign database for helping to fully develop GMPE prediction. However, there are significant tectonic differences between Taiwan and foreign regions that should be taken into consideration. In this study, California, a region in America that has greater events and a wider distance range, is investigated for the database, first checking for regional differences in the Fourier amplitude spectra (FAS) with shallow events in Taiwan in order to fix the magnitude gap between Mw 7.0 and 7.6 or larger, with the goal of application to future construction of a GMPE.

Database

Shallow events recorded in the California database were selected from the Next Generation Attenuation Relationships for Western US (NGAW2) project because the magnitude–distance range (M-R bin) was wide enough for analysis of large-magnitude–near-source records. A comparison of the databases of California and Taiwan is shown in

[1] Assistant Researcher, National Center for Research on Earthquake Engineering

[2] Associate Researcher, National Center for Research on Earthquake Engineering

[3] Research Fellow, National Center for Research on Earthquake Engineering

[4] Division Head, National Center for Research on Earthquake Engineering; Professor, National Central University

Figure 1. The selection criteria of the records to be compared were as follows: M-R bin within 0.1, rupture distance (Rrup) bin within 5 km, depth of rupture to surface (Ztor) within 5 km, and average shear wave velocity of top 30 m (VS30) within 50 m/s. For instance, red circles represent recorded pairs from both datasets that correspond to Mw = 5.0–5.1, Rrup = 75–80 km, Ztor = 20–25 km, and Vs30 = 500–550 m/s.

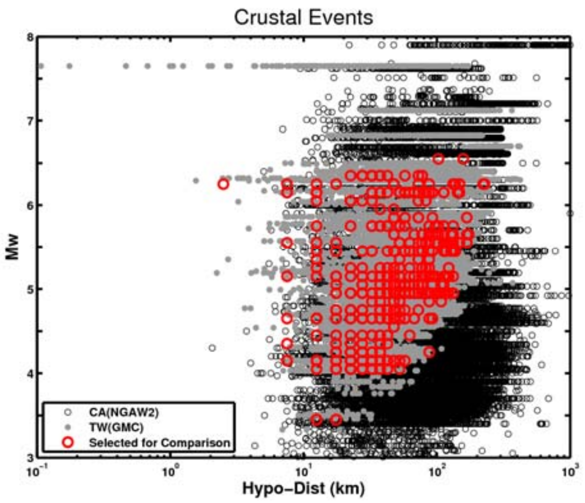

Fig. 1. M-R bin of California (black circle) and Taiwan (gray dot) database, red circle denotes records selected for comparison in this study.

Results and Discussions

Four pairs of records are shown in Figure 2 as examples for comparison. The white-colored frequency band was used because the available frequencies were different for the datasets of each member of each pairing. FAS ratios were calculated for the abovementioned data and are shown in Figure 3. In general, the special features within the low- and high-frequency bands were quite different for the four pairs. Therefore, the average FAS ratios were calculated for three different bands, first including low (usable frequency or at least from 0.5 Hz to 1 Hz; light blue lines in Fig. 3), medium (1 to 5 Hz; green lines), and high (5 to 20 Hz or at least usable frequency to 10 Hz; purple lines). Figure 4 shows the average FAS ratio of each pair from the low- to high-frequency bands against Mw, Rrup, VS30, and Ztor. The results indicate that the significant difference between low and high frequencies is mainly related to source scaling (Mw), path attenuation (Rrup), and seismogenic depth (Ztor). and slightly related to site classification (VS30).

In general, high-frequency energy for large earthquakes (Mw 4.5–6.2) was significantly lower in Taiwan than in California (Fig. 5) , which indicates a relatively lower corner frequency or stress drop, as well as a source term and higher kappa in Taiwan that would also be found in a stochastic point-source simulation between the two regions (Fig. 6).

Secondly, a faster attenuation relation for high frequency was found in California and the reverse for low frequency, especially for larger distances (Fig. 7). This was also examined using a stochastic point-source simulation (Fig. 8). Stochastic simulation of these two regions showed that California had faster attenuation across the whole frequency range due to geometrical spreading, and faster attenuation in the high-frequency band but slower in the low-frequency band due to the quality factor.

The large difference between the high- and low-frequency bands for larger Ztor (Fig. 9) might be due to the significant difference in seismogenic depth between California (15 km) and Taiwan (35–50 km). Finally, the FAS ratios are completely different for different frequencies on account of the different site conditions (Fig. 10). For instance, the FAS ratio for the medium band was higher at a softer site in California (low VS30), the FAS ratio for the low band was higher at a harder site (VS30 greater than 400 m/s) and also at the same VS30 condition. These features could be a result of the comprehensive effect of the amplification function in combination with high-frequency attenuation (Fig. 11).

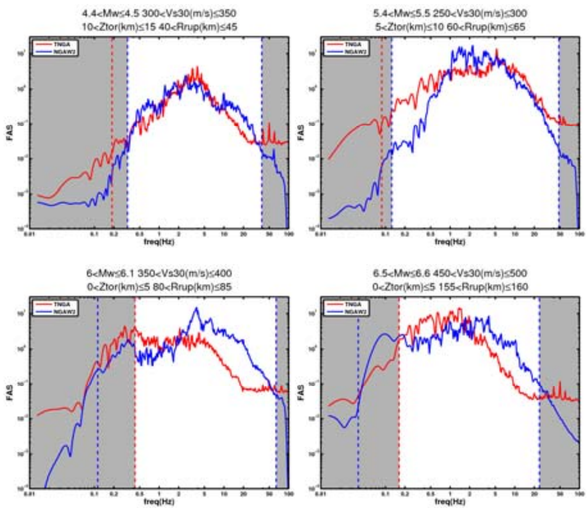

Fig. 2. Comparison of FAS records of selected bins for Taiwan (red) and California (blue).

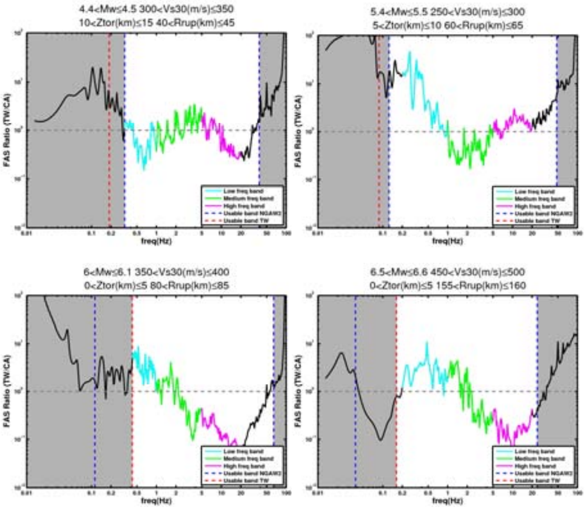

Fig. 3. FAS ratios calculated from Taiwan FAS divided by California FAS.

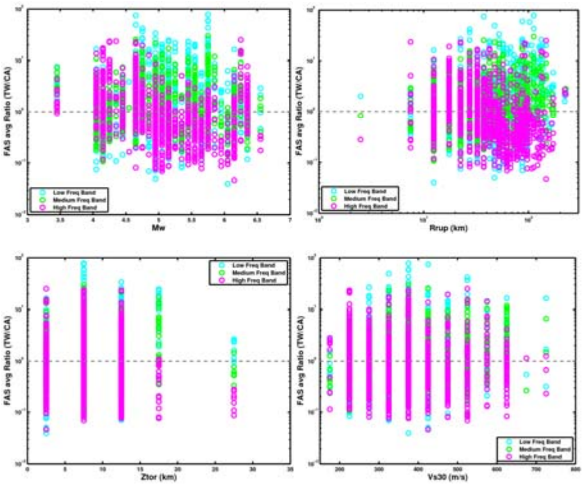

Fig. 4. Average FAS ratios for different frequency bands, including low frequency in light blue, medium frequency in green, and high frequency in purple. Individual ones were compared with Mw, Rrup, Ztor, and VS30.

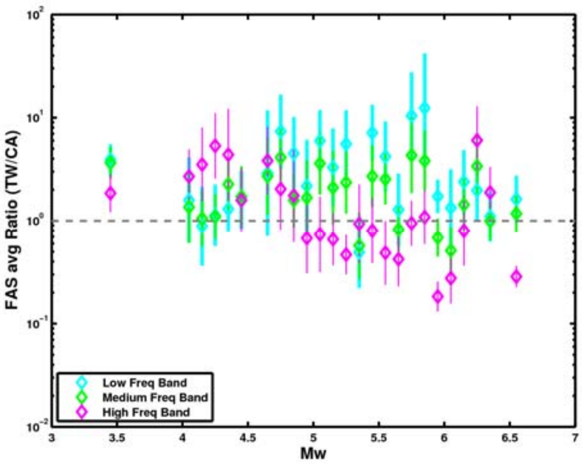

Fig. 5. Mean FAS ratios for different frequency bands compared with magnitude (Mw). Colors indicate different bands as per Fig. 4.

Parameters	Atkinson (2015)-California	Huang et al. (2017)-Taiwan
Stress parameter, Δσ (bars)	300	Mw <5.5, 60 5.5<Mw <6.5, 80 Mw >6.5, 90
Kappa, κ_0 (sec)	0.02	0.0517 (by Prof. Kuo-Liang Wen @ WM #2)

Fig. 6. Parameters used in stochastic point-source simulation related to stress and high-frequency attenuation in Taiwan and California.

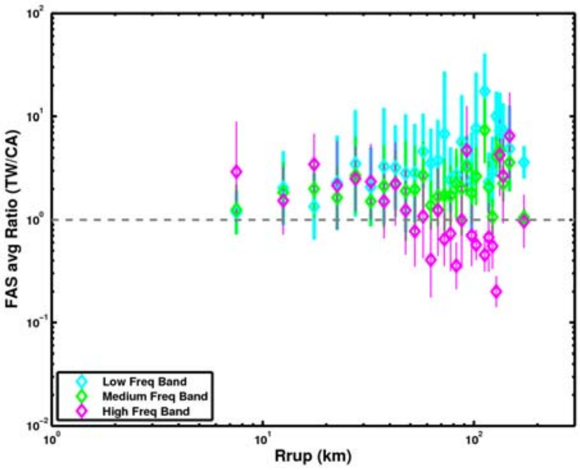

Fig. 7. Mean FAS ratios for different frequency bands compared with rupture distance (Rrup). Colors indicate different bands as per Fig. 4.

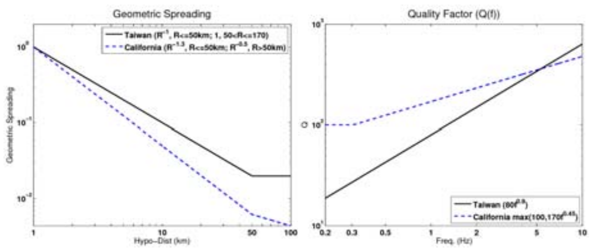

Fig. 8. Attenuation relations of Taiwan and the California region for stochastic point-source simulation.

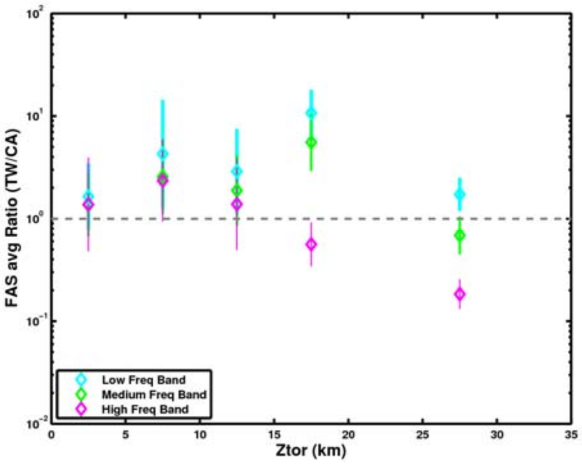

Fig. 9 Mean FAS ratios for different frequency bands compared with depth to the rupture surface (Ztor). Colors indicate different bands as per Fig. 4.

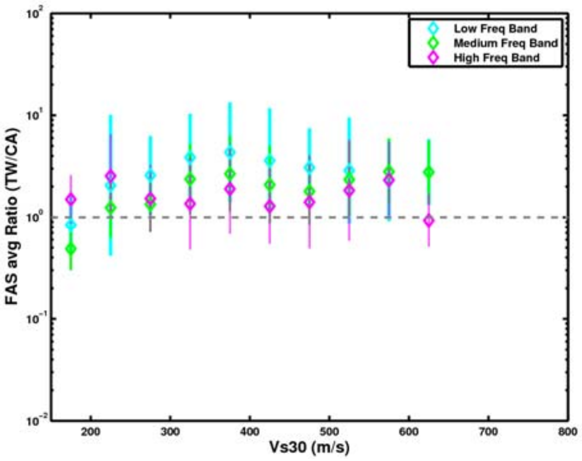

Fig. 10. Mean FAS ratios for different frequency bands compared with depth to the VS30. Colors indicate different bands as per Fig. 4.

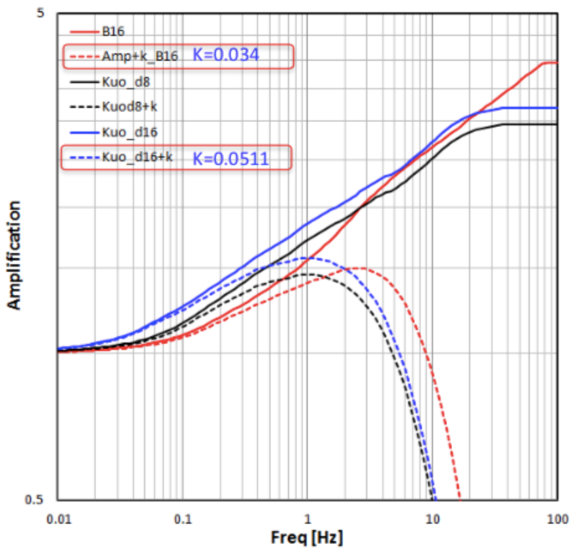

Fig. 11. Theoretical amplification functions compiled from velocity structures in California and Taiwan. Dashed lines are amplification functions that have considered the high-frequency attenuation (kappa) relation. The red dashed line is from California and the blue dashed line is from Taiwan. Both assume a shallow structure of 16 km.

Conclusions

The Fourier amplitude spectra (FAS) features of shallow crustal earthquakes in California and Taiwan were compared. Records that had overlapping or similar ,magnitude, rupture distance, depth of rupture to surface, and average shear wave velocity of top 30 m were selected for use in this study. Preliminary results showed that the FAS were quite different from low to high frequency. In general, for low-frequency FAS, Taiwan's were greater than California's. In contrast, they were at a similar level for the high-frequency band. These differences were mainly a result of the source (stress drop) and site (amplification function and kappa) effects. The abovementioned effects could compensate for the opposite trend of the path effect (faster attenuation relation in California, including quality factor and geometrical spreading) that resulted in the FAS ratio relationship found between California and Taiwan.

References

Huang J.-Y., Wen, K.-L., Lin, C.-M., Kuo, C.-H., Chen, C.-T. and Chang, S.-C., (2017), "Site correction of a high-frequency strong-ground-motion simulation based on an empirical transfer function", *Journal of Asian Earth Sciences* 138, 399-415.

Seismic Design Method for Reducing the Variation of Peak Inter-Story Drifts along Building Height

Jui-Liang Lin [1], Jyun-Ying Dai [2] and Keh-Chyuan Tsai [3]

林瑞良 [1]、戴均穎 [2]、蔡克銓 [3]

Abstract

This study develops a seismic design approach, which has no need of additional structural members, to uniformly distribute the peak inter-story drift ratios along building heights. The generalized building model (GBM), which can effectively imitate a building, is employed to achieve this aim. The flexural-shear deformation factor of a GBM, denoted α, characterizes the deformation type of the corresponding building. Varying the deformation type of a building changes the distribution of the peak inter-story drift ratios over the stories. Therefore, the proposed optimization approach searches for the optimal value of α, denoted α_{opt}, so that the GBM's normalized variation of peak inter-story drift ratios is minimized. In light of α_{opt}, the member properties of the original building model are adjusted.

Keywords: structural optimization, uniform inter-story drifts, seismic design, weak story, response spectrum analysis

Introduction

When the ratio of a story's shear capacity to shear demand is much lower than that of its neighboring stories (*i.e.*, a weak story deficiency), the weak story is very likely to yield earlier than others. Once the weak story yields, the whole deformation of the building gradually concentrates on the softened weak story, preventing the spread of plastic hinges to other stories. As a result, a collapse mechanism is formed at the weak story, due to an excessive inter-story drift ratio, which leads to serious seismic losses. Therefore, recent research has proposed seismic design methods aimed at producing uniform inter-story drift ratios over a building (Moghaddam *et al.*, 2005).

The cantilever beam model (Fig. 1(a)) has been extensively utilized to investigate the seismic responses of wall-frame tall building systems. The cantilever beam model, however, is not suitable for simulating the deformations of low-rise and mid-rise buildings because the story masses are simulated as a continuous mass distributed along the cantilever beam. This study proposes the generalized building model (GBM) (Fig. 1(b)) to extend the scope of applicability of the cantilever beam model. The GBM, consisting of a pure shear stick (Fig. 1(c)) and a pure flexural stick (Fig. 1(d)), is a variation of the cantilever beam model (Lin 2019). Using the GBM, this study proposes an optimization approach through an adjustment of the properties of the structural members, instead of using supplementary structural members/systems to achieve uniform inter-story drift ratios.

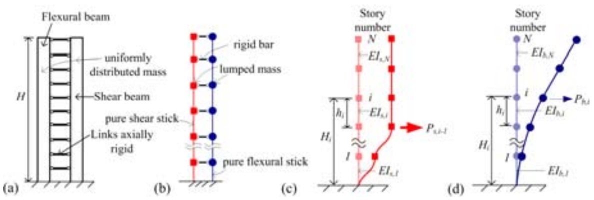

Fig 1. (a) The cantilever beam model. (b) A sketch of the GBM. (c) The lateral deformation of the pure shear stick. (d) The lateral deformation of the pure

[1] Research Fellow, National Center for Research on Earthquake Engineering.

[2] Graduate Student, Department of Civil Engineering, National Taiwan University

[3] Professor, Department of Civil Engineering, National Taiwan University

flexural stick subjected to a concentrated lateral load.

Generalized Building Model

In light of the cantilever beam model (Fig. 1(a)), the GBM simulating an N-story building, in which the r-th story height is h_r and the story diaphragms are rigid, consists of two sticks (Fig. 1(b)). The deformation types of the two sticks subjected to lateral loads are pure shear and pure flexure, respectively (Figs. 1(c) and (d)). These two sticks are laterally connected to each other by axially rigid bars at all levels of the lumped story masses. Once the story masses of the N-story building are given, the mass matrix of the GBM, which is an $N\times N$ diagonal matrix, is straightforwardly obtained. The displacement vector of the GBM is expressed as $u = [u_N\ u_{N-1}, \ldots, u_1]^T$, where the subscript of u indicates the story number. Assuming that the ratio of the lateral stiffness of the r-th story to that of the first story of the N-story building is κ_r, the lateral stiffness matrix of the pure shear stick is:

$$\mathbf{K}_s = k_{s,1}\mathbf{E}_s \tag{1}$$

where $k_{s,1} = EI_{s,1}/h_1^3$ and $EI_{s,1}$ is the flexural rigidity of the bottom segment of the pure shear stick. Additionally, the matrix $\mathbf{E_s}$ (Eq. 1) is a matrix with a diagonal band of non-zero elements. On the other hand, the lateral stiffness matrix of the pure flexural stick is:

$$\mathbf{K}_b = \mathbf{F}_b^{-1} \tag{2}$$

where $\mathbf{F}_b$ represents the $N\times N$ flexibility matrix of the pure flexural stick. By using the unit-load method, the i-th row and j-th column element of $\mathbf{F}_b$, denoted as f_{ij}, is:

$$f_{ij} = \frac{e_{ij}}{k_{b,1}} \tag{3}$$

where $k_{b,1} = EI_{b,1}/h_1^3$ and $EI_{b,1}$ is the flexural rigidity of the bottom segment of the pure flexural stick. Additionally, e_{ij} (Eq. 3) is:

$$e_{ij} = \begin{cases} \displaystyle\sum_{r=1}^{N+1-i} \frac{1}{\kappa_r} \left\{ \begin{aligned} &\bar{H}^r_{N+1-j}\bar{H}^r_{N+1-i}\left(\bar{H}^r_r - \bar{H}^r_{r-1}\right) - \\ &\frac{\left(\bar{H}^r_{N+1-j} + \bar{H}^r_{N+1-i}\right)}{2}\left[\left(\bar{H}^r_r\right)^2 - \left(\bar{H}^r_{r-1}\right)^2\right] + \\ &\frac{1}{3}\left[\left(\bar{H}^r_r\right)^3 - \left(\bar{H}^r_{r-1}\right)^3\right] \end{aligned} \right\}, & i \ge j \\ e_{ji}, \quad i < j \end{cases} \tag{4}$$

where $\bar{H}^r_s = H_s/h_r$. Here, H_s represents the height measured from the ground to the s-th story and h_r is the story height of the r-th story (Fig. 1(d)). Therefore, $\mathbf{K}_b$ (Eq. 2) can be expressed as:

$$\mathbf{K}_b = k_{b,1}\mathbf{E}_b \tag{5}$$

where $\mathbf{E}_b$ is the inverse of the matrix consisting of elements e_{ij}, in which i and j range from 1 to N. As a result, the total lateral stiffness matrix of the GBM, denoted as $\mathbf{K}$, is:

$$\mathbf{K} = \mathbf{K}_s + \mathbf{K}_b = k_{s,1}\mathbf{E}_s + k_{b,1}\mathbf{E}_b = k\left[\alpha\mathbf{E}_s + \left(1-\alpha\right)\mathbf{E}_b\right] \tag{6}$$

where:

$$k = k_{s,1} + k_{b,1} = \frac{EI_{b,1} + EI_{s,1}}{h_1^3} = \frac{EI_{GBM}}{h_1^3}, \quad \alpha = \frac{k_{s,1}}{k_{s,1} + k_{b,1}} \tag{7}$$

The value of α is clearly between 0 and 1. When the value of α equals zero, the lateral deformation of the GBM is of a pure flexural type. When the value of α equals 1, the lateral deformation of the GBM is of a pure shear type.

Seismic Design Method

Unlike ideal shear buildings, the deformation type of an ordinary building is usually a mixture of shear-type and flexural-type deformations. It is clear that reinforced concrete walls/cores deform much like the pure flexural type (Fig. 2(a)), whereas the deformations of moment-resisting frames are closer to the pure shear type (Fig. 2(b)). Figure 2(a) indicates that the deflection slope is larger at lower stories and smaller at upper stories. In other words, the lower stories experience smaller inter-story drifts compared with the upper stories. Conversely, Figure 2(b) indicates that the deflection slope is smaller at lower stories and larger at upper stories. In other words, the lower stories experience larger inter-story drifts compared with the upper stories. Figure 2(c), which is a combination of shear-type and flexural-type deformations, shows much more uniform inter-story drifts over the building's height. This means that, by adjusting the deformation type of a building, it is possible to create a relatively uniform distribution of inter-story drifts. Besides adding walls/braces to a building, the deformation type can be changed by varying the properties of ordinary structural members. The essential task is determining the optimal deformation type of a building that results in minimum variation of peak inter-story drifts along the building's height. The challenge is that the optimal deformation type should consider the influence of higher modes and be irrespective of input ground motions.

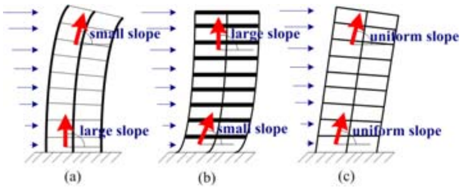

Fig. 2. Three different buildings: (a) a flexural-type building, (b) a shear-type building, and (c) a typical building with combined flexural-type and shear-type deformations.

The steps of the proposed optimization approach are as follows:

Step 1: Perform eigenvalue analysis of the complete finite element model (FEM) of the N-story building to obtain its vibration periods and mode shapes.

Step 2: Compute the lateral stiffness of the FEM's i-th story, for i = 1 to N, by pushing the i-th story with a concentrated lateral load applied to its center of mass. Note that, while pushing the i-th story, all the degrees of freedom for the stories below are fixed. The lateral stiffness of the i-th story is equal to the required load, producing one unit of elastic lateral displacement at the i-th story's center of mass.

Step 3: The ratios of the lateral stiffness of the i-th story to that of the first story (*i.e.*, κ_i), for i = 1 to N, are thus obtained.

Step 4: By means of κ_i, for i = 1 to N, compute the matrices $\mathbf{E}_s$ and $\mathbf{E}_b$.

Step 5: Construct the GBM with N lumped masses. The $N\times N$ diagonal mass matrix of the GBM, denoted $\mathbf{M}$, is the same as that of the target building. By varying α from 0 to 1 with a 0.01 increment, the GBM's stiffness matrix $\mathbf{K}$ (Eq. 6) corresponding to every α is computed. Then, perform eigenvalue analysis of every GBM. Note that the parameter k shown in Eq. 7 is varied so that the first vibration periods of all GBMs are equal to that of the FEM. This is the basic requirement for enabling the GBMs to satisfactorily simulate the target building.

Step 6: Compute the values of the index I_D (Eq. 8) for all GBMs. The α of the GBM that minimizes the value of the index I_D is the flexural-shear deformation factor of the FEM, denoted $\alpha^{(0)}$. The index I_D is expressed as:

$$I_D = \sum_{n=1}^{3} MR_n \sqrt{\sum_{i=1}^{N} \left(\frac{\varphi_{n,i}^{FEM}}{\varphi_{n,N}^{FEM}} - \frac{\varphi_{n,i}}{\varphi_{n,N}} \right)^2} \tag{8a}$$

where:

$$MR_n = \frac{\Gamma_n^2 M_n}{sum\left(diag\left(\mathbf{M}\right)\right)}, \quad M_n = \boldsymbol{\varphi}_n^T \mathbf{M} \boldsymbol{\varphi}_n \tag{8b}$$

and $\varphi_{n,i}^{FEM}$ and $\varphi_{n,i}$ are the i-th components of the n-th mode shape of the FEM and the GBM, respectively. In addition, MR_n is the effective modal participation mass ratio, Γ_n is the modal participation factor of the GBM's n-th vibration mode, and $sum\left(diag\left(\mathbf{M}\right)\right)$ is the summation of the diagonal elements of the mass matrix (*i.e.*, the total mass of the building). I_D (Eq. 8(a)) represents the summation of the weighted root mean square of the discrepancy between the normalized mode shape of the GBM and FEM (*i.e.*, $\phi_{n,i}/\phi_{n,N}$ and $\phi_{n,i}^{FEM}/\phi_{n,N}^{FEM}$, respectively). Additionally, in order to take the varying importance of different vibration modes into account, the effective modal participation mass ratio (*i.e.*, MR_n) is adopted as the weighting factor.

Step 7: Compute the peak inter-story drift of the i-th story of every GBM with:

$$\theta_{i,\max} \approx \sqrt{\sum_{n=1}^{3} \left(\Gamma_n \left(\frac{\varphi_{n,i} - \varphi_{n,i-1}}{h_i} \right) S_{dn,in} \right)^2}, \quad i = 1 \sim N \tag{9}$$

where h_i is the i-th story height and $S_{dn,in}$ is the inelastic spectral displacement of the n-th vibration mode. $S_{dn,in}$ is approximately estimated from the elastic spectral displacement $S_{dn,e}$ as follows (Chopra and Chintanapakdee, 2004):

$$S_{dn,in} \approx C_{Rn} S_{dn,e} \tag{10a}$$

$$C_{Rn} = 1 + \left[\left(L_{Rn} - 1 \right)^{-1} + \left(\frac{61}{R_{yn}^{2.4}} + 1.5 \right) \left(\frac{T_n}{T_c} \right)^{2.4} \right]^{-1} \tag{10b}$$

$$L_{Rn} = \frac{1}{R_{yn}} \left(1 + \frac{R_{yn} - 1}{\beta_n} \right) \tag{10c}$$

where R_{yn} is the yield-strength reduction factor and β_n is the post-yielding stiffness ratio of the n-th vibration mode. R_{yn} and β_n are obtained by performing modal pushover analysis (Chopra and Goel, 2002) of the FEM. In addition, T_n is the vibration period of the n-th vibration mode and T_c is the vibration period separating the acceleration- and velocity-sensitive regions of the design response spectrum. By this means, the column vector $\boldsymbol{\theta} = \left[\theta_{1,\max}, \ \cdots, \ \theta_{N,\max} \right]^T$ of each GBM is obtained. Note that $S_{dn,in}$ in Eq. 9 is simply replaced by $S_{dn,e}$ when the distribution of elastic peak inter-story drifts is the focus of the optimization design. Certainly, both $S_{dn,in}$ and $S_{dn,e}$ can be obtained by performing elastic and inelastic dynamic analyses of the single-degree-of-freedom modal systems, respectively, as long as the concerned ground motion is given. The corresponding optimization results, however, are only effective for that particular ground motion. To produce a generalized optimization result, which is independent of the input ground motions, this study uses the elastic design response spectrum with Eqs. 9 and 10 to estimate $S_{dn,e}$ and $S_{dn,in}$.

Step 8: Compute the values of the index I_V (Eq. 11) for all GBMs. The α of the GBM that minimizes the value of the index I_V is the optimal flexural-shear deformation factor, denoted α_{opt}. That is to say, the index I_V is the criterion used in this study to measure the improvement in the distributions of the peak inter-story drifts of the target buildings. The index I_V is expressed as:

$$I_V = \frac{\hat{\sigma}}{mean(\boldsymbol{\theta})} \tag{11a}$$

and:

$$\hat{\sigma} = \sqrt{\sum_{i=1}^{N} \frac{\left(\theta_{i,\max} - mean(\boldsymbol{\theta})\right)^2 pf_i}{N-1}}, \quad pf_i = \frac{\sum_{x=i}^{N} w_x H_x}{\sum_{x=1}^{N} w_x H_x} \tag{11b}$$

where $mean(\boldsymbol{\theta})$ represents the average value of the column vector $\boldsymbol{\theta}$, H_x is the x-th story height measured from the ground, and w_x is the x-th story weight. Finally, I_V represents the normalized variation of the peak inter-story drifts over the building's height, which is similar to the coefficient of variation of $\boldsymbol{\theta}$ except that the penalty factor pf_i is incorporated into the computation of the standard deviation (Eq. 11b).

Step 9: If $|\alpha^{(0)} - \alpha_{\text{opt}}| > 0.01$, then modify the properties of the FEM's structural members and return to Step 1 for iteration. Otherwise, it indicates that the FEM possesses the desired small variation of the peak inter-story drifts over the building's height. The iteration process is thus stopped. Note that $\alpha^{(0)}$, which is obtained from Step 6, represents the flexural-shear deformation factor of the FEM.

When $\alpha^{(0)}$ is smaller than α_{opt}, the flexural-shear deformation factor should be increased (*i.e.*, the deformation type should be shifted towards the pure shear type). Conversely, if $\alpha^{(0)}$ is larger than α_{opt}, then the flexural-shear deformation factor should be decreased (*i.e.*, the deformation type should be shifted towards the pure flexural type). It is known that increasing the cross-sectional area of columns (denoted A_c), increasing the cross-sectional moment of inertia of beams (denoted I_b), or decreasing the cross-sectional moment of inertia of columns (denoted I_c) intensifies the shear-type deformation (*i.e.*, increases the value of α). On the contrary, decreasing A_c, decreasing I_b, or increasing I_c intensifies the flexural-type deformation (*i.e.*, decreases the value of α).

Numerical Validation

One nine-story steel moment-resisting frame is used as the example building in this study. The results of elastic response spectrum analysis show that the peak elastic inter-story drift ratios of the optimized building are less varied between stories than those of the original building. In addition, thirteen out of twenty nonlinear response history analysis results are consistent with the trends observed from the elastic response spectrum analyses. As a result, the effectiveness of the proposed optimization approach on the investigated building is confirmed.

Conclusions

The highlights of this study are as follows. The generalized building model (GBM) was introduced as a simplified numerical model for a target building whose number of stories and the distributions of story masses and story stiffnesses were arbitrary. Through the GBM, the building's deformation type was quantified by a flexural-shear deformation factor, denoted $\alpha^{(0)}$. This factor, which reflects the overall characteristics of the deformation type, is an intrinsic property of the building regardless of ground motions. The optimal deformation type, denoted α_{opt}, which results in the least variation of the peak inter-story drift ratios over a building's height, is identified by using the GBM along with the design response spectrum. The factor α_{opt} adequately takes the influences of higher modes into account. Comparing $\alpha^{(0)}$ with α_{opt} enables designers to understand how to adjust the building's deformation type. By examining the effect of the cross-sectional properties of beams/columns on the flexural-shear deformation factor, the optimal deformation type can be achieved by modifying the properties of existing structural members.

References

Moghaddam, H., Hajirasouliha, I. and Doostan, A. (2005), "Optimum seismic design of concentrically braced steel frames: concepts and design procedures", *Journal of Constructional Steel Research*, 61, 151-166.

Lin, J. L. (2019), "Approximate quantification of higher-mode effects on seismic demands of buildings", *International Journal of Structural Stability and Dynamics*, 19(3), 1950023.

Chopra, A. K. and Chintanapakdee, C. (2004), "Inelastic deformation ratios for design and evaluation of structures: single-degree-of-freedom bilinear systems", *Journal of Structural Engineering*, 130(9), 1309-1319.

Chopra, A. K. and Goel, R. K. (2002), "A modal pushover analysis procedure for estimating seismic demands for buildings", *Earthquake Engineering and Structural Dynamics*, 31, 561-582.

Seismic Evaluation and Fragility Curves of the Design Example of the Civil 404-100 Code

Yeong-Kae Yeh [1] and Te-Kuang Chow [2]

葉勇凱 [1]、周德光 [2]

Abstract

In this report, incremental dynamic analysis (IDA) is performed on a sample new ten-story building based on the civil 404-100 concrete engineering design code, in order to study its seismic performance. Additionally, from the results of IDA, a seismic fragility curve is built in order to check whether the performance target is satisfied under the estimated performance target earthquake. From the analysis results, a seismic evaluation based on the capacity spectrum method yields a conservative result as applied to the *x*-direction frame-and-shear-wall binary system with smaller period. However, a non-conservative evaluation result is obtained when applied to the *y*-direction ductile moment-resisting frame with a larger period. IDA combined with fragility analysis requires extensive computation time for nonlinear dynamic analysis; however, it is an effective tool for examining the seismic performance of structures with specific seismic intensity.

Keywords: detailed seismic evaluation, capacity spectrum method, incremental dynamic analysis, seismic fragility curve

Introduction

The seismic capacities of existing buildings are examined using detailed seismic evaluation methods. Buildings need to meet the designed seismic demands during earthquakes. The TEASPA (NCREE, 2013), which is a detailed seismic evaluation method commonly used by engineers in Taiwan, uses nonlinear pushover analysis to obtain the capacity curve of a building structure. This capacity curve is the relationship between the base shear and roof displacement. Based on a building's performance needs, a performance target point is set on the capacity curve and through the use of the capacity spectrum method, a design earthquake is sought that can cause this target roof displacement (ATC, 1996).

For a typical three-story school building, incremental dynamic analysis (IDA) has already been used with fragility analysis to show that the capacity spectrum method is conservative for low-rise buildings (Yeh and Chow, 2015). However, for mid-rise buildings, determining whether the capacity spectrum method is still a conservative evaluation method is worthy of further discussion. In this paper, a ten-story reinforced-concrete building based on the concrete engineering design code Civil 404-100 (CICHE, 2011) is used as a sample structure to study its seismic vulnerability by IDA (Vamvatsikos and Cornell, 2002). This is done to evaluate the probability of each performance level as Immediate Occupancy (IO), Collapse Prevention (CP), and Global Instability (GI) under the intensity of a performance-target earthquake.

The third edition of the NCREE Technology Handbook (TEASPA) (NCREE, 2013) is used to define the nonlinear hinges of the structure, and the software package PERFORM3D (CSI, 2006) is adopted to perform the nonlinear dynamic analysis.

IDA Procedures and Fragility Curves

To evaluate the seismic capacity of the structure, in addition to a detailed evaluation using nonlinear static analysis, one can also use a more accurate nonlinear dynamic analysis to perform IDA procedures. Through multiple sets of seismic records,

[1] Research Fellow, National Center for Research on Earthquake Engineering

[2] Assistant Technician, National Center for Research on Earthquake Engineering

the IDA curve can be defined and fragility curves can be established for each performance level in order to study the probability of each performance level under specific seismic intensities.

IDA uses a series of nonlinear dynamic analyses with a gradually enlarged seismic intensity measure (*IM*) to calculate the damage measure (*DM*) of a structure until the structure collapses. The relationship between *DM* and *IM* is the IDA curve. In this paper, $S_a(T_1)$ of the response spectrum with a 5% damping ratio is chosen as *IM* and the maximum inter-story drift θ_{max} is chosen as *DM*.

On the IDA curve, the performance points for IO, CP, and GI need to be specified as damage states. If *DM* is less than IO, then there is no structural damage or there is only minor damage, and residents can live there as normal. If *DM* is less than CP, then the structure still has some safety and the collapse state has not yet been reached. If *DM* reaches the GI level, then the structure is unstable and on the verge of collapse.

Ideally, if an *IM* parameter can be found to specify the seismic intensity, then various earthquakes with the same *IM* value will cause the structure to have the same *DM* response. In reality, however, there is no such *IM* parameter. Instead, corresponding to each input seismic intensity IM_i, the structure has a response of DM_i, with the specific values belonging to a probability distribution. Vulnerability analysis is required to evaluate the structure's performance. The function of the fragility curve is represented by a cumulative distribution function (CDF):

$$P[DM \geq C / IM = IM_i]$$
$$= \Phi\left(\frac{\ln(IM_i)-\mu}{\beta}\right) = \int_0^{IM_i} \frac{1}{z\beta\sqrt{2\pi}} e^{-\frac{(\ln z-\mu)^2}{2\beta^2}} dz \qquad (1)$$

where μ is the log mean of IM_i and β is the log standard deviation of IM_i.

Twenty observation points for IM_i for each performance level can be gained from the derivation of the IDA curves. Then, according to the maximum likelihood estimation (MLE) method (Lallemant *et al.*, 2015), the fragility curves of every performance level can be defined.

Nonlinear Dynamic Analyses of the Design Example Building Based on Civil 404-100

The design example building is a 33.3-m-high ten-story, reinforced-concrete building with a two-story basement and a 6-m-high, two-story penthouse located in Taichung City. This building belongs to the first type of site classification with a short period and a 1-s-period design spectral acceleration having coefficients of 0.8 and 0.45, respectively.

The *x*-direction building structure is a binary system with a ductile moment-resisting frame and shear wall. From the modal analysis, the third mode was found to be the dominant mode with a period of 0.733 s, a mass participation factor of 68.97%, and a performance target ground acceleration of 0.8086 g (Yeh and Chow, 2016). The *y*-direction building structure is a ductile moment-resisting frame system. From the modal analysis, the second mode was found to be the dominant mode with a period of 1.24 s, a mass participation factor of 83.25%, and a performance target ground acceleration of 0.521 g (Yeh and Chow, 2016).

Prior to the dynamic analysis, it is necessary to choose the input seismic records. From the geophysical database management system of the Central Weather Bureau (http://gdms.cwb.gov.tw) and the engineering geological database for the Taiwan Strong Motion Instrument Program (TSMIP) of the NCREE (http://egdt.ncree.org.tw), twenty seismic records were selected. Their seismic intensities are larger than five and their seismic stations are all located on class-1 ground. These twenty seismic records are the input earthquake samples for the IDA. The seismic intensity corresponding to the structural collapse point GI for each sample seismic record must be determined. At the point GI, the structure is unstable and its nonlinear dynamic analysis may have numerical divergence. As the analysis sample is a newly designed structure, it has a strong-column–weak-beam structural system and its performance is in a state of beam ductility exhaustion.

The performance point IO is defined as an immediate occupancy performance level, meaning that the structure has either no damage or only minor damage as *DM* is smaller than IO and people can stay in their buildings after the earthquake. Here, θ_{max} is set to 0.5% at performance level IO and no structural components reach the yielding state. Performance point CP is defined as the collapse prevention performance level. The structure still has stability and does not reach a state of collapse as the *DM* is less than CP. The minimum value of $\theta_{\max}$ of the GI points of the twenty seismic records of the *x*-direction binary system with ductile moment-resisting frame and shear wall is 2.0678%. Thus, the $\theta_{\max}$ value is defined as 1.86%, as it is 90% of the minimum value of $\theta_{\max}$ of the GI points of the x-direction structure or the point on the IDA curve whose slope is 20% of the initial slope of the curve. The performance point CP is the smallest of the above two values. The performance point GI is defined as the global instability performance level, and the structure is unstable and may collapse when the *DM* reaches the GI point.

The *DM* and *IM* points for IO, CP, and GI can be set on each IDA curve according to the definitions of each performance level. The completed twenty IDA curves form the IDA curve group. Figure 1 shows the IDA curve group of the *x*-direction structure. With different *IM* values, the twenty IDA curves can provide twenty *DM* values and their 16% fractile, 50% fractile, and 84% fractile DM values. Thus, IDA curves can be plotted for the 16% fractile, 50% fractile, and 84% fractile, with the fractile points of IO, CP, and GI shown in Fig. 1.

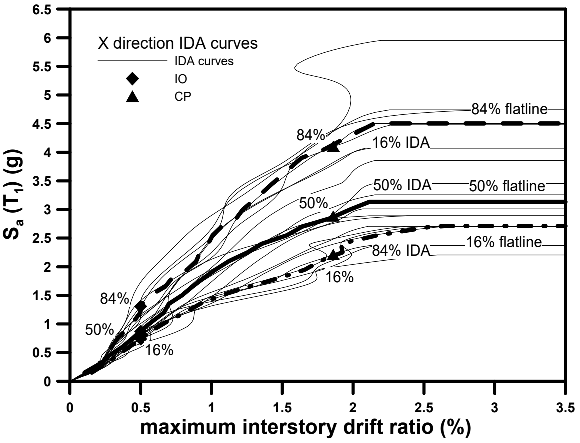

Fig. 1 IDA curve group, performance points, and fractile points of the *x*-direction structure

By using twenty *IM* values for each performance level, their fragility curves can be established. The fragility curve is the cumulative distribution function of Eq. (1). Fragility curves for the three performance levels of the *x*-direction structure are shown in Fig. 2. From the fragility functions of each performance level, the probabilities for each damage state can be calculated for a specified seismic intensity *IM*.

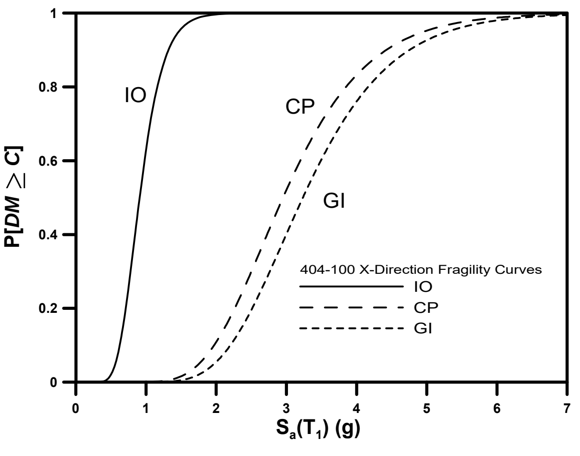

Fig. 2. Performance levels and fragility curves of the *x*-direction structure

The allowable probabilities for each performance level for each building make it difficult to have an objective standard. The United States PEER Center design criteria for tall buildings (PEER, 2010) recommended that, at the maximum considered earthquake level, a collapse or unstable state of a newly designed building should have a low probability of occurrence, which can be set at around 10%.

According to the report NCREE-16-013 (NCREE, 2016), the design example building is located in Taichung City and belongs to the first type of site classification. The x-direction building structure is a binary system with a ductile moment-resisting frame and shear wall with a dominant period T_1 of 0.733 s. For the detailed seismic evaluation, if the performance target is set at the roof displacement corresponding to 0.8 times the maximum strength on the descent part of the capacity curve, the performance target ground acceleration A_P is 0.8086 g and the corresponding $S_a(T_1)$ is 1.5513 g. Using the fragility functions, the corresponding probabilities of occurrence for each damage state are shown in Table 1. The probability of the unstable GI state is 0.72%, which is less than 10% and thus lies in the acceptable range, so the performance target is a reasonable choice. The probability between the CP and GI states is 1.36%. The probability of no damage, which is less than IO, is 3.27%. The probability between the IO and CP states is 94.65%, which matches the assessment criteria for moderate damage from a performance-target earthquake. Thus, the detailed seismic evaluation based on the capacity spectrum method produces a conservative result for this ten-story building with the binary system of the ductile moment-resisting frame and shear wall.

Table 1 The corresponding probabilities of occurrence for each damage state at the performance target of the *x*-direction structure.

P[DM≧GI]	P[DM<IO]	P[IO≤DM<CP]	P[CP≤DM<GI]
0.72%	3.27%	94.65%	1.36%

The *y*-direction building structure is a ductile moment-resisting frame system and its dominant period T_1 is 1.24 s. For the detailed seismic evaluation, if the performance target is set at the roof displacement corresponding to 0.8 times the maximum strength on the descent part of the capacity curve or the roof displacement of the last stable state, the performance target ground acceleration A_P is 0.521 g and the corresponding $S_a(T_1)$ is 0.5909 g. Using the fragility functions, the corresponding probabilities of occurrence for each damage state can be calculated. The probability of the GI unstable state is 25.87%, which is larger than 10% and thus lies in the unacceptable range. The probability between the CP and GI states is 13.37%. The probability of no damage, which is less than IO, is 0.00%. The probability between the IO and CP states is 60.76%. Thus, the detailed seismic evaluation based on the capacity spectrum method produces a non-conservative result for this ten-story building with the ductile moment-resisting frame system.

Conclusions

This paper focused on a newly designed ten-story structure and performed IDA with twenty randomly selected seismic records. The IM and DM values were set for IO, CP, and GI performance points and the MLE method was used to establish the fragility curve of the structure at each performance level. Then, the probabilities of various damage states of the structure under the specific seismic intensity *IM* were calculated, demonstrating the conservatism of the current detailed seismic evaluation method. From these analysis results, we can make the following conclusions:

1. For a newly designed ten-story structure the dominant periods in both directions are different. A detailed seismic evaluation based on the capacity spectrum method, when applied to the smaller period x-direction structure with a binary system of a ductile moment-resisting frame and shear wall produces a conservative analysis result. However, for the larger period y-direction structure with a ductile moment-resisting frame system, the analysis result is not conservative.

2. While IDA combined with a vulnerability analysis requires extensive computation time for nonlinear dynamic analysis, it is an effective tool for examining the seismic performance of structures at specific seismic intensity.

References

Applied Technology Council (ATC) (1996), "ATC-40 Seismic Evaluation and Retrofit of Concrete Buildings", prepared by the Applied Technology Council, Redwood City, Calif.

CICHE (2011), Application of Concrete Engineering Design Code Civil 404-100, Chinese Institute of Civil and Hydraulic Engineering, Taipei.

CSI (2006), PERFORM 3D: Nonlinear Analysis and Performance Assessment for 3D Structures, Version 4, Computers and Structures, Inc., Berkeley, California.

Lallemant, D., Kiremidjian, A. and Burton, H. (2015), Statistical Procedures for Developing Earthquake Damage Fragility Curves, *Earthquake Engineering and Structural Dynamics*, 44(9), pp. 1373-1389.

NCREE (2013), "Technology Handbook for Seismic Evaluation and Retrofit of School Buildings", NCREE report NCREE-13-023, Taipei.

PEER (2010), "Guidelines for Performance-Based Seismic Design of Tall Buildings", Report No. 2010/05, Pacific Earthquake Engineering Research Center, College of Engineering University of California, Berkeley, Page 7.

Vamvatsikos, D., and Cornell, C. A. (2002), Incremental Dynamic Analysis, *Earthquake Engineering and Structural Dynamics*, 31, pp. 491-514.

Yeh, Y.-K. and Chow, T.-K. (2015), "A study for the seismic evaluation and fragility curve of a typical school building", NCREE report NCREE-15-008, Taipei.

Yeh, Y.-K. and Chow, T.-K. (2016), "To study the nonlinear static and dynamic analysis of the design example of Civil 404-100", NCREE report NCREE-16-013, Taipei.

Structural Behavior of a Retrofitted Reinforced Concrete Building During a Near-Fault Earthquake

F.P. Hsiao[1], R.J. Tsai[2], P.W. Weng[3], W.C. Shen[3], Y.A. Li[3], T. Paramitha[2] and S.J. Hwang[4]

蕭輔沛[1]、蔡仁傑[2]、翁樸文[3]、沈文成[3]、李翼安[3]、Tirza[2]、黃世建[4]

Abstract

The near-fault effect on buildings is a significant issue in Taiwan due to its numerous active faults. The special near-fault characteristics of large displacement and high velocity can be observed, however, it is difficult to reproduce the near-fault earthquake record using the existing test facilities of the National Center for Research on Earthquake Engineering. Thus, experimental studies on the near-fault effect are rare. Many buildings, including some mid-to high-rise buildings, were severely damaged in recent earthquake events, which caused numerous casualties. In Taiwan, more and more mix-use residential and commercial buildings have been constructed due to the population density. Thus, the casualty risk caused by the collapse of these buildings should not be underestimated. The method of seismic assessment to identify buildings with a high risk of collapsing has become a critical issue. A high-performance seismic simulation testing system that can simulate the near-fault motions has been established in the NCREE Tainan Laboratory. After the NCREE Tainan Laboratory was completed. NCREE provided better seismic experimental services to government agencies, academia, and industry, which is beneficial to improving public safety against earthquake disasters. This study is based on the experimental results of retrofitted reinforced concrete (RC) structure tests using the novel shaking table system. The experimental results were compared with a non-retrofitted model in order to verify benefits of retrofitting. This experiment can offer abundant information on RC frames and the response of retrofitting members to near-fault earthquakes.

Keywords: Near-fault earthquake, Reinforced concrete, shaking table.

Introduction

Taiwan is located on the Pacific seismic belt and is near numerous active faults. A near-fault earthquake would cause drastic damage to, and even the collapse of neighboring buildings. Near-fault earthquakes threaten the safety and properties of residents of Taiwan, thus studying the near-fault earthquake effect on buildings is a major issue.

The characteristics of near-fault earthquakes, including large ground displacement and a high ground velocity, were observed during the Chi-Chi near-fault earthquake, which was a serious disaster and caused many casualties at that time.

Similar situations were also observed in 2016 Meinong and 2018 Hualien earthquakes. During the post-earthquake investigations, it was found that several mid-to high-rise buildings were severely damaged or even collapsed. Those collapsed buildings were found to have a weak story problem where the lateral stiffness of one story is quite different from the adjacent stories.

The current major issue is how to understand the behavior of mid-to high-rise reinforced concrete (RC)

[1] Research Fellow, National Center for Research on Earthquake Engineering.
[2] Project Research Assistant, National Center for Research on Earthquake Engineering
[3] Research Assistant, National Center for Research on Earthquake Engineering
[4] Professor, National Taiwan University
Director, National Center for Research on Earthquake Engineering

structures during near-fault earthquakes and to develop various retrofitting methods in order to cope with different construction techniques. Hence, National Center for Research on Earthquake Engineering (NCREE) conducted two half-scale seven-story RC structure dynamic experiments, which were tested by new shaking table equipment. These experiments offer abundant information on dynamic responses, and can help researchers study the behavior of mid- to high-rise buildings and the response of retrofitting members to near-fault earthquakes.

Introduction of Model

Two half-scale experiments were tested at the NCREE Tainan Laboratory in July 2018. One was retrofitted and the other was an original construction. The model was designed as modular (Shen et al. 2018), and can be conveniently assembled for different story requirements. In this experiment, a seven-story model was assembled to simulate a mid-to high-rise building. Its design referenced a mixed-use residential and commercial building, and the bottom story was a frame system in order to create the weak story effect. Besides that, the bottom module has suffered slight damage since it was tested in 2017.

The material properties were tested before the experiment. The average yield strength of the longitudinal bar and stirrup were 4630 kgf/cm^2 and 3569 kgf/cm^2, respectively. The average strength of concrete cylinders was 238 kgf/cm^2 at 28 days.

Introduction of Retrofitting Method

The conventional retrofitting methods can effectively improve the seismic capacity of building, like RC column jacketing, adding wing wall, infilled RC wall and steel frame with steel braces and any more. However, those constructions are complex and need to enhance the tension capacity of RC frame by post-installed rebar and anchor bolt. It would also produce noise pollution and a lot of dust while constructing. These would interfere with the resident's daily life. Thus, conventional methods have hardly been accepted.

Therefore, NCREE modified the disadvantages of conventional methods and developed a new retrofitting method (Tsai et al. 2018; Kono and Watanabe 2006; Kono and Katayama 2009). It is called "Self-Jointing Compression Brace", which characteristic is compression capacity only. This method can fully utilize the advantage of reinforced concrete which compression strength is higher than tensile strength. Furthermore, it can be prefabricated and easily constructed without a lot of post-installed rebars and anchor bolts. In particular, it produces less dust and noise during the construction, reduce construction period and without interference from construction.

In the future, NCREE will propose many different retrofitting methods to cope with difficult construction conditions and satisfy the resident's requirements. Thus, this test took this method as a paradigm. The test specimens and retrofitting members as Figure 1 shown.

Input Ground Motion

The models were tested using bi-directional ground motion in the longitudinal and vertical directions. This consideration was made in order to avoid the torsion effect. The selected input ground motion was the record of 2016 Meinong earthquake that was measured at the CHY063 station. The velocity record in Figure 2 shows that the input motion has an instantaneous velocity pulse feature, which is similar to the characteristic of a near-fault earthquake. The peak acceleration, velocity pulse, and ground displacement stroke in the longitudinal direction is 410 Gal, 45 cm/s, and 8 cm, respectively. Although the test sequence included far-field and near-fault earthquakes, this study will focus on the near-fault earthquake test.

Instrumentation Scheme

The motion of the shaking table and the response of the model were monitored by accelerometer, displacement transducer, string pot, and a motion capture system.

The tri-axial accelerometers were distributed on the center of each floor in order to measure the acceleration. The displacement transducers were arranged from the 1st floor to the 3rd floor to record the internal story displacement in three dimensions. 48 strain gauges were attached to the retrofitted braces and were used to measure deformation to estimate the energy dissipation. The string pots were arranged on the retrofitted braces in order to record the axial displacement of the braces.

A motion capture system named OptiTrack (OptiTrack 2017) was adopted to capture the motion of the entire model during the test. 169 markers were deployed around the model and their movements were recorded by a high-performance camera system.

Experiment Result

This study was focused on the displacement of the weak story and the response of the retrofitting members. The internal story displacement at the 1st and 2nd story of the original and retrofitted specimen as Figure 3 shown. As Figure 3(a) shows, the peak displacements at the 1st story in the negative direction for the retrofitted and original models were 6.6 cm and 13.3 cm, respectively. The retrofitting members could contribute extra lateral strength to the model, as well as effectively restrain the displacement response at the retrofitted story. Besides that, the displacement rebound rate of the retrofitted specimen was faster than the original specimen after the peak response. Furthermore, it was also found that there is a phase lag from the comparison. From the above observations, it is speculated that the stiffness changed where the braces acted, meaning that the retrofitting members assist the RC frame to resist seismic activity. However, the displacement is no different in the positive direction due to the characteristics of the members. A similar observation was found in the 2^{nd} story, as shown in Figure 3(b).

Figure 4 shows the energy dissipation of the brace as estimated by the strain gauge. Taking the brace at the 2^{nd} story as an example, it can be clearly observed that the energy dissipation is concentrated at the compression side. This behavior is as expected since the tension capacity of the brace was eliminated, therefore, pull-out failure will not occur on the RC frame because of the brace. These retrofitting members can contribute extra lateral strength to the model to resist the seismic force and restrain the displacement response.

Conclusions

Almost one-third of the population in Taiwan would be affected by the occurrence of a near-fault earthquake in Taiwan. Moreover, as the population continues to increase and the majority of new buildings continue to be built taller, the amount of mid- to high-rise buildings has been increasing. The recent earthquake disasters demonstrate the significant effect of near-fault earthquakes on mid- to high-rise buildings, showing that we need to conduct more research on mid- to high-rise buildings under near-fault earthquakes. Moreover, the seismic design code must be improved to prevent structures suffering from severe damage and collapse.

The experiments from the new established high-performance earthquake simulation system in NCREE Tainan Laboratory, which can reproduce the characteristics of near-fault earthquakes, can offer abundant research on structure behaviors and responses. This data can help researchers and engineers understand the responses of structures to near-fault earthquakes, and also aid to improve the seismic design code for new and retrofitted buildings.

References

Shen, W.C., Hsiao, F.P., Weng, P.W., Li, Y.A., Chou, C.C. and Chung, L.L. (2018), "Seismic Tests of a Mixed-Use Residential and Commercial Building using a Novel Shaking Table," *Proceedings of 11th US National Conference on Earthquake Engineering*, June 22-29, Los Angeles, California.

Tsai, R.J., Hsiao, F.P. and Hwang, S.J. (2018). "Retrofitting Method with Compression Brace within Self-jointing device," *The 14th National Conference on Structural Engineering and The 4th National Conference on Earthquake Engineering*, November 6-8, Taichung, Taiwan.

Kono, S. and Watanabe, F. (2006). "Retrofitting RC Structures with Precast Pre-stressed Concrete Braces," *8th U.S. National Conference on Earthquake Engineering*. No. 635, April 16-22, San Francisco.

Kono, S. and Katayama, T. (2009). "Seismic Retrofit of Reinforced Concrete Building Structures with Pre-stressed Braces," *Journal of Advanced Concrete Technology*, Vol. 7 No. 3, 337-345, October.

OptiTrack (2017). "Motion Capture Systems," available on: http://optitrack.com.

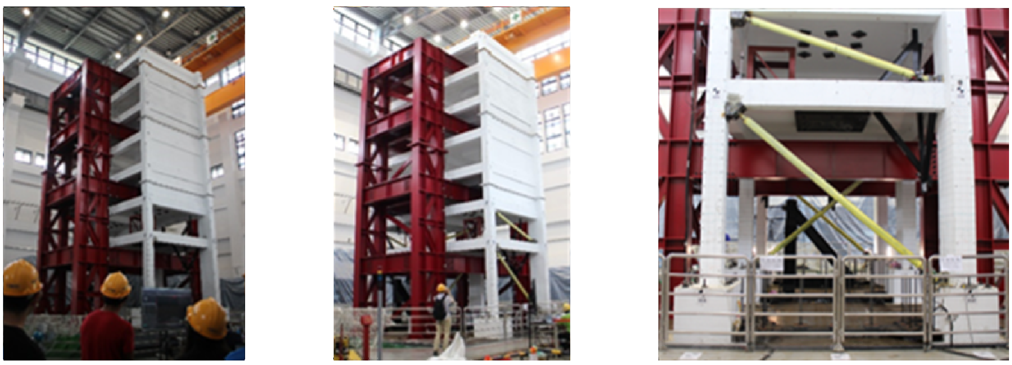

(a) Original (b) Retrofitted (c) Retrofitting members

Figure 1. The retrofitted and original specimen.

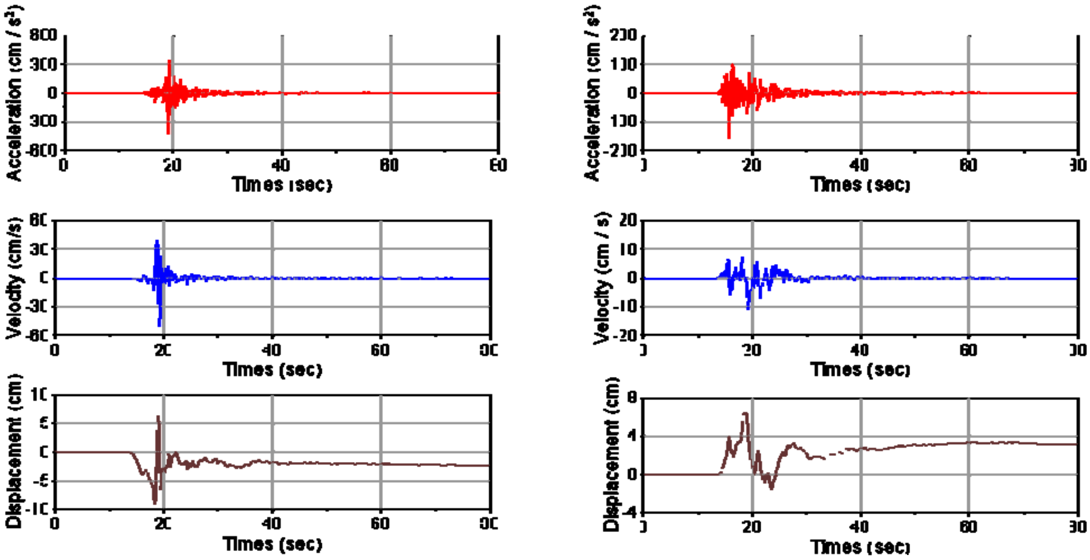

(a) Long direction (b) Vert direction

Figure 2. Input ground motion

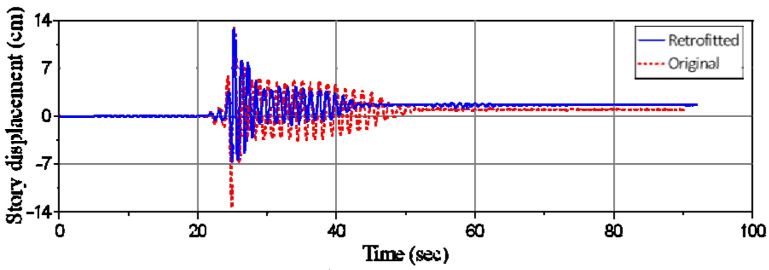

(a) 1st Story displacement

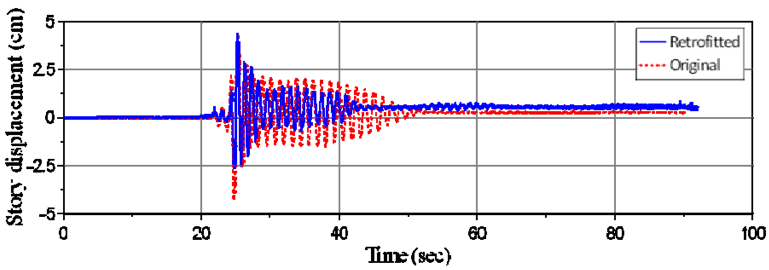

(b) 2nd Story displacement

Figure 3. The comparison of story displacement.

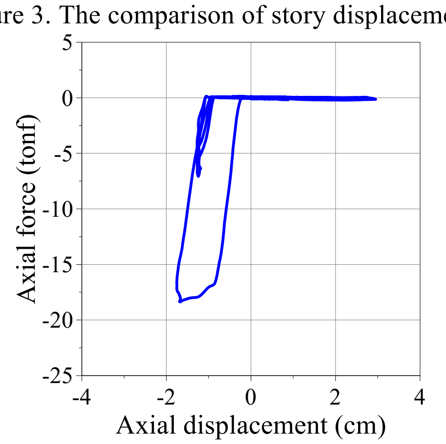

Figure 4. The energy dissipation of brace at 2nd story

Seismic Behavior for Steel-Plate-Embedded High-Strength Reinforced-Concrete Coupling Beams of Shear Walls

Min-Lang Lin[1], Chao-Hsun Huang[2] and Sung-Yi Yang[3]

林敏郎[1]、黃昭勳[2]、楊松逸[3]

Abstract

This study explores the seismic behavior of embedded steel plate in the coupling beam through five sets of specimens. The experimental results show that for coupling beam with a vertical main reinforcement in straight-through configuration, when the lateral displacement increases, the concrete may be crushed due to the decrease of the shear capacity and shear damage occurs. The scheme of using lateral stirrups can effectively provide a composite mechanism between steel plates and concrete. With an embedded steel plate and a good composite of the steel plate and concrete, the shear capacity of the beam can be improved and the failure mode of the test specimens can be transformed into flexural failure. The design of the end bearing plate and the stiffening plate may cause the concrete around the end to be crushed. This shows that the anchoring mechanism of the steel plate can be further improved.

Keywords: coupling beams, shear steel plate, shear capacity, shear studs, steel plate ratio

Introduction

In order to improve the seismic performance and construction convenience of reinforced concrete coupling beams, for preliminary research, a small amount of steel plates have been placed into the reinforced concrete coupling beams of the main steel reinforcement in a straight-through configuration. The steel plate has not been treated or equipped with any shearing studs. It has been found that the anchor length of the steel plate can control the development of the flexural strength of the connecting beam. In the case of a section reinforcement ratio of 3%, adding 1% to 2% of steel plate can achieve the effect of improving the seismic resistance of the coupling beam. Therefore, the placement of the steel plate into the coupling beam has great developmental advantages.

For the case of the embedded steel plate with no shearing studs on the surface of the steel plate, there is no mechanism for shear transmission between the steel plate and the concrete. Therefore, the steel plate cannot be fully utilized to achieve its purpose of improving the shear capacity of the beam. When the applied lateral deformation increases, the strength of the test specimen rapidly degrades, the core concrete is crushed, and steel plate buckling occurs. The seismic performance is still not as good as the ACI 318-14 diagonal reinforcement type.

This study attempts to configure lateral stirrups in the specimen to provide a composite mechanism between the concrete and the steel plate. The steel plate is expected to fully exert its shear strength, thereby improving the seismic resistance of the overall reinforced concrete coupling beam.

Specimen Design

This experiment was conducted at the National Earthquake Engineering Research Center. To simulate the deformation of the reinforced concrete coupling beam under actual earthquakes, a test frame is designed to allow the test beam to produce a double curvature deformation. In this study, a beam section of 30 cm × 50 cm^2 was selected. The length of the beams was 100 cm, 150 cm and 200 cm, and the corresponding span-to-depth ratios were 2, 3, and 4.

Table 1 Specimen design parameters

Specimens	Beam section	Thickness of Steel plate	Embedded length
CB20SP1	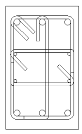	None	10cm

[1] Associate Researcher, National Center for Research on Earthquake Engineering
[2] Associate Professor, National Taipei University of Technology
[3] Graduate Assistant, National Taipei University of Technology

CB20SP2	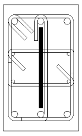	1.5cm	10cm
CB20SP3	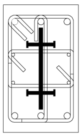	1.5cm (with shear studs)	10cm
CB30SP1	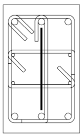	0.6cm	10cm
CB40SP1	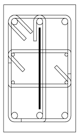	0.6cm	10cm

A total of five specimens were designed and tested in this experiment. The specimens were named CB20SP1, CB20SP2, CB20SP3, CB30SP1, and CB40SP1. The design parameters of the test specimens are listed in Table 1. The longitudinal steel bars were #8 SD685, the stirrups were #4 SD785, and the steel plates were made of A36. For all specimens, 70 MPa high-strength concrete was used.

The coupling beam with span-to-depth ratio of 2 was used to investigate whether the use of high-strength materials, the addition of steel plates and the use of lateral stirrups can improve the seismic behavior of traditional coupling beams. Lateral stirrups and shearing studs were placed on the steel plate to observe the difference in the composite effect between the reinforced concrete and the steel plate. The specimens with a span-to-depth of 3 and 4 were mainly used to investigate the improvement of the seismic performance of other shorter span-depth specimens, and to discuss the design theory of steel plates.

Test Setup and Cyclic Loading Tests

This test simulates the deformation of the double curvature when the specimen is subjected to seismic force. An L-shaped steel frame and two vertical MTS actuators are used to ensure that the upper foundation does not rotate during the test. Two horizontal MTS actuators are used to apply a progressively increasing displacement to the test specimen. The test setup for the test is shown in Figure 1.

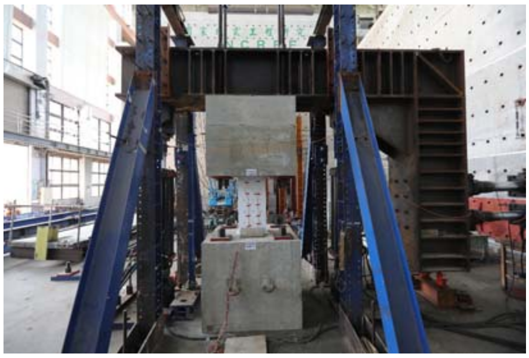

Fig. 1 Test Setup

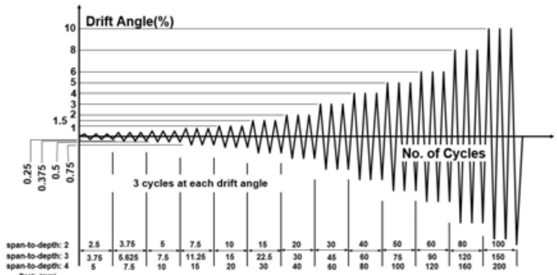

Fig.2 Test protocol

To simulate the repetitive characteristics of earthquakes, this test refers to the loading protocol of ACI 374.1-05. A total of three loops were performed for each displacement load. The displacement increments were 0.25%, 0.375%, 0.5%, 0.75%, 1%, 1.5%, 2%, 3%, 4%, 5%, 6%, 8%, and 10%, respectively. The increment of lateral displacement is shown in Figure 2.

Test Results

The maximum strength of both specimens occurred at a displacement angle of 2%. At this point, the longitudinal main reinforcement developed to achieve the yielding strain. The CB20SP1 longitudinal main steel bar yielding point was earlier than the CB20SP2. In their displacement capacity, the displacement ductility (ultimate drift ratio, UDR) of CB20SP1 and CB20SP2 were 3.32% and 3.45%, respectively. The displacement ductility of CB20SP2 only increased by 0.13%. Due to serious damage to the foundation, the early loss of the anchoring ability of the steel plate caused it to yield. The initial stiffness of CB20SP1 and CB20SP2 were 123.2kN/mm and 136.7kN/mm respectively. Due to the presence of steel plate, the stiffness of CB20SP2 is increased by about 11%.

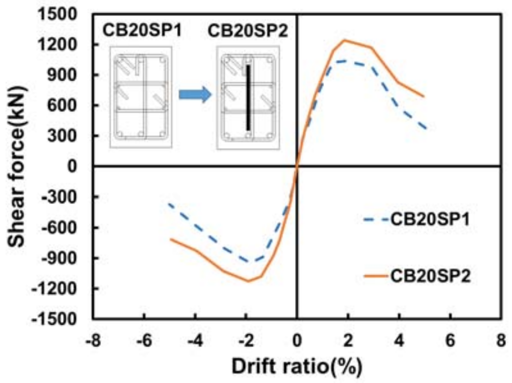

Fig. 3 Comparison of the behavior of coupling beams with and without embedded steel plates

In terms of energy dissipation, the cumulative energy dissipation of CB20SP2 was about 1.7 times higher than that of CB20SP1. In terms of strength degradation, CB20SP1 had a 10% higher attenuation at 4% displacement than CB20SP2. At 5% displacement, CB20SP1's strength degradation was 20% higher than CB20SP2.

The core concrete of CB20SP1 was severely crushed in a large drift, resulting in a large degradation of its strength. The failure mode was flexural-shear failure. At the end of the CB20SP2 test, the core concrete of the beam was still intact, and the failure mode was flexural failure. The envelope of the two test specimens CB20SP3 and CB20SP2 is shown in Figure 4. CB20SP3 and CB20SP2 were placed in the same steel plate, but CB20SP3 had an additional 36 shear studs. The maximum strength points of CB20SP2 and CB20SP3 were 2%, and the maximum lateral strength values were 1241.2kN and 1251.1kN respectively. The maximum strength of the two specimens was very close. The longitudinal main steel bars reached the yielding strain before reaching the maximum strength point, and the time for the main steel bars to yield was very close for both specimens.

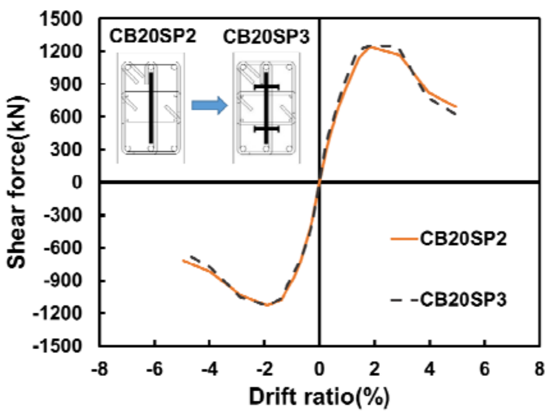

Fig.4 Comparison of the behavior of coupling beams with and without shear studs

In terms of displacement capacity, the UDRs of CB20SP2 and CB20SP3 were 3.45% and 3.4%, respectively, a difference of only 0.05%. The initial stiffness of CB20SP3 was approximately 9% higher than that of CB20SP2 due to the inclusion of the extra shear studs. In terms of energy dissipation, when the 5% drift test was completed, the cumulative energy dissipation of CB20SP2 and CB20SP3 was quite similar. The strength degradation of the two specimens after the maximum strength point was also similar. After the end of the test, peeling of the concrete cover occurred at both ends of the test specimens, but the core concrete remained in good condition, and the steel plate was not found to have any obvious buckling. As can be seen from the above discussion, the two specimens have close behavioral responses, which confirms that increasing the lateral stirrups can good composite steel plate and concrete, thus realizing the design goal of improving the shear strength of the coupling beams.

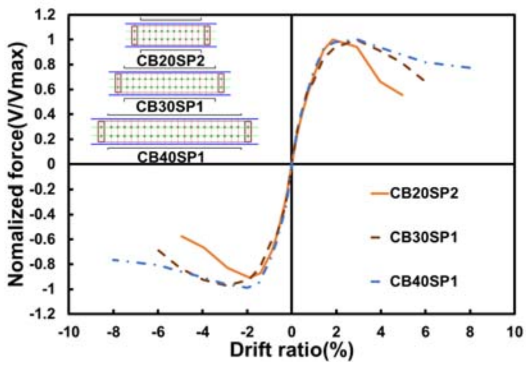

Fig.5 Comparison of envelope curves of coupling beams with different span-to-depth ratios

Figure 5 is the envelope response curve of three different aspect ratio specimens: CB20SP2, CB30SP1, and CB40SP1. The lateral strengths of CB20SP2, CB30SP1 and CB40SP1 were 1241.2 kN, 886.7 kN, and 642.5 kN. The initial stiffness values of CB20SP2, CB30SP1, and CB40SP1 were 136.7 kN/mm, 71.2 kN/mm and 43.1 kN/mm, respectively. The longer the specimen is, the smaller its initial stiffness.

For the total energy dissipation accumulated, CB40SP1 had the best energy dissipation capability. Its hysteresis loop is fuller and has no obvious strength decay. The total energy dissipation of CB30SP1 was approximately 92% of CB40SP1. The energy dissipation capacity was less due to the decrease of strength in the later stage of the experiment. CB20SP2 was faster in the late stage of the experiment due to the strength decay, resulting in energy dissipation of only 56% of CB40SP1. In terms of strength degradation, at a displacement of +5% (1st), CB20SP1 had a large amount of peeling off of the concrete cover and severe cracking of the foundation, resulting in a 44% strength drop and a UDR limit of 3.45%. The foundation of CB30SP1 also had obvious cracking. The beam only had plastic hinges at both ends without any obvious damage. The strength only declined by 17%, and the UDR was 5.04%. The foundation of CB40SP1 was also damaged, while the beam had no obvious damage, the intensity was slightly reduced by 12%, and the UDR was 6.83%. The failure modes of the three groups tested were all flexural failure.

Conclusions

This study explored the seismic behavior of embedded steel plate in a coupling beam through five sets of specimens. Based on the experimental results, the following conclusions can be made: For a coupling beam with a vertical main reinforcement in straight-through configuration, when the lateral displacement increases, the concrete may be crushed due to the decrease of the shear capacity and shear damage occurs. The scheme of using lateral stirrups can effectively provide a composite mechanism between the steel plates and the concrete. With an embedded steel plate and a good composite of the steel plate and concrete, the shear capacity of the beam can be improved and the failure mode of the test body can be transformed into flexural failure. The design of the end bearing plate and the stiffening plate may cause the concrete around the end to be crushed. This shows that the anchoring mechanism of the steel plate can be further improved.

References

ACI Committee 318, Building Code Requirements for Structural Concrete (ACI 318-14) and Commentary (ACI 318R-14), American Concrete Institute, Farmington Hills, 2014.

ACI Committee 374, Acceptance Criteria for Moment Frames Based on Structural Testing and Commentary, American Concrete Institute, Farmington Hills, 2005.

Lin, M.L., Huang, C. S., and Yao, P., H., “Seismic Behavior for Steel Plate Reinforced Concrete Coupling Beams of Shear Walls”, National Center for Research on Earthquake Engineering, Report No. NCREE-18-013 (2018).

Lin, M.L., Huang, C. S., and Yang, S., Y., “Seismic Behavior for Steel Plate Embedded High Strength Reinforced Concrete Coupling Beams of Shear Walls”, National Center for Research on Earthquake Engineering, Report No. NCREE-19-001 (2019).

Study on Toughness Test of Electro-Slag Welding of SM570 Steel

Sheng-Jhih Jhuang[1] Ker-Chum Lin[2] Hsiang-Ming Tsai[3] Chui-Hsin Chen[4] and Eric Chuang[5]

莊勝智 [1]、林克強 [2]、蔡相明 [3]、陳垂欣 [4]、莊士誠 [5]

Abstract

Electro-slag welding (ESW) is one of the most efficient welding methods for manufacturing the inner diaphragms of steel box column. The box column members of the steel structural buildings in Taiwan widely use ESW to weld connections between the inner diaphragms and box columns. This study mainly discusses the toughness performance of SM570 high strength steel used to manufacture connection specimens that used ESW between the inner diaphragm and the box column. The Chapy V-Notch toughness test was carried out for three kinds of specimens, namely, the T-shape connection between the inner diaphragm and column plate in the actual box column, the cross connection used by the Japanese Institute of Architecture, and the butt connection currently in used in Taiwan. Two grades of welding materials have been used to compare three types of connection specimens. Two different thicknesses of the column plate were used to explore the effect of column plate thickness on the toughness of the T-shape connection specimen and the cross connection specimen. The test results showed that the toughness values of the heat affected zone of the column plate and the diaphragm of the three types of connection specimens are mostly less than the required 15J at -5 °C. From the toughness test results of the T connection and cross connection specimens, it was found that the thicker column plate, the greater the toughness. However, the influence of the grade of the welding material on the toughness of the heat affected zone of the column plate and the diaphragm is less significant.

Keywords: electro-slag welding, high strength steel, heat affected zone, toughness

Foreword

A box column composed of four steel plates is popularly adopted in steel building structures in Taiwan. In order to effectively transmit the beam end moment to the box column, two inner diaphragms of the box column are general designed and arranged at the beam flange level within the beam-to-box column connection to transfer the strain hardening force of the beam flange to the column. To consider the convenience of the inner diaphragm and the symmetry of the welding thermal stress in the practice of making steel box column members in Taiwan, at least one pair of the welds between the inner diaphragm and the four side column plates was produced by an automatic electro slag welding (ESW) machine, and the other pair adopted a semi-automatic CO2 arc-shielded welding technique of the complete joint penetration groove welds, as shown in Figure 1. The manufacturing approach of the of box columns with inner diaphragms has become the industrial standard welding and production procedure of steel box column in the steel structural industry of Taiwan.

The steel structural industry in Taiwan generally uses steel with strength equal to 350 MPa or SN490 grade steel. In recent years, SM570 high strength steel has been widely used in steel structures. With increase

1 Assistant Researcher, National Center for Research on Earthquake Engineering
2 Research Fellow, National Center for Research on Earthquake Engineering
3 Student, Department of Civil Engineering, National Chiao Tung University
4 Assistant Professor, Department of Civil Engineering, National Chiao Tung University
5 President, GOODWELD Corporation

in the ultimate strength of steel to 570 MPa and the use of box section, the corresponding ESW production procedure and the mechanical properties of the heat affected zone (HAZ) must be confirmed. Therefore, this study mainly use SM570 high strength steel to make ESW connection specimens in order to explore the toughness of this steel used in box column when subjected to high heat welding; this provides information to engineers for reference in design and construction. Three types of connection specimens, shown in Figure 2, are studied. The first connection type is the T-shaped connection between the inner diaphragm and the column plate in the actual box column. The second is the cross connection used by the Japanese Architectural Society. Finally, the third is the butt connection used in Taiwan. Various thicknesses of the column plate and types of welding filler are tested for the T-shape and cross connection specimens.

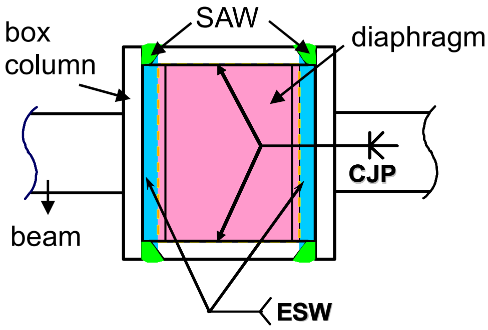

Fig.1 Welding diagram of the inner diaphragm in the box column

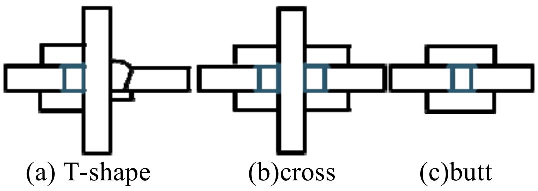

Fig.2 Types of ESW connection specimens

Test Plan

This study primarily used different welding fillers and different thicknesses of the column plate to conduct Charpy V-Notch (CVN) toughness test for the three connection specimens shown in Figure 2 to investigate the influence of the connection type, welding filler, and thickness of the SM570 steel column plate on the impact toughness of ESW and their heat affected zone. This study used the SM570-CHW China Steel specification steel plate. The GOODWELD factory produced ESW connection specimens of T-shape, cross, and butt. Table 1 shows the parameters of each specimen. G1 specimens used the YM60E welding filler for ESW, and had column plate thicknesses of 32 mm and 50 mm. This was to observe the effect of varying column plate thickness on the toughness of the HAZ. G2 specimens used the PS56 welding filler for ESW, and only used 32 mm thick column plate, this was to compare with G1 specimens. Tables 2 and Table 3 show the chemical properties of the welding filler and the chemical properties of the SM570 CHW steel respectively.

Table1 Parameters of each specimen

	T Joint		Cross Joint		Butt Joint
	Column Plate Thickness (mm)	Weld Filler	Column Plate Thickness (mm)	Weld Filler	Weld Filler
G1	32	YM60E	32	YM60E	YM60E
	50		50		
G2	32	PS56	32	PS56	PS56

Table2 Chemical properties of the welding filler

Weld Filler	C(%)	Si(%)	Mn(%)	P(%)	S(%)	Ni(%)	Cr(%)
YM60E	0.07	0.50	1.45	0.005	0.003	1.99	0.04
PS56	0.04	0.56	1.63	0.007	0.015		

Table3 Chemical properties of SM570 CHWsteel

Steel Material	C(%)	Si(%)	Mn(%)	P(%)	S(%)
SM570 CHW	0.14	0.28	1.3	0.016	0.002

The backing bar material of all specimens was the same as the steel plate material. The ESW procedure was performed with a current of 380 amps and a voltage of 48 volts. After ESW of the T-shape specimen was complete, the melt range of ESW was measured by ultrasonic testing (UT) inspection on the outside of the column plate, and then the CO_2 gas-shielded full-penetration of the beam flange was performed on the outside of the column plate. For the cross specimens, after the first ESW was finished and had been inspected with UT, a second ESW was made. After the ESW connection specimens were complete, the specimens were cut by the cutting machine and processed to complete CVN coupons for the toughness test. T-shape and cross connection specimens of G1 used 39 CVN coupons, and butt connection specimens of G1 used 21 CVN coupons. T-shape and cross connection specimens of G2 used 31 and 39 CVN coupons, respectively, and butt connection specimens of G2 used 21 CVN coupons. The location diagrams of the CVN coupons of G1 and G2 specimens are shown in Figure 3 and Figure 4, respectively. The coupon numbers are coded as follows: (1) The first two letters represent the sampling location: HP is the HAZ of complete joint penetration (CJP), HD is the HAZ of ESW on diaphragm side, HC is the HAZ of ESW on column side, EM is ESW, CC is the center of the column plate, CP is the column plate, BP is the beam plate. Number 1 and 2 after two letters indicate, first welding and post welding. (2) The first letter after the horizontal line symbol represent the longitudinal (denoted by a L) and the transversal (denoted by a T) positions of the sampling location. (3) The second letter after the horizontal line symbol is the notch length direction of the CVN coupon: V is the notch length direction perpendicular to the plane of the beam flange or the diaphragm and, H is the notch length direction parallel to plane of the beam flange or the diaphragm.

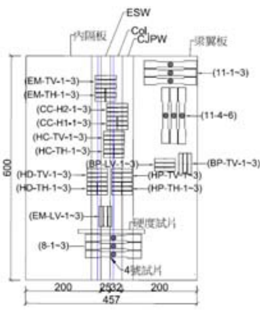

(a)T Joint

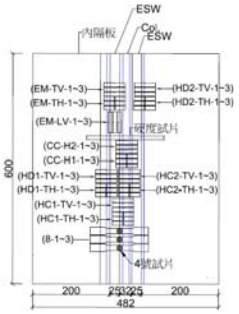

(b)Cross Joint

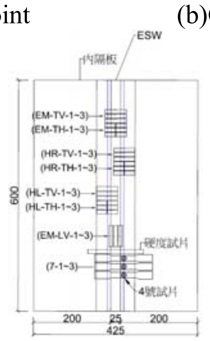

(c)Butt Joint

Fig.3 Coupon location diagram of G1

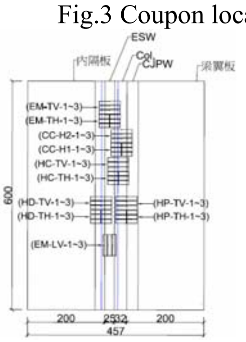

(a)T Joint

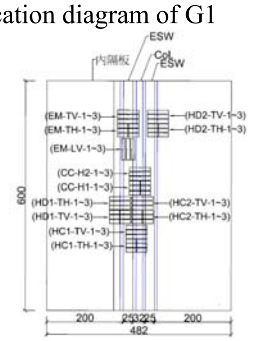

(b)Cross Joint

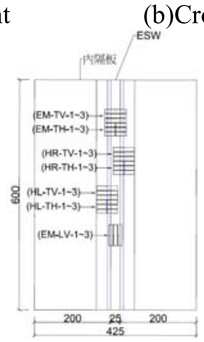

(c)Butt Joint

Fig.4 Coupon location diagram of G2

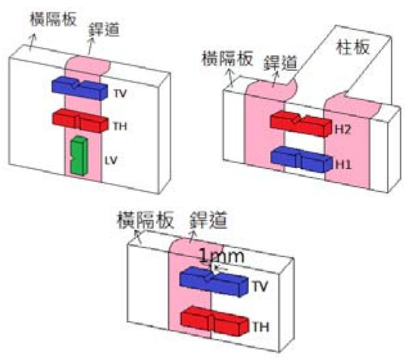

Fig.5 Schematic diagram of the symbol after the horizontal line of the CVN coupons

Test Results and Discussion

Figure 6 to Figure 10 are the CVN test results for this study. The horizontal dotted line on these figures represents 27 J. It's convenient to distinguish whether the toughness value meets the standard value of 27 J of the SM570 material at -5 °C according to the Taiwan Steel Structure Limit Design specification (Ministry of The Interior, 2007). The test results are summarized in terms of a comparison of the toughness values of ESW, the center of the column plate and the HAZ for G1 and G2 specimens.

1. ESW

From Figure 6, the toughness of the cross specimens was larger than the T-shape specimens when the two kinds of specimens had the same plate thickness. It is speculated that the cross specimens had a higher toughness value due to the influence of the second ESW, the first ESW has the possibility of tempering. In addition, the toughness of the ESW using the YM60E welding filler was larger than ESW using the PS56 welding filler.

2 Center of the Column Plate

The comparison of the toughness values at the center of the column plate of G1 specimens is shown in Figure 7. As the thickness of column plate increases, the toughness value reduced. It is speculated that the rolling times for thicker column plates are less, so there are more impurities in the center of the column plate, resulting in a lower toughness value. For a column plate thickness of 50 mm, the toughness value of the cross specimens is lower than that of the T-shape specimens. It is hypothesized that the cross specimens have a poor toughness value due to the influence of two ESW. Figure 8 shows that using two different welding fillers (PS56 and YM60E) has little effect on the toughness value of the center of the column plate.

3. Heat Affected Zone

Figure 10 and Figure 11 showed the toughness values of the HAZ of the cross specimens and T-shape specimens of G1 and G2, respectively. The toughness values of the HAZ are found to be generally low, and the use of higher-grade welding fillers does not significantly increase the toughness value. The HAZ on the column plate side is slightly larger than the HAZ on the inner diaphragm side. It is also found that when column plate is thicker, the toughness is greater. It is hypothesized that when the thickness of the steel plate is increased, there is better heat dissipation capacity, so it has a higher toughness value.

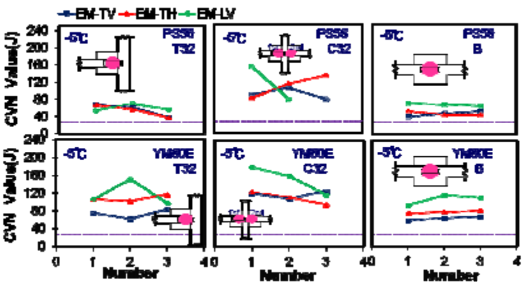

Fig.6 Comparison of toughness values of ESW of G1and G2

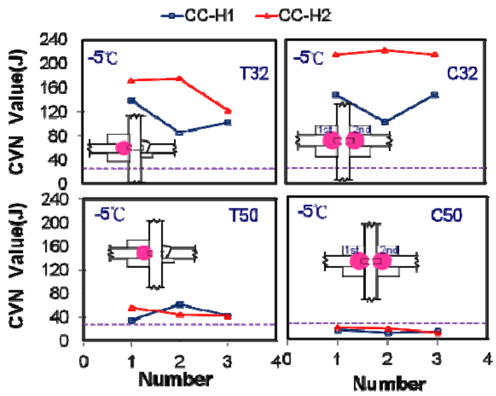

Fig.7 Comparison of toughness values of the center of the column plate (different thicknesses) of G1

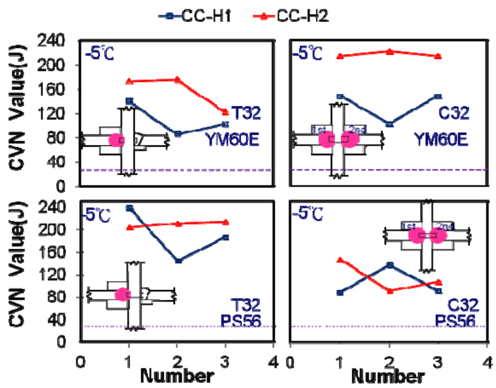

Fig.8 Comparison of toughness values of the center of the column plate of G1 and G2 (different welding filler)

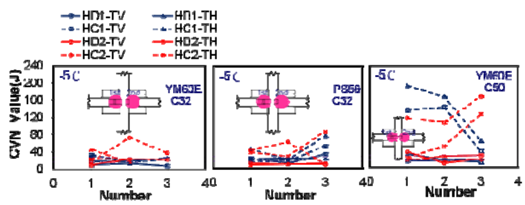

Fig.9 Comparison of toughness values of HAZ of G1 and G2 for cross specimens

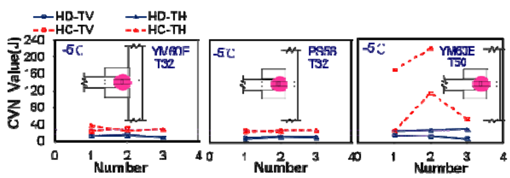

Fig.10 Comparison of toughness values of HAZ of G1 and G2 for T-shape specimens

Conclusions and Suggestions

1. The results of this study showed that the toughness values of the HAZ of ESW produced by using the three type of SM570 steel connection specimens were mostly less than 27J at -5 °C.

2. The effect of different welding fillers on toughness value of the HAZ of ESW is not significant.

3. An increase in the thickness of the column plate, yields a higher heat dissipation effect, so the toughness is greater at the HAZ of ESW. However, at the center of the column plate, when the thickness of the column plate increases, the rolling times are less, resulting in lower toughness.

4. In the preparation of the ESW procedure specification, it is recommended that a butt connection specimen not be used instead of a T-shape.

5. The column plate of the cross connection specimen may be welded by two ESW. Due to the large change in heat input, a more conservative evaluation result may be obtained. Therefore, in order to save the fabrication time, it is recommended to replace the T-shape specimens with cross specimens.

6. For, The welding and the HAZ of steel that require high heat input welding should meet the performance requirements of the material of the welding connection. Therefore, the toughness target of this study on HAZ of ESW should meet the requirement of 27J for SM570 CHW steel, and not the recommended requirement of 15J of China Steel.

References

AWS (R2009) AWS A5.25 Specification for Carbon and Low–Alloy Steel Electrodes and Fluxes for Electroslag Welding, American Welding Society.

AWS (2015) AWS D1.1 Structural Welding Code – Steel, American Welding Society.

Construction and Planning Agency Ministry of the Interior (2007), Design and Technique Specifications of Steel Structures for Buildings(2) Load and Resistance Factor Design Specifications and Commentary.

JASS (2007), JASS 6, Building construction standard specification, Japanese Architecture Society.

Lin, K. C., Jhuang, S. J., Li, C. H., and Lin, C. H. (2015), “Quality Assessments on T-Shape Electro-Slag Welds (ESWs) of Internal Diaphragm to Box-Column Plate[J],” Structural Engineering, Vol. 30, No. 2, pp. 23-38.

Building up the Level Sensing System for Bridges by Gravity, Water, Laser and Optical Fiber

Zheng-Kuan Lee[1]

李政寬 [1]

Abstract

This paper focuses on the design and application of optical-fiber differential settlement measurement (DSM) sensors for bridges. By using the law of connected vessels, the buoyancy principle, an equilibrium force condition, and the photoelasticity of Fiber Bragg Grating (FBG), the DSM sensor is easily manufactured and is sensitive to the level change. Aside from the design principle, this study illustrates the application of the DSM sensors on underpass bridges. From the field results, it is shown that the proposed DSM sensors are stable and precise enough to monitor the behavior of multiple-span underpass bridges. The aim of this study is to share the optical fiber DSM field results.

Keywords: bridge safety monitoring, settlement sensor, FBG

Introduction

Bridges are large-scale linear structures that are used to cross obstacles to extend traffic routes (e.g., roads and railways), cross natural barriers (e.g., rivers, straits, and canyons), or cross artificial barriers (e.g., highways and railway lines). Bridges also connect urban and rural areas, and transport water and energy, making them indispensable structures in modern civilization [1].

Bridges are profoundly affected by environmental factors, such as external natural forces (including earthquakes, typhoons, and floods), and by the aging of materials (such as deformation due to creep and shrinkage of concrete) [2]. Therefore, regular manual level surveys for elevation is important in bridge inspections.

Due to the growth of cities, the increasing number of bridges demands increased efforts for these inspections. Therefore, adapting technologies from other domain knowledge for bridge level surveys to save human resources and enhance efficiency has continuously been a concern to bridge managers and engineers. With the advent of the Internet of Things (IoT), it is expected that automatic bridge safety monitoring technologies will flourish.

This study designed and produced a fiber Bragg grating–based differential settlement sensor (DSM), which was applied to the in-situ monitoring of elevation changes in bridges. Based on application results, it is shown that the proposed DSM sensor can be used as an instrument for the automatic leveling of bridge elevation.

Brief Review on the Development of Laser, Optical Fiber, and Fiber Bragg Grating

The invention of lasers and optical fibers in the mid-20th century has substantially improved quality of life and facilitated convenient worldwide communication, an influence that was difficult to imagine at the time they were invented. The key periods in optical communication are as follows: (1) Albert Einstein first predicted the possibility of stimulated emission in his 1917 paper [3]. (2) Light-transmitting optical fibers were invented in the 1930s; however, they could only be used as art lighting and endoscopes. (3) In 1960, Maiman produced a laser by stimulating a ruby through a high-intensity light, thereby providing the first necessary condition for light to transmit information. (4) In 1966, Kao and Hockham discovered that the rapid loss of light was mainly due to impurities within the optical fibers, and determined that increasing the purity of the glass enabled the transmission distance of the optical signals to exceed 100 km. (5) In 1970, a low-loss optical fiber was mass-produced by Corning Inc. (6) In 1977, the

[1] Associate Researcher, National Center for Research on Earthquake Engineering

world's first optical fiber communication system was developed for commercial use in Chicago in the United States. (7) In 1978, Hill and his colleagues discovered the photosensitivity of an erbium-doped optical fiber and used an argon-ion laser to induce chemical changes in photosensitive optical fibers [4]. (8) In 1989, Meltz and his colleagues employed high-energy ultraviolet lasers by using the transverse holographic method to change the molecular structure of a photosensitive optical fiber, turning it into an optical filter [5]. (9) In 1993, Hill and his colleagues developed the phase-mask method to produce fiber Bragg grating (FBG), thereby enabling the production technology of FBG to mature [6]. Today, FBGs are mass-produced and commercialized, enabling them to be purchased and applied in various fields.

Introduction to FBG

This study only describes the application of FBG; a detailed explanation of FBG can be found in [7]. Fig. 1 shows the optical and the mechanical behavior of FBG: the amount of change in the wavelengths of reflected light depends on the amount of change in strain and temperature.

If both ends of one FBG are clamped using a heat-shrink tube as in Fig. 2, through which the force medium is introduced, the local organization forms sensing elements.

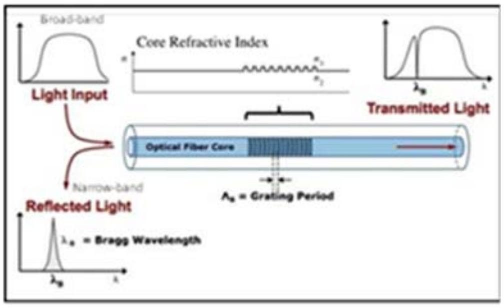

Fig. 1. Structure and spectral response of FBG

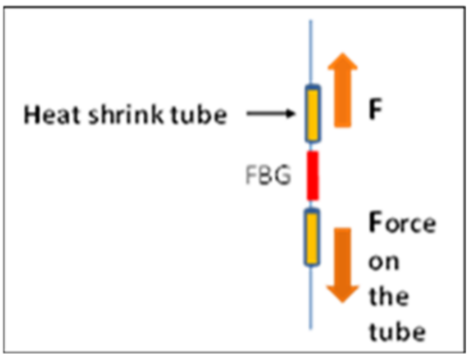

Fig. 2. Heat-shrink tubes placed on both ends of the FBG act as the application medium for external force F

FBG-based Differential Settlement Sensor

Fig. 3 shows the structure of a set of FBG-based differential settlement sensors, which contain two water-filled containers connected by a communicating tube. The upper and lower ends of the FBG were clamped by two heat-shrink tubes, with one end fixed at the top of the container and the other end fixed with the cylinder buoy to withstand part of the cylinder weight [8]. The elevations of the two sensors in Fig. 3 may change into the elevations in Fig. 4. From the wavelength signals, the elevation difference between Fig. 3 and Fig. 4 could be calculated.

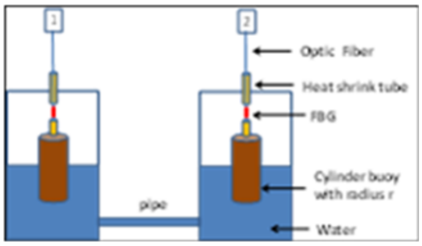

Fig. 3. FBG-based differential settlement sensors

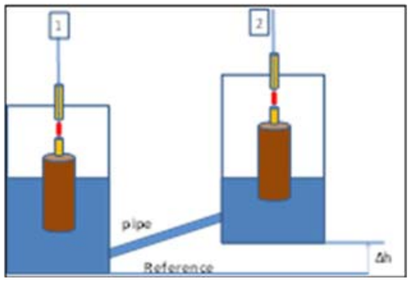

Fig. 4. Elevation change of the sensors

Bridge Monitoring Project

Fig. 5 shows that three DSM sensors were deployed within each box girder and were connected by pipes to observe the midpoint deflection as well as the elevation difference at both ends of the girder. Additionally, optical fiber thermometers were placed on the roof plate and base plate inside some girders of a continuous 14-span underpass bridge at Tainan City, Taiwan [9].

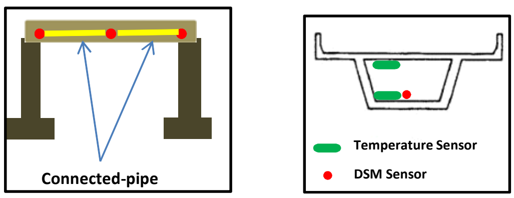

Fig. 5. Three DSM sensors were deployed at each span, with optical fiber thermometers in some girders

Fig. 6 shows the monitoring data of Span 1 for about 24 hours, with the abscissa and ordinate representing time (min) and length (cm), respectively. The blue lines show the deflection variations at the midpoints of Span 1, while the red lines indicate the elevation changes at both ends of the girder. Fig. 7 presents the temperature (°C) data collected by the optical fiber thermometer in the box girder. The blue line and the red line show the temperature variation on the roof plate and the base plate inside the girder, respectively. Evidently, the deflection of the girder is affected by the temperature, and there is a time-delay effect.

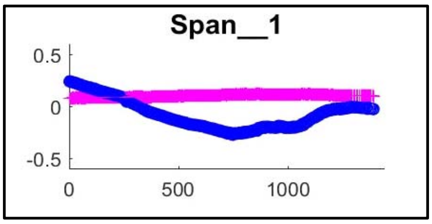

Fig. 6. Observation from 19:00 on June 10, 2018 to 18:30 on June 11, 2018. The blue line represents changes at the midpoint girder deflection and the red line represents the elevation changes at both ends of the girder. Abscissa and ordinate represent minutes and centimeters, respectively

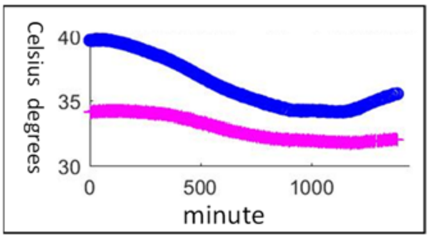

Fig. 7. Temperature observation of the box girder. The blue line and the red line indicate the temperature change of the roof plate and the base plate, respectively

Discussion of the Bridge Structure Based on the Monitoring Data

The monitoring was conducted for more than 1 year with a sampling rate 0.5 Hz. Fig. 8 graphs the maximum deflections (absolute value) by month and by span. The maximum deflections took place at the abutment spans (Span 1 and Span 14) and at those spans on both sides of the expansion joint between Span 7 and Span 8. Fig. 8 shows that the bridge deflection was stable with a fixed “W” pattern. Fig. 9 graphs the maximum elevation difference between the two ends of each girder by month and by span, revealing that all spans were stable within a range from 0.03 to 0.37 cm.

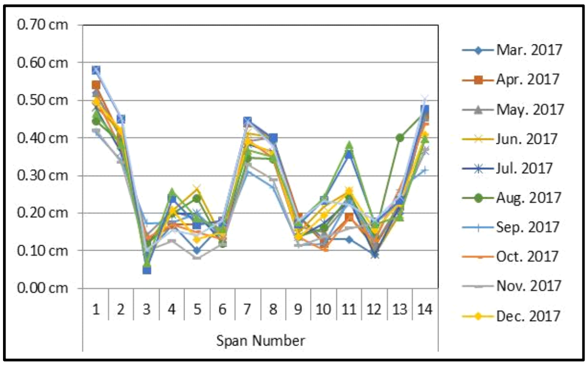

Fig. 8. Maximum girder deflection (absolute value) by month and by span.

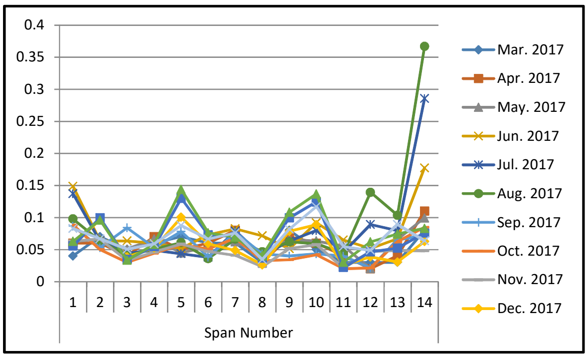

Fig. 9. Maximum elevation difference (absolute value) between two ends of each girder by month and by span

Conclusion

1. This study briefly introduces the development history of lasers, optical fibers, and FBG. It is realized that science and material science facilitate the progress of engineering technologies.

2. This paper proposes a simple design method for DSM sensors, integrated with the law of connected vessels, the buoyancy principle, the equilibrium condition for two-force members, and the photoelasticity of FBG.

3. A 14-span underpass bridge was monitored with the proposed DSM sensor. It is proved that the sensors are sensitive and reliable enough to clarify some subtle behavior of bridge structure.

4. From the field case in this study, it is shown that optical fiber and FBG sensors demonstrate great advantages especially for the long and multiple-span bridges.

Reference

[1] “Bridge,” Wikipedia, Retrieved July 18, 2018 from https://en.wikipedia.org/wiki/Bridge

[2] “Koror–Babeldaob Bridge,” Wikipedia, Retrieved July 18, 2018 from https://en.wikipedia.org/wiki/Koror%E2%80%93Babeldaob_Bridge

[3] “Einstein Predicts Stimulated Emission,” APS NEWS, American Physical Society, Retrieved July 18, 2018 from https://www.aps.org/publications/apsnews/200508/history.cfm

[4] K. O. Hill, Y. Fujii, D. C. Johnson, and B. S. Kawasaki, "Photosensitivity in optical fiber waveguides: application to reflection fiber fabrication," Appl. Phys. Lett. 32 (10): 647, 1978.

[5] G. Meltz, W. W. Morey, W. H. Glenn, "Formation of Bragg gratings in optical fibers by a transverse holographic method," Opt. Lett. 14, 823-825, 1989.

[6] K. O. Hill, B. Malo, F. Bilodeau, D. C. Johnson, and J. Albert ,“Bragg gratings fabricated in monomode photosensitive optical fiber by UV exposure through a phase mask” Appl. Phys. Lett. 62, 1035, 1993.

[7] “Fiber Bragg grating,” Wikipedia, Retrieved July 18, 2018 from https://en.wikipedia.org/wiki/Fiber_Bragg_grating

[8] Z.K. Lee, “Bridge safety monitoring integrated system with full optical fiber and the method for sensing thereof,” U.S. Patent No. 9183739, November 10, 2015.

[9] B. S. Huang, C. H. Chiang, Y. H. Chen, “Restoration of Lateral Deviation in Bridge No. 24 at Provincial Highway 86 after the 2016 Southern Taiwan Earthquake,” Journal of the Chinese Institute of Civil & Hydraulic Engineering, Vol. 44, No. 3, pp.20–26, June 2017.

The Development of Seismic Performance Evaluation and Retrofit Design for Highway Bridges

Yu-Chi Sung[1], Hsiao-Hui Hung[2], Kuang-Wu Chou[3], Chin-Kuo Su[3], Chia-Chuan Hsu[4]

宋裕祺 [1]、洪曉慧 [2]、周光武 [3]、蘇進國 [3]、許家銓 [4]

Abstract

The seismic performance evaluation and effective retrofitting design for bridges can directly minimize the risk of structural damages and avoid the impact of social economy causing by traffic disruption. If the intended purpose of maintaining the basic function for existed bridges after disaster could be achieved, the inflicting losses on macroeconomic will be drastically reduced, and a rapid recovery for the nation's economy might be realized. Hence, the objective of this study is to investigate the development of seismic evaluation and retrofit methods in Taiwan. It is expected that the results could provide practical perception to those who are interested in the domains of bridge engineering and academic research.

Keywords: highway bridges, seismic performance, performance levels, retrofit design

Guidelines of Aseismic Safety Evaluation and Retrofit for Telecommunication and Transportation Systems

In Taiwan, the earliest specification of seismic evaluation for infrastructure is the "Guidelines of Aseismic Safety Evaluation and Retrofit for Telecommunication and Transportation Systems". This specification was written in 1996 by National Taiwan University's Center for Earthquake Engineering Research, which Ministry of Transportation and Communications (MOTC) authorized to implement this specification. For seismic assessment, what this specification suggests is the strength ductility method. Using this method considering the information of cross section, reinforcement, and material strength, engineers can evaluate a bridge's stiffness and ductility capacity (For a bridge being designed, its cross sections, reinforcement, and material strengths should satisfy the requirements of normalized spectral acceleration, structure system seismic reduction factor, site-dependent horizontal design spectrum acceleration factor, and resilient design provision). According to the evaluated stiffness and ductility capacity, engineers can compute a bridge's collapse ground accelerations under different failure modes, including pier failure, bearing damage, soil liquefaction, and the collapse of the superstructure. On the demand side for seismic evaluation of bridges, the design ground accelerations can be obtained by hazard analysis. Then by comparing the collapse ground accelerations with design ground accelerations, engineers are able to determine if the seismic capacity of a bridge suffices.

Seismic Assessment and Retrofit Manual for Highway Bridges

In December 2009, Directorate General of Highways MOTC entrusted National Center for Research on Earthquake Engineering (NCREE) with drafting a guideline, the "Seismic Assessment and Retrofit Manual for Highway Bridges". As shown in Table 1, four seismic performance levels PL3, PL2, PL1, and PL0 of bridges are defined according to safety, serviceability, and restoration. PL3 represents the yielding point in Fig. 1; PL2 denotes a bridge reaches 1/3 of its plastic deformation capacity (one-fourth if located in Taipei Basin); PL1 denotes a bridge reaches almost 2/3 of its plastic deformation capacity (1/2 if located in Taipei Basin); PL0 indicates the plastic deformation capacity of a bridge is used up (In Taipei Basin, PL0 indicates that a bridge reaches 3/4

[1] Professor, National Taipei University of Technology
[2] Researcher, National Center for Research on Earthquake Engineering
[3] Associate Researcher, National Center for Research on Earthquake Engineering
[4] Assistant Researcher, National Center for Research on Earthquake Engineering

of its plastic deformation).

Table 1. Bridge performance levels

Performance Levels	Safety	Serviceability	Restoration	
			Short-Term（Serviceability）	Long-Term（Safety）
PL3	Bridges remain elastic, being prevented from collapse	Full service	Only simple repair is needed	Regular maintenance
PL2	Bridges are prevented from collapse and could suffer repairable plastic deformations	The service of a bridge may be recovered by short-term repair	Short-term repair may be done by applying the existing methods of emergent repair	Long-term restoration may be done by applying the existing repair methods
PL1	Bridges are prevented from collapse. The residual deformations of Piers should not exceed the allowable residual deformations	Bridges, through short-term repair, may be reopened with speed limitations and weight controls on vehicles.	Replace damaged components, or carry out structural retrofitting	Closing the bridge is required to reconstruct it partially.
PL0	Bridges are prevented from collapse. Pier failure is also prevented	The traffic is prohibited. Alternative routes or temporary bridges are used to serve the traffic.	Partial or full bridge reconstruction is allowed	Partial or full bridge reconstruction is allowed

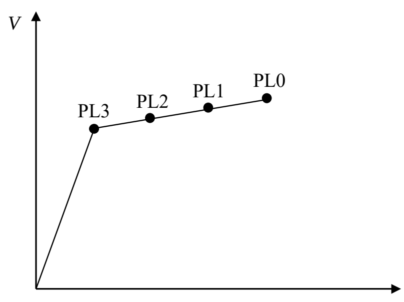

Fig. 1. Four seismic performance levels corresponding to the plastic deformation capacity of a structural system

On the perspective of seismic performance objective, different importance factors I are correlated with different performance levels in this guideline draft, as shown in Table 2 and 3. Bridges designed according to different versions of codes should behave as follows at the following two earthquake intensity levels:

(1) Mediate earthquakes occurring frequently (30-year return period): bridges remains elastic during such earthquakes, getting no obvious damages. Any repair on structural components are not required to maintain bridge traffics.

(2) Design base earthquakes (475-year return period): bridges could become inelastic during such earthquakes. For design of those bridges, their ductility demands should not exceed their allowable ductility capacities to prevent them from collapse.

Table 2. The performance objectives for standard bridges (importance factor I = 1.0)

earthquake intensity level	Version of seismic design code		
	1995 and 2000	1960 and 1987	Before 1960
Mediate earthquakes occurring frequently	PL3	PL3	PL3
Earthquakes for bridge design	PL2	PL1	PL0

Table 3. The performance objectives for important bridges (importance factor I = 1.2)

earthquake intensity levels	Version of seismic design code		
	1995 and 2000	1960 and 1987	Before 1960
Mediate earthquakes occurring frequently	PL3	PL3	PL3
Earthquakes for bridge design	PL2	PL1	PL1

Seismic Evaluation and Retrofit Design Code Draft for Highway Bridges

In January 2018, Freeway Bureau MOTC entrusted NCREE with drafting Seismic Evaluation and Retrofit Design Code for Highway Bridges. In this draft, the seismic performance objectives are expressed with site-adjusted spectral response acceleration parameters at short periods (S_{DS}) and at 1 second period (*SD1*). And such parameters are used to define three different earthquake intensity levels: level I for 30-year return period, level II for 475-year return period, and level III for 2500-year return period. For each earthquake intensity level, what follow describe the seismic performance objective for bridges:

(1) Under level I earthquakes, no obvious damage is found in bridges' main structures and bridges should remain their traffic function.

(2) Under level II earthquakes, bridges are allowed to suffer different degrees of repairable damages that depend on which version of design code or which importance factor is applied on those bridges. But the super structures of bridges should be prevented from collapse; the piers of bridges should be prevented from failure.

(3) Under level III earthquakes, the collapse of bridges and the ultimate failure of piers are not permitted.

The seismic performance of a bridge is evaluated according to the bridge's deformation. The deformation of the bridge as a whole and that of every bridge component demanded by earthquakes of each level should not exceed the regulated deformations. Such performance-based seismic evaluation of bridges are classified into three different earthquake intensity levels:

(1) Under level I earthquakes, a bridge should remain elastic. That means its spectral displacement $S_{d,I}$ demanded by such earthquakes should be less than the spectral displacement capacity $S_{d,A}$ corresponding to performance status A , as shown in Fig. 2. Table 4 shows how to define a bridge's spectral displacement capacity $S_{d,A}$ for level I.

(2) Under level II earthquakes, a bridge may suffer repairable plastic deformation. That means its spectral displacement $S_{d,II}$ demanded by such earthquakes should be less than its spectral displacement capacity $S_{d,B}$ corresponding to performance status B (See Fig. 2). Table 5 shows how the spectral displacement capacity $S_{d,B}$ is defined.

(3) Under level III earthquakes, the deformation of a bridge should not exceed its allowable ductility capacity. That means its spectral displacement $S_{d,III}$ demanded by such earthquakes should be less than its spectral displacement capacity $S_{d,C}$ corresponding to performance status C (See Fig. 2). Table 5 shows how the spectral displacement capacity $S_{d,C}$ is defined.

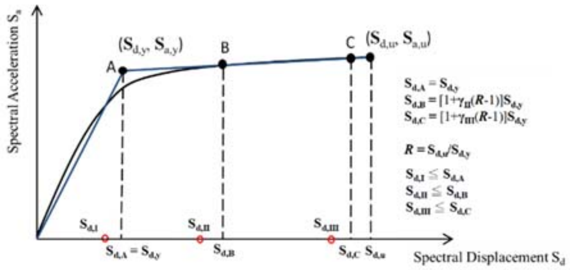

Fig. 2. The seismic evaluation of a bridge

Table 4. The ratio of spectral displacement and yield displacement ($S_{d,A}/S_{d,y}$) for performance status A

Performance Status	standard bridge	important bridge
A	1	1

Table 5. The ratio of spectral inelastic capacity r_{II} and r_{III} for performance status B and C

Site /Version of Design code \ Importance of bridge	r_{II} (Performance Status B)				r_{III} (Performance Status C)	
	General and near-fault region		Taipei Basin		General and near-fault region	Taipei Basin
	After 1995	Before 1987	After 1995	Before 1987		
standard bridge	2/3	3/4	1/2	2/3	-	-
important bridge	1/2	2/3	1/3	1/2	1*	1*

Development of Seismic Retrofit Design for Bridges

For the development of seismic retrofitting methods in Taiwan, the evolution process can be found in several specifications as shown in Table 6. In those specifications, the seismic retrofitting plans are aimed at improving loading capacity and general structural strength to satisfy all kinds of function. With reference to relevant literatures and experiences, the retrofitting construction methods can be classified approximately as shown in Fig. 3.

Moreover, for the seismic retrofitting strategies, it can be categorized into two groups:

(1) The local component retrofitting techniques:

The local component retrofitting object can be subdivided into superstructure, pier and foundation. To superstructure and pier retrofitting, the targets are focused on the toughness, shear strength, longitudinal steel lap splice and bending strength. To foundation retrofitting, the detailed evaluations for safety concerns about scouring, earthquake, and bearing capacity after on-site inspection are needed.

(2) The global structural retrofitting techniques:

The basically advantages of global structural retrofitting are reducing external force transfer to substructure, avoiding large-scale excavation for construction, increasing structure safety and saving construction cost. The representative techniques are superstructure continuity, support reaction dispersion, and base isolation.

Table 6. The seismic retrofitting specifications of bridge in Taiwan

No	Year	Specification
1	2008	Inspection and Retrofit Codes for Highway Steel Bridges
2	2009	Seismic Assessment and Retrofit Manual for Highway Bridges
3	2010	Inspection and Retrofit Codes for Railway Steel Bridges
4	2015	Inspection and Retrofit Codes for Highway RC Bridges
5	2018	Inspection and Retrofit Codes for Highway Bridges

Conclusions

In this study, the development with an emphasis on seismic performance assessment and retrofit design for highway bridges are collected and organized. The requirements for performance levels, performance objectives, and performance status in each code with the seismic capacity of bridge are also investigated, respectively. Furthermore, the evolution of the seismic retrofitting construction methods are classified according to different retrofitting strategies. The summarized results can be applied to structural safety evaluation of bridges and to implement the consequent retrofitting works.

References

Ministry of Transportation and Communications (MOTC) R.O.C, (1996), “Guidelines of Aseismic Safety Evaluation and Retrofit for Telecommunication and Transportation Systems”.

Directorate General of Highways, MOTC, (2009), “Seismic Assessment and Retrofit Manual for Highway Bridges”.

Taiwan Area National Freeway Bureau, MOTC, (2018), “Seismic Evaluation and Retrofit Design Code Draft for Highway Bridges”.

Ministry of Transportation and Communications (MOTC) R.O.C, (2018), “Inspection and Retrofit Codes for Highway Bridges”.

Wang, J.-L., Chiang, C.-H., Chi, S.-J., Su, C.-K., (2016), “The development of seismic evaluation and retrofit design code for Highway Bridges,” CECI Engineering Technology, special report, No.111, pp. 124~135.

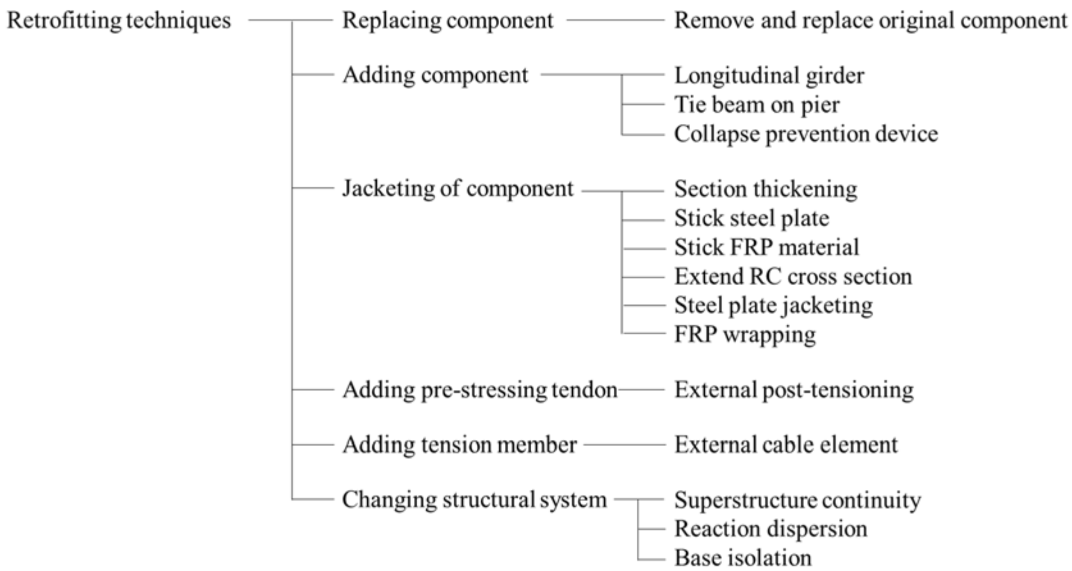

Framework of Automated Beam Assembly and Disassembly System for Temporary Bridge Structures

Yao-Yu Yang[1], Fang-Yao Yeh[2], Chia-Ming Chang[3] and Shih-Chung Kang[4]

楊耀畬[1]、葉芳耀[2]、康仕仲[3]、張家銘[4]

Abstract

Temporary bridges play an important role in disaster relief operations. However, during such operations, availability of workers and limited time are major constraints. The requirement of human resources and construction safety measures may hinder completion of temporary bridge construction within the expected time, thereby delaying subsequent rescue operation. To address these issues of worker safety and shortage during a disaster event, an automated beam assembly approach for temporary bridge segments is proposed in this study. The approach includes a framework for automated assembly of temporary bridge segments using a crane and a construction process based on the framework. The framework and the construction process are examined with both virtual and small-scale models.

Keywords: automated construction, construction safety, mobile crane control, autonomous structural connector, disaster relief

Introduction

When a bridge structurally loses its workability during a disaster, installing a temporary bridge is a recognized approach in disaster relief operations. In 2013, Russell et al. classified portable and rapidly deployable temporary bridges into four types [1]. Those bridges still have issues related to their span length and maximum load-carrying capacity. Therefore, in 2015, Yeh et al. applied glass-fiber-reinforced plastic (GFRP) in a segmental temporary bridge design, thus making it lightweight and reusable [2]. The actual load-carrying capacity of the GFRP bridge is 5 tons, and the span is 20 m. However, the assembly of a GFRP bridge in an actual working environment may be difficult because not only may the weather be unsuitable for construction but also recruitment of sufficient workers may be difficult on-site.

To clarify the main reasons for these problems, we analyzed the video of the construction process of GFRP temporary bridges. The beam hoisting and assembly processes were found to be critical and to majorly control the entire construction process and worker safety in bridge construction. This process put emphasis on the technique of beam assembly.

Background

Automated steel beam assembly has been extensively researched. One research team focused on automated construction of high-rise buildings by setting up a construction factory at the top of a building [3, 4]. They developed robotic bolting and robotic transport of steel beams and tested beam assembly in a real construction site. This application, however, has a constraint related to architectural design because of the geometrical limitation of the working space of the construction factory. In 2016, an approach was developed to help construction workers assemble steel beams with an automated wire control machine [5]. By using this approach, worker safety could be ensured in the case of assembling steel beams at a height, although the pre-installation of the guiding ropes for automated assembly may still be risky for workers. Another study attempted to achieve remote steel beam assembly by using structural connector design and controllable rotation of a crane hook [6]. The rotating

[1] Ph. D. Candidates, Department of Civil Engineering, National Taiwan University
[2] Research Fellow, National Center for Research on Earthquake Engineering
[3] Assistant Professor, Department of Civil Engineering, National Taiwan University
[4] Professor, Department of Civil Engineering, National Taiwan University

hook triggers the opposite rotation of the attached steel beam, thus finishing beam assembly. However, object avoidance during beam rotation was a challenge for this method.

This study proposes an automated beam assembly framework for constructing segmental temporary bridges while taking into consideration worker safety and shortage during disaster events as well as comprehensive steel beam assembly using a crane.

Automated Beam Assembly Framework

For this automated beam assembly framework, critical elements for research development are identified and a temporary bridge construction process is proposed on the basis of an automated approach utilizing a mobile crane.

Elements of the Framework

The critical elements are categorized into two parts: the structure and the automated process. The structure part, named "Temporary bridge" in Fig. 1, which includes segmental structure, lightweight structure, and structural connector, defines the requirement of the material and structural geometry to be used in bridge construction. The automated process part, named "Mobile crane" in Fig. 1, considers the technical requirement for a mobile crane to perform beam hoisting and assembly tasks without any worker on site.

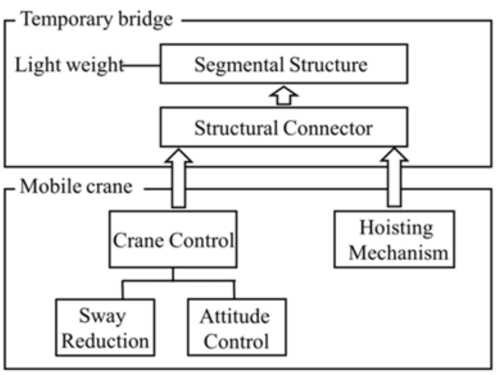

Fig. 1. The framework of automated beam assembly

(1) Segmental Structure (SS)

Construction of a temporary bridge for disaster relief must be completed within a limited time. Therefore, a segmental structure is a feasible option to satisfy this requirement. Before a disaster occurs, each segment of the temporary bridge can be compactly stored in a container, placed close to the potential damage site, and shipped to the site when need arises.

(2) Lightweight (LW)

To achieve a longer span, it is important for a temporary bridge to be lightweight. According to the information from officers of Taiwan Directorate General of Highways, a minimum of 30 m is the commonly repaired span of bridges damaged in a disaster. In addition, the lightness of a bridge would aid in its convenient shipping to sites that are often difficult to access, such as a valley or a river in a mountain.

(3) Structural Connector (SC)

A structural connector allows the assembly of two segments of a bridge. To realize automated bridge construction, autonomous assembly of the structural connector should be focused on in beam design. The designed connector should also consider the construction feasibility when using a crane. In this study, we utilized a connector from our previous research on autonomous beam assembly [7]. The previous research demonstrated the feasibility of a hook-shaped structural connector for autonomous assembly. The design concept involves autonomous locking of a male connector and a female connector.

(4) Crane Control– Sway Reduction (SR)

It is necessary to reduce the magnitude of the sway of a payload. The payload such as a beam with a designed connector should be stabilized to a suitable level to execute precise position control, thereby allowing autonomous attachment of the male and female connectors.

(5) Crane Control– Attitude Control (AC)

When a connector is at the target position, the male connector can be rotated to attach to the female connector via attitude control of the structural component. By taking advantage of the sway reduction and attitude control, the automated assembly of the two connectors becomes easier.

(6) Hoisting Mechanism (HM)

Before transporting a beam using a crane, it should be firmly attached to the crane hook, and after the transportation, the beam needs to be conveniently detached from the hook. An automated mechanism for attaching and detaching the beam without manual operation is necessary.

Construction Process

The construction process defines each step of the beam assembly and disassembly.

(1) Assembly Process

Step 1: Connect the crane hook to the beam. Step 2: Lift up the beam. Step 3: Transport the beam to the target position for assembly. Step 4: Adjust the attitude of the male connector to attach the female connector on the bridge. Step 5: Release the beam for assembly by the action of gravity. Step 6: Lock the beam on the bridge structure. Step 7: Disconnect the beam from the crane hook.

(2) Disassembly Process

Step 1: Connect the crane hook to the beam to be disassembled. Step 2: Unlock the beam. Step 3: Lift the beam. Step 4: Detach the male connector from the female connector on the bridge structure. Step 5: Transport the beam to the storage area. Step 6: Release the beam. Step 7: Disconnect the beam from the crane hook.

Experiment and Result

The framework and the construction process were validated by the experiment described in this section. The following three assumptions were made in the experiment. (1) If the assembly steps are feasible, the disassembly steps are also feasible. (2) Attitude control rotates the beam in the longitudinal direction. According to a study by Lee et al. in 2012, the attitude control of a beam is probable to be implemented [8]. In the experiment, the beam was rotated by manual operation. (3) Hoisting mechanism connects to the end of a beam and can be remote-controlled. The experiment was conducted on-site as well as using a virtual model with a commercial physics engine.

On-site Experiment

The first four steps of the proposed assembly process were validated by an on-site experiment that measured the placement deviation from the target position of the hoisted structural component for assembly (Fig. 2). A crane with a hydraulic retractable boom with the maximum load capacity of 3.4 tons was used in the experiment. The payload was a 1.45 m beam weighing approximately 80 kg. The crane was operated by a graduate student, who learnt crane operations from a professional crane operator and practiced the required operation for sway reduction before the experiment.

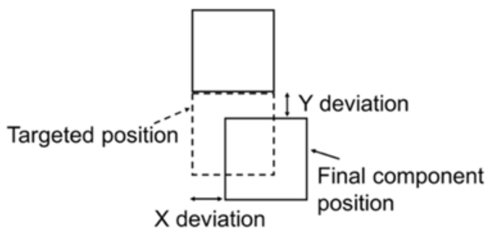

Fig. 2. Measurement of structural component deviation from selected target

Table 1 Placement deviation from selected target

Test	X deviation [cm]	Y deviation [cm]
1	4.0	2.9
2	1.9	0.0
3	3.2	1.2

The results of X and Y deviation were 3.03 cm and 1.37 cm on average, respectively. Figure 3a-1 shows the environment of the experiment. We placed a short beam, indicated approximately at the center of the picture, as the target position for beam assembly. The overview of the crane we used and the test environment is presented in Fig. 3a-2. Figure 3b shows the recorded first four steps of the assembly process. In the experiment, the end of the beam was connected to the crane hook using steel cables (Fig. 3b-1). The beam was lifted approximately 50 cm from the ground (Fig. 3b-2). The crane operator transported the beam using the crane in a slewing motion only (Fig. 3b-3). Figure 3b-4 presents the state at which the beam was positioned at the target position; the crane operator reduced the sway by manual crane operation and rotated the beam in the longitudinal direction for attitude control. After the position and the attitude of the beam were stable, the crane operator placed the beam on the ground, and the placement deviation was measured (Fig. 3b-5).

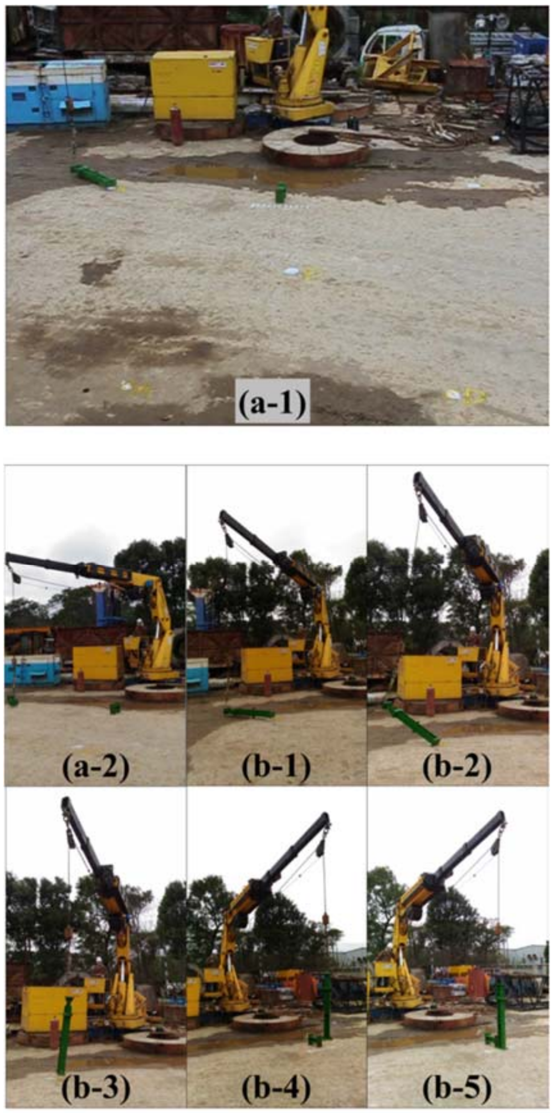

Fig. 3. (a) On-site experiment environment, (b) The results of the automated process

Virtual Model Experiment

To validate step 5 of the assembly process, that is, "release the beam for assembly by the action of gravity", we created a virtual structural component and used a virtual mobile crane to simulate the rotation of the structural connector. The virtual model was created on a commercial physics engine, Unity3D. The virtual model successfully demonstrated step 5 (Fig. 4).

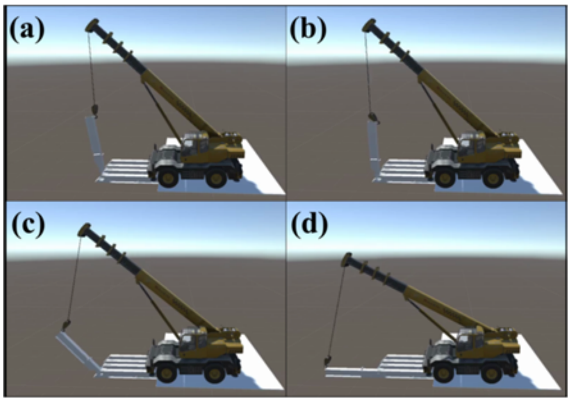

Fig. 4. Results of virtual beam assembly by a mobile crane

Discussion

The placement deviation from the target position demonstrated that sway reduction was difficult to achieve, mainly caused by the unstable slewing torque generated by the hydraulic system of the crane. The hydraulic control system could not maintain a constant angular velocity of slewing during the transportation of the beam although the control stick of slewing was kept in the same inclination level. Another crane control issue was the limitation of the degrees of freedom of control. Only one degree of freedom could be controlled at one time, indicating that the hoisted beam could not move as smoothly as we expected. To minimize the abrupt change in the transportation path, we only applied slewing rotation in the experiment.

Conclusions

This study aimed to clarify the construction process of automated beam assembly and identify key elements required for the automated assembly of temporary bridges using a crane. The key elements including the structure part and the automated process part form the proposed framework of the automated assembly process. An on-site experiment and a virtual simulation were conducted to validate the construction process. The beam placement deviation from the target position was determined, which can serve as a reference for autonomous structural connector design. The results showed the feasibility of the proposed framework and the construction process, which may contribute to the development of an automated beam assembly approach using crane operations. Future research must focus on crane control, including sway reduction and attitude control. We suggest that the sway reduction for crane operation can be performed after the hoisted beam arrives at the target position. Since it is difficult for the crane hydraulic system to apply stable output force on the hoisted beam, it is easier to apply the sway reduction by controlling the crane boom to follow the motion of the beam. To control the beam attitude for connection, the benefit of controlling two crane hoist lines may be taken into consideration.

References

1. Russell, B.R. and A.P. Thrall, Portable and Rapidly Deployable Bridges: Historical Perspective and Recent Technology Developments. Journal of Bridge Engineering, 2013. 18(10): p. 1074-1085.
2. Yeh, F.-Y., et al., A novel composite bridge for emergency disaster relief: Concept and verification. Composite Structures, 2015. 127(Supplement C): p. 199-210.
3. Chu, B., et al., Robot-based construction automation: An application to steel beam assembly (Part I). Automation in Construction, 2013. 32: p. 46-61.
4. Jung, K., B. Chu, and D. Hong, Robot-based construction automation: An application to steel beam assembly (Part II). Automation in Construction, 2013. 32: p. 62-79.
5. Kim, C.-W., et al., Advanced Steel Beam Assembly Approach for Improving Safety of Structural Steel Workers. Journal of Construction Engineering and Management, 2016. 142(4).
6. Liang, C.-J., S.-C. Kang, and M.-H. Lee, RAS: a robotic assembly system for steel structure erection and assembly. International Journal of Intelligent Robotics and Applications, 2017.
7. Yang, Y.-Y., et al., Crane-Based Autonomous Erection and Assembly System, in The 3rd International Conference on Civil and Building Engineering Informatics. 2017: Taipei, Taiwan.
8. Lee, C., et al., Analysis of field applicability of the rotation-controllable tower-crane hook block. Automation in Construction, 2012. 21: p. 81-88.

Assessment of Water Systems for Seismic Hazard Mitigation

Gee-Yu Liu[1], Chin-Hsun Yeh[2], Lee-Hui Huang[3] and Gee-Jin Yu[4]

劉季宇 [1] 葉錦勳 [2] 黃李暉 [3] 於積璢 [4]

Abstract

Implementation of a seismic assessment tool for the Kaohsiung metropolitan area water supply systems is introduced in this paper. The assessment was undertaken based on earthquake scenario simulation that employed the Twater software system developed by NCREE. Twater is able to simulate damage to the component pipelines and facilities of a metropolitan water system, as well as any impacts to their functionality and the system's serviceability following an earthquake event. As the input data, Twater utilizes the inventory and hierarchy of relevant system components including raw water aqueducts, water treatment plants, major clear water conveyance trunks, and water transmission and distribution pipeline networks, as well as their relationship with the water supply areas in a system. Based on the assessment results, suggestions to improve the Kaohsiung metropolitan area water supply systems have been made for future hazard mitigation.

Keywords: water supply system, seismic assessment, hazard mitigation

Introduction

The service region of the Seventh Branch, Taiwan Water Corporation (TWC) includes Kaohsiung City, Pingtung County, and Penghu County. Kaohsiung is the third largest metropolitan area within this region of Taiwan, and it is also the political and economic center of southern Taiwan. According to the active fault map published by the Central Geological Survey, MOEA, there are three active faults lying in Kaohsiung: Chishan (Category I), Hsiaokangshan () and Chaochou (both Category II). Consequently, the threat arising from major earthquakes in these areas should not be overlooked.

This study focuses on the water supply systems in Kaohsiung. There were two objectives: (1) to collect and calibrate the inventory of water pipelines and facilities, and to divide the large systems into smaller evaluation units suitable for seismic analysis; (2) to perform a seismic risk assessment to estimate the likely damages and losses due to the designated earthquake scenarios and give suggestions for hazard mitigation.

Framework of Twater Software

In the past two decades, a GIS-based Windows application called Taiwan Earthquake Loss Estimation System (TELES) has been developed and maintained by NCREE in Taiwan. It aims to provide solutions for scenario-based quantitative damage assessment and loss estimation of buildings and infrastructure, as well as any induced secondary loss arising from earthquake events in Taiwan.

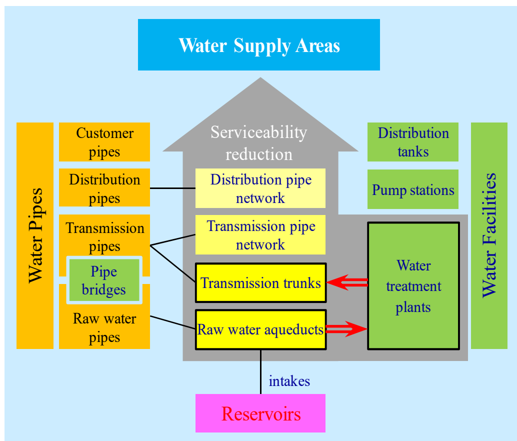

Figure 1 Conceptual diagram of a water supply system with component serviceability reduction after earthquakes.

[1] Research Fellow, National Center for Research on Earthquake Engineering
[2] Research Fellow, National Center for Research on Earthquake Engineering
[3] Assistant Researcher, National Center for Research on Earthquake Engineering
[4] Assistant Researcher, National Center for Research on Earthquake Engineering

Recently, TELES has been customized to estimate damage and loss to water supply systems from earthquakes. This new software is called Twater and it is a subsystem of TELES. Generally, a water supply system can be conceptually simplified, as shown in Figure 1. As the input data, Twater utilizes an inventory and hierarchy of the water supply system components including raw water aqueducts, water treatment plants, major clear water conveyance trunks, and water transmission and distribution pipeline networks, as well as their relationship with the service areas in the system. When an earthquake occurs, the water systems components may suffer a reduction in serviceability, as shown by the gray area in Figure 1, whilst all service areas will experience water outages of varying severity.

Twater uses the following procedure to complete an assessment of a water supply system:

1. Divide the entire region of the system into several smaller water supply areas to form the basic units employed in the performance analysis;
2. Specify the water treatment plant(s) and clear water transmission trunks associated with each water supply area;
3. Specify the raw water aqueduct(s) associated with each water treatment plant;
4. Divide the remaining pipelines into each water supply area; classified as of the distribution or transmission network according to the pipe diameter;
5. Perform the simulation and decide: (1) the damage and impact to the functionality of all raw water aqueducts, water treatment plants, and transmission trunks, (2) the repair rates for the distribution and transmission networks of each water supply area;
6. Compute the water outage experienced by each water supply area by considering the serviceability reduction of all the components as per step 5 above.

Simulation of Damage, Functionality and Post-earthquake serviceability

This section explains Twater's methodologies for simulating damage to buried water pipelines, the functionality of water treatment plants, and the serviceability of water supply systems following earthquakes. Technical details can be found in research reports by the authors (WRA, 2016 & 2017; TWC, 2018).

Water pipelines: For an earthquake scenario, Twater estimates the repair rates for in-service water pipes of various types and sizes. It then estimates the damage, repair costs and restoration time. The repair rate (also called the damage rate) is defined as the number of repairs per unit pipe length. The repair rate of water pipes is a function of ground shaking and permanent ground deformation due to either soil liquefaction or fault rupture. The repair rate function is defined as

$$RR = \max\left[RR_{PGA}, p_{fault} \cdot RR_{PGD(fault)}, p_{liq} \cdot RR_{PGD(liq)} \right],$$

where RR_{PGA} and RR_{PGD} are the empirical repair rate formulas based on ground shaking (in terms of peak ground acceleration, PGA; in g) and permanent ground deformation (PGD; in cm), p_{fault} and p_{liq} are the encounter probabilities of fault rupture and soil liquefaction, respectively. The functional forms of RR_{PGA} and RR_{PGD} are

$$RR_{PGA} = 4.501 \cdot C_{S_i-PGA} \cdot C_{T_j} \cdot (PGA - 0.1)^{1.97},$$

$$RR_{PGD} = 0.04511 \cdot C_{S_i-PGD} \cdot C_{T_j} \cdot PGD^{0.728},$$

where C_{S_i} ,and C_{T_j} denote the correction coefficients for different pipe sizes (S_i) and pipe materials or joints (T_j), where C_{S_i-PGA} and C_{S_i-PGD} further denote that the effect of pipe damage arising from ground shaking differs from that due to ground deformation.

Twater differentiates pipe damage into two categories, breaks and leaks, in order to distinguish severity, simulate the functionality, and estimate the required cost and efforts to repair any damage. Twater assumes that the pipe break rate, a value between 0 and 1 that denotes the probability of a pipe breaking, is proportional to the hazard of ground shaking and deformation up to a ceiling value (namely 0.6g for ground shaking and 100cm for ground deformation). The formulae applicable to pipe break rates due to ground shaking and deformation are

$$BR_{PGA} = \begin{cases} B_{S_iT_j-PGA} \cdot 2 \cdot (\mathrm{PGA} - 0.1) & 0.1\mathrm{g} < \mathrm{PGA} < 0.6\mathrm{g} \\ B_{S_iT_j-PGA} & \mathrm{PGA} \geq 0.6\mathrm{g} \end{cases},$$

$$BR_{PGD} = \begin{cases} B_{S_iT_j-PGD} \cdot 0.01 \cdot \mathrm{PGD} & \mathrm{PGD} < 100\mathrm{cm} \\ B_{S_iT_j-PGD} & \mathrm{PGD} \geq 100\mathrm{cm} \end{cases},$$

where $B_{S_iT_j-PGA}$ and $B_{S_iT_j-PGD}$ are the upper limits of the pipe break ratio due to ground shaking and ground deformation, respectively. These parameters depend on the pipe size (S_i) and material or joint properties (T_j), as indicated by the subscripts.

Water treatment plants: Water treatment plants usually consist of various types of basins and tanks that are used for different treatment processes. For example, relevant treatment processes include coagulation, sedimentation, filtration and disinfection. For large water treatment plants, each type of process may consist of several basins or tanks that can work independently, which allows the plant to function with several parallel and independent "water treatment units,". These basins and tanks are usually not very tall, and are structurally very robust under the influence of ground shaking. However, a large water treatment plant usually occupies a vast area. Past experiences indicate that such plants are susceptible to severe damage only under fault rupture-induced ground failure. As a result, it is crucial to estimate the portion of a water treatment plant located in a fault zone.

Given an earthquake scenario, Twater will first calculate the exceeding probabilities of a slight, moderate, severe and complete damage state occurring to a water treatment plant. The corresponding probabilities of each damage state and the reduction ratio of functionality are p_i and s_i $(i = 2,3,4,5)$, respectively. Twater estimates the ratios of each water treatment unit under damage state i $(i = 2,3,4,5)$ as

$$d_{r,i} = \min\left[1, \frac{\mathrm{R}\left(1 + A_{r,i} \cdot n\right)}{n}\right],$$

$$A_{r,i} = \min\left[1, 2^{d_n - i} \cdot \frac{S_r}{S_p}\right],$$

where $R(\cdot)$ denotes the round-off operator, $d_i = i$ is defined as the discrete damage state values and n is the number of water treatment units. The d_n parameter is a value between 1 (for no damage) and 5 (for complete damage) such that the exceeding probability of 0.5 is employed to interpolate the "continuous damage state value" of the plant. The parameter S_p denotes the plane dimension of the plant whilst S_r describes the largest portion of the plant of its four damage states.

Finally, the remained ratio of the capacity of the plant is given by

$$O = 1 - \sum_{i=2}^{5}\left(p_i \cdot d_{r,i} \cdot s_i\right).$$

Water systems: Twater estimates the serviceability of a water supply system by simulating the total amount of water received by each of its water supply areas after an earthquake and comparing it with the amount received before an earthquake. Suppose that a water supply area is serviced by N water treatment plants, before an earthquake, each plant supplies a daily water amount of $\bar{D}_k$ $(k = 1,\ldots,N)$ to this area. If there are M_k clear water transmission trunks from the plant k to this area, and λ_j $(j = 1,\ldots,M_k)$ is the portion of water supplied through trunk j, then the water received D by this area after earthquake can be expressed by

$$D = \sum_{k=1}^{N}\left[\bar{D}_k \cdot O_k \cdot \sum_{j=1}^{M_k}(\lambda_j \cdot \Omega_j)\right],$$

where O_k and Ω_j are the functionality reduction rates of the plant k and trunk j, respectively.

Seismic Assessment of Water Supply Systems in Kaohsiung

The water systems in Kaohsiung were selected for this case study. There are a total of 12 systems providing water to 2.74 million people, where the daily water supply is 1.53 million cubic meters. Figure 2 depicts the distribution of reservoirs, water treatment plants, and the major water pipes in Kaohsiung City.

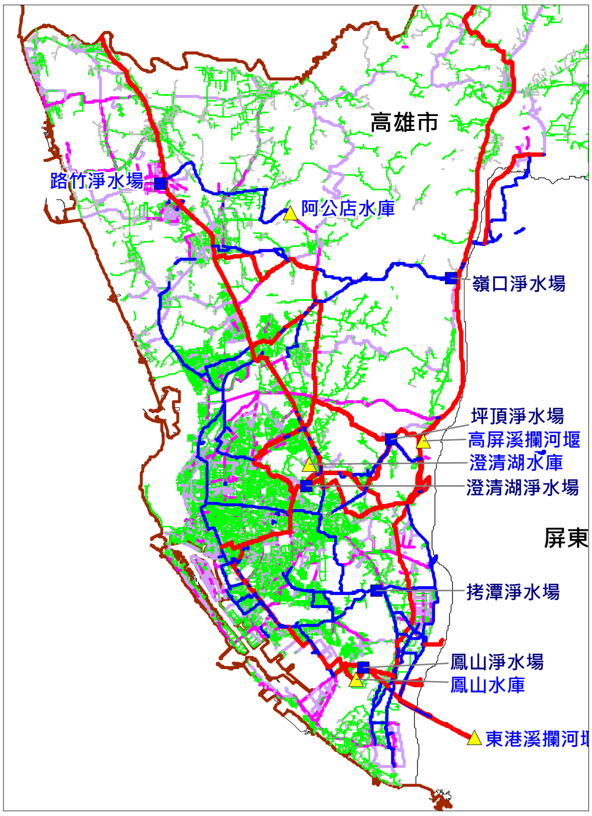

Figure 2 The distribution of reservoirs, water treatment plants, and major water pipes in Kaohsiung.

Several earthquakes scenarios have been chosen and applied to these water systems. Due to content limitations, only the worst case scenario is summarized in this paper, which is the M7.2 Chishan Fault earthquake. Key estimates by TELES and Twater are summarized as follows:

1. Most areas will experience ground shaking of Seismic Intensity VII (PGA ≥ 0.4 g). Fault offset greater than 1.5 m will be observed along the Chishan Fault trace, resulting in huge damages to buildings, bridges, and lifelines. Widespread soil liquefaction will occur, especially along the coast.
2. More than 6,000 casualties and serious injuries are expected.
3. The largest water treatment plants will suffer little or no damage because the sites are away from the Chishan Fault. Significant damages to important raw water aqueducts, clear water transmission pipes (ϕ500 mm or larger; 60 damage points), distribution pipes (ϕ100-450 mm; 3,600) and customer pipes (2,900) are expected. These will not

only limit the water output of the largest treatment plants but will also be time consuming and expensive to repair. Figure 3 depicts a thematic map of the number of pipes damaged.

4. Immediately following the earthquake, a 67% shortage in water supply is expected. As a result, 730,000 households will be left without water. Figure 4 depicts a thematic map of the number of households without water.
5. The readiness to repair the 60 damage points in the water transmission pipes will significantly affect the restoration of the water supply. Therefore, the corresponding preparedness regarding availability of spare pipes, tools and manpower becomes essential.

According to the assessment results, the following suggestions have been made: (1) enhancements to the capability of quickly repairing at least 10 large water pipe damage sites concurrently is recommended in order to restore the water supply swiftly after a major earthquake occurrence; (2) the seismic safety of the water supply to the Chishan District should be enhanced as it is subject to a very high seismic threat (Chishan fault earthquake).

Concluding Remarks

Utilizing the Twater software for assessing the damage and serviceability of water supply systems following earthquakes has been introduced in this paper. It has been successfully employed to analyze the water supply systems in Kaohsiung to support future seismic hazard mitigation.

References

1. WRA (Water Resources Agency), A Study on the Seismic Scenario Simulation Technology for Public Water Supply Systems, WRA Research Report, Project No. MOEA-WRA-1050316, Taipei, Taiwan, 2016 (in Chinese).
2. WRA (Water Resources Agency), A Study on Seismic Risk Assessment Technology for Public Water Supply Systems with Raw Water Aqueducts, WRA Research Report, Project No. MOEA-WRA-1060241, Taipei, Taiwan, 2017 (in Chinese).
3. TWC (Taiwan Water Corporation), "Seismic Hazard Exposure and Risk Assessment of Water Supply Systems in Kaohsiung Metropolitan Area," TWC Research Report, Taichung, Taiwan, 2018 (in Chinese).

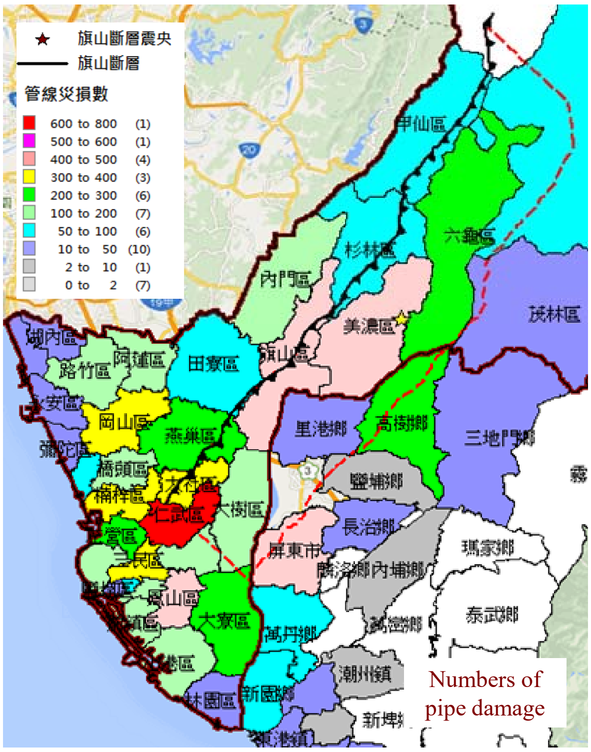

Figure 3 A thematic map of the extent of pipe damages in Kaohsiung under the M7.2 Chishan Fault earthquake.

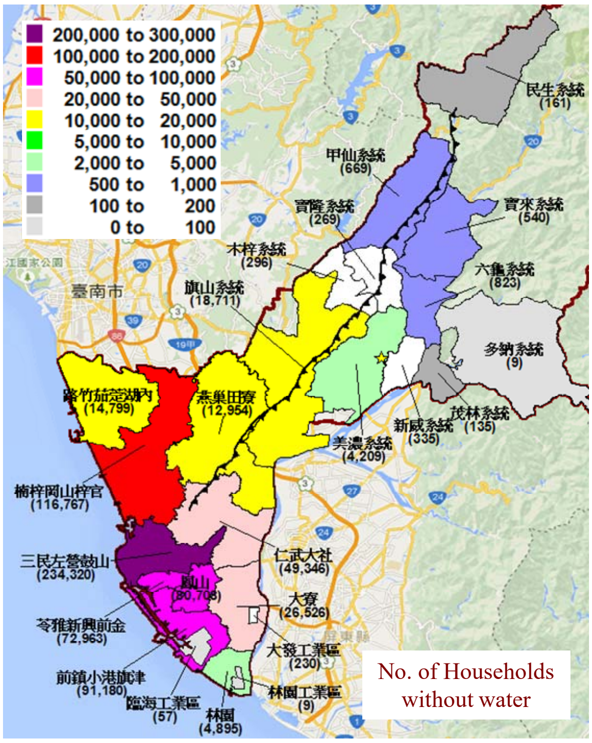

Figure 4 A thematic map of the number of households without water in Kaohsiung under the M7.2 Chishan Fault earthquake.

Seismic Evaluation Method of Typical Sprinkler Piping Systems in Hospitals

Yung-An Tsai[1] Fan-Ru Lin[2] Juin-Fu Chai[3] and Kuo-Chun Chang[4]

Abstract

Recently, the seismic capacity of critical building structures (such as hospitals and high-tech factories) has improved due to the vigorous development of performance design concepts. As a result, major damage and economic losses caused by earthquakes has changed from predominantly structural to non-structural systems such as piping systems.

The common failures to fire protection sprinkler systems resulting from seismic events include impact damage to ceiling boards, leaks to the one-inch threaded joints, and breakage of the hangers. In order to better understand the seismic vulnerability of the components mentioned above, this research revised the detailed numerical analysis method (Method A) developed by Yeh (2016) [1]. As an example, the NTU Hospital Yunlin branch was used to conduct fragility analysis of the components associated with the fire protection sprinkler system.

Keywords: Near-fault earthquake, Fire protection sprinkler system, Ceiling, Threaded joint, Hanger, Fragility curve, Detailed analysis

Introduction

Based on the improvement of performance design concept for critical building structures (e.g. hospitals and schools) in recent years, seismic damage to non-structural elements (e.g. sprinkler piping systems) are now more common than structural damages. Fire protection sprinkler systems play an important role in preventing fire disasters and ensuring occupant safety, where the failure of fire protection sprinkler systems may result in a threat to occupant safety, the shutdown of medical functionality, and related repair expenses. Therefore, an accurate assessment method to evaluate the seismic susceptibility of a buildings fire protection system is necessary.

Common failures to fire protection sprinkler systems resulting from seismic damage include impact damage to the ceiling boards, leaks to the one-inch threaded joints and breakage of the hangers. This research revises the detailed numerical analysis method (Method A) developed by Yeh (2016) [1] in order to understand the seismic susceptibility of the components mentioned above. The NTU Hospital Yunlin branch is used as an example in order to conduct the fragility analysis of the fire protection sprinkler systems componentry.

The main results are briefly described below:

1. *Performance design method for piping systems*: Referring to FEMA P58 [2], an assessment of the sprinkler piping systems will only be meaningful when the buildings structures are judged as reparable. In this study, seismic performance of the sprinkler piping will only be evaluated when the structure is deemed as reparable.

2. *Category of floor response time history*: This research selects two methods of obtaining the floor response time history. One is by inputting an original far-field earthquake and a near-fault earthquake into a nonlinear numerical model of the RC structure of the example hospital building. This is established using MIDAS software. The other is referring to AC156 [3], employing a Required Response Spectrum (RRS) to determine a compatible floor response time history.

3. *Detailed evaluation method:* A detailed numerical model of the horizontal sprinkler piping system was established using SAP2000 software to simulate the nonlinear behavior of the hanger and the nonlinear relationship between the piping and ceiling systems or partition walls (Method A). The fragility parameters for the three seismic performances of the piping system were then obtained through incremental dynamic analysis.

Fragility Analysis of Sprinkler Piping System

As shown in Figure 1, based on the performance evaluation framework of FEMA P-58 [2], a modified assessment procedure for the fragility analysis of the nonstructural components (NSCs) was proposed in Lin's paper [4] and applied to this study:

1. *Selection of ground motions*:
   FEMA P695 [5] requires selecting more than 11

[1] Project Researcher Assistant, National Center for Research on Earthquake Engineering
[2] Associate Researcher National Center for Research on Earthquake Engineering
[3] Research Assistant, National Center for Research on Earthquake Engineering
[4] Professor, Dept. of Civil Engineering, National Taiwan University

records for fragility analysis. In this study, 12 far-field ground motion (FQ type) records and 13 near-fault ground motion (NQ type) records were selected from 9 stations, and applied in FEMA P695 to compare the effects of each on the sample piping system. The FQ and NQ types of ground motions were initially normalized referring to FEMA P695;

2. *Distribution of the intensity levels of earthquakes*:

In order to improve the accuracy of the fragility curves, this study attempted to collate more groups with intensity levels close to the median value of the sprinkler piping system fragility curves. Thus, eight groups of ground motion intensity levels were distributed with unequal intervals according to the risk contribution of each failure mode of the sprinkler piping systems. The risk contribution was then calculated based on the generic parameters of fragility of the sprinkler piping system offered by FEMA P58 and the normalized hazard curve applicable to the Taiwan area [6];

3. *Analysis for floor responses*:

In this study, both specific and generic floor responses were produced to investigate the influence of different types of seismic floor responses on the behavior of the sprinkler piping system. The specific floor response of the sample hospital was calculated by executing a nonlinear time-history analysis of the numerical model mentioned above whereas, artificial floor responses were calculated in accordance with the AC-156 code. AC156 provides a generic RRS for use in the seismic certification of NSCs and requires the artificial floor acceleration to be compatible with the RRS. In contrast with the generic floor response spectra, specified floor response spectra were amplified significantly around the fundamental period of 0.5 sec and some of those appear as nonlinear behavior expressed as high-period spectral responses;

4. *Upper limit of the scaling intensity level of ground motions*:

Considering that prediction of the seismic response of the piping system subjected to the extremely nonlinear behavior of the building structure is unreliable, the assessment of the sprinkler piping is judged to only be meaningful when the buildings structures are reparable. In this study, the upper limit of the intensity level of ground motion used for analysis is determined to be the smaller value of the maximum considered earthquake (MCE) multiplied by an importance factor (*I*=1.5 for hospitals) and a value corresponding to a 84% non-exceedance probability of irreparability. Referring to FEMA 356 [7], the damage state of buildings constructed with concrete walls with a maximum transient drift ratio exceeding 1% or 2% is judged as irreparable or collapsible. As depicted in Figure 2, the repair fragility of the sample structure in terms of $S_a(T_1)$ indicates that the intensity of 2.25g causes an 84% non-exceedance probability of irreparability. Thus, the upper bound for the intensity level of ground motion used for the numerical analysis of piping is limited by 1.5MCE and is defined as $S_a(T_1) = 1.5\text{g}$. For the artificial floor responses compatible with AC156 RRS in this study, comparing 1.5MCE ($I \cdot S_{MS}$) to the short-period spectral acceleration (S_{AS}) corresponding to the 84% non-exceedance probability of irreparability is based on the assumption that the buildings structure has a 16% non-exceedance probability of irreparability under the design basis earthquake (DBE). Whereas the smaller value of 1.168g is controlled by an 84% non-exceedance probability of irreparability of the building and is adopted as the upper limit of intensity of AC156 floor acceleration for the numerical analysis of the piping system. The procedure for the derivation of the upper limit is as follows.

$$\frac{S_{AS,84th}}{S_{DS}|_{\Delta=\Delta_{allow.}} \equiv S_{AS,16th}} = \frac{\theta_Y \cdot e^{\beta_Y}}{\theta_Y \cdot e^{-\beta_Y}} \quad \text{(EQ.1)}$$

$$S_{AS,84th} = S_{DS} \cdot e^{2\beta_Y} = e^{0.6} S_{DS} \approx 1.46 S_{DS} = 1.168g \quad \text{(EQ.2)}$$

$$(S_{AS})_{max} = \min(1.46 S_{DS}, I \cdot S_{MS}) \quad \text{(EQ.3)}$$

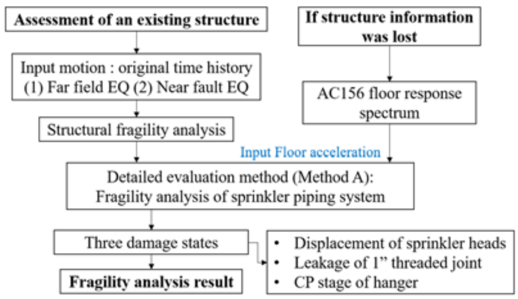

Figure 1 Procedure for fragility analysis of piping systems used in this study.

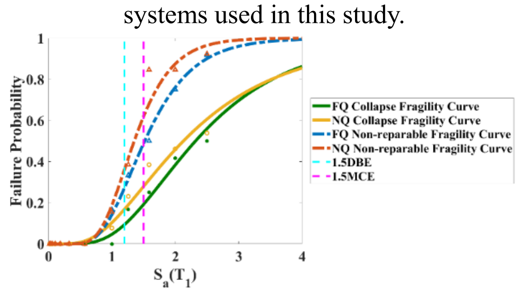

Figure 2 Non-reparable and collapse fragility of the buildings structure.

5. *Evaluation of the fragility of the sprinkler-piping system in the sample hospital:*

Following the procedure shown in Figure 1, seismic fragility functions were performed using incremental demand analysis (IDA), which is the traditional method for fragility analysis. Detailed analysis was executed at eight intensity levels for two types of floor accelerations. Considering the consequences of seismic damage to the performance and functionality of the hospitals NSCs, three failure modes with corresponding damage states to the sprinkler-piping system were defined as follows:

(a) *Broken ceiling panels*: Broken pieces and dust arising from damage to the ceiling panels may affect the medical functionality of the space below. Ceiling panels may be damaged by the impact of the sprinkler head if the resulting force applied to the ceiling panel from the sprinkler head during an earthquake exceeds the yield strength. According to the average displacement corresponding to the yield strength obtained from block-shear-loading tests, if the relative displacement of the sprinkler head and ceiling exceeds 1.66 cm it is considered to result in block shear failure of the ceiling panel caused by the adjacent sprinkler head.

(b) *Leakage*: Continuous and considerable leakage may cause malfunction to the medical equipment nearby. Based on observations of several leakage cases, caused by damaged sprinkler-piping systems, bending failure of the one-inch threaded joints is regarded as the contributing failure mode of this damage state. The capacity of the one-inch threaded joint was evaluated according to the results of numerical analysis and shaking table tests. A numerical model was established to obtain the seismic demands of the sprinkler piping using SAP 2000 software. Consistent with the shaking table test results, the most vulnerable point of the numerical model was found to be located at the threaded joint of the one-inch drop at the tee branch due to excessive flexural demand.

(c) *Regional collapse of piping*: Detachment of the suspended sprinkler piping components may hurt occupants or obstruct building egresses. Referring to the requirement for allowable deflection of the pipe between supports in ASME B31.9 [8], Equation 4 depicts scenarios of regional collapse of piping under the assumption that the damaged expansion anchors or hangers (depicted in Table 1) are no longer undertaking vertical loading.

$$
\begin{aligned}
&Hanger\begin{cases} V > V_u \\ F > F_u \\ M > M_p \text{ and } F > F_y \end{cases} \\
&\text{Expansion anchors}\begin{cases} \phi N_n \geq N_{ua} \\ \phi V_n \geq V_{ua} \\ (\frac{N_{ua}}{\phi N_n})^{\xi} + (\frac{V_{ua}}{\phi V_n})^{\xi} \leq 1 \end{cases}
\end{aligned}
\qquad \text{EQ.4}
$$

Table 1 Damage of the reginal collapse of piping.

	Case 1	Case 2	Case 3
Location of hangers reaching fully plastic moment	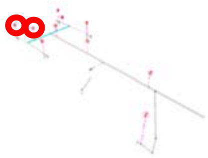	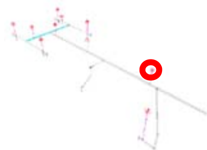	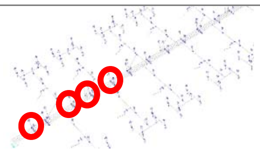 damaged adjacent hangers of the main pipe

Results of Fragility Analysis

The fragility curves of the three failure modes in terms of PGA are depicted in Figure 3. Figure 3 (a) shows the probability of damage between the ceiling and the sprinkler head. Both curves have more than a 90% probability of damage under a 0.05g scaled earthquake. Figure 3 (b) shows the fragility curves for the threaded joint, for which the FQ and NQ results are also similar. When the structure has reached the irreparable standard, even if the piping system itself is strong enough, it is still determined to be unusable. In the numerical model analysis results of this study, the hanger still has no damage under high seismic intensity. However, from the fragility curve derived for the structure, some earthquakes have caused the buildings structures to become irreparable, so the fragility curve for the collapse of piping is controlled by the structure (as shown in the Figure 3 (c)). The results show that the NQ has a greater probability of damage than the FQ. This finding occurs because the Midas software is used in this study to analyze the building cases and when inputting NQ for analysis, it may cause the analysis to not converge. This study determined that when the analysis results do not converge, the structure is destroyed, so the fragility curve of NQ has a higher probability of damage. In summary, compared with the fragility curves between the far-field and near-fault ground motions, it is found that there is little difference between the two. This findings arises because the hospital in this case is a low-rise building with a small structural period, and the spectral acceleration corresponding to the two main structural periods is theoretically similar.

Using the PGA as an engineering demand parameter, the probability of damage of the piping system at the peak ground acceleration of an earthquake can be expressed. The PGA of the AC156 is derived by dividing the PFA by the building height amplification factor (equal to 3). The fragility curves of the three failure modes is shown in Figure 4. It can be seen from Figure 4 (a) and Figure 4 (b) that the fragility curves of the ceiling and the threaded joint between the original earthquake and AC-156 have little differences. As shown in Figure 4 (c), the original fragility curve for the hanger is positioned at the right side of the AC156 curve.

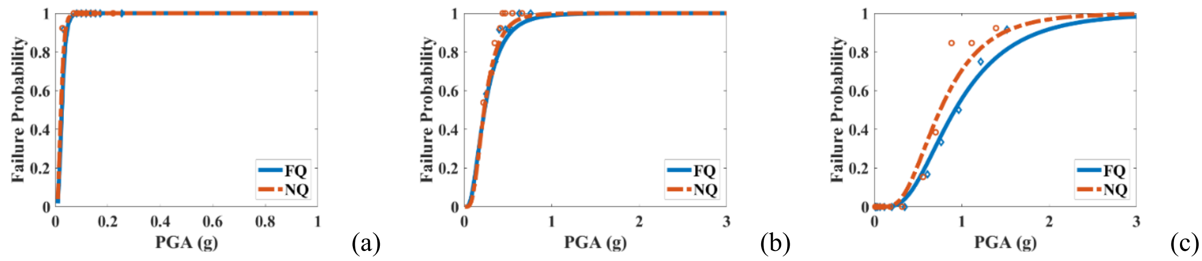

Figure 3 Comparison of the fragility curves between far-field earthquake and near-fault earthquake (a) ceiling damages; (b) leakage; (c) collapse of piping.

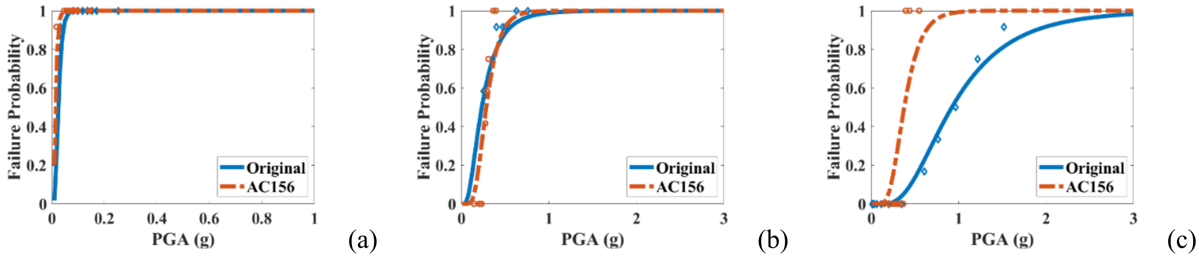

Figure 4 Comparison of the fragility curves between original earthquake and AC-156 input motion (a) ceiling damages; (b) leakage; (c) collapse of piping.

This indicates that the AC156 is a more conservative approach when compared to the original earthquake. A possible explanation is that the two motions do not cause the hanger to exceed the failure criterion. Therefore, the fragility curves of the hanger are controlled by the fragility curve of the irreparable structure. The irreparable criterion of AC156 occurs when the S_{DS} value is greater than 1.08g, at this intensity the floor response caused by the original earthquake does not necessarily destroy the hanger.

Comparing the fragility curves prepared for the far-field original earthquake and the AC156 floor response, shows that the three failure modes are different for each method. The fragility curves for the ceiling are almost the same for each of the methods, where both are conservative. Comparing the fragility curves of the threaded joints, the original earthquake method is more conservative. Whereas the fragility curves of the hanger show that the AC156 method is more conservative than that of the original earthquake method.

Conclusions

Under seismic conditions, the associated failure modes and limiting conditions have been established in order to quantify the capacity of critical NSC components. Seismic fragility curves were established for the fire sprinkler system in the sample hospital under three types of floor responses. The fragility curves of the piping were dependent on the frequency parameters of the floor acceleration. The accuracy of the numerical analysis under original ground motion conditions was verified by the real damage state of the sprinkler-piping system in the example hospital resulting from the 2010 JiaXian earthquake.

In future studies, strengthening strategies will be proposed to improve the three failure modes of the sprinkler piping systems under seismic conditions. Further numerical analysis will be conducted based upon the numerical model and methods proposed in this study. The efficiency will also be compared with the seismic design results according to NFPA13 [9].

References

Yeh CC, Simplified methodology of seismic fragility analysis on fire protection sprinkler piping systems in hospital, 2016

Applied Technology Council, Seismic Performance Assessment of Buildings, Volume 1 – Methodology, FEMA P-58-1, FEMA, Washington, D.C., 2012.

ICC Evaluation Service Inc., Seismic Certification by Shake-table Testing of Nonstructural Components, AC156, ICC-ES, CA, 2010.

Lin FR, Yeh CC, Hu PW, Chai JF and Chang KC, Fragility analysis of typical sprinkler-piping systems in hospitals, Proceedings of the 11th National Conference in Earthquake Engineering, EERI, Los Angeles, CA. 2018.

Applied Technology Council, Quantification of Building Seismic Performance Factor, FEMA P-695, FEMA, Washington, D.C., 2009.

Chang YW, Chien WY, Loh CH, Taiwan Ground-Motion Relationships for the Horizontal Component of 5%-Damped Response Spectra for Periods between 0.01s and 10.0s, Annual Congress of Chinese Geophysical Society and Geological Society of Taiwan, Taipei, 2011.

American Society of Civil Engineers (ASCE), Prestandard and commentary for the seismic rehabilitation of buildings, FEMA 356, FEMA, Washington, D.C, 2000.

American Society of Mechanical Engineers (ASME), Building Services Piping, ASME B31.9, New York, NY, 2011

National Fire Protection Association (NFPA), Standard for the Installation of Sprinkler Systems, NFPA 13, U.S, 2010.

Seismic Performance Evaluation of Strengthened Typical Sprinkler Piping Systems in Hospitals

Yung-An Tsai[1] Fan-Ru Lin[2] Juin-Fu Chai[3] and Kuo-Chun Chang[4]

Abstract

In recent years, due to the vigorous development of performance design concepts, the seismic capacity of critical building structures, such as hospitals and high-tech factories, has improved. Major disasters and economic losses caused by earthquakes have shifted from structural to non-structural systems, which include piping systems.

This study considered a medium-scale hospital in Southern Taiwan as an example for discussing the effects of installing strengthening elements recommended by NFPA 13 on sprinkler piping systems. First, this research used detailed analysis results to construct and compare the fragility curves of original and strengthened systems. Second, this study proposed a simplified assessment method of the original and strengthened systems according to the dynamic characteristics of the sprinkler piping system. It provided engineers with an alternative method that enables rapid and approximate judgment of the seismic performance of piping systems based on in situ observations and a generic floor response spectrum.

Keywords: seismic assessment procedure for nonstructural systems, sprinkler piping systems, fragility analysis, strengthened

Introduction

Based on the experience of recent earthquakes that have occurred in Taiwan, losses result is not caused by damage to the building structure, but to damage of non-structural components. For instance, piping system leakage and dust from broken ceiling boards in a hospital building caused by small earthquakes could not only compromise fire protection and medical function, but also result in the malfunction of medical equipment. The collapse of sprinkler systems could even undermine the safety of human life. In the United States, the seismic design of sprinkler piping systems is specified in the standard NFPA 13 [1]. The design concept of the NFPA 13 is to provide sufficient bracings and seismic resistant devices to avoid excessive inertia force and imposed drift ratio on sprinkler pipes. Considering the situation of engineering practice, stress analysis of pipes is avoided and only static force analysis is conducted in the NFPA 13.

Using the fire protection sprinkler system in a medium-scale hospital in Southern Taiwan as an example, this paper verified the accuracy and feasibility of seismic design guidelines proposed by the NFPA 13 in regards to the following two aspects:

1. This study proposed four strengthening schemes of piping systems based on the NFPA 13. The effectiveness of seismic strengthening works was determined by comparing the fragility curves of original and strengthened configurations of the sample piping system. The fragility curves were obtained according to detailed analysis results.

2. This study proposed a simplified assessment method of original and strengthened systems according to the dynamic characteristics of the sprinkler piping system. It provided engineers with an alternative method that enables rapid and approximate judgment in the seismic performance of sprinkler piping systems based on in situ observations and a generic floor response spectrum, such as AC156 [2].

Fragility Analysis of Sprinkler Piping System

This research proposed a fragility analysis procedure for the sprinkler piping system. First, the floor response acceleration was obtained by the floor response spectrum AC156 [2]. Second, the floor response acceleration was input to a numerical sprinkler piping system model. Finally, the fragility analysis was performed. These procedures are depicted in Fig.1.

1 Project Researcher Assistant, National Center for Research on Earthquake Engineering
2 Associate Researcher, National Center for Research on Earthquake Engineering
3 Research Fellow, National Center for Research on Earthquake Engineering
4 Professor, Dept. of Civil Engineering, National Taiwan University

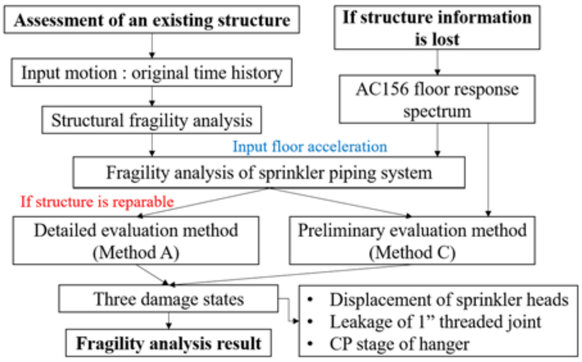

Fig.1 Flow chart of this research

Mathematical model of Fragility Function

The fragility curve of the piping system can be expressed by the cumulative distribution function under lognormal scale (Equation 1), where λ is the median of the random variable and β is the dispersion.

$$F_x(x)=\int_0^x f_x(x')dx'=\phi\left(\frac{\ln x-\lambda}{\beta}\right)=\phi\left(\frac{\ln x-\left(\frac{x}{x_m}\right)}{\beta}\right).$$

(Eq. 1)

The Federal Emergency Management Agency (FEMA) P58 [3] indicates Engineering Demand Parameters (EDPs) such as peak ground acceleration (PGA). In this study, different types of EDPs were used to investigate the sensitivity of the expression of the fragility of sprinkler piping in buildings.

Input motion - AC156 floor response spectrum

In cases where engineers are unable to obtain structural information or need to save analysis time, the artificial floor acceleration compatible with the AC156 floor response spectrum, presented in Fig. 2, can be used.

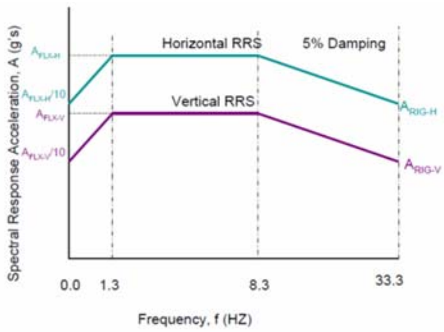

Fig. 2 AC156 floor response spectrum

Damage states

This research defined three performance points. First point was the dust from the ceiling due to the impact between the piping and ceiling. The damage state was defined as the relative displacement between the sprinkler head and the ceiling exceeding 1.66 cm according to the capacity test results. The second performance point was leakage. According to the seismic experience of sprinkler piping systems in Taiwan, leakages are usually caused by the damage of one-inch sprinkler heads. The most fragile part of one-inch sprinkler heads and pipes are the threaded joints between them. In the shaking table test conducted in previous studies, there were no sensors at the location of one-inch threaded joints; therefore, a maximum moment of 2.01 kN-m at the one-inch threaded joint from a verified numerical model was considered as the damage state in this study. The third performance point was the destruction of the hangers or the damage of the anchor bolts, both of which will lead to the collapse of piping in the entire sickrooms under a specific damage mechanism.

Detailed evaluation method

Detailed numerical analysis was performed to create fragility curves of the sprinkler piping system. To obtain input motions of the sprinkler piping system, incremental dynamic analysis (IDA) was conducted to nonlinear numerical model of the hospital structure and the floor response is the demand of the sprinkler piping system.

A. Numerical model of original sprinkler piping system

The numerical model of the sprinkler piping system of the sample hospital was established for fragility analysis using SAP2000 v.20 software. To achieve more accurate analysis results, in this study, a nonlinear spring was added between each hanger and the floor, which simulated the behavior of the hanger after the force yielded or the anchor bolt expanded. A gap link was added at the connection point of the one-inch branch pipe and the partition wall to simulate the behavior of the piping after hitting the partition wall. The free end of the sprinkler head was without a constraint to simulate the behavior between the sprinkler head and the ceiling, because the ceiling material has minimal stiffness.

B. Numerical model of strengthened sprinkler piping system

Based on the NFPA 13, this study used four cases of strengthened piping systems. First, the earthquake-resistant diagonal bracing was installed on the main pipe. The purpose was to suppress the displacement of the main pipe. The position of the main pipe bracing was calculated according to Juin-Fu Chai et al. (2015) [4], and the affected area and distribution were calculated. However, the proposal using NFPA 13 did not effectively inhibit the displacement of the sprinkler head. Therefore, three additional cases were proposed based on the NFPA 13 recommendations. The second case involved adding braces to the branch pipes adjacent to the braces for main pipes. The third case included four steel wires to each sprinkler head in addition to the above-mentioned seismic strengthening devices. In order to understand the effect of the steel wire on suppressing the displacement of the sprinkler head, the fourth case is added in this study. The fourth scheme is to add four steel wires to each sprinkler head and to add earthquake-resistant diagonal bracing on main pipe.

C. Comparison with fragility curves between original and strengthened models

As Fig. 3 shows, with EDP = $S_a(T_1)$, scheme 1 did not show much benefit in reducing the displacement of the sprinkler head. However, as the device was strengthened by more strengthening components, the probability of ceiling destruction was considerably lowered. In case 3, the displacement of the sprinkler head under the 1.08 g spectral acceleration median earthquake group still did not exceed the permissible performance point of 1.66 cm. However, the structure defined by AC156 was already irreparable, so the ceiling at 1.08 g was judged as completely destroyed. As Fig.3 (b) shows, after the main pipe bracing was installed, the probability of the threaded joint breaking was significantly lower than that of the original configuration. However, the fragility curves of the four schemes completely overlap, indicating that adding the main pipe bracing was the main reason for the reduction in the bending moment of the threaded joints. Figure 5 shows that the four fragility curves almost completely overlap under different EDPs. This is because in the original configuration, the demand of the hanger did not exceed damage criteria of the hanger. The fragility curve was controlled by the irreparable structure recommended by AC156. After adding the strengthening device, the hanger was less likely to reach the failure criteria; therefore, the strengthening devices have no substantial effect on the fragility curves of the hanger.

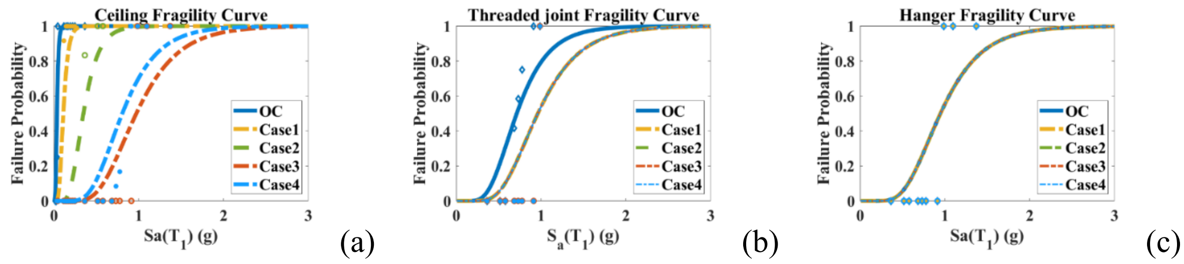

Fig.3 EDP=$S_a(T_1)$ Comparison with fragility curves of ceiling between original and strengthened schemes

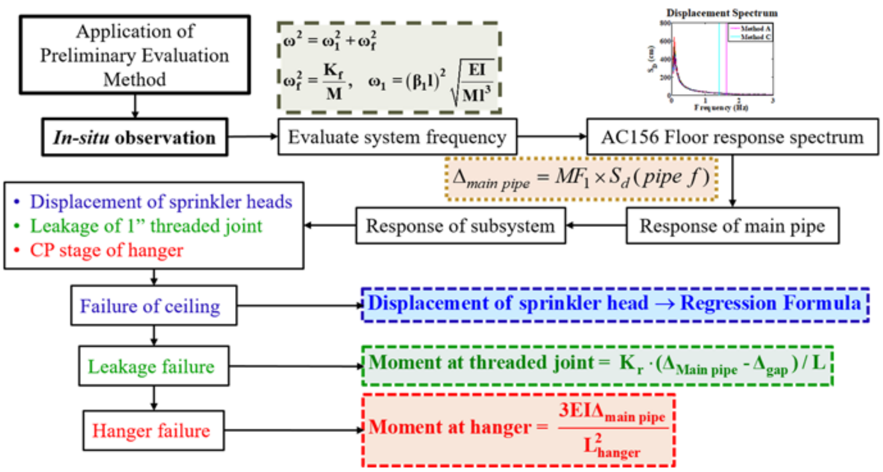

Fig.4 Flow chart of preliminary evaluation method

Preliminary evaluation method

Since detailed evaluation analysis is time-consuming and requires considerable information, the general engineer may not be able to obtain the design drawings of the piping, or there could be financial constraints in performing a complete numerical analysis. Therefore, by using a preliminary evaluation method, the engineer can predict whether the piping system components have sufficient seismic performance without conducting a complete numerical analysis. The preliminary evaluation method is shown in Fig.4. First, a site investigation was conducted to determine the length and size of the main pipe and the branch pipe as well as the number of hangers in order to estimate the frequency of the piping system. Then, the corresponding AC156 spectral displacement was obtained with the initial estimated frequency. The relationship between the AC156 spectral displacement and the main pipe displacement could be evaluated according to the results of the numerical model analysis in this study. The regression formula could be used to evaluate the maximum displacement of the main pipe. Then, a static method was used to estimate whether the piping components in the sick room had reached the damage criteria.

Comparison fragility analysis results between Detailed and preliminary evaluation method

The following is the analysis results of the original configuration:

Fig. 5(a) presents the comparison of the fragility curves of the ceiling obtained by the detailed and preliminary evaluation methods. We observed that under a small earthquake, the preliminary evaluation method yielded a higher probability of damage than the detailed evaluation method. Fig. 5(b) presents the comparison of the fragility curves of the leakage obtained by the two methods. Under an intensity of less than 2 g, a greater probability of damage was shown by the preliminary evaluation method. Fig. 5(c) presents the fragility curves of the collapse of piping obtained by the two methods. Under an intensity of less than 2.3 g, the preliminary evaluation method yielded a greater probability of destruction.

From the above results, it can be concluded that the preliminary evaluation method is more conservative. This result is in line with expectations, because the preliminary evaluation method is expected to simplify the complicated calculation, hence increasing uncertainty. Therefore, the method must be more conservative than the detailed analysis method.

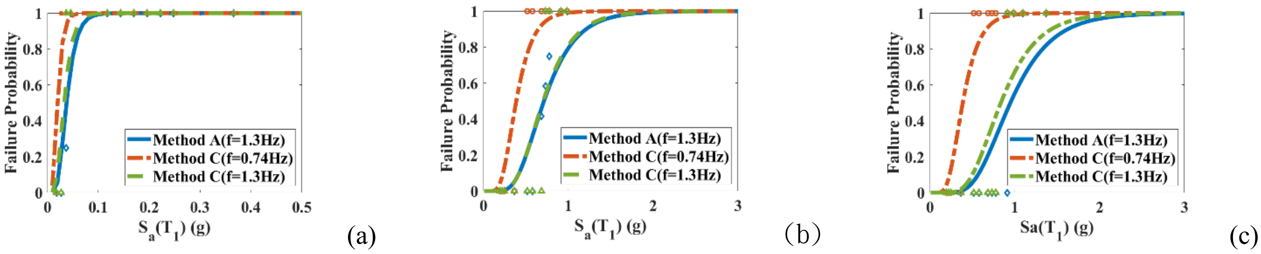

Fig.5 Fragility curves in terms of $Sa(T_{pipe})$: (a) ceiling Damages; (b)Leakage ; (c) Collapse of piping

Conclusions

This study compared the results of fragility analyses on the original configuration and four strengthened configurations. The fragility curves showed that the strengthened devices have different effects for different performance points. The main pipe bracing could effectively reduce the bending moment of threaded joints, and the steel wire could effectively reduce the displacement of the sprinkler head.

The preliminary evaluation of this study is only applicable to the original configuration of a piping system and the strengthened configuration with the addition of main pipe bracing only. The estimation of the probability of destruction is more conservative than that of the detailed analysis method. This method is expected to serve as a reference for the engineering community in the future.

References

NFPA13 - Installation of Sprinkler Systems, 2010.

Acceptance Criteria For Seismic Certification By Shake-Table Testing of Nonstructural Components AC156. 2010.

FEMA P58 - Seismic Performance Assessment of Buildings- Methodology 2012.

Juin-Fu Chai, Jemm-shin Hwang et al. ,Seismic Evaluation and S*trengthened Guidelines for Hospital Buildings 2015*

Experimental Study of Near-Fault Effects on the Sloshing Mode of Liquid in a Storage Tank – Test Results

Tzu-Chieh Chien[1], Zhen-Yu Lin[2], Zih-Yu Lai[2], Juin-Fu Chai[3] and Fan-Ru Lin[4]

簡子婕 [1] 林震宇 [2] 賴姿妤 [2] 柴駿甫 [3] 林凡茹 [4]

Abstract

This report uses the results of the "Experimental Study of Near-Fault Effects on the Sloshing Mode of Liquid in a Storage Tank - Test Plan" [1] to check the accuracy and conservation of the sloshing and impulsive modes, sloshing height, and volume of water splashing out of the tank of GIP, ACI 350-06, API 650, SPID, and other specifications for different liquid depths (H/R) under near-fault ground motion. This paper describes the test setup for measuring instruments and the experimental procedures. The analysis results are compared with code-specified values determined from industrial standards and guidelines for general seismic conditions.

Keywords: Near-fault ground motion, storage tank, sloshing mode, sloshing height.

Introduction

According to the Haroun–Housner model [2], the fluid–structure response of a flexible tank during seismic excitation consists of three principal modes: the sloshing mode (also called a convective mode), the impulsive mode (also referred to as a flexible mode), and the rigid mode. The sloshing mode shape is that each side of the water's surface vertically oscillates in turn with a relatively low frequency. The impulsive mode shape represents simultaneous motion of the fluid and surrounding tank wall with a higher frequency depending on the flexibility of the tank wall. The rigid mode represents the bottom water moving rigidly with the tank base under horizontal input motion. In order to assess the seismic demand caused by sloshing modes, the industrial standard ACI 350.3-06 [3], gives equations to evaluate the sloshing frequency of stored water in a circular tank as below:

$$T_c = \left(\frac{2\pi}{\lambda}\right)\sqrt{D} \qquad (1)$$

$$\lambda = \sqrt{3.68g \tanh\left[3.68\left(\frac{H_L}{D}\right)\right]} \qquad (2)$$

Where T_c is the natural period of the first mode of sloshing, D is the insideinternal diameter of the circular tank, and H_L is the design depth of stored water. The guidelines, ACI 350.3-06 [3] and GIP-3A [4], give an equation that can be used to estimate the sloshing height h_s respectively as:

$$h_s = IR\left(\frac{S_a}{g}\right) \qquad (3)$$

$$h_s = 0.837R\left(\frac{S_a}{g}\right) \qquad (4)$$

respectively, where I is the importance factor, R is the internal radius of the circular tank and S_a is the 0.5% damped horizontal design spectral acceleration of the ground or floor on which the tank is mounted at the frequency of the sloshing mode. It can be seen that the evaluated sloshing height is more conservative in ACI 350.3-06 [3]. Moreover, the predicted theoretical sloshing height in the SPID [5] is suggested to be increased by 20% to account for the higher sloshing modes of sloshing and nonlinear sloshing effects on upward splash movement observed during stronger shaking.

Test Configuration

Measuring Instrument

During shaking-table tests, accelerometers, action cameras (GoPro cameras), and magnetostrictive

[1] Project Assistant Researcher, National Center for Research on Earthquake Engineering
[2] Research Assistant, National Center for Research on Earthquake Engineering
[3] Research Fellow, National Center for Research on Earthquake Engineering
[4] Associate Researcher, National Center for Research on Earthquake Engineering

linear-position sensors (Temposonic transducers) were used to record the responses of tank specimens and water contents. As shown in Figure 1, three ±5 g tri-axial accelerometers depicted as black blocks were arranged on the steel bottom plate and the tops of the tank walls to the record acceleration responses of the tank specimens. The recorded acceleration data were used to determine that the tanks were rigid enough to minimize the influence of impulsive modes on the dynamic response of water. Eight displacement transducers were used for water-level sensing applications by the magnetic interaction between the floating position magnet and the sensing rod.

As shown in Figure 1 and Figure 2, a total of five action cameras were attached directly on the tops of the tank walls to record the movement of the water surface over the entire testing process. The video records were also used to observe the sloshing and wave conditions of the water surface and to ensure the accuracy of water level measurements by the transducers, which was done by watching the achieved water levels measured with attached waterproof rulers.

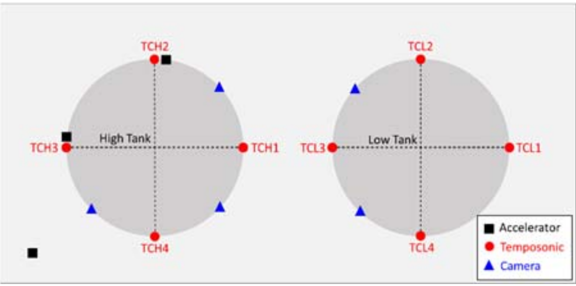

Figure 1 Instrument configuration.

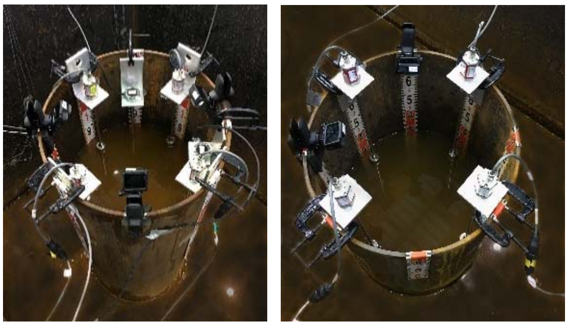

Figure 2 Actual status of sensor installation.

Test Process

During system-identification tests, different water levels were selected to verify the accuracy of Eq. (1) for sloshing frequency. As listed in Table 1, test water levels of 8 cm, 10 cm, 12 cm, 14 cm, 16 cm, 18 cm, 20 cm, 22 cm, 24 cm, 26 cm, 28 cm, 30 cm, 32 cm, 34 cm, 36 cm, 38 cm, 40 cm, 50 cm, 60 cm, and 80 cm were adopted to cover the range of gradual change and convergence of the relationship between sloshing frequency and water level (Figure 3). For each tested water level, uniaxial (Y or Z) and biaxial (Y and Z, Y and −Z) tests were arranged to observe the effects of multi-axis inputs and the direction of vertical motion on sloshing frequency and damping of water.

Table 1 Procedures for system identification.

Test name	Test direction	High tank water level (cm)	Low tank water level (cm)
CH60CL30_SINE	X/Y/Z	60	30
CH60CL30_IP	Y/Z/YZ/Y-Z		
CH08CL10_IP	Y/Z/YZ/Y-Z	8	10
CH28CL12_IP	Y/Z/YZ/Y-Z	28	12
CH32CL14_IP	Y/Z/YZ/Y-Z	32	14
CH34CL16_IP	Y/Z/YZ/Y-Z	34	16
CH36CL18_IP	Y/Z/YZ/Y-Z	36	18
CH38CL20_IP	Y/Z/YZ/Y-Z	38	20
CH40CL22_IP	Y/Z/YZ/Y-Z	40	22
CH50CL24_IP	Y/Z/YZ/Y-Z	50	24
CH80CL26_IP	Y/Z/YZ/Y-Z	80	26

* SINE:Sinewave ; IP:Impulse

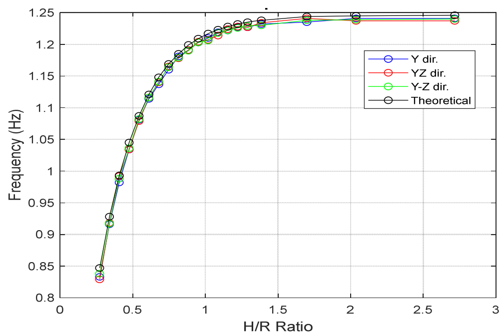

Figure 3 The relationship between sloshing frequency and H/R.

A total of 150 seismic tests were carried out in this study. Table 2 depicts the test procedures for eight ground motions selected from the PEER NGA West database. As described in a previous paper [1], the spectral acceleration at 1.2 Hz of the FN component of each ground motion was normalized to 1.0 g, and scaled down to 20%, 50%, and 75% to observe the possible nonlinear increase of sloshing height. Table 2 also shows that RSN 1529 and RSN 1550 were limited by the maximum displacement capacity of the shaking table. In addition, 100% velocity pulse (VP), residual velocity pulse (RVP), and full water (FW) tests of RSN451 and 75% velocity pulse (VP), residual velocity pulse (RVP), band pulse (BP), and residual band pulse (RBP) tests of RSN1550 were performed in this study. Uniaxial (X, Y, or Z), biaxial (X and Y), and tri-axial tests were arranged to observe the effects of multi-axis inputs on sloshing height. Only one specific X, Y, and −Z component of excitation was studied for the FW RSN451 test in order to observe the effect of the direction of vertical motion.

Table 2 Procedures of the ground-motion tests.

Test name	Test direction	Scale
RSN1051	X/Y/XY/XYZ	20%/50%/75%/100%
RSN1529	X/Y/XY/XYZ	20%/50%/75%
RSN568	X/Y/XY/XYZ	20%/50%/75%/100%

RSN1503	X/Y/XY/XYZ	20%/50%/75%/100%
RSN1050	X/Y/XY/XYZ	20%/50%/75%/100%
RSN1550	X/Y/XY/XYZ	20%/50%/75%
RSN828	X/Y/XY/XYZ	20%/50%/75%/100%
RSN451	X/Y/XY/XYZ	20%/50%/75%/100%
RSN451_VP	X/Y/XY/XYZ	100%
RSN451_RVP	X/Y/XY/XYZ	100%
RSN451_FW	X/Y/XY/XYZ/XY-Z	100%
RSN1550_VP	X/Y/XY/XYZ	75%
RSN1550_RVP	X/Y/XY/XYZ	75%
RSN1550_BP	X/Y/XY/XYZ	75%
RSN1550_RBP	X/Y/XY/XYZ	75%

Preliminary Test Results

Frequency

From the measured acceleration data for the tank specimens, the tank frequencies are between 70 and 80 Hz (Figure 4). Although the real frequencies are lower than the numerical values (Table 3), they are still much higher than the frequency content of the input motions and the sloshing frequencies of the contained water. This implies that the effect of the impulsive mode might be neglected in the analysis of the dynamic behavior of the sloshing modes. Figure 3 shows the relationship between the measured sloshing frequency and H/R. The black line is the theoretical sloshing frequency evaluated from Eqs. (3) and (4). The blue, red, and green lines depict the relationship between the measured sloshing frequency and H/R ratio under horizontal and vertical impulse motions. From Figure 3, it can be seen that the measured sloshing frequencies are quite close to but slightly higher than the theoretical values. Furthermore, it is confirmed that the effect of vertical input on the sloshing frequency is not significant.

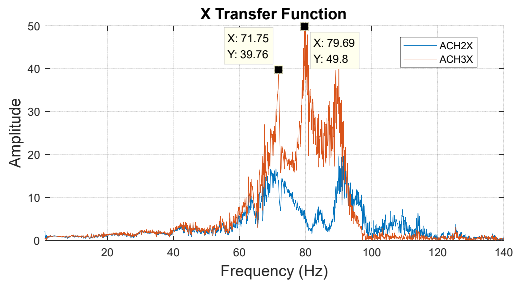

Figure 4 Analysis results for tank frequency.

Table 3 Model analysis results.

Set	Table Height (m)	Thickness (m)	Frequencies of 1st mode (Hz)
1	0.5	0.0103	364.96
	1	0.0103	181.28
2	0.7	0.0103	272.16
	1.2	0.0103	141.16

Damping

According to the GIP 3A [4] Section 7, the convective response damping ratio of the vertical tank is 0.5%. In order to verify the damping ratio, in this test, the Temposonic measurement values are used to calculate the results of the impulse test.

Assume the internal water of the tank has only a single degree of freedom. By using the logarithmic decrement method to calculate the free oscillation results of the impulse test, the damping ratio of the internal water can be obtained. The formula is as follows:

$$\delta = \frac{1}{n}\left|\frac{X_1}{X_{n+1}}\right| \quad (5)$$

$$\xi = \frac{\delta}{\sqrt{4\pi^2 + \delta^2}} \quad (6)$$

where,

X_1 : the first amplitude,
X_{n+1} : the n+1th amplitude,
n : number of cycles,
δ : logarithmic decrement,
ξ : damping ratio,

Figure 5 shows the displacement time-history results of the impulse test. The blue line represents the amplitude of the shaking table and the red line represents the amplitude of the internal water. The damping ratio is calculated using the amplitude values at 10 s, 20 s, and 30 s after the peak amplitude of the shaking table. The negative amplitudes (water sloshing upwards) of the TCH2, TCH4, TCL2, and TCL4 tests are used. Finally, the relationships between damping ratio and water levels for the three different directions are shown in Figure 6.

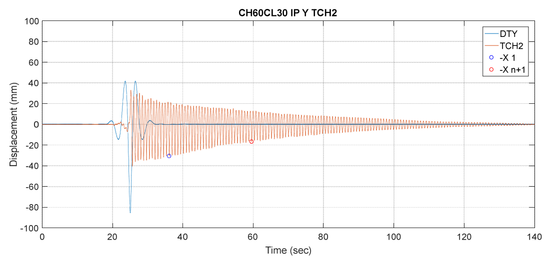

Figure 5 Water amplitude results of the impulse test (CH60CL30_IP_Y_TCH2).

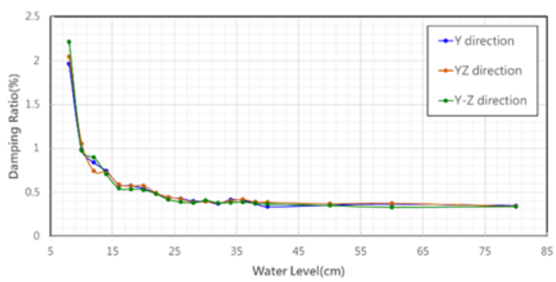

Figure 6 Relationship between water level and damping ratio.

It can be seen from Figure 6 that the damping ratio has no correlation with the direction of the earthquake, but it is inversely proportional to the water level. The final damping ratio is approximately 0.4%, which is smaller than that specified in GIP 3A [4].

Sloshing High

The test results for a single component of the excitation are plotted in Figure 7 (VP, RVP, BP, and RBP were exclusive). The X-axis shows the spectral acceleration of the shaking table at frequencies corresponding to water levels of 30 cm and 60 cm. The Y-axis shows the sloshing height. The theoretical response damping ratio in the specifications is 0.5%, but the conclusion from the above section shows that the real damping ratio is approximately 0.4%, so spectral accelerations using 0.5% and 0.4% damping ratios are plotted in Figure 7. Compared to the theoretical values from SPID [5], GIP 3A [4], and ACI350.3-06 [3], the sloshing height using a 0.4% damping ratio is closer to the theoretical value than that using a 0.5% damping ratio, but it is still evident that the sloshing height from the experiments is much higher than the theoretical value.

Conclusions

The purpose of this experiment is to estimate the slosh height and the associated total volume of water splashing out of the tank under near-fault ground motions. Eight near-fault ground motions are picked out to to determine the relationship between the resonant response and the input velocity pulse, and a total of 150 seismic tests were executed. On the other hand, the validity of evaluation method for the frequency and sloshing height and designated damping ratio value of sloshing mode provide by SPID [5], GIP 3A [4] and ACI350.3-06 [3] are discussed based on the results of system identification tests. From preliminary test results, it can be seen that the evaluation of convective frequency is quite accurate under free vibration. However, the observed damping ratio decreased dramatically while the water level is smaller than 15 cm. The value of damping ratio is converged to about 0.4%, which is smaller than the value of 0.5% specified in GIP 3A [4]. On the other hand, the sloshing height exceeds predicted values significantly while the spectral acceleration larger than 0.5g. Thus, the evaluation method for sloshing height proposed by Housner [2] is recommended to be used under limited-scale earthquakesThe purpose of this experiment was to estimate the sloshing height and the associated total volume of water splashing out of the tank under near-fault ground motions. Eight near-fault ground motions were selected to determine the relationship between the resonant response and the input velocity pulse, and a total of 150 seismic tests were performed. The validity of the evaluation methods for the frequency, sloshing height, and the damping ratio of the sloshing mode provide by SPID [5], GIP 3A [4], and ACI350.3-06 [3] were discussed based on the results of system identification tests. From preliminary test results, it can be seen that the evaluation of the convective frequency is quite accurate under free vibration. However, the observed damping ratio decreased dramatically when the water level was less than 15 cm. The damping ratio converged to approximately 0.4%, which is smaller than the value of 0.5% specified in GIP 3A [4]. The sloshing height significantly exceeded the predicted values while the spectral acceleration was larger than 0.5 g. Thus, the evaluation method for sloshing height proposed by Housner [2] is recommended to be used under limited-scale earthquakes.

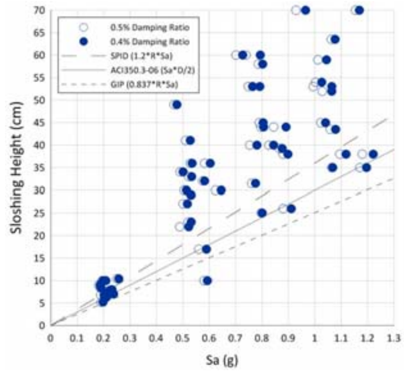

(a)

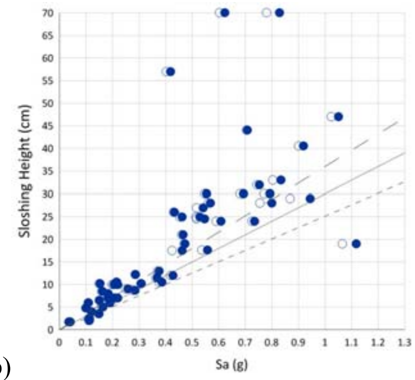

(b)

Figure 7 Sloshing response to a specific spectral acceleration in the (a) X and (b) Y directions

References

Hsu W.H. & Lin F.R. & Chai J.F. Experimental Study of Near-Fault Effect on Sloshing Mode of Storage Liquid in Tank – Test Plan, NCREE, 2019.

Haroun, M.A. & Housner, G.W. Seismic design of liquid-storage tanks, Journal of the Technical Councils of the American Society of Civil Engineers, Vol. 107, No. TCI, pp. 191-207, 1981

ACI Committee 350.3-06, Seismic Design of Liquid-Containing Concrete Structures and Commentary, American Concrete Institute, Farmington Hills, MI, 2010.

GIP, Rev. 3A, Generic Implementation Procedure for Seismic Verification of Nuclear Plant Equipment, SQUG, 2001.

EPRI, Seismic Evaluation Guidance- Screening, Prioritization, and Implementation Details for the Resolution of Fukushima Near-Term Task Force Recommendation 2.1: Seismic, EPRI Report 1025287, 2013.

Performance Identification of the Bi-Axial Dynamic Testing System

Wang-Chuen Lin[1], Chiung-Lin Liu[2], Cho-Yen Yang[3], Chung-Han Yu[4], Shiang-Jung Wang[5] and Jenn-Shin Hwang[6]

林旺春 [1]、劉瓊琳 [2]、楊卓諺 [3]、游忠翰 [4]、汪向榮 [5]、黃震興 [6]

Abstract

The bi-axial dynamic testing system (BATS) was established in the Tainan Laboratory of the National Center for Research and Earthquake Engineering (NCREE) in 2017. It is presently one of the few advanced large-scale testing machines that possess dynamic compression and shear testing capabilities. It is globally beneficial for not only research and development of seismic isolation technology but also for performing prototype and production tests on full-scale seismic isolators. Identifying its essential parameters, including the effective mass and friction coefficients, and its dynamic performance in an explicit manner is imperative before it can service the public. Therefore, a series of tests, including triangle wave cyclic loading tests with varied horizontal displacements and velocities as well as sin wave cyclic loading tests with varied horizontal displacements and excitation frequencies, were conducted to clearly understand the crucial parameters and dynamic performance of the BATS. Three stages with different test conditions and specimens were schemed as follows: (1) Triangle wave and sin wave cyclic loading tests on the bare testing system without applying any compression load were performed to identify the relation between horizontal velocities and average friction coefficients as well as the effective mass of the BATS; (2) Triangle wave and sin wave cyclic loading tests on flat sliding bearings under different vertical compression loads were performed, and a simple linear regression method was adopted to identify the average friction coefficients of the BATS at different horizontal velocities; (3) Through comparing the identification results with the test results of full-scale friction pendulum bearings and further discussions, the rationality and applicability of the identified effective mass and average friction coefficients of the BATS can be further demonstrated.

Keywords: bi-axial dynamic testing system; essential parameter; dynamic performance;

Introduction

Seismic isolation technology has been regarded as one of the most effective strategies to enhance the safety and functionality of buildings, infrastructures, and equipment. The bi-axial dynamic testing system (BATS) was designed and established in the Tainan Laboratory of the National Center for Research and Earthquake Engineering (NCREE) in 2017. The major mission of the BATS is to serve academia to develop seismic isolation technology and industry to perform prototype and production tests on full-scale seismic isolators. As shown in Figure 1, the BATS consists of a reaction frame, platform, foundation, and servo-hydraulic actuators. Four dynamic servo-hydraulic actuators whose maximum force capacity is 2 MN are installed and connected between the platform and foundation in the horizontal direction. One static servo-hydraulic actuator with a maximum force capacity of

[1] Associate Researcher, National Center for Research on Earthquake Engineering
[2] Research Assistant, National Center for Research on Earthquake Engineering
[3] Assistant Researcher, National Center for Research on Earthquake Engineering
[4] Assistant Researcher, National Center for Research on Earthquake Engineering
[5] Division Head, National Center for Research on Earthquake Engineering
[6] Courtesy Researcher, National Center for Research on Earthquake Engineering

30 MN and six dynamic servo-hydraulic actuators with a maximum force capacity of 5 MN are mounted on the foundation to support the platform in the vertical direction. The maximum longitudinal stroke, velocity, and force capacity of the BATS are ±1.2 m, ±1 m/s, and ±4 MN, respectively. The maximum vertical stroke and velocity are ±75 mm and ±150 mm/s, correspondingly. A maximum vertical compressive force of 60 MN, which includes a dynamic force of 30 MN and a static force of 30 MN, can be achieved. Before its service can be provided to the public essential parameters, including the effective mass and friction coefficients, must be identified. Therefore, a series of tests, including triangle wave cyclic loading tests with varied horizontal displacements and velocities and sin wave cyclic loading tests with varied horizontal displacements and excitation frequencies, were conducted. A comparison of the identification results with the test results are discussed to validate its rationality and applicability.

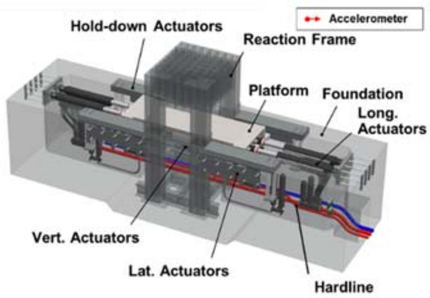

Figure 1. Bi-axial dynamic testing system

Research Method

Under the isolation bearings performed in the BATS, the dynamic equilibrium equation can be described in accordance to the free-body diagram of the platform (see Figure 2).

$$P(t) = F_B(t) + F_I(t) + F_F(t) \quad (1)$$

where, $P(t)$ is the horizontal force of the actuators; $F_B(t)$ is the horizontal force of the isolation bearing; $F_I(t)$ is the inertial force of the platform; $F_F(t)$ is the friction force of the platform. Additionally, $F_B(t)$, $F_I(t)$ and $F_F(t)$ are respectively given by:

$$F_B(t) = \mu_B(t) N_B \operatorname{sgn}(\dot{x}(t)) \quad (2)$$

$$F_F(t) = \mu(t) N \operatorname{sgn}(\dot{x}(t)) \quad (3)$$

$$F_I(t) = m_{eff}\, \ddot{x}(t) \quad (4)$$

where, $\mu(t)$ is the friction coefficient of the platform; N is the total normal force applied to the platform from self-weight, the load of the vertical actuators, the load of the lateral actuators, and the load of the hold-down actuators; m_{eff} is the effective mass of the platform; $\dot{x}(t)$ and $\ddot{x}(t)$ are the velocity and acceleration of the platform, respectively. Assuming that the isolation bearing is a friction pendulum bearing, $\mu_B(t)$ and N_B are the friction coefficients of the bearing and the vertical force of the bearing in Equation (2), respectively.

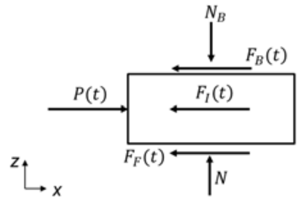

Figure 2. The free-body diagram of the platform

(a) Triangle wave cyclic loading tests on the bare testing system

Because the motion of the platform is a constant velocity and the isolation bearing is not installed on the platform, the acceleration of the platform is assumed as zero, i.e. $F_I = 0$ and $F_B = 0$. The total normal force applied to the platform is from a combination of the self-weight, the load of the lateral actuators, and the load of the hold-down actuators, i.e. $N{=}N_0$. The dynamic equilibrium equation is given below:

$$P(t) = F_F(t) {=} \mu_0(t) N_0 \operatorname{sgn}(\dot{x}(t)) \quad (5)$$

where, $\mu_0(t)$ is the friction coefficient of the platform without applying any compression load.

The average friction coefficient of the platform, ($\mu_{0,avg}$) can be calculated according to the result of the friction coefficient of the platform ($\mu_0(t)$) at time t divided by the total number of time steps. Furthermore, the relation between the horizontal velocities and the average friction coefficients can be obtained using a simple linear regression method as shown below:

$$\mu_{0,avg} = a_1 \left|\dot{x}\right| {+} a_2 \quad (6)$$

where, a_1 and a_2 are identified parameters adopted by a simple linear regression method.

(b) Sin wave cyclic loading tests on the bare testing system

Because the acceleration of the platform does not remain at zero, the friction force of the platform can be represented as the following:

$$F_F(t) = P(t) - m_{eff}\, \ddot{x}(t) \quad (7)$$

Based on Equations (3) and (6), the friction force of the platform can also be obtained using the following:

$$F_F'(t) = \mu_{0,avg}(t) N \operatorname{sgn}(\dot{x}(t)) \quad (8)$$

If the friction force of the platform is obtained by assuming Equation (7) is equal to Equation (8), the effective mass of the platform can be identified using a simple linear regression method as below:

$$m_{eff} = \sum_{t=1}^{n} \frac{P(t)\ddot{x}(t) - \mu_{0,avg}(t) N \operatorname{sgn}(\dot{x}(t)) \ddot{x}(t)}{\left(\ddot{x}(t)\right)^2} \quad (9)$$

Additionally, the average effective mass of the platform ($m_{eff,avg}$) can be calculated using varied horizontal displacements and excitation frequencies.

(c) Triangle wave cyclic loading tests on the flat sliding bearings

Based on triangle wave cyclic loading tests on flat sliding bearings under different vertical compression loads, Equation (1) can be represented as the following:

$$P(t) = F_B(t) + F_F(t) \tag{10}$$

Substituting Equations (2) and (3) into Equation (10) as well as $N{=}N_0{+}N_B$, the friction coefficient of the bearing can be obtained at the horizontal displacement and velocity as follows:

$$\mu_B(t){=}\frac{\left|P(t)-\mu(t)N\,\mathrm{sgn}(\dot{x}(t))\right|}{N_B} \tag{11}$$

Therefore, the average friction coefficient of the bearing can be calculated at the horizontal displacement and velocity as shown below:

$$\mu_{B,avg} = \frac{\sum_{t=1}^{n}\mu_B(t)}{n} \tag{12}$$

(d) Sin wave cyclic loading tests on the flat sliding bearings

Assuming that the maximum velocity and displacement under sin wave cyclic loading tests are equal to the triangle wave cyclic loading tests, i.e. $\mu_B(t){=}\mu_{B,avg}$ and $m_{eff}{=}m_{eff,avg}$, Equation (1) can be represented as below:

$$\mu(t) = \frac{\left|P(t)-[\mu_{B,avg}N_B\,\mathrm{sgn}(\dot{x}(t))+m_{eff,avg}\ddot{x}(t)]\right|}{N_0{+}N_B} \tag{13}$$

Additionally, the sum of the maximum and minimum velocity at the time t_k is p in total. The average friction coefficient of the platform (μ_{avg}) can be obtained at the horizontal displacement and velocity as shown below:

$$\mu_{avg}{=}\frac{\sum_{k=1}^{p}\mu(t_k)}{p} \tag{14}$$

Therefore, assuming that the average friction coefficient of the platform ($\mu_{0,avg}$) is substituted from Equation (6) into Equation (11) in the first iteration by adopting an iterative method, the average friction coefficient of the platform can be calculated using Equations (11) to (14). Finally, considering the friction coefficient of the platform with different horizontal velocities, the relation between the horizontal velocities and the average friction coefficients under different vertical compression loads can be obtained using a simple linear regression method as shown below:

$$\mu_{avg} = b_1\left|\dot{x}\right|{+}b_2 \tag{15}$$

where, b_1 and b_2 are the identified parameters adopted by a simple linear regression method.

Test Results

In this study, the diameter and the maximum compressive stress of the bearing material of the flat sliding bearing are 1130 mm and 4 kg/mm^2, respectively. The test setup is illustrated in Figure 3. As shown in Tables 1 and 2, the compression loads are 10 MN and 30 MN under triangle wave cyclic loading tests with varied horizontal displacements and velocities and sin wave cyclic loading tests with varied horizontal displacements and excitation frequencies, respectively. The relation between the horizontal velocities and the average friction coefficients on the bare testing system can be obtained with N_0 equal to 11889.72kN as shown below:

$$\mu_{0,avg} = 3\times10^{-6}\left|\dot{x}\right|{+}0.0008 \tag{16}$$

Based on Equation (16), the average effective mass of the platform ($m_{eff,avg}$) was found to be 96.69 ton.

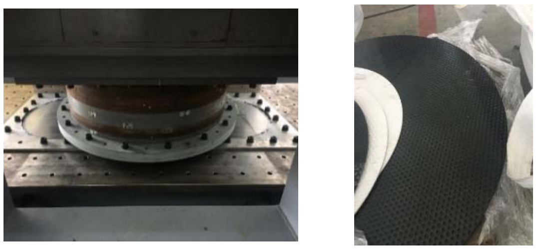

(a) Test setup (b) friction material

Figure 3. Test setup and friction material

Table 1. Test protocols without applying any compression load

	Displacement amplitude (mm)	Loading rate (mm/s)	Number of cycles
Triangular wave	300	200、300 400、500 600	4
	500		
	700		
	900		
	1000		
Sinusoidal wave	300	100、200 300、400 500、600	4
	400		
	500		
	700		
	900		

Table 2. Test protocols with applying compression load

Compression load (MN)	Displacement amplitude (mm)	Loading rate (mm/s)	Number of cycles
10	100	50、100 500、800	3
	700		
	1000		
30	300	50、100 300、800	3
	700		

The relation between the horizontal velocities and the average friction coefficients under a vertical compression load of 10 MN and 30 MN, respectively, are identified as follows:

$$\mu_{avg} = 3\times10^{-6}\left|\dot{x}\right|{+}0.0003 \tag{17}$$

$$\mu_{avg} = 3\times10^{-7}\left|\dot{x}\right|{+}0.0002 \tag{18}$$

Figure 4 shows that the relation between the horizontal velocities and the average friction coefficients, without applying any compression load, is larger than other identified results with a vertical compression load. The larger the vertical compression load is, the more significantly the average friction coefficient of the platform decreases. Therefore, the relation between the horizontal velocities and the average friction coefficients are obtained by using a linear interpolation method when the vertical compression load is between 0 MN to 10 MN and 10 MN to 30 MN in this research, respectively.

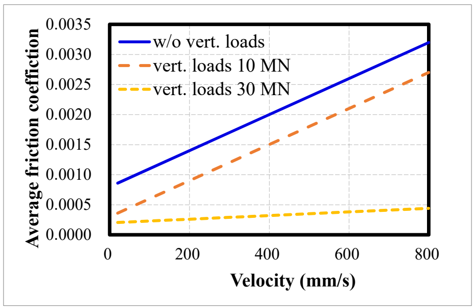

Figure 4. The average friction coefficients of BATS

Experimental Verification and Discussions

As shown in Figure 5, the full-scale double concave friction pendulum bearing dynamic tests were performed to demonstrate the rationality and applicability of the identified effective mass and average friction coefficients of the BATS. Additionally, the diameter and radius of the curvature of the bearing material are 400 mm and 4500 mm, respectively. The normal friction coefficient is 0.043. The testing items are listed in Table 3.

Figure 5. The installation of specimen

Table 3. Test protocols of full-scale friction pendulum bearing

test	Compression load (kN)	Displacement amplitude (mm)	Loading rate (mm/s)	Number of cycles
1	5027	200	20	3
2	5027	200	20	3

The friction coefficient (μ^i) of this bearing at the ith cycle is calculated as follows [CEN, 2009]:

$$\mu^i = \frac{E_d^i}{2N_{\mathrm{B}}(d_i^+ - d_i^-)} \tag{19}$$

where, d_i^+ and d_i^- are the maximum and minimum displacements at the ith cycle of lateral loading, respectively; E_d^i is the enclosed hysteresis loop area at the ith cycle. The theoretical hysteresis loop is defined by previous research [Fenz and Constantinou, 2006], while the tested ones are obtained by Equation (1) and the identified essential parameters in Figure 6. The results revealed that the hysteresis characteristics of the tested loops are consistent with the theoretical loop with two different testing velocities. The average friction coefficients of the bearing are calculated as 0.0409 and 0.0424 by Equation (19) and are also consistent with the normal friction coefficients, as shown in Table 4.

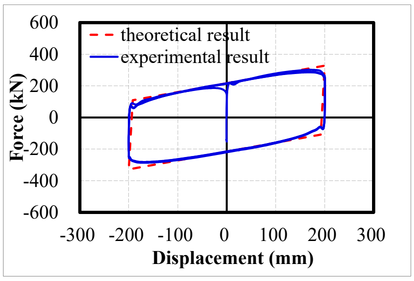

(a) hysteresis loop (20 mm/s)

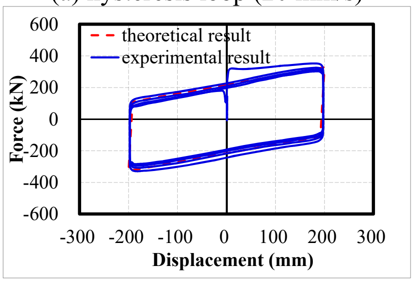

(b) hysteresis loop (400 mm/s)

Figure 6. Loading test results

Table 4. Friction coefficient

Number of cycles	Test 1 Friction coefficient	Test 2 Friction coefficient
1	0.0412	0.0457
2	0.0408	0.0420
3	0.0407	0.0395
average	0.0409	0.0424

Conclusions

In this study, a series of tests, including triangle wave cyclic loading tests with varied horizontal displacements and velocities as well as sin wave cyclic loading tests with varied horizontal displacements and excitation frequencies, were conducted to identify the essential parameters of the BATS. According to the tests performed without applying any compression load and under a vertical compression load of 10 MN and 30 MN, the average effective mass and the relation between horizontal velocities and average friction coefficients of the BATS were obtained using a simple linear regression method and the iterative method. Finally, comparing the identification results with the test results of the full-scale friction pendulum bearings, the rationality and applicability of the identified effective mass and average friction coefficients of the BATS can be further demonstrated.

References

Daniel M. Fenz, and Michael, C. Constantinou. Behavior of the double concave friction pendulum bearing. Earthquake Engineering and Structural Dynamics; 35, 1403–1424, 2006.

European Committee for Standardization (CEN), EN 15129:2009 - Anti-seismic devices, CEN, November, 2009.

Study on the Actual Responses of Seismically Isolated Structures in the Hualien TzuChi Medical Center

Chung-Han Yu[1], Shiang-Jung Wang[2] Cho-Yen Yang[1] Wang-Chuen Lin[3] Kuo-Chun Chang[4]

游忠翰[1]、汪向榮[2]、楊卓諺[1]、林旺春[3]、張國鎮[4]

Abstract

The HeXin Building, which is one of the hospital buildings in the TzuChi Medical Center located in Hualien City, is designed as a seismically base-isolated building. This structure was completed in February 2005 and is installed with real-time monitoring systems to measure its structural responses. Four representative and significant earthquakes that struck the HeXin Building on April 30th, 2005, December 19th, 2009, October 31st, 2013, and February 6th, 2018, are measured and discussed in this study. Owing to a mere 2 km distance from the Milun Fault, most of earthquakes measured near the HeXin Building feature the near-fault phenomenon. The reconnaissance and monitoring results are first exhibited in this study, and then a numerical model is established according to the system identification results from the measurement data of the 2009 earthquake. The accuracy of this model is verified through dynamic time history analysis of the other earthquakes mentioned above. Then, the displacement responses of the isolation system are compared through numerical analysis to two identical design-response-spectrum-compatible ground motions that originated from earthquake records with and without near fault phenomenon. The results show that even though these two input ground motions possess similar response spectra, the near-fault phenomenon still caused an isolation displacement of 64% more than one without the phenomenon. Therefore, it is noteworthy for designers to consider any earthquake record with near-fault phenomenon near the site to ensure a conservative design.

Keywords: base isolation, near fault phenomenon, structural monitoring, actual seismic response of structure

Introduction

Near-fault ground motions possess impulsive high-velocity waves and significant acceleration in the middle to long period of the response spectrum. This phenomenon often imposes an additional seismic hazard on structures with longer natural periods, such as high-rise buildings and seismically isolated structures. Through monitoring data and numerical analysis, this study addresses the problems and challenges for seismically isolated structures when they face near-fault ground motions.

Introduction of the Seismically Isolated Structure: HeXin Building

The Hualien TzuChi Medical Center is one of the most important medical institutions in the east of Taiwan. The medical center comprises four buildings completed in different years, and the HeXin Building is the most recently built. Its facilities include operating rooms, emergency rooms, intensive care units, and wards. The HeXin Building, which is a steel-reinforced concrete structure, is designed as a seismically base-isolated building with an eleven-story height and one basement. The isolation system is composed of lead rubber bearings (LRBs) with various specifications and sliding bearings. The well-arrangement of the bearings makes consistence of the mass center of the superstructure and the rigidity center of the isolation system and prevents additional torsional behavior during earthquakes.

The HeXin Building was installed with a structural monitoring system, as shown in Figure 1, which includes 26 accelerometers and 4 displacement transducers. The accelerometers are installed at the center and corners of specific floors and measure both

[1] Assistant Researcher, National Center for Research on Earthquake Engineering
[2] Division Head, National Center for Research on Earthquake Engineering
[3] Associate Researcher, National Center for Research on Earthquake Engineering
[4] Professor, National Taiwan University

the responses in the longitudinal and transverse directions. On the other hand, the displacement transducers are installed across the isolation interface, between the basement floor and foundation layer, at the center and corners, to monitor the isolation displacement in both horizontal directions.

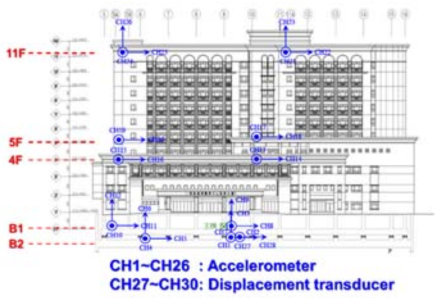

(a) Front view

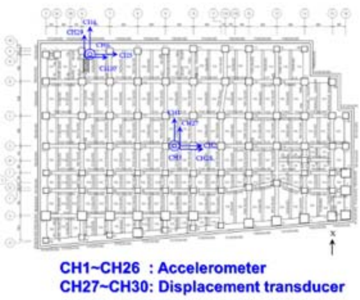

(b) Plan view

Figure 1. The structural monitoring system

Seismic Reconnaissance

One earthquake with a Richter magnitude of 6.9 struck Hualien City and caused intensity five on the Modified Mercalli Intensity Scale on Dec. 19, 2009. The epicenter was located at a depth of 43.8 km about 21.4 km southeast of the Hualien City seismic station. After the earthquake, there was no structural damage, or damage to the non-structural components or facilities. Merely slight damage occurred on the paving across the isolation gap, as shown in Figure 2.

Figure 2. Paving damage in the Dec. 19, 2009, event

On Feb. 6, 2018, another earthquake with a Richter magnitude of 6.0 hit Hualien City and caused an intensity scale seven. The epicenter was located merely 5.3 km deep and about 18.3 km northeast of the Hualien County Government. This earthquake led to the dislocation of Milun Fault, which is only 2 km from the TzuChi Medical Center. There was still no damage to the structure or facilities of the seismically isolated building. Merely some damage occurred to the paving and non-essential piping system, as shown in Figure 3. However, all the displacement transducers were broken owing to a large isolation displacement and improper measurement design, photographed in Figure 4.

Figure 3. Paving and non-essential piping damages

Figure 4. The damage of displacement transducer

Actual Structural Acceleration Responses

From the acceleration measurement results of the structure in the longitudinal direction, as shown in Figure 5, the near-fault ground motion phenomenon and the upward transmission of the excitation with an enlarged period, owing to the function of the isolation system, along the structure floors was observed. According to the acceleration response at corner of basement floor (B1F, red line), which is the top floor of the isolation system, few spikes occurred at the peak of the long period waves. The main reason might be the impact and damage of the paving and components that cross the isolation gap during the functioning of the isolation system. However, the impact phenomenon, which did not transmit into the center of the floor and upward stories, verified in Figure 5, did not affect the dynamic behavior of the entire structure.

In order to more comprehensively discuss the seismic response of this structure, in addition to the monitoring data from earthquakes that occurred in 2009 and 2018 mentioned above, this study considers two other representative ground motions that resulted in the intensity scale of five in Hualien City. These two earthquakes occurred on Apr. 30, 2005, and Oct. 13, 2015; the depth of epicenter and Richter magnitude of the first earthquake were 8.5 km and 5.6, respectively; and 15 km and 6.4, respectively, for the latter earthquake. Taking the measurement result of the accelerometer installed on the foundation layer (B2F) as input ground motion, the response spectra, scaled to an effective peak acceleration (EPA) equaling 1 g, of these four ground motions in the longitudinal direction are shown in Figure 6. Compared to the design spectrum of the seismic code, which is also scaled to the same level, it can be observed that except for the 2005 earthquake, the other three cases exhibit near-fault phenomenon seen as the much larger spectrum acceleration over the design spectrum in the middle to long period.

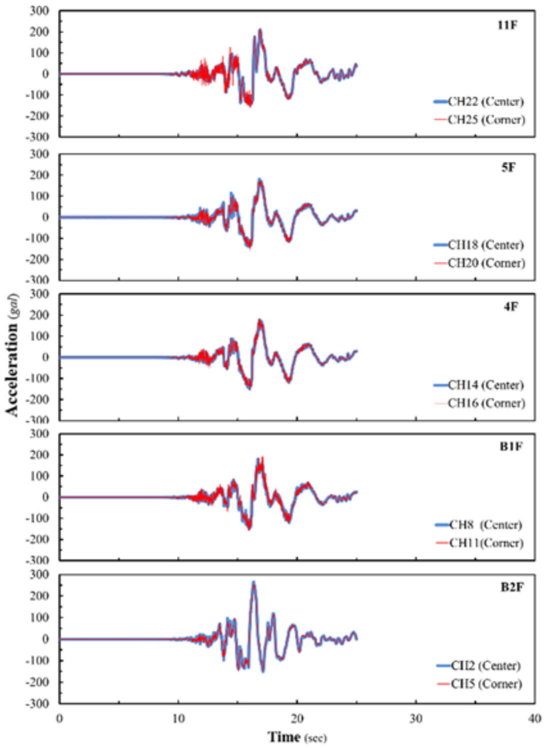

Figure 5. Longitudinal Acceleration Responses under 2018 Earthquake

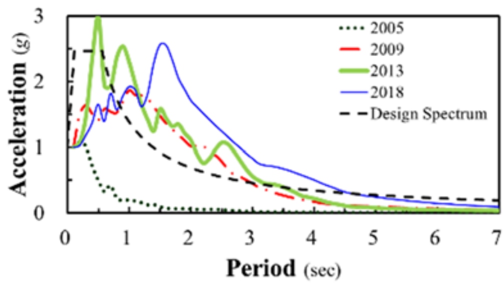

Figure 6. Comparison of normalized spectrum

The maximum longitudinal acceleration of each specific floor and their ratios to the input (B2F) are listed in Table 1. The influence of the near-fault ground motion can be observed by comparing the 2005 and 2009 earthquakes. The maximum input accelerations of these two cases are similar. However, the near-fault phenomenon of the 2009 earthquake induces larger responses. On the other hand, the ratios of maximum acceleration of the top floor to the input decreases with the increasing excitation scale. This evidence verifies the function of the isolation system.

Table 1. Maximum acceleration and their ratios to the foundation layer (B2F)

	Floor	2018	2013	2009	2005
Acceleration (gal)	11F	209	92	102	79
	5F	182	54	64	56
	4F	178	50	62	49
	B1F	181	52	71	38
	B2F	266	80	104	103
Ratio	11F / B2F	79%	115%	98%	76%
	5F / B2F	68%	68%	62%	54%
	4F / B2F	67%	63%	60%	48%
	B1F / B2F	68%	66%	69%	37%

Isolation Displacements

The isolation displacement records for the 2018 earthquake are not available because of the damage to the displacement transducers. Therefore, in this study, a numerical model was established and modified according to the structural identification results from the monitoring data of the 2009 earthquake to help predict the displacement responses, as shown in Figure 7. The non-structural partition wall and external wall were appropriately considered to adjust the stiffness and model behavior of the superstructure. The model was verified by the other three cases. For example, as illustrated in Figure 8, the prediction results not only fit the actual response of the isolation system (B1F), but also the actual response of the top floor (11F) to the 2018 earthquake. This indicates that the numerical model matches the real structure of both the isolation system and superstructure, even if the structure is struck by 2.5 times larger near-fault ground motion.

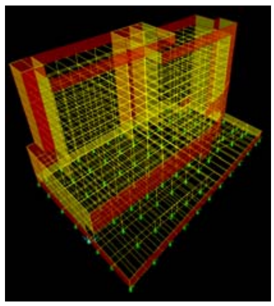

Figure 7. The numerical model of HeXin Building

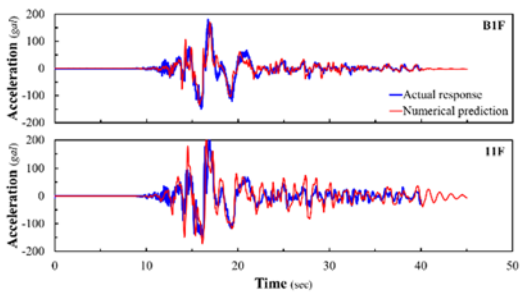

Figure 8. The comparisons between actual response and numerical prediction under 2018 earthquake

Through numerical analysis, the displacement response of the isolation system to the 2018 earthquake is illustrated in Figure 9. The maximum displacements correspond to the actual record of the pushed distance of the sounding flower nursery, which is contacted by part of the extended paving. Figure 9 points out that the maximum longitudinal displacement is 285 mm, which corresponds to a peak ground acceleration of 266 gal. However, according to the original design, the maximum isolation displacement is 240 mm, at a corresponding effective peak acceleration of 330 gal. The isolation displacement reaches the target value under only 80% of the design requirement, which verifies that additional isolation displacement is induced by the near-fault ground motion.

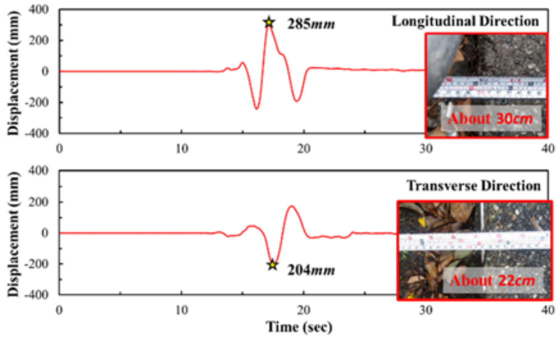

Figure 9 Isolation displacements and their comparisons to the actual surface record

In order to further compare the influence of near-fault ground motions, two design-spectrum-matched input ground motions are adopted for numerical analysis to observe the displacement response of the isolation system. These two ground motions were chosen as the 2005 earthquake, which is not a near-fault ground motion, and 2018 earthquake, which is a near-fault ground motion, as illustrated in Figure 10.

The analysis results are plotted in Figure 11. It was found that the maximum isolation displacement of the analysis case with the spectrum-matched 2005 input ground motion was 16.74 cm; in contrast, the value for the other case is 27.40 cm, which is 64% larger than the former one. This result reveals that even if one near-fault ground motion is scaled to match a design spectrum without significant increase in the middle to long period, the seismically isolated structure will still be affected by the original property of input ground motion and will exhibit a large isolation displacement.

Conclusions

According to the actual response and numerical analysis of seismically isolated structures under near-fault ground motions, although the seismic isolation system can efficiently mitigate the structural response, the near-fault ground motion will induce additional displacement of the isolation system. On the other hand, in the dynamic time history analysis procedure, even if the time history record is scaled to match a design spectrum, the property of near-fault phenomenon will still cause significant isolation displacement. Therefore, for a seismically isolated structure located in a near-fault area, or close to any active fault, the historic neighboring near-fault ground motion should be considered to guarantee conservative design.

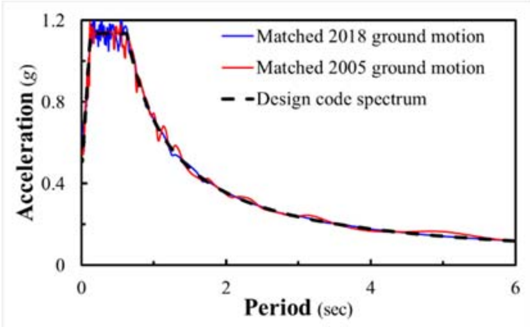

Figure 10. Spectrum matched result of ground motion with/out near-fault phenomenon

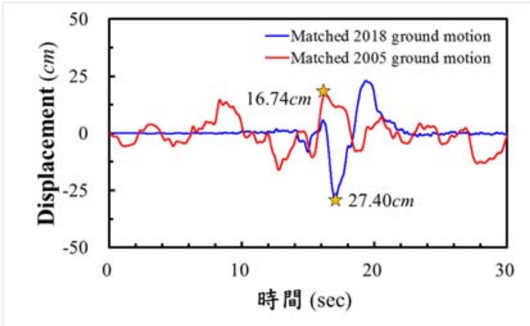

Figure 11. Comparison of isolation displacement responses

References

J. W. Baker, "Quantitative classification of near-fault ground motions using wavelet analysis," Bulletin of the Seismological Society of America, Vol.97, No.5, pp. 1486-1501, 2007.

C. H. Zhai, Z. W. Chang, S. Li, Z. Q. Chen, and L. L. Xie, "Quantitative identification of near-fault pulse-like ground motions based on energy." Bulletin of the Seismological Society of America, Vol.103, No.5, pp. 2591-2603, 2013.

R. S. Jangid, and J. M. Kelly, "Base isolation for near-fault motions." Earthquake Engineering & Structural Dynamics, Vol.30, No.5, pp. 691-707, 2001.

Parametric Study of Sloped Sliding-Type Bearing

Chih-Kuan Lin[1], Cho-Yen Yang[2], Shiang-Jung Wang[3], Wang-Chuen Lin[4], Chung-Han Yu[2], Lap-Loi Chung[5] and Kuo-Chun Chang[6]

林致寬[1] 楊卓諺[2] 汪向榮[3] 林旺春[4] 游忠翰[2] 鍾立來[5] 張國鎮[6]

Abstract

Seismic isolation design has been regarded as one of the most effective strategies to reduce seismic threat to must-be protected targets, including structures, bridges, and equipment. Recently, much research has aimed at developing nonlinear seismic isolation systems. The sloped sliding-type bearing can achieve the nonlinear goal by mechanically designing a simple slope. Therefore, this bearing does not have a fixed isolation frequency. In addition, seismic isolation performance can be realized through the sliding mechanism, an inherent self-centering capability can be achieved through the slope design, and the sliding friction can contribute an excellent energy dissipation capability. In this study, the equation of motion of the bearing is first deduced. A sensitivity analysis is then performed, whose results demonstrate that the maximum acceleration transmitted to the superstructure is dependent on two important design parameters, the sliding friction coefficient and sloping angle, and most importantly, it is unaffected by various external disturbances. The maximum acceleration after isolation is precisely controlled by the two design parameters.

Keywords: seismic isolation, sloped sliding, nonlinear, sensitivity analysis, numerical simulation

Introduction

Conventional seismic isolators have a linear restoring force, and the isolation system composed of these bearings has a fixed isolation frequency. If the main frequency of an earthquake coincides with the isolation frequency, it may cause response amplification due to resonance and could even lead to the failure of the seismic isolation design. Therefore, recently, research toward developing nonlinear seismic isolation systems has attracted immense attention. The nonlinear characteristic has been achieved through the design of various mechanisms that guarantee seismic isolation performance and thus avoid resonance. In this study, a new type of nonlinear sliding-type isolation bearing-sloped sliding-type bearing (SSB) will be introduced and studied. First, its simplified equation of motion is theoretically derived. Then, sensitivity analysis is performed to numerically discuss the influence of two important design parameters, sliding friction coefficients and sloping angles, on its dynamic behavior and seismic isolation performance.

Equation of Motion

To simplify the derivation, several reasonable assumptions are made. First, it is assumed that SSBs are only subjected to a horizontal uniaxial seismic wave and the assumption of small sloping angles is applied. In addition, the following assumptions were made: (1) The superstructure is regarded as a rigid body; (2) The pounding effect when the slider is passing through the intersection of two slopes is neglected; (3) The influence of the force component of horizontal disturbance on the normal force exerting on the slope is neglected; (4) The vertical responses arising from horizontal disturbance are neglected, and vice versa. The simplified single-degree-of-freedom (SDOF) analytical model of a rigid superstructure isolated with SSBs is shown in Fig. 1, in which m is the total mass of the superstructure; θ is the sloping

[1] Graduate Student, National Taiwan University
[2] Assistant Researcher, National Center for Research on Earthquake Engineering
[3] Associate Professor, National Taiwan University of Science and Technology
[4] Associate Researcher, National Center for Research on Earthquake Engineering
[5] Deputy Director General, National Center for Research on Earthquake Engineering
[6] Professor, National Taiwan University

angle; μ is the sliding friction whose positive sense is the same as the positive x axis; and $\ddot{u}_g$ is the input ground acceleration. The equation of motion shown as Eq. (1) can be derived by using Lagrange's equation.

$$m\left(1+\tan^2\theta\cdot\mathrm{sgn}(x)^2\right)\ddot{x}+mg\tan\theta\cdot\mathrm{sgn}(x)+f\sec\theta=-m\ddot{x}_g \tag{1}$$

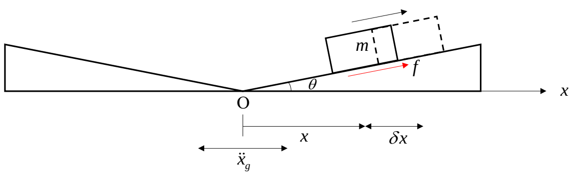

Fig. 1. A simplified SDOF model for a seismically isolated structure with SSBs

Parametric Study

Based on the derived equation of motion as given in Eq. (1) and considering the varied sliding friction coefficients and sloping angles, the influences arising from the two design parameters on the seismic performance of SSBs subjected to periodic harmonic excitation are numerically discussed. To have an insight into the steady-state response of SSBs under external disturbance and to minimize the effect of the transient response, a uniaxial periodic harmonic excitation with a linearly increasing amplitude is taken into consideration until reaching the target peak ground acceleration (PGA), which is demonstrated in Fig. 2. The sensitivities of the following two author-defined performance indices to the two design parameters and characteristics of external disturbances are numerically discussed. To have a better and more direct expression in the following, the original design parameter μ will be replaced by a normalized friction coefficient $\mu g/\mathrm{PGA}$, which is also a dimensionless physical quantity. The peak acceleration index (I_{acc}) is a dimensionless ratio of the maximum transmitted acceleration to the PGA, which is used for discussing the influences of the two design parameters of SSBs and the characteristics of the external disturbance on the transmitted acceleration response.

$$I_{acc}=\frac{\left|\ddot{x}^t\right|_{\max}}{\mathrm{PGA}}=\frac{g\tan\theta}{\mathrm{PGA}}+\frac{\mu g}{\mathrm{PGA}} \tag{2}$$

The peak displacement index (I_{disp}) is a ratio of the maximum isolation displacement to the PGA value, which has the dimensions of time squared and is used for discussing the influences of the two design parameters of the SSBs and the characteristics of the external disturbance on the isolation displacement response. With the same I_{acc}, if I_{disp} is smaller, it means that the seismic isolation design is more space efficient.

$$I_{disp}=\frac{|x|_{\max}}{\mathrm{PGA}} \tag{3}$$

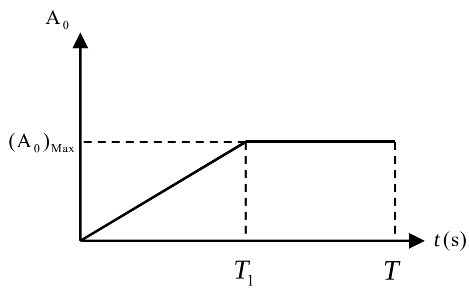

Fig. 2. Illustration of the amplitude of harmonic disturbance varying with time

In the numerical model of SSBs, assume that the isolated superstructure mass m is 34.08 tons. The sloping angle is designed to be 1.5°. The normalized friction coefficient $\mu g/\mathrm{PGA}$ changes from 0.05 to 1.2. Since the frequency contents of most earthquake records vary from 0.1 to 1 second, a harmonic excitation with a disturbance frequency of 2 Hz, i.e., f_g =2 Hz, was chosen. Four different target PGA levels (0.2, 0.4, 0.6, and 0.8 g) are considered for $(A_0)_{\max}$ in Fig. 2. The influences of $\mu g/\mathrm{PGA}$ on I_{acc} and I_{disp} under harmonic excitation are presented in Fig. 3. As observed from Fig. 3(a) and Eq. (2), when SSBs perform well, I_{acc} is linearly proportional to $\mu g/\mathrm{PGA}$ with a slope of 1 and a vertical axis intercept of $\frac{g\tan\theta}{\mathrm{PGA}}$ until I_{acc} reaches the upper bound and thus no seismic isolation performance is exhibited, i.e., I_{acc}=1. The greater the PGA value, the smaller $\frac{g\tan\theta}{\mathrm{PGA}}$ obtained, and I_{acc} will reach the upper bound at the value of $\frac{g\tan\theta}{\mathrm{PGA}}$ closer to 1. From Fig. 3(b), I_{disp} is inversely proportional to $\mu g/\mathrm{PGA}$ until I_{disp} reaches zero and thus no seismic isolation performance is exhibited. In addition, with the same $\mu g/\mathrm{PGA}$, it can be seen that I_{acc} and I_{disp} are different under diverse PGA levels. The smaller the PGA value, the greater I_{acc} and I_{disp} obtained. Nevertheless, with the same μ, there is no difference to the maximum transmitted acceleration under different PGA levels, which coincides with the observed results from the equation of motion as given in Eqs. (1) and (2).

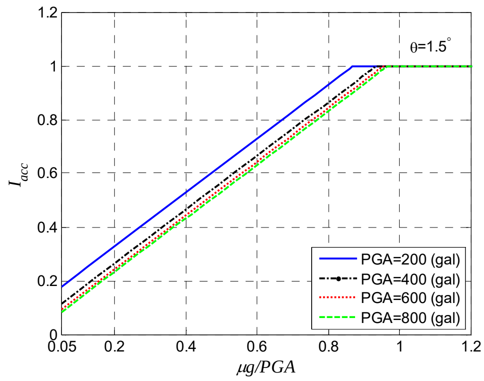

Fig. 3(a). Relationship of $\mu g / \mathrm{PGA}$ and I_{acc}

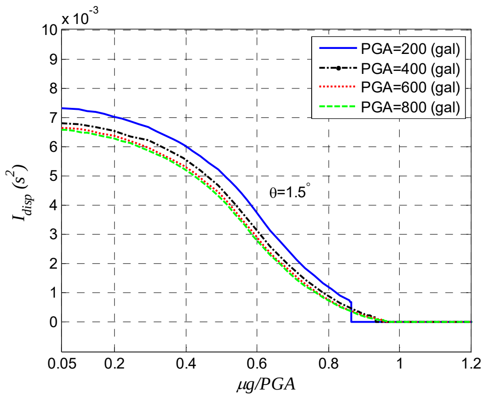

Fig. 3(b). Relationship of $\mu g / \mathrm{PGA}$ and I_{disp}

On the other hand, assume that m is 34.08 ton and the sliding friction coefficients are designed to be 0.01, 0.06, and 0.1. The sloping angles θ changes from 0.5° to 5° with an interval of 0.5°. As observed from Eq. (2), with $\theta = 0.5°$ and $\mu = 0.1$, the seismic isolation mechanism cannot be activated until the target PGA reaches at least 0.184 g. Therefore, $(A_0)_{\max} = 0.4$ g and $f_g = 2$ Hz are, respectively, taken as the target PGA and disturbance frequency of the harmonic excitation. The influences of θ on I_{acc} and I_{disp} under harmonic excitation are presented in Fig. 4. As can be seen from Fig. 4(a), the increase of θ will lead to an increase of I_{acc}. There exists an approximately linear relationship between I_{acc} and θ. Based on the assumption of small angles, Eq. (2) can be rewritten as

$$I_{acc} \approx \frac{g\theta}{\mathrm{PGA}} + \frac{\mu g}{\mathrm{PGA}} \tag{4}$$

From Eq. (4), I_{acc} is linearly proportional to θ with a slope of g / PGA and a vertical axis intercept of $\mu g / \mathrm{PGA}$. In other words, I_{acc} will linearly increase when θ is enlarged. As observed from Fig. 4(b), the increase of θ will lead to an increase of I_{disp}, and there exists an approximately linear relationship between I_{disp} and θ. This is based on the assumption that with the same target PGA and μ, the maximum relative acceleration of SSBs also increases with an increase of θ. The approximate relation between the steady-state maximum relative acceleration response $\left|\ddot{x}_{steady}\right|_{\max}$ and the steady-state maximum isolation displacement response $\left|x_{steady}\right|_{\max}$ as given in Eq. (5) shows that the maximum isolation displacement response also increases linearly as θ is enlarged. In addition, the increase of μ will cause a decrease of I_{disp}.

$$\left|x_{steady}\right|_{\max} = \frac{\left|\ddot{x}_{steady}\right|_{\max}}{(2\pi f_g)^2} \tag{5}$$

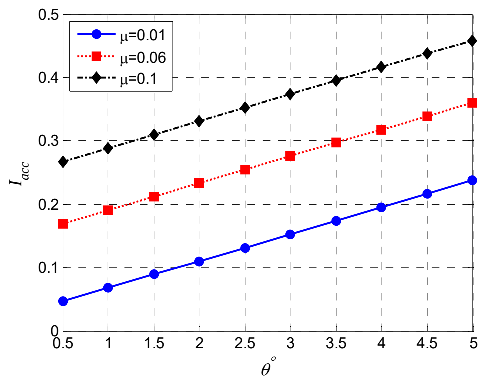

Fig. 4(a). Relationship of θ and I_{acc}

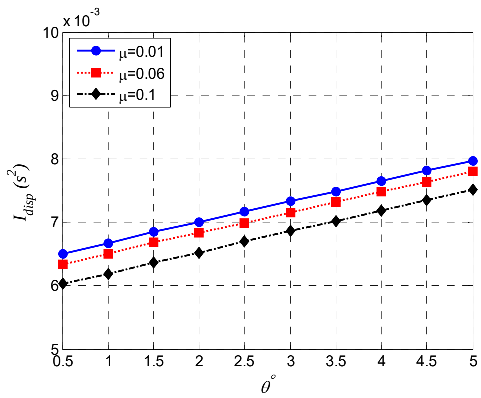

Fig. 4(b). Relationship of θ and I_{disp}

In the numerical model of SSBs, assume that m = 34.08 ton, and the sliding friction coefficient and sloping angle are designed to be 0.06° and 1.5°, respectively. Similarly, to ensure that the seismic isolation functions, 0.4 g is taken as the target PGA of the harmonic excitation as illustrated in Fig. 2, i.e., $(A_0)_{\max}$ = 0.4 g. Since the frequency contents of most earthquake records vary from 0.1 to 1 second, the disturbance frequencies of the harmonic excitation (f_g) were chosen to vary from 0.1 to 10 Hz. The influences of f_g on I_{acc} and I_{disp} under harmonic excitation are presented in Figs. 5(a) and 5(b), respectively. As observed from Fig. 5(a) and Eq. (2), regardless of any change of f_g , I_{acc} remains constant, implying that I_{acc} is independent of f_g . That is, the maximum transmitted acceleration will not change with varying f_g . As can be seen from Fig. 5(b), the logarithm of I_{disp} is inversely proportional to that of f_g with a negative and constant slope. This is based on the assumption that with the same target PGA, the maximum isolation displacement of SSBs will not change with varying f_g . Therefore, as observed from Eq. (5), when $\left|\ddot{x}_{steady}\right|_{\max}$ remains unchanged, $\left|x_{steady}\right|_{\max}$ is inversely proportional to the square of f_g , which coincides with the linear relation between the logarithms of f_g and I_{disp} with a slope of -2 as shown in Fig. 5(b). In short, the analysis results under harmonic excitation show that the maximum transmitted acceleration is insensitive to the change of f_g , which demonstrates that SSBs do not have a fixed isolation frequency and will not resonate with a harmonic external disturbance at a specific frequency. In addition, the maximum isolation displacement is inversely proportional to the square of f_g . In other words, a larger isolation displacement will be obtained when SSBs are subjected to a harmonic excitation with a lower disturbance frequency.

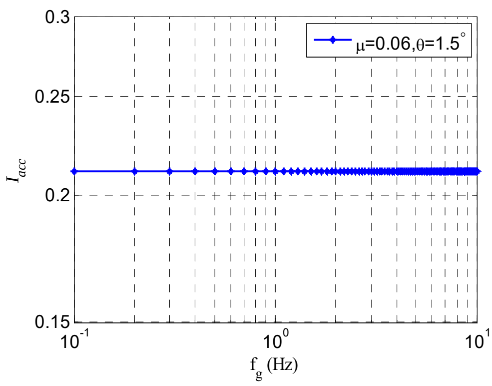

Fig. 5(a). Relationship of f_g and I_{acc}

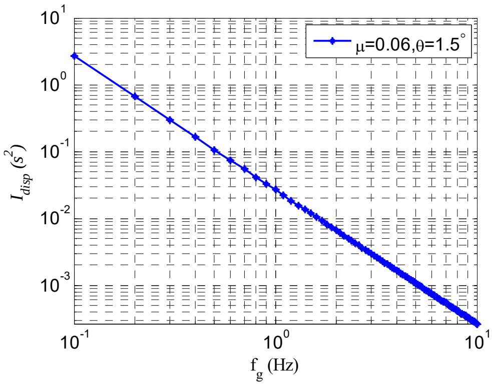

Fig. 5(b). Relationship of f_g and I_{disp}

Conclusions

According to the sensitivity analysis results under harmonic excitation, no matter what and how large the external disturbance is, the maximum transmitted acceleration of the SSBs will remain constant. If the SSBs are designed with a greater sliding friction coefficient, the maximum transmitted acceleration will linearly increase, whereas the maximum isolation displacement will be reduced. In addition, with a larger sloping angle, the maximum transmitted acceleration will linearly increase. The sensitivity analysis results under harmonic excitation indicate that with a larger sloping angle, the maximum isolation displacement will linearly increase. In addition, the maximum transmitted acceleration is not sensitive to changes in the disturbance frequency. However, the lower the disturbance frequency, the greater the maximum isolation displacement obtained.

References

Shiang-Jung Wang, Jenn-Shin Hwang, Kuo-Chun Chang, Chia-Yi Shiau,Wang-Chuen Lin, Mu-Sen Tsai, Jia-Xiang Hong and Yin-Han Yang, "Sloped multi-roller isolation devices for seismic protection of equipment and facilities", Earthquake Engineering & Structural Dynamics (2014).

Wei Xiong, Shan-Jun Zhang, Li-Zhong Jiang and Yao-Zhuang Li, "Introduction of the convex friction system (CFS) for seismic isolation", Structural Control And Health Monitoring (2016).

Online Model Updating for Hybrid Simulations of a Steel Panel Damper Substructure

Ming-Chieh Chuang [1]

莊明介 [1]

Abstract

Hybrid simulations allow for the integration of numerical and physical substructures, such that the interaction between them can be taken into account in a seismic performance assessment. As a result, hybrid simulation can offer a cost-effective alternative to the shaking table test. However, conventional hybrid simulations are always restricted by the limited number of facilities and specimens. Some or many structural elements that are similar to or the same as the physical substructures (PS), must be modeled in hybrid simulations. Thus, the advantages and applicability of hybrid simulations diminish as a result of inaccurate modeling of the numerical substructures (NS). To address this problem, the gradient-based parameter identification (PI) method for Online Model Updating (OMU) was proposed by the researchers of Taiwan's National Center for Research on Earthquake Engineering (NCREE). A novelty of the proposed PI method is to identify certain parts of parameters during identification stages for different stress states, leading to a reduction in the number of design variables to be determined. The time consumed in computing the gradients can be reduced accordingly to improve the identification efficiency. In this study, the proposed PI method is applied to OMU schemes for hybrid simulations of a steel panel damper (SPD) substructure conducted using a multi-axial testing system at the NCREE in 2017. The structure under investigation is a three-dimensional, six-story moment-resisting frame with four SPDs installed on each story. In the hybrid simulations, only one SPD is represented with the PS, and the rest of the structure is represented with the NS. Through OMU, the proper parameter values of the constitutive model that are utilized to represent the observed force vs. deformation relationships of the PS, namely the SPD specimen, can be identified effectively. With the identified parameter values, the material models of relevant SPD elements in the NS can be rectified online during the hybrid simulations. The accuracy of the hybrid simulations can be improved accordingly. The actual hybrid simulations of the SPD substructure demonstrate the effectiveness and benefits of OMU with the proposed PI method for advanced hybrid simulations.

Keywords: Parameter identification, model updating, hybrid simulation, optimization, steel panel damper

Introduction

In a hybrid simulation (HS), the target structure under investigation can be partitioned into multiple substructures. These substructures can be divided into two categories: the numerical substructure (NS) and the physical substructure (PS). Hybrid simulation allows the numerical and physical substructures to be integrated such that the interaction between them can be taken into account in a seismic performance assessment. As a result, hybrid simulation can offer a cost-effective alternative to the shaking table test for investigating large-scale target structures.

In general, multi-story seismic-resistant buildings are often equipped with many dampers. Distributed damage or plasticity can be expected when the building is subjected to a high-intensity earthquake. To investigate the seismic behavior of such a structure with distributed plasticity developing on dampers using a hybrid simulation, several PSs corresponding to the dampers are required, as shown in Fig. 1. However, the strategy of using a conventional hybrid simulation is usually restricted, owing to the limited

[1] Assistant Researcher, National Center for Research on Earthquake Engineering

numbers of experimental facilities and specimens. Figure 2 shows an example of a hybrid simulation in which only one damper, out of a five-story frame equipped with four dampers, is physically represented as the PS. The remainder of the target structure, comprising a moment-resisting frame (MRF) and three dampers, is numerically modeled as an NS while the hybrid simulation is conducted. However, there will be challenges in modeling the nonlinear behavior of dampers in the NS. Improper numerical modeling of the dampers is likely to jeopardize the accuracy of the hybrid simulation. Thus, the applicability and benefits of hybrid simulation will diminish.

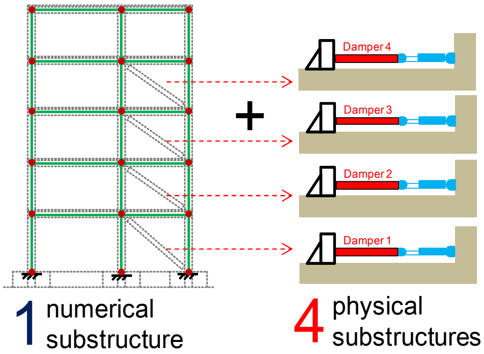

Fig. 1. Hybrid simulation with one NS and four PSs.

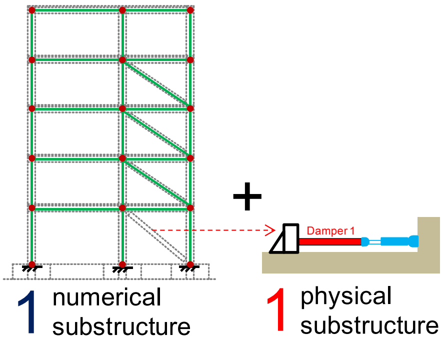

Fig. 2. Hybrid simulation with one NS and one PS.

To address these problems, the development of online model updating (OMU) has attracted increasing attention (Chuang *et al.*, 2018; Wang *et al.*, 2018). Through advanced hybrid simulation with OMU, the proper parameter values used to represent damper behavior can be calibrated or identified using experimental data measured from the PS. With the identified parameter values, the material models of relevant damper elements in the NS can be rectified online during the hybrid simulation. Based on recent research (Chuang *et al.*, 2018) and experiments (Wang *et al.*, 2018) conducted by Taiwan's National Center for Research on Earthquake Engineering (NCREE), this paper presents an advanced hybrid simulation with OMU and demonstrates the effectiveness and benefit of using OMU via actual hybrid simulations on a steel panel damper substructure.

Hybrid Simulation of a Six-story SPD-MRF

The steel panel damper (SPD) (Tsai *et al.*, 2018) is an energy-dissipation device that promotes the shear yielding mechanism of a steel wide-flanged section to dissipate earthquake-induced input energy. To experimentally investigate the performance of the SPD and the MRF equipped with SPDs (SPD-MRF) during seismic events, the NCREE researchers conducted a series of hybrid simulations performed on the SPD specimen by using a multi-axial testing system (MATS) (Fig. 3) (Wang *et al.*, 2018). The target structure under investigation was a three-dimensional, six-story MRF equipped with 24 SPDs, with four SPDs installed at each story. The details of the six-story SPD-MRF were documented by Tsai *et al.* (2018).

According to results from a series of nonlinear response history analyses conducted on the same six-story SPD-MRF (Tsai *et al.*, 2018), it can be found that the 3rd story SPDs exhibited the most nonlinearity during the selected seismic excitations. Thus, the north-west 3rd story SPD (Wang *et al.*, 2018) was chosen as the physical specimen. However, only the north-west SPD installed on the 3rd story was tested as a PS in the hybrid simulation, as shown in Fig. 3. Since the SPD-MRF is a symmetric-plane building, the other three SPDs on the same story were modeled using the duplicated PS responses via the RecdexElement objects (Wang *et al.*, 2018). Clearly, it is natural to represent the remaining twenty SPDs numerically as the NS.

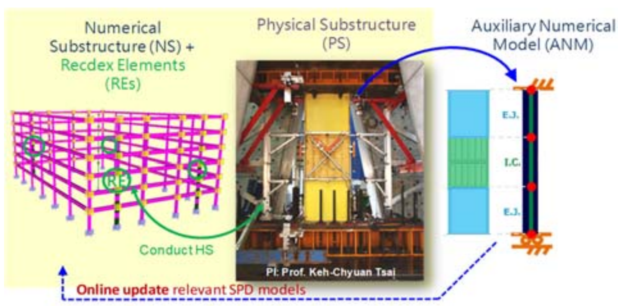

Fig. 3. Advanced hybrid simulation with online model updating.

To numerically simulate the nonlinear behavior of the SPD for the NS or an auxiliary numerical model (ANM) (Fig. 3), the three-segment SPD, which comprises one inelastic core (IC) and two elastic joints (EJ), is represented using three beam–column elements. The two-surface plasticity material model (Dafalias and Popov, 1975), combining the isotropic and kinematic hardening effects, is adopted for the beam–column element used for the IC segment. Fortunately, PISA3D (Lin *et al.*, 2009), the nonlinear structural analysis program developed by the NCREE, offers both beam–column elements and the two-surface model, which is called the hardening material model in PISA3D. Hence, in this study, PISA3D was utilized to construct the SPD analytical model for SPDs of the NS and the ANM of the hybrid simulations with OMU.

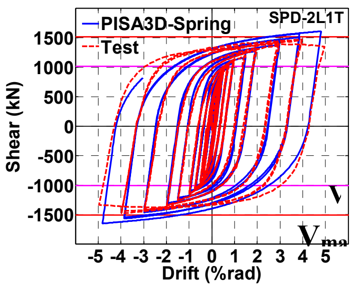

Fig. 4. Experimental and PISA3D numerical SPD shear vs. drift ratio relationships for the SPD specimen SPD-2L1T (Tsai *et al.*, 2018).

By using the proposed parameter identification (PI) method (Chuang *et al.*, 2018), the proper parameter values of the two-surface models of the ICs of the ANM, which can numerically represent the PS, can be identified. Through the OMU technique, the parameter values of the two-surface models of the ICs of these relevant SPDs of the NS can be updated with the aforementioned identified parameter values during the hybrid simulation. The proposed gradient-based PI method was verified in the previous study (Chuang *et al.*, 2018) and employed in the hybrid simulations of the SPD-MRF for efficiently performing the OMU.

Proposed Gradient-based Method for Parameter Identification

When the analytical results are compared with the experimental responses, the simulation errors can be evaluated by the root-mean-square error (RMSE) as follows:

$$\mathrm{RMSE}=\sqrt{\frac{\sum_{i=1}^{n}\left(r_{sim}{}^{(i)}-r_{\exp}{}^{(i)}\right)^2}{n}}, \tag{1}$$

where r_{sim} and r_{exp} are the analytical and experimental results of the SPD shear, respectively. Furthermore, i indicates the ith experimental data point and n indicates the total number of data points used for evaluation. In the study, for online model updating, Equation (1) was used as the objective function $F(X)$ to identify the approximate best-fit parameter values. Thus, the optimization problem of model fitting can be expressed as:

$$min\ F\left(X\right) \tag{2}$$

$$\text{subject to } X\in R^6,$$

where X = [Parameter Ratio (PR) of *Hiso1*+, PR of *Hiso2*+, PR of *Hiso1*−, PR of *Hiso2*−, PR of *Hkin1*, PR of *Hkin2*]^{T} as the design vector while parameter identification with the optimization method is conducted. It should be noted that the six hardening parameters (*i.e.*, *Hiso1*+, *Hiso2*+, *Hiso1*−, *Hiso2*−, *Hkin1*, *Hkin2*) are normalized for the design variables. Thus, the six design variables are dimensionless parameters in the proposed parameter identification method presented later. Finding a set of parameter values that can reduce simulation errors compared to the observed experimental response can be achieved by solving the constrained optimization problem with a single objective function, as in Equation (1).

In the proposed gradient-based parameter identification method for OMU (Chuang *et al.*, 2018), the gradient of the parameters, as the design variables, must be computed using the finite difference method (FDM) with the perturbed parameter values. Specifically, the gradient is computed with a set of (m + 1) points in $\mathbf{R}^m$, where m indicates the total number of design variables. In the proposed method, the gradient descent method is adopted as a basis for parameter identification in OMU. The successive design variables from the kth step to the (k+1)th step can be obtained with:

$$X_{k+1}=X_k-\lambda_k\nabla F\left(X_k\right), \tag{3}$$

where λ_k is a positive scalar parameter used as the reduction factor to set the perturbed values in the iteration procedures. Whenever the gradient is nonzero, $-\nabla$ F(X_k) represents the descent direction at X_k for the kth step. While the OMU is conducted, the parameter identification for model updating can be resolved with the ANM. By monitoring the stress state of the two-surface model of the ANM including the elastic, isotropic hardening, and kinematic hardening, a novel modification of the classical gradient descent method is proposed to identify certain parts of parameters during the identification stages for different stress states, leading to a reduction of the number of design variables to be determined. The time spent on computing the gradients can be reduced accordingly to improve the identification efficiency.

Results of OMU of the Hybrid Simulation

In the hybrid simulations of the SPD-MRF, the PI operation was conducted on a computer with general specifications (Intel® Core™ i7-2600 3.40 GHz processor and 12 GB of RAM). The PI operations are carried out every three integration steps. For most operations, it takes less than 10 s (6 iterations) to identify the most appropriate parameter values. This suggests that the proposed OMU is applicable for hybrid simulations without real-time requirements. OMU of the relevant SPD elements of the NS with the identified parameter values were carried out until 12.5 s, when the peak ground acceleration had occurred. At that moment, the hardening parameter values were expected to have already been identified since the SPD specimen should have already experienced large enough deformations in the test.

Figure 5 shows a portion of the time history of the normalized identified values of the four material parameters. It should be noted that the normalized values all remain at 1.0 prior to around the 1100th step. In other words, the PI operation was not triggered until the experiment progressed to around the 1100th step, when the ANM numerically representing the SPD specimen started to experience inelastic responses. At this moment, as can be clearly found in Fig. 5, the values of *Hiso1+* and *Hiso2+* started to vary while the values of *Hkin1* and *Hkin2* remained unchanged. This suggests that the involved plasticity at this moment is in the isotropic hardening state. Kinematic hardening did not occur until around the 1137th step. It is also evident that, at any time instance, the PI operation is either not triggered (the SPD specimen is in the elastic range) or is working on either isotropic or kinematic hardening parameters only.

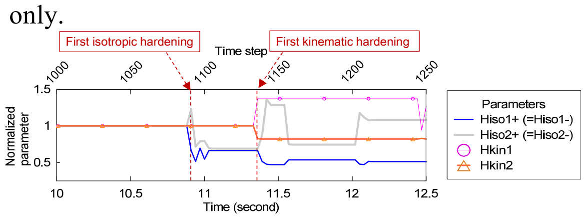

Fig. 5. Results of parameter identification using the proposed gradient-based method.

Figure 6 compares the experimental results with the ANM hysteresis, which is obtained by using parameter values that are continuously identified from the test results. It is evident that the proposed gradient-based PI method can significantly improve the accuracy of ANM for modelling SPD hysteresis.

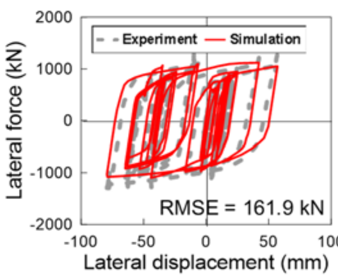

Fig. 6. Shear vs. drift ratio relationships for the PS and the ANM.

Conclusions

The OMU technique effectively identified the proper parameter values of the two-surface model to represent the physical SPD specimen hysteresis, and accordingly updated the numerical models of relevant SPD elements to enhance the model fidelity of the NS. As a result, the accuracy of the hybrid simulation can be improved. The novelty of the proposed gradient-based PI method is to identify certain parts of parameters during the identification stages for different stress states, leading to a reduction in the number of design variables to be determined. The time consumed in computing the gradients can be reduced accordingly to improve the identification efficiency. The effectiveness of the proposed gradient-based PI method for OMU has been verified by using the hybrid simulations of the six-story SPD-MRF.

References

Chuang MC, Hsieh SH, Tsai KC, Li CH, Wang KJ, Wu AC. (2018). Parameter identification for on-line model updating in hybrid simulations using a gradient-based method. *Earthquake Engineering and Structural Dynamics*, **47**(2): 269-293.

Dafalias YF, Popov, EP. (1975). A model of nonlinearly hardening materials for complex loading. *Acta Mechanica*, **21**(3): 173-192.

Lin BZ, Chuang MC, Tsai KC. (2009). Object-oriented development and application of a nonlinear structural analysis framework. *Advances in Engineering Software*, **40**(1): 66-82.

Tsai KC, Hsu CH, Li CH, Chin PY. (2018). Experimental and analytical investigations of steel panel dampers for seismic applications in steel moment frames. *Earthquake Engineering and Structural Dynamics*, DOI: 10.1002/eqe.3023.

Wang KJ, Chuang MC, Tsai KC, Li CH, Chin PY, Chueh SY. (2018). Hybrid testing with model updating on steel panel damper substructures using a multi-axial testing system. *Earthquake Engineering and Structural Dynamics*, DOI: 10.1002/eqe.3139.

Development of Reginal Seismic Source Characteristic Zones in and around Taiwan

Hsun-Jen Liu[1] and Chih-Wei Chang[2]

劉勛仁 [1]、張志偉 [2]

Abstract

The identification and recreation of the characteristic activity of seismic sources in time and space are part of frontline seismic hazard analysis. The classification of seismic sources mainly identifies active faults, subduction zones, and undetermined structures. Undetermined structures refer to all the other types of seismic sources, including blind faults that have not yet ruptured to ground surface and questionable faults that exhibit the offset characteristic but require confirmation. With respect to the geometric modeling of seismic sources, because rupture locations and direction of source movement in a subduction intraslab or questionable fault are undetermined, the customary measure is to delineate a zone consisting similar seismic source features to show that an earthquake may occur at any location within this area; these sources are called areal sources. According to the tectonic evolution theory of modern Taiwan and the latest relocated earthquake catalog, this study proposes an areal source characteristic model for Taiwan. This model completely divides shallow, deep, and subduction earthquakes and covers the spatial range of 19°–29°N, 115°–126°E, extending 300-km deep. Additionally, this study details the characteristic parameters of historical maximum earthquake magnitude, earthquake activity rate, a focal depth distribution model, and the focal mechanism of each subzone for the purpose of undertaking probabilistic seismic hazard analysis; the broad subzone is fit to conduct spatial analysis for seismic activity parameters.

Keywords: areal source zones, seismic source characteristic parameters, Taiwan region, seismic hazard analysis

Introduction

Taiwan is located on the convergent zone between the Philippine Sea Plate and the Eurasian Plate, and its tectonic structures include faults, subduction zones, and oceanic and continental plates. Seismic sources mainly consist of active faults, subduction interfaces, subduction intraslabs, and undetermined structures. The term undetermined structure refers to all seismic sources generated by something other than an active fault or subduction zone, including blind faults that have not ruptured to ground surface and questionable faults that exhibit the offset characteristic but require further confirmation.

With respect to the construction of a geometrical seismic source model in seismic hazard analysis, sources in an active fault or a subduction interface can be incorporated into a three-dimensional (3-D) rupture plane according to adequate historical earthquake data or geological survey evidence because the active fault or subduction interface features notable geometric patterns, dislocation mechanisms, and activity levels; these sources are called fault sources. Because rupture locations and directions of source movement in a subduction intraslab or a questionable fault are undetermined, the customary measure is to delineate a zone consisting similar seismic source features to show that an earthquake may occur at any location within this area; these sources are called areal sources.

On the basis of seismic hazard analysis, scholars such as Tsai et al. (1987), Loh et al. (1994), and Cheng (2002) have developed Taiwan areal source models. These models have covered the study range within 119°–124°E and 21°–26°N, where earthquakes were categorized into shallow, deep, and subduction earthquakes. In the past, such models have been

1 Assistant Researcher, National Center for Research on Earthquake Engineering, hjliu@ncree.narl.org.tw

2 Assistant Technologist, National Center for Research on Earthquake Engineering, chihwei@ncree.narl.org.tw

applied to comprehensively evaluate the seismic safety of major construction projects such as nuclear power plants and dams. Other zoning models established for the purpose of earthquake research include a model of the Taiwan neotectonic domains proposed by Shyu et al. (2005), four seismic zones in Taiwan modeled by Wu et al. (2007), a model of seven zones of seismic activities in Taiwan established by the Seismological Center of the Central Weather Bureau (2009), and the tectonic block model of crustal deformation proposed by Ching et al. (2011). Each model has its own purpose and study area, but none of them was established for the purpose of areal source hazard evaluation.

Because of the advancement of seismological technology, an increase in quality and volume of recorded data, and the increasingly demanding level of seismic safety in recent years, this study established an areal source characteristic model that meets the requirements of probabilistic seismic hazard analysis and reflects the seismicity distribution and tectonic characteristics of earthquakes in Taiwan. Specific features of this model are as follows: (1) Wide spatial range: the model territory covers 19°–29°N, 115°–126°E, and extends a depth of 300 km; (2) adequate seismic source delineation: on the basis of the tectonic evolution theory regarding modern Taiwan and the relocated earthquake data, a spatial analysis of seismic sources was conducted and earthquakes were divided into shallow, deep, and subduction earthquakes; (3) broad subzones: delineation from a macroscopic perspective facilitates the spatial analysis of relevant parameters of seismic activities such as the evaluation of smoothed-distributed seismic rate (Liu et al., 2018).

This study documented the results of evaluating the seismic characteristic parameters of each subzone in detail, including the maximum historical earthquake magnitude, earthquake activity rate, a focal depth distribution model, and the focal mechanism. The results were used to establish the areal source model for seismic hazard analysis and input documentation to serve as a reference for calculation.

Delineation of Areal Source Zones

In this study, the division of areal sources was mainly based on the following studies: (1) tectonic framework of Taiwan proposed by Teng (2004; 2007), (2) relocated earthquake catalog proposed by Wu et al. (2016), and (3) the 3-D geometric models of Ryukyu and Manila subduction zones established by Chang et al. (2018). Depending on type of seismic source, zones include shallow, deep, and subduction seismic sources. Figure 1 presents 2-D and 3-D zoning schemes for shallow, deep, and subduction sources. Table 1 lists the code, tectonic attribute, and depth range of each subzone. The details of seismic source zone models are as follows.

Table 1. Tectonic descriptions and depth ranges for areal source zones in this study

Subzone Code	Tectonic Attribute	Upper Margin Depth (km)	Lower Margin Depth (km)
	Shallow Source Zones		
ZS01	Taiwan Central Mountain Range and Western Foothill Range	0	35
ZS02	Transitional crust of the Okinawa Trough	0	35
ZS03	Oceanic crust of the Philippine Sea Plate	0	50
ZS04	Oceanic crust of the South China Sea	0	35
ZS05	Continental crust of the Taiwan Strait region	0	35
ZS06	Continental crust of the mainland Chinese region	0	35
	Deep Source Zones		
ZD01	Taiwan island and southwestern offshore region	35	300
ZD02	Okinawa Trench region	35	300
ZD03	Philippine Sea Plate region	50	300
ZD04	Manila Trench region	50	300
	Subduction Source Zones		
ZB01	Ryukyu beneath interface crustal zone	0	35
ZB02	Upper Ryukyu intraslab zone	35	100
ZB03	Middle Ryukyu intraslab zone	100	150
ZB04	Lower Ryukyu intraslab zone	150	300
ZB05	Manila beneath interface crustal zone	0	50
ZB06	Upper Manila intraslab zone	50	100
ZB07	Middle Manila intraslab zone	100	150
ZB08	Lower Manila intraslab zone	150	300

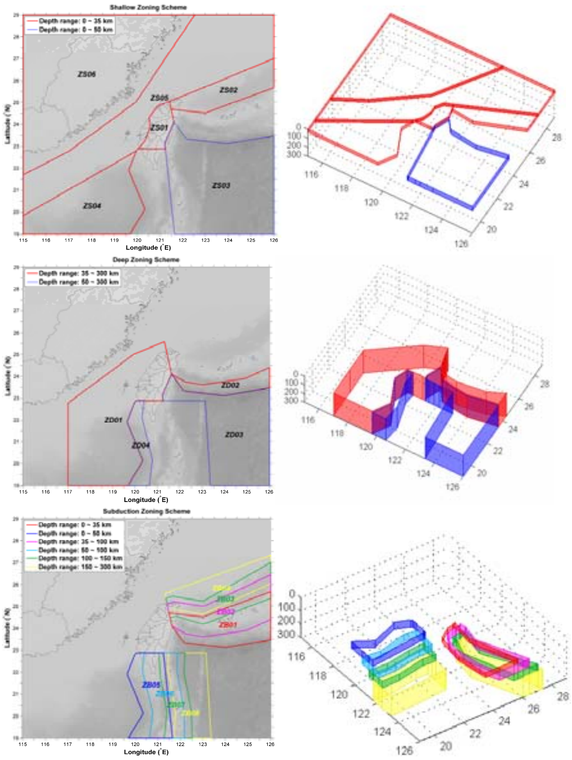

Fig. 1. The 2-D and 3-D zoning schemes for shallow, deep, and subduction sources from top to bottom.

Shallow Source Zones

According to the Quaternary tectonics of Taiwan which is based on the continent-arc collision evolving model proposed by Teng (2007) and the Cenozoic tectonic evolution of the China continental margin proposed by Teng and Lin (2004), a total of six subzones for shallow areal sources were established. These subzones are the Taiwan Central Mountain Range and the Western Foothill Range (ZS01), transitional crust of the Okinawa Trough (ZS02), oceanic crust of the Philippine Sea Plate (ZS03), oceanic crust of the South China Sea (ZS04), continental crust of the Taiwan Strait (ZS05), and the continental crust of the mainland Chinese region (ZS06). Overlaying the historical epicenter locations and seismic source mechanisms on the subzone model revealed that the model is representative of seismic activities and dislocation distributions.

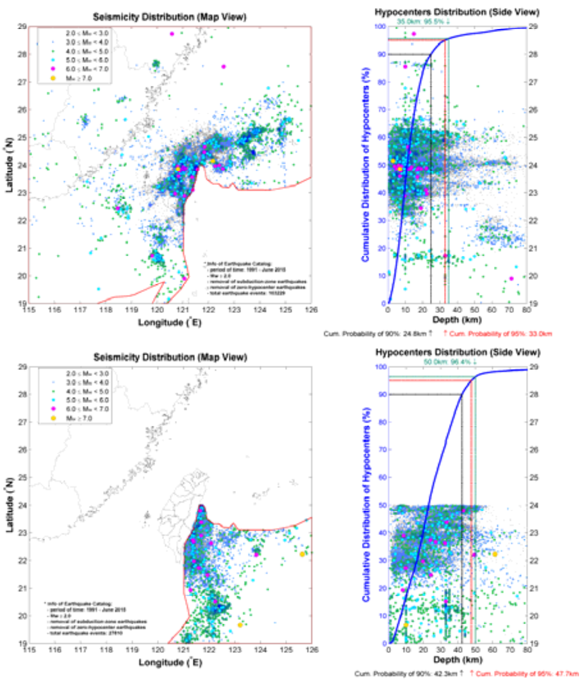

Fig. 2. Focal depth statistics for continental and oceanic crust areas from top to bottom.

The depth range of each subzone was set in accordance with the following data and statistical analysis results: (1) the relocated earthquake catalog between January 1991 and June 2015 with a moment magnitude scale (M_w) higher than 2.0, but excluding subduction earthquakes and those with a focal depth of zero. The Central Weather Bureau started modern and intensive seismic network in 1991, and a magnitude of 2.0 was the lowest detectable microseism at that time; (2) on the basis of the tectonic framework proposed by Teng (2007), the territory of Taiwan was divided into a continental crust area and an oceanic crust area. Then, the cumulative distribution statistics of historical focal depth, according to the aforementioned catalog, were determined for both areas. The results corresponded to a 95% confidence level for approximately 33 km and 48 km of depth (Figure 2). Finally, the depth of the shallow seismic source zone was set at 50 km for ZS03, which is oceanic crust area, and at 35 km for all other subzones with continental crust areas.

Subduction Source Zones

The delineations of the Ryukyu and Manila subduction zones was based on the research results of Chang et al. (2018), which entailed performance of a 3-D spatial analysis on the basis of the relocated earthquake catalog. Specifically, nine and seven cross-sections were made perpendicular to the Ryukyu Trench and the Manila Trench, respectively. Then, according to earthquake distribution within 15 km of both the left and right sides of the cross-section, the upper and lower margins of the subduction plate were extended to 300 km of depth and 50 km of width. Finally, the Kriging interpolation was applied to all the upper and lower margins of all cross-sections to construct the 3-D geometric model of the subduction zone.

Therefore, the four staircase-style subzones were established for the Ryukyu and Manila subduction zone sources in this study. These subzones, from top on down, are the beneath interface crustal zone (ZB01 and ZB05), upper subduction intraslab zone (ZB02 and ZB06), middle subduction intraslab zone (ZB03 and ZB07), and lower subduction intraslab zone (ZB04 and ZB08). Regarding the setting of the depth range of each subzone, ZB01 and ZB05 were set at 35 km and 50 km, respectively, according to the focal depth statistics of continental and oceanic crust areas presented in Figure 2. According to the cross-section diagram of the seismicity in the subduction zone established by Chang et al. (2018), seismic activity characteristics are different at 100 km and 150 km of depth; therefore, the subduction intraslab was divided into 3 subzones, with the deepest going to 300 km.

Deep Source Zones

According to the seismic distribution in areas other than the previously mentioned shallow and subduction zones, earthquakes of M_w 4.0 or higher and with focal depths of 35 km or more rarely occurred in the East China Sea area and the mainland China (Figure 3). Therefore, deep seismic source zones were established mainly on the southeast and southwest sides of Taiwan. A total of four subzones were established, namely Taiwan island and southwestern offshore regions (ZD01), Ryukyu Trench region (ZD02), Philippine Sea Plate region (ZD03), and Manila Trench region (ZD04).

Considering the locating error of a focal depth and the variability of the thickness of a plate in a subduction zone, the deep earthquakes that occurred vertical outside of a subduction intraslab were all categorized as subduction seismic sources. Therefore, no deep seismic source zone was established in upper or lower subduction intraslab zones. The depth range of each deep subzone was closely related to shallow and subduction zones. That is, the upper boundary of ZD01 and ZD02 was set at 35 km deep, whereas that of ZD03 and ZD04 was set at 50 km; the deepest was set at 300 km for all deep subzones.

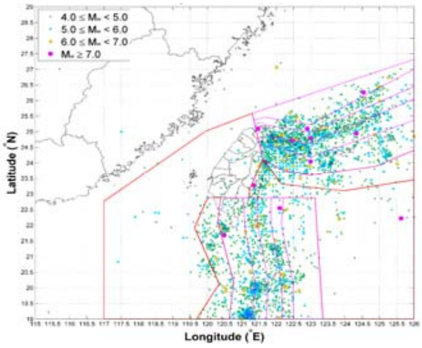

Fig. 3. The seismicity distribution with earthquakes of 4.0 or higher and with focal depths of 35 km or more overlapping with deep and subduction zones.

Seismic Source Characteristic Parameters of Each Subzone

Table 2 presents in detail the seismic source characteristic parameters of each subzone for the reference of hazard evaluation. Based on the relocated earthquake catalog published by Wu et al. (2016), each seismic source parameter was evaluated as follows:

Table 2. The lists of seismic source characteristic parameters of each subzone

Subzone Code	*b*-value	N(5.0)[1]	M_{max}[2]	Focal Depth Distribution Func.	Focal Mechanism[3] NM	SS	RV
Shallow Source Zones							
ZS01	1.006 (±0.044)	1.243	7.3	normal (μ=12.99, σ=7.38)	44	134	174
ZS02	1.006 (±0.038)	1.942	7.99	Normal (μ=15.75, σ=8.71)	61	38	4
ZS03	0.941 (±0.022)	4.867	7.3	Normal (μ=25.14, σ=12.10)	47	151	293
ZS04	1.243 (±0.101)	0.373	6.31	Normal (μ=20.88, σ=10.02)	10	1	0
ZS05	0.926 (±0.076)	0.439	6.71	Normal (μ=14.18, σ=7.33)	4	15	9
ZS06	0.654 (±0.087)	0.293	7.41	Normal (μ=17.19, σ=7.79)	0	0	0
Deep Source Zones							
ZD01	0.846 (±0.138)	0.157	6.57	Inv. triangular	7	4	3
ZD02	0.970 (±0.126)	0.292	6.7	Inv. triangular	2	11	15
ZD03	0.669 (±0.104)	0.179	7.25	Inv. triangular	2	2	0
ZD04	1.030 (±0.157)	0.239	6.5	Inv. triangular	3	4	7
Subduction Source Zones							
ZB01	0.935 (±0.021)	5.380	7.7	Normal (μ=19.50, σ=8.44)	57	176	276
ZB02	0.981 (±0.034)	2.687	7.7	Uniform	34	93	170
ZB03	0.937 (±0.050)	1.140	7.6	Uniform	15	28	30
ZB04	0.860 (±0.056)	0.926	7.8	Uniform	7	4	2
ZB05	1.102 (±0.030)	3.995	7.4	Normal (μ=28.77, σ=13.67)	75	54	112
ZB06	0.996 (±0.054)	1.233	7.4	Uniform	3	17	28
ZB07	0.912 (±0.131)	0.240	5.57	Uniform	3	3	6
ZB08	0.726 (±0.084)	0.400	6.9	Uniform	6	1	0

1. Maximum earthquake magnitude (M_{max}): The maximum M_w observed and recorded in the subzone since January 1900.
2. Earthquake activity rate: The maximum likelihood method (Weichert, 1980) was adopted to conduct regression analysis of *a*- and *b*-value of the G-R relation. The earthquakes rate with magnitude of M_w 5.0 and above (N(5.0)) and *b*-value and its standard deviation was calculated. The spatial-temporal completeness of earthquake catalog from 1900 to June 2015 was considered, and foreshocks, aftershocks, and fault earthquakes were excluded.
3. Focal depth distribution function: After examining the distribution trend of the focal depth of each zone, this study determined that the function of normal distribution, inverse triangular distribution, and uniform distribution should be applied for shallow, deep, and subduction zones, respectively. The mean value and standard deviation of normal distribution were obtained using the earthquake data of M_w 4.0 and higher from January 1991 to June 2015, excluding foreshocks, aftershocks, fault earthquakes, and those with a focal depth of zero.
4. Focal mechanism statistics: According to the rake angle, the faulting is divided into three types: (1) Reverse faults (30° to 150°), (2) strike–slip faults (−30° to 30°, −180° to −150°, and 150° to 180°), and (3) normal faults (−150° to 30°). The data used included earthquakes of M_w 4.0 and higher from January 1977 to June 2015, excluding foreshocks, aftershocks, and fault earthquakes.

Conclusions

This study proposed an areal source characteristic model for Taiwan based on the tectonic evolution of modern Taiwan, the relocated earthquake catalog, and the 3-D geometric models of the subduction zones. Figure 1 and Table 1 present the subzone delineations and Table 2 presents the seismic source characteristic parameters, which serve as reference for application of the high-level requirements of seismic hazard analysis.

References

Chang, Y. R., Chen, Y. P., Chang, Y. W., Liu, H. J., Chang, C. W., Chen, K. Y., Kuo, Y. P., and Chien, W. Y. (2018). “Development of 3-D Subduction Interface Models around Taiwan,” NCREE Research Programs and Accomplishments Report, 5-8. (in Chinese)

Teng, L. S. and Lin, A. T. (2004). “Cenozoic Tectonics of the China Continental Margin: Insights from Taiwan,” *Geological Society*, Special Publications, 226, pp. 313-332.

Teng, L. S. (2007). “Quaternary Tectonics of Taiwan,” Special Publication of the Central Geological Survey, MOEA, 18, 1-24.

Wu, Y. M., Cheng, S. N., and Liu, T. Y., (2016). “A Foundation and Basic Analysis of Earthquake Catalog and Historical Earthquakes Database,” Final report, prepared for Taiwan SSHAC Level 3 PSHA Project, 90 p.

Liu, H. J., Abrahamson, N. A., and Yeh, C. H. (2018) Development of adaptively smoothed seismicity model. 2017 NCREE Research Programs and Accomplishments Report, 129-132.

NARLabs

National Center for Research on Earthquake Engineering
No. 200, Sec. 3, Xinhai Rd., Taipei 10668, Taiwan(R.O.C.)
Tel: +886-2-6630-0888 Fax: +886-2-6630-0858
http://www.ncree.org.tw